

# **A New Search for the Neutron Electric Dipole Moment**

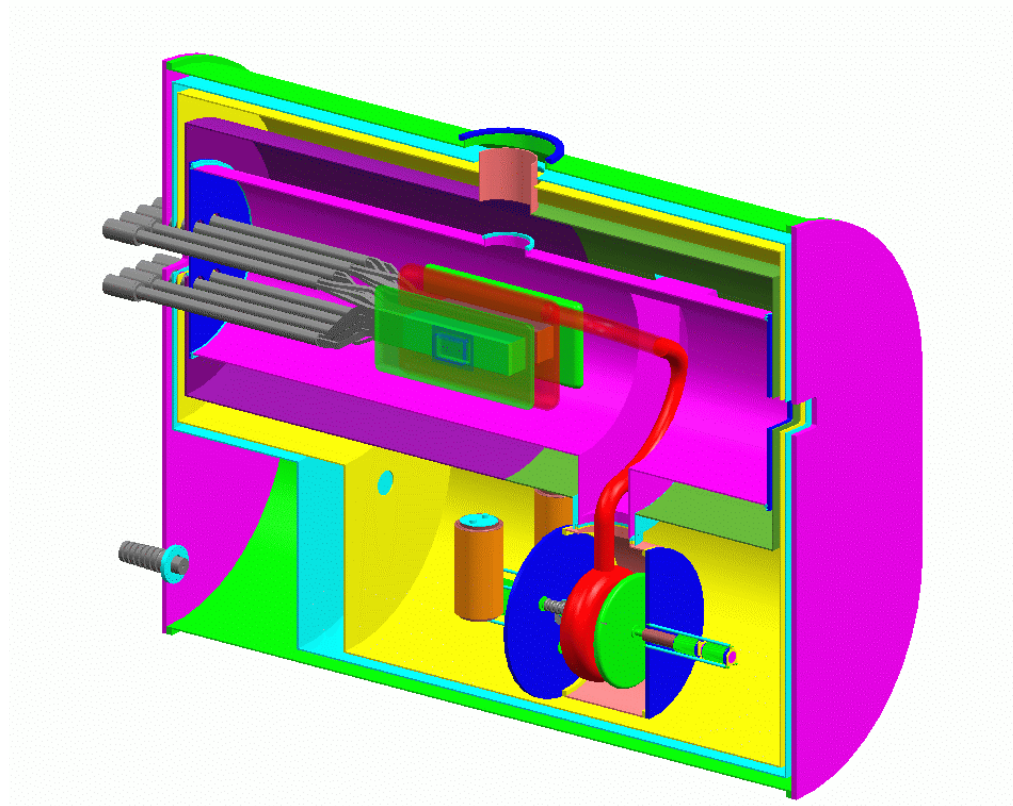
**Funding Pre-proposal**

**submitted to**

**The Department of Energy**

**prepared  
by**

**The EDM Collaboration**



**March 28, 2002**

# **A New Search for The Neutron Electric Dipole Moment**

**Funding Pre-proposal  
submitted to the  
The Department of Energy  
prepared by**

## **The EDM Collaboration**

D. Budker, A. Sushkov, V. Yashchuk  
*University of California at Berkeley, Berkeley, CA 94720, USA*  
B. Filippone, T. Ito, R. McKeown  
*California Institute of Technology, Pasadena, CA 91125, USA*  
R. Golub, K. Korobkina  
*Hahn-Meitner Institut, D-14109 Berlin, Germany*  
J. Doyle  
*Harvard University, Cambridge, MA 02138, USA*  
D. Beck, D. Hertzog, P. Kammel, J.-C. Peng, S. Williamson  
*University of Illinois, Urbana-Champaign, IL 61801, USA*  
J. Butterworth  
*Institut Laue-Langevin, BP 156 - 38042 Grenoble Cedex 9, France*  
G. Frossati  
*University of Leiden, NL-2300 RA Leiden, The Netherlands*  
P. Barnes, J. Boissevain, M. Cooper, M. Espy, S. Lamoreaux, A. Matlachov, R. Mischke,  
S. Penttila, J. Torgerson  
*Los Alamos National Laboratory, Los Alamos, NM 87545, USA*  
E. Beise, H. Breuer, P. Roos  
*University of Maryland, College Park, MD 20742, USA*  
D. Dutta, H. Gao  
*Massachusetts Institute of Technology, Cambridge, MA 02139, USA*  
T. Gentile, P. Huffman  
*National Institute of Standards and Technology, Gaithersburg, MD 20899, USA*  
A. Babkin, R. Duncan  
*University of New Mexico, Albuquerque, NM 87131, USA*  
V. Cianciolo  
*Oak Ridge National Laboratory, Oak Ridge, TN 37831, USA*  
M. Hayden  
*Simon-Fraser University, Burnaby, BC, Canada V5A 1S6*

**March 28, 2002**

# A New Search for the Neutron Electric Dipole Moment

## CONTENTS

|   |            |
|---|------------|
| SUMMARY.....  | iv         |
| <b>I. INTRODUCTION .....</b>  | <b>1</b>   |
| <b>II. PHYSICS MOTIVATION .....</b>                                     | <b>6</b>   |
| <b>III. STATUS OF EXISTING NEUTRON EDM MEASUREMENTS .....</b>           | <b>17</b>  |
| <b>IV. PROPOSED MEASUREMENT — OVERVIEW .....</b>                        | <b>34</b>  |
| <b>V. EXPERIMENTAL DESIGN ISSUES</b>                                    |            |
| <b>A. LANSCE Pulsed Neutron Beam .....</b>                              | <b>49</b>  |
| <b>B. Production of UCN in Superfluid <math>^4\text{He}</math>.....</b> | <b>61</b>  |
| <b>C. Trap Design and Scintillation Light Detection.....</b>            | <b>76</b>  |
| <b>D. <math>^3\text{He}</math> Polarization and Transport .....</b>     | <b>85</b>  |
| <b>E. Magnetic and Electric Field Configuration .....</b>               | <b>98</b>  |
| <b>F. SQUID Detector Design and Performance.....</b>                    | <b>113</b> |
| <b>G. EDM Experimental Apparatus .....</b>                              | <b>122</b> |
| <b>H. Expected Sensitivity and Systematic Effects .....</b>             | <b>140</b> |
| <b>VI. COLLABORATORS AND RESPONSIBILITIES .....</b>                     | <b>148</b> |
| <b>VII. MANAGEMENT, COST, AND SCHEDULE .....</b>                        | <b>151</b> |
| <br>  |            |
| <b>APPENDIX A — TECHNICAL ISSUES</b>                                    | <b>159</b> |
| <b>APPENDIX B — WORK BREAKDOWN STRUCTURE</b>                            | <b>161</b> |
| <b>APPENDIX C — BIBLIOGRAPHIES FOR THE COLLABORATION</b>                | <b>166</b> |

# A New Search for the Neutron Electric Dipole Moment

## Summary

The possible existence of a nonzero electric dipole moment of the neutron is of great fundamental interest in itself and directly impacts our understanding of the nature of electro-weak and strong interactions. The experimental search for this moment has the potential to reveal new sources of T and CP violation and to challenge calculations that propose extensions to the Standard Model. In addition, the small value for the neutron EDM continues to raise the issue of why the strength of the CP violating terms in the strong Lagrangian are so small. This result seems to suggest the existence of a new fundamental symmetry that blocks the strong CP violating processes.

The goal of the current experiment is to significantly improve the measurement sensitivity to the neutron EDM over what is reported in the literature. The experiment has the potential:

- a) to measure the magnitude of the neutron EDM; or
- b) to lower the current experimental limit by one to two orders of magnitude.

Achieving these objectives will have major impact on our understanding of the physics of both weak and strong interactions.

The experiment is based on the magnetic resonance technique of rotating a magnetic dipole moment in a magnetic field. We describe in this report a new method to make a precision measurement of the neutron precession frequency under the influence of an electric field. The strategy is innovative and unique. It features:

- a) using a dilute mixture of polarized  $^3\text{He}$  in superfluid  $^4\text{He}$  as a working medium for the very high electric field environment;
- b) determining in situ the magnetic field experienced by the neutrons, using a direct SQUID measurement of the precession frequency of the  $^3\text{He}$  magnetic dipoles; and, finally,
- c) making a comparison measurement of changes in the precession frequency, under E field reversal, of the neutron and  $^3\text{He}$  components of the fluid, where the neutral  $^3\text{He}$  atom does not have an EDM.

Additional innovative features include loading the neutron trap with UCNs through a superfluid  $^4\text{He}$  phonon recoil process, introducing highly polarized  $^3\text{He}$  atoms into the trap in order to align the trapped UCN spins, operating the trap at extremely cold temperatures ( $\sim 300$  mK) to minimize UCN losses at the walls, and, finally, detecting the n- $^3\text{He}$  precession frequency difference, independently of the SQUID detectors, by viewing the induced  $^4\text{He}$  scintillation light with photomultipliers. The process of validating these techniques and determining their limits is well started, but realization of the experiment requires the resources requested here in order to fully exploit this new approach. A two-year study of this measurement strategy has not revealed any fatal problems.

This search for the neutron electric dipole moment is a major technical challenge and requires a research team with a broad base of technical knowledge and extensive research experience. We have assembled a growing group of research physicists (currently over 30 physicists from fourteen institutions), who are committed to taking on this challenge. Indeed, some are world experts in their specialties. A number have experience with previous EDM experiments. In addition, we anticipate that the fundamental and innovative character of this physics research will attract outstanding postdoctoral physicists and graduate students from the research institutions in the collaboration, and will generate a set of significant thesis projects.

This project is challenging at both small and large scales. It requires, for example, development of special low noise SQUIDS, laser techniques to measure high electric fields, and hardware to generate highly polarized  $^3\text{He}$  beams. It also requires operation with very high electric fields and construction of large scale vacuum and cryogenic systems capable of handling over 1500 L of superfluid  $^4\text{He}$ . In the UCN traps, we require a  $^4\text{He}$  purity with respect to  $^3\text{He}$ , that can be controlled at the level of one part in  $10^{14}$ .

The equipment to achieve all of this will require three years to manufacture, assemble and commission as well as \$11M of construction funds that include 40% contingency, institutional burden, and escalation. We regard this effort as a ten year project for which we are now in about the third year. The seed money (~\$5M of salaries and equipment) for preliminary design and initial validation tests of the experiment, has come from discretionary funds at LANL. The development work, described throughout the pre-proposal, has removed the most serious concerns of feasibility, and at its conclusion at the end of FY'04, should remove the technical risks summarized in Appendix A. We are now seeking DOE funds for construction of the full project in FY05-07. Though we will seek support from other agencies at a future time as an offset of the burden on DOE, until these funds are secure, we ask DOE for the full amount.

The physics goals of this experiment are timely and of unquestioned importance to modern theories of electro-weak and strong interactions. The technique builds on 30 years of experience with neutron EDM experiments and seeks to improve the current EDM limit by a factor of 50 to 100. The collaboration includes researchers with expertise developed in previous neutron EDM searches and in the new technologies required for this innovative technique. We request funds to construct this important and ambitious project during the period FY05-FY07.

## Chapter I. INTRODUCTION

Precision measurements of the properties of the neutron present an opportunity to search for violations of fundamental symmetries and to make critical tests of the validity of the Standard Model (SM) of Electro-Weak (EW) Interactions. These have been pursued with great energy and interest since Chadwick [1] discovered the neutron in 1932. The currently accepted values for the properties of the neutron, and related particles, from the Particle Data group [2] are listed in Tables I.A and I-B. In the past few years, the development of more intense sources of cold and ultracold neutrons and the invention of new trapping and detection techniques have sparked a new attack on these fundamental measurements. Examples of these are the new measurement of the neutron lifetime being developed with a  $^4\text{He}$  based ultra-cold neutron (UCN) trap at the NIST reactor [3] and the new proposed measurement of the neutron beta decay asymmetry parameter,  $A$ , using a solid deuterium based UCN moderator at LANSCE [4].

In this proposal we discuss a new technique for searching for the electric dipole moment (EDM) of the neutron which offers unprecedented sensitivity. It is based on the traditional magnetic resonance technique in which a neutron's magnetic dipole moment is placed in a plane perpendicular to parallel magnetic and electric fields,  $B_0$  and  $E_0$ . It will precess with a Larmor frequency,  $\nu_n$  (Hz),

$$h\nu_n = -[2\mu_n B_0 + 2d_n E_0], \quad (\text{I.1})$$

Here  $\mu_n$  ( $d_n$ ) is the magnetic (electric) dipole moment of the neutron, (see Table I-B), where  $\mu_{\text{nuclear}}$  is the nuclear magneton.

Table I-A. Experimental limits on the EDM of fundamental particles, [2].

| Particle                  | Experimental EDM Value / Limit ( $e \cdot \text{cm}$ ) |
|---------------------------|--|
| Electron, $e$             | $0.18 \pm 0.16 \pm 0.10 \times 10^{-26}$               |
| Neutron, $n$              | $< 0.63 \times 10^{-25}$ [90% C.L.]                    |
| Proton, $p$               | $-3.7 \pm 6.3 \times 10^{-23}$                         |
| Lambda Hyperon, $\Lambda$ | $< 1.5 \times 10^{-16}$ [95% C.L.]                     |
| Tau Neutrino, $\nu_\tau$  | $< 5.2 \times 10^{-17}$ [95% C.L.]                     |
| Muon, $\mu$               | $3.7 \pm 3.4 \times 10^{-19}$                          |
| Tau, $\tau$               | $< 3.1 \times 10^{-16}$ [95% C.L.]                     |

The impact of the  $E$  field on the precession of the neutron is characterized by the first moment of the neutron charge distribution,  $d_n$ , its EDM. All experiments to date have assigned a zero value to the neutron EDM.

Table I-B. Fundamental properties of the neutron, atomic  ${}^3\text{He}$ , and superfluid  ${}^4\text{He}$ , [2].

| <b>The Neutron</b>                            |   |
|---|---|
| Intrinsic Spin, $S$                           | $1/2\hbar$  |
| Mass, $m_n$                                   | $939.565330 \pm 0.000038$ MeV<br>$1.00866491578$ a.m.u. |
| Mean Life, $\tau_n$                           | $886.7 \pm 1.9$ s                                       |
| Magnetic Moment, $\mu_n$                      | $-1.91304272 \pm 0.00000045$ $\mu_{\text{nuclear}}$     |
| Electric Dipole Moment, $d_n$                 | $< 0.63 \times 10^{-25}$ [90% C.L.]                     |
| Electric Polarizability, $\alpha_n$           | $0.98 \pm 0.21 \times 10^{-3}$ fm <sup>3</sup>          |
| Charge, $q$                                   | $-0.4 \pm 1.1 \times 10^{-21}$ $e$                      |
| <b>Atomic <math>{}^3\text{He}</math></b>      |   |
| Intrinsic Nuclear Spin, $S$                   | $1/2\hbar$  |
| Mass, $m_{{}^3\text{He}}$                     | $3.016030$ a.m.u.                                       |
| Mean Life, $\tau_{{}^3\text{He}}$             | stable  |
| Magnetic Dipole Moment, $\mu_{{}^3\text{He}}$ | $-2.12762486$ $\mu_{\text{nuclear}}$                    |
| $\mu_{{}^3\text{He}}/\mu_n$                   | $1.11217$   |
| Electric Dipole Moment, $d_{{}^3\text{He}}$   | $\sim 0$  |
| <b>Superfluid <math>{}^4\text{He}</math></b>  |   |
| Density at 3.5°K                              | $0.14$ gm/cm <sup>3</sup>                               |
| Dielectric Constant, $\epsilon$               | $1.05$ $\epsilon_0$                                     |

Searches for the EDM of the neutron date back to a 1957 paper of Purcell and Ramsey [5]. This led to an experiment using a magnetic resonance technique at ORNL, where they established a value of  $d_n = -0.1 \pm 2.4 \times 10^{-20}$   $e\cdot\text{cm}$  [6]. Using Bragg scattering, an MIT/BNL experiment used neutron scattering from a CdS crystal to search for the neutron EDM [7], and obtained a value of  $d_n = 2.4 \pm 3.9 \times 10^{-22}$   $e\cdot\text{cm}$ . In the intervening 30 years, a series of measurements of increasing precision have culminated in the current best limit of  $d_n < 0.63 \times 10^{-25}$   $e\cdot\text{cm}$  [90% C.L.] obtained in measurements at the ILL reactor at Grenoble [8]. Thus there has been an impressive reduction with time of the experimental limit for  $d_n$  as illustrated in Fig I-1 and reviewed in Chapter III.

We describe here a new technique [9] that promises a two order of magnitude improvement over the ILL result [8]. An overview of this new technique is presented in Section IV of this proposal. A detailed and quantitative analysis of the method is presented in Section V.

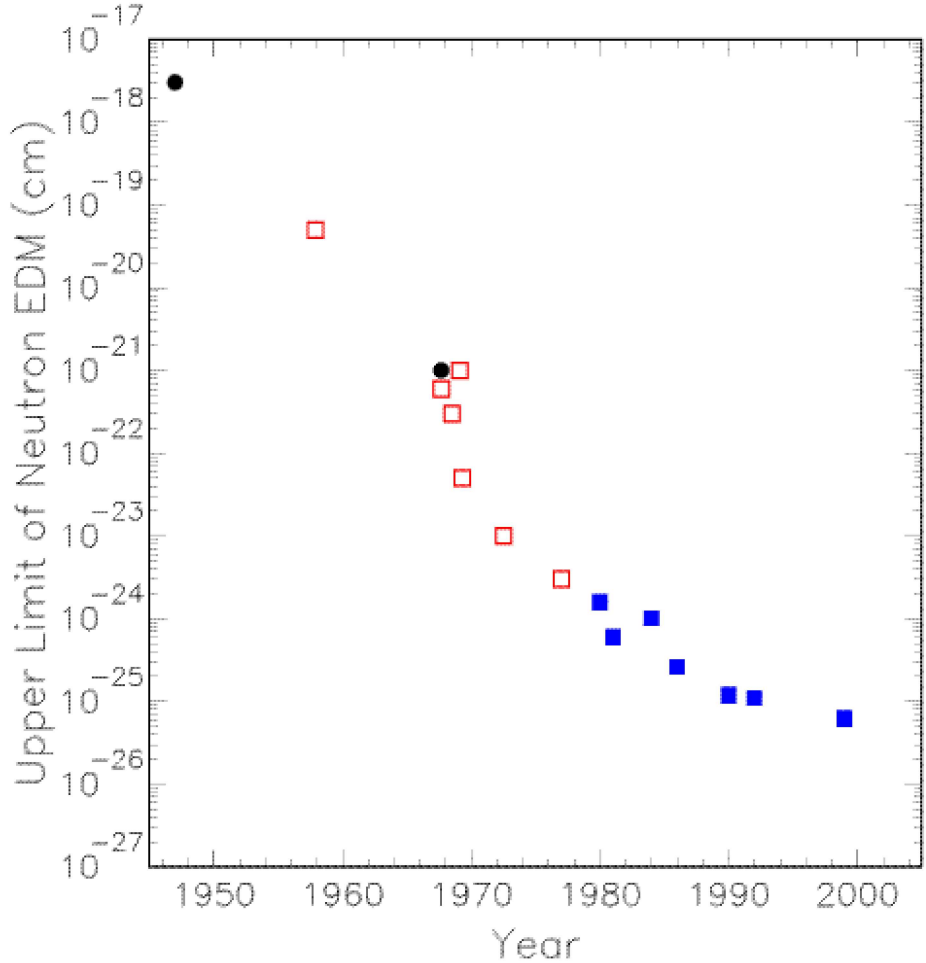


Fig. I-1. Upper limits of neutron EDM plotted as a function of year of publication. The solid circles correspond to neutron scattering experiments. The open squares represent in-flight magnetic resonance measurements, and the solid squares signify UCN magnetic resonance experiments.

The physics motivation for these measurements has been widely discussed. A search for a non-zero value of the neutron EDM is a search for a violation of T invariance. To date there is only one measurement (a comparison of neutral  $K$  and  $\bar{K}$  meson decay) in which T violation has been seen directly [10]. The asymmetry in these rates is found to be  $6.6 \pm 1.3 \pm 1.0 \times 10^{-3}$ . In the EW sector, one has a strong prejudice that the combined symmetry operation, CPT, is invariant in all processes. However, examples have been known for several decades where both P and C invariance are separately violated. Thus

observation of a violation of T invariance through measurement of the neutron EDM would be of fundamental significance.

The SM prediction for the neutron EDM, as characterized by the CKM matrix, is at the  $10^{-31}$  e·cm level, below the reach of current measurements by six orders of magnitude [11]. Although no violation of the SM has been observed (except perhaps for recent measurements of the neutrino mass), there are many proposed models of the EW interaction which are extensions beyond the SM and which raise the predicted value of the neutron EDM by up to seven orders of magnitude (see Chapter II). Some of these are already excluded by the current limit on the neutron EDM. The proposed experiment has the potential to reduce the acceptable range for predictions by two orders of magnitude and to provide a significant challenge to these extensions to the SM. Conversely, if a new source of CP violation is present in nature, beyond the CKM matrix description in the SM, and which is relevant to this hadron system, this experiment offers an intriguing opportunity to measure a non-zero value of the neutron EDM.

Our understanding of the origins of baryogenesis provides one reason for thinking that other sources of CP violation might exist beyond that found in the K-Kbar and B-Bbar systems. In the Big Bang one expects the generation of equal populations of particles and anti-particles. Current experimental observations yield the predominately particle universe and we have no mechanism that would push the anti-particle universe away to a different region of space. Thus it is tempting to assume that in some unknown reaction process, occurring early in the life of the universe and involving CP violation, the anti-particles were largely consumed. The required character of this unknown process has been analyzed by Sakharov [12] as discussed in Chapter II. Recent calculations suggest that the strength of the CP-violating mechanism required to produce the observed baryon asymmetry, would have to be much stronger than that required to explain the  $\epsilon'$  measurements in the  $K\bar{K}$  system [13]. This observation provides a hint that the SM calculation may not be complete and invites investigation of extensions to the SM. Thus predictions that the EDM of the neutron may be larger than the predictions in the SM need to be taken seriously.

The current experimental limits on the EDM of other fundamental particles, are compared with the neutron in Table I-A. We believe the EDM of the neutron and the electron provide the most sensitive tests of the SM. In theories of the weak interaction, the EDM of the electron is zero in first order. There have been a number of precision measurements of the EDM of paramagnetic atomic systems, from which limits for the EDM of the electron can be inferred. For example, the measurements in Tl by Commins et al [14] suggest a value of  $0.18 \pm 0.12 \pm 0.10 \times 10^{-26}$  e·cm. This experimental limit is about 13 orders of magnitude above the SM predictions. The electron EDM is discussed further in Chapter II.

Thus a neutron EDM measurement, with two orders of magnitude improvement over the current experimental limits, presents an excellent opportunity to challenge the extensions beyond the SM and to search for new physics in the CP sector. It also provides an opportunity to search for T violation in non-strange systems. A review of the physics implications of neutron EDM measurements is presented in Section II followed by a discussion of previous EDM measurements in Section III. After a description of the proposed technique in Sections IV and V, we discuss the collaboration, schedule, and costs associated with this project in Chapters VI and VII. Some outstanding technical issues are discussed in Appendix A.

## References

- [1] J. Chadwick, *Nature* **129**, 312 (1932); *Proc. Roy. Soc. (London)* **A136**, 692 (1932).
- [2] D. E. Groom et al. (Particle Data Group), *Eur. Phys. J.* **C15**, 1 (2000).
- [3] P. R. Huffman et al., *Nature* **403**, 62 (2000).
- [4] R. E. Hill et al., *Nucl. Instrum. Methods* **440**, 674 (2000).
- [5] E. M. Purcell and N. F. Ramsey, *Phys. Rev.* **78**, 807 (1950).
- [6] J. H. Smith, E. M. Purcell, and N. F. Ramsey, *Phys. Rev.* **108**, 120 (1957).
- [7] C. G. Shull and R. Nathans, *Phys. Rev. Lett.* **19**, 384 (1967).
- [8] P. G. Harris et al., *Phys. Rev. Lett.* **82**, 904 (1999).
- [9] G. Golub and S. K. Lamoreaux, *Phys. Rep.* **237**, 1 (1994), I. B. Khriplovich and S. K. Lamoreaux, *CP Violation without Strangeness* (Springer Verlag, 1997).
- [10] A. Angelopoulos et al. (CPLEAR Collaboration), *Phys. Lett.* **444B**, 43 (1998).
- [11] G. Buchalla et al., *Nucl. Phys.* **B370**, 69 (1992); A. J. Buras et al., *Nucl. Phys.* **B408**, 209 (1993); M. Ciuchini, *Nucl. Phys. Proc. Suppl.* **59**, 149 (1997).
- [12] A. D. Sakharov, *JETP Lett.* **5**, 24 (1967).
- [13] I. I. Bibi and A. I. Sanda, *CP Violation* (Cambridge University Press, 2000), p. 355.
- [14] E. D. Commins, S. B. Ross, D. DeMille, and B. C. Regan, *Phys. Rev.* **A50**, 2960 (1994).

## Chapter II PHYSICS MOTIVATION<sup>1</sup>

### A. Introduction and Background

The present proposal, with its potential for measuring the neutron EDM  $d_n$  with a sensitivity of  $10^{-27}$  e-cm is one of a class of new-generation experiments aiming to search for new physics in the CP violating sector. A focus on CP violation is suggested by the critical importance which symmetry has assumed in constructing theories of modern particle physics. More broadly, it acknowledges the importance of CP violation in shaping our understanding of the origins and evolution of the Universe. Empirical evidence for physics beyond the standard model of electroweak interactions (SM) is provided by recent experimental results on neutrino oscillations.

The role of symmetry, including the observed breaking of the discrete symmetries of parity P and CP, has been particularly significant for the construction of the SM. Parity violation, which has been measured in many systems, is well represented in the SM through a definitive chiral V-A coupling of fermions to gauge bosons. The information available on CP violation, while much more limited, still has had a profound impact; e.g., the decay of neutral kaons anticipated the three-generation structure of the SM as we now know it. Although neither P nor CP violation has been understood at a deep level in the SM, CP violation is arguably the less understood of the two, appearing tentatively through the complex phase  $e^{i\delta_{\text{CKM}}}$  characterizing  $\Delta S = 1$  transitions in the CKM matrix. Because of the limited information available and the many open questions, searching for new sources of CP violation has become an attractive focus in the quest for New Physics.

The observation of CP violation also implies time-reversal symmetry T violation (and vice-versa) through the CPT theorem. This theorem asserts that field theories with local, Lorentz invariant, and hermitian Lagrangians (believed to be the only acceptable ones [3]) must be invariant under the combined transformation C, P, and T. In the absence of degeneracy, the energy of a spin-1/2 particle, say a neutron, in an electric field  $\mathbf{E}$  is related to  $d_n$  by  $E_n = d_n \boldsymbol{\sigma} \cdot \mathbf{E}$  where  $\boldsymbol{\sigma}$  is its Pauli spin matrix. Since this expression is odd under T (and P), measuring a non-vanishing  $d_n$  is also a unique signature for CP violation. The same arguments apply to  $d_e$  for the electron, whose value is determined from measurements of the EDM of paramagnetic systems (those having unpaired electrons), such as atomic  $Tl$ . The current experimental bounds on the neutron and electron EDMs are  $d_n < 0.63 \times 10^{-25}$  e-cm (90% CL) and  $d_e = (0.18 \pm 0.16) \times 10^{-26}$  e-cm, respectively [3a].

---

<sup>1</sup> Two excellent resources are Refs. [1] and [2].

In the SM, there are actually two sources of CP violation. In the electroweak sector it appears, as already mentioned, through  $\delta_{\text{CKM}}$ . The other is a term in the QCD Lagrangian itself, the so-called  $\theta$ -term,

$$L_{\text{eff}} = L_{\text{QCD}} + \frac{\theta g_s^2}{32\pi^2} G_{\mu\nu} \tilde{G}^{\mu\nu}, \quad (\text{II.1})$$

which explicitly violates CP symmetry because of the appearance of the product of the gluonic field operator  $G$  and its dual  $\tilde{G}$ . Since  $G$  couples to quarks but does not induce flavor change,  $d_n$  is much more sensitive to  $\theta$  than it is to  $\delta_{\text{CKM}}$ ; additionally, the  $\theta$ -term is practically irrelevant to  $d_e$  and kaon decays. Thus, measurement of  $d_n$  would uniquely determine an important parameter of the SM. Calculations [4,4a] have shown that  $d_n \sim \text{O}(10^{-16} \theta) e\text{-cm}$ .

Although the value of the strength  $\theta$  is unknown, the observed limit on  $d_n$  allows one to conclude that  $\theta < 10^{-9\pm 1}$  [2]. A comparable limit on  $\theta$  comes from the EDM of the  $Hg$  atom. However, the natural scale apparent in Eq. (II.1) suggests rather that  $\theta \sim \text{O}(1)$ . The extreme smallness of  $\theta$  (The so-called strong CP problem) begs for an explanation. One attempt [5] augments the SM by a global U(1) symmetry (referred to as the Peccei-Quinn symmetry), imagined to be spontaneously broken and to give rise to Goldstone bosons called axions. The  $\theta$ -term is then essentially eliminated by the vacuum expectation value of the axion. Subsequently, much experimental effort and millions of dollars have been spent on the search for axions. The fact that axions have not been observed is, however, not in conflict with the empirical limit on the  $\theta$  because other proposals exist [5a] to explain the small value of  $\theta$ . For example, if CP violation is implemented spontaneously,  $\theta = 0$  as the leading effect arises naturally. Clearly, an experimental determination of  $d_n$  has the potential to lead to a new paradigm for CP violation.

## B. Previous Measurements of CP Violation and Future Possibilities

A CP violation signal has now been observed in both the decay of neutral K and B mesons. The CP violation signal observed in the decay of neutral kaons into two pions is characterized by parameters  $\varepsilon$  and  $\varepsilon'$ . The parameter  $\varepsilon'$ , signifying *direct* CP violation, indicates a channel-dependent effect in  $\pi^0\pi^0$  and  $\pi^+\pi^-$  decay. The parameter  $\varepsilon$  characterizes *indirect* CP violation, an asymmetry in the  $\Delta S = 2$  mixing of the neutral kaon with its anti-particle, equivalent to  $K_0 - \bar{K}_0$  oscillation. The early data [6] gave

$\varepsilon = 0.002$  and  $\varepsilon' = 0$ . A possible explanation was given by the superweak (SW) theory of Wolfenstein [7], implying purely indirect CP violation. The most recent experimental results [8–10] are:

$$\text{Re} \frac{\varepsilon'}{\varepsilon} = (21.6 \pm 3.0) \times 10^{-4} . \quad (\text{II.2})$$

These results show quite convincing evidence for the existence of  $\varepsilon' \neq 0$ , implying a mixture of both direct and indirect CP violation. Additionally, time-reversal violation in the neutral kaon system has been observed by the *CPLEAR* collaboration [11].

Typical predictions of the SM using the complex CKM phase are [12,13]:

$$\begin{aligned} -2.1 \times 10^{-4} &\leq \frac{\varepsilon'}{\varepsilon} \leq 13.3 \times 10^{-4} \\ -0.5 \times 10^{-4} &\leq \frac{\varepsilon'}{\varepsilon} \leq 25.2 \times 10^{-4} \end{aligned} \quad (\text{II.3})$$

depending, among other things, upon the mass taken for the strange and charmed quarks. Thus, while it appears that Refs. [8–10] have definitely opened a new window on CP violation, the interpretation of the observed signal is far from settled. It could represent another success of the CKM ansatz, but it also leaves considerable room for New Physics.

In any case, since CP violation as represented in the CKM matrix, embodies flavor mixing,  $d_n$  is very small in the SM: calculations predict it to be  $10^{-32}$  to  $10^{-31}$   $e\cdot\text{cm}$  [14] ( $10^{-30}$   $e\cdot\text{cm}$  [15]) well beyond the reach of any experiment being considered at present. An estimate in the superweak theory gives  $d_n$  (SW)  $\sim 10^{-29}$   $e\cdot\text{cm}$  [16], beyond the range of our proposed EDM measurement. Because of the experimental evidence indicating the presence of direct CP violation, a pure  $\Delta S = 2$  interaction is now known to be insufficient, and the SW prediction for  $d_n$  is no longer relevant. As  $d_e$  cannot originate in the SM even from three-loop diagrams, the prediction of the SM,  $d_e(\text{SM}) < 10^{-40}$   $e\cdot\text{cm}$  [17], is also well beyond current experimental capabilities.

As will be discussed in Sect. II.D, models of New Physics, including left-right symmetric models, non-minimal models in the Higgs sector, and supersymmetric models, allow for CP violating mechanisms not found in the SM, including terms that do not change flavor. For this reason searches for  $d_n$  and  $d_e$ , which are particularly insensitive to flavor-changing parameters (such as  $\delta_{\text{CKM}}$ ), have been significant for the development of such

models. The models allow for effects that might be observed in a variety of experiments including the new searches for  $d_n$  and  $d_e$ , B-meson decay, transverse polarization of muons in  $K_{\mu 3}$  decay; decays of hyperons; decays of  $\tau$  leptons; and CP violation in charmed hadron decays.

If the origin of CP violation is essentially correctly described in the SM through  $\delta_{\text{CKM}}$ , large characteristic CP asymmetries are predicted for B-decay [2]. Recent results from the *Belle* and *BaBar* collaborations present compelling evidence for CP violation in the neutral B meson system roughly consistent with these expectations [17a]. However, the large, CP violating effects in B decay arising in the SM could be obscuring signals of New Physics that would be manifest otherwise in these decays. In this case, the fact that CP violation arising from the CKM matrix is very small in  $d_n$  leaves open the possibility that measurable effects will be found in  $d_n$  even if further analysis finds no deviation from the SM in B decays.

More generally, models of New Physics contain sources of CP violation that affect both flavor-changing and flavor-conserving sectors with a relative weighting characteristic of the model. Correlations between flavor-changing and flavor-non-changing observables (such as between B decay and EDMs) can provide important clues to distinguish among competing theories. Of course, if no CP asymmetries had been found in B decays on a measurable level, we would know immediately that the CKM ansatz is not a significant factor in neutral kaon decays and that physics beyond the SM drives these reactions. Here again, measurement of  $d_n$  would narrow the possible sources of New Physics.

### C. CP Violation and the Baryon Asymmetry of the Universe (BAU)

One of the great puzzles of physics is the fact that the Universe contains any matter at all. The naïve expectation is rather that matter and antimatter in the universe should balance out, i.e. that the baryon asymmetry  $\Delta n_{\text{Bar}} / (n_{\text{Bar}} + n_{\overline{\text{Bar}}})$ , where  $\Delta n_{\text{Bar}} = n_{\text{Bar}} - n_{\overline{\text{Bar}}}$  is the difference in the abundances of baryons and antibaryons, should have vanished in the creation of the Universe.

The baryon asymmetry can be quantified in terms of estimates of the number of baryons in the Universe today,  $n_{\text{Bar}} |_{\text{today}}$ , and the number of photons in the cosmic background  $n_{\gamma}$ . One observes that the ratio  $r_{\text{Bar}} \equiv n_{\text{Bar}} |_{\text{today}} / n_{\gamma}$  is just a few  $10^{-10}$ , i.e., that the Universe is strikingly dilute, containing just a single baryon for every  $10^9$  or so photons.

Of course,  $n_{\text{Bar}}$  changes over time. During an earlier epoch, when the temperature was above the threshold for production of nucleons and anti-nucleons ( $T \sim 10^{13}\text{K}$ ), both species were plentiful and were in thermal equilibrium with the photons. At this time,  $\Delta n_{\text{Bar}} \approx n_{\text{Bar}}|_{\text{today}}$ , and  $n_{\text{Bar}} + n_{\overline{\text{Bar}}} \cong n_{\gamma}$ , ( $n_{\gamma}$  is roughly constant in time) [18]. The baryon asymmetry at this earlier epoch is therefore approximately equal to the value of  $r_{\text{Bar}}$ ,

$$\frac{\Delta n_{\text{Bar}}}{n_{\text{Bar}} + n_{\overline{\text{Bar}}}} = r_{\text{Bar}} \approx \sim \text{few } 10^{-10}. \quad (\text{II.4})$$

The basic question is: how could this BAU result from physical processes happening since the birth of the Universe in the Big Bang some  $\tau_U \sim 10^{10}$  years ago?

In a seminal paper, A. Sakharov [19] raised the definite possibility of calculating the BAU from basic principles. He identified three criteria that, if satisfied simultaneously, will lead to a baryon asymmetry: (1) reactions that change baryon number have to occur; (2) these reactions must be CP violating; and (3) they must occur in non-equilibrium processes. Attempts to understand the BAU from this point of view has focused on two distinct eras of Big Bang evolution. One, the era of grand unified theory (GUT) baryogenesis, occurred when the temperature of the Universe was  $T \approx 10^{29}\text{K}$ , corresponding to the mass  $M_x \approx 10^{16}\text{ GeV}$  expected of a GUT gauge particle. The other, the era of electroweak baryogenesis, corresponds to  $T \approx 10^{15}\text{K}$  or energies of about 100 GeV comparable to the mass of a  $W$  or  $Z$  gauge boson. For us, the important point is that a quantitative characterization of CP violation is an essential element for achieving an understanding of  $r_{\text{Bar}}$  along the lines suggested by Sakharov.

Electroweak baryogenesis [20] is currently one of the most actively pursued scenarios since electroweak dynamics is fairly well understood. Shaposhnikov [21] has analyzed this in the SM. In the SM and other non-Abelian gauge theories there exist multiple and topologically distinct vacuum states distinguished by their baryon number  $B$  (and lepton number  $L$ ). Although baryon current conservation strictly forbids transitions among states of different  $B$  at the classical level, one finds quantum mechanically that the divergence of the baryon current is subject to triangle anomalies that signify symmetries broken at a quantum mechanical level but conserved classically. Thus,  $B$ -violating transitions are no longer forbidden, and the corresponding probability may be expressed in terms of instanton-like gauge field configurations [22], sometimes called sphalerons. This probability is extremely small for  $T \approx 0$  as in the Universe today (the proton lifetime  $\tau_p (> 10^{32}\text{ yr.}) \gg \tau_U$ ); however, when  $T > 10^{17}\text{K}$ , sphalerons are easily excited,

in which case anomalous  $B$  violation may be extremely rapid [23]. In this way the first Sakharov condition is satisfied in the SM. The second Sakharov condition is satisfied in the SM through the explicit CP violation present in the CKM matrix. Finally, if conditions of supercooling prevail at electroweak-scale temperatures, then the third Sakharov condition would be satisfied in the first-order transition, occurring as droplets of the broken phase began to nucleate out. Supercooling refers to the situation where the universe cools (through expansion) beyond the point at which a phase change would already have occurred under equilibrium conditions.

However, Shaposhnikov [21] was unable to describe  $r_{\text{Bar}}$  quantitatively in the SM. The SM has two shortcomings. First, the SM does not supply enough CP violation. Secondly, it is now believed that a single Higgs doublet as incorporated into the SM would not support a first-order electroweak phase transition. This is because a single Higgs doublet with mass,  $M_H$ , greater than 70 GeV is known, from Lattice Gauge calculations [24], to be insufficient for supercooling and because LEP measurements suggest that  $M_H$  exceeds 100 GeV. Clearly, some physics beyond the SM, including new sources of CP violation that may lead to a measurable value for  $d_n$ , must exist if the observed BAU is to be understood.

One such source might be found in the minimal supersymmetric extension of the SM (MSSM). It has been shown recently [25] that small values of the CP violating phases (consistent with constraints from  $d_n$ ) can provide values of  $r_{\text{Bar}}$  comparable to the empirical value given in Eq. (II.1).

Another such source could be GUT physics. It is generally believed that GUT physics would easily satisfy the three Sakharov conditions, with baryon number being generated in most GUTs through C- and CP-violating asymmetries in the decays of particles of masses near  $M_x$ . However, the following concerns have been raised about GUT baryogenesis [23,26]. The first problem is that the physics involved, is not likely to be directly testable in the foreseeable future. The second is the erasure of symmetry, meaning that the thermal sphaleron-mediated  $B$ -changing reactions discussed in connection with baryogenesis during the electroweak era, would be capable of undoing any  $B + L$  production having arisen prior to or during Grand Unification.

However, there is yet another possibility for generating BAU. If at some temperature, well above the electroweak phase transition, an excess of leptons over anti-leptons is generated, sphaleron mediated processes, which conserve  $B - L$ , can communicate this asymmetry to the baryon sector [27]. The simplest way this can be realized is by adding

a heavy right-handed Majorana neutrino to the SM. Since such a neutrino is its own CPT image, its decay necessarily violates lepton number conservation, which can be translated into a lepton asymmetry through a CKM analog to the neutrino mass matrix. The resulting lepton asymmetry is transferred into a baryon number through the sphaleron-mediated processes in the unbroken high energy phase of  $SU(2)_L \times U(1)$ . Whether this would have an observable impact on  $d_n$  would depend on the actual scenario by which CP violation is realized in the lepton-number violating processes.

The most relevant conclusion to be drawn from the above discussion is the following: to explain the BAU through GUT or electroweak baryogenesis, substantial New Physics in the CP violating sector is required. As we have indicated, identifying the new source is subject to scrutiny through a variety of new experiments—and the value of  $d_n$  may well play an important role in quantifying it. Identification of any new source of CP violation, beyond that presently represented in the SM, may have a significant impact on our understanding of baryogenesis.

#### **D. Models of New Physics**

As we have mentioned, the evidence that the SM adequately represents CP violation is clearly not compelling, leading to the somewhat obvious conclusion that finding any new measure of CP violation would be enormously significant. To anticipate how hard we would have to look to find it by a measurement of  $d_n$ , and what we might conclude from such a measurement, we turn to models embodying New Physics. The models provide a natural and reasonable expectation that the values of  $d_n$  may lie at levels just beyond current empirical limits. Additionally, these models clearly show that significant correlations among different CP measurements can be expected, and that knowledge of these correlations is essential to unraveling the origin of the effects once they are found. If  $d_n$  is *not* seen at levels just beyond current empirical limits, one would arrive at the important conclusion that something quite special is going on.

In the following discussion of models we focus on  $d_n$ , but it is perhaps worth noting that the EDM of atoms (see below) and of the electron are also relevant. In many models  $d_e$  is predicted to lie at least an order of magnitude below  $d_n$ . The reasons for this are the smaller chirality flip and weaker gauge couplings for leptons [28]. However, there is a great deal of model dependence and in the absence of experimental information,  $d_e$  or  $d_n$  may be favored by the specific choice of parameters. In parallel to our efforts to improve the experimental sensitivity to  $d_n$ , ambitious attempts to improve on the electron EDM measurements are being vigorously pursued (see e.g., [29] in which a factor of  $10^4$

improvement in statistical sensitivity is being sought in a measurement on an excited metastable state of PbO). Based on experience with these theoretical models, and the current empirical limits, one may infer that new experiments to measure  $d_e$  or  $d_n$  would have to exhibit about the same improvements in sensitivity over existing measurements to be competitive.

Left-right symmetric gauge models [30] have many intriguing features such as the highly symmetric starting point that motivates them. Although many potential dynamical sources of CP violation exist, the EDM in these models is driven by  $W_L - W_R$  mixing, the scale of which is set by the mass of the  $W_R$ . These models are interesting for us because they show that it is possible, through  $W_L - W_R$  mixing, to have  $\epsilon'$  agree with neutral kaon decay, yet have  $d_n$  large enough to be observable (at the level of  $O(10^{-27}) e\cdot\text{cm}$  [2]). The electron EDM can be naturally in the range of  $10^{-26}$  to  $10^{-28} e\cdot\text{cm}$  [28]. The most strict limits on the relevant parameters in these models [31] have been determined from measurement of the EDM of diamagnetic atoms (atoms with paired electrons such as  $^{129}\text{Xe}$  and  $^{199}\text{Hg}$ ). Diamagnetic systems are sensitive to CP violating effects predominantly through the nuclear force rather than through  $d_e$  (see, *e.g.*, Eq. (II.6), below).

CP violation in the CKM matrix of the SM is envisioned to occur “minimally” via the complex couplings of the Higgs to the fermions. A class of non-minimal models arises in the Higgs sector through CP violation generated from spontaneous symmetry breaking. There is considerable latitude in constructing these models, since the Higgs sector represents the largest area of unknown physics of the SM and lacks direct experimental support. One may discuss the EDM in these models in terms of the following classification: (1) Higgs exchanges which generate an EDM for individual quarks  $d_q$  or leptons. Such direct one-loop contributions with charged Higgs, tend to give a large  $d_n$  incompatible with experimental upper limits, if one insists that the empirical value of  $\epsilon$  also originates entirely within this sector [32]. Thus, for these models to be viable, one must arrange for  $\epsilon$  to arise in part (or entirely) from other sources (such as the CKM phase). (2) CP odd gluonic operators which induce a  $d_n$ . Since the contribution of these operators is suppressed by successively higher powers of  $M_H$  with increasing operator dimension, the operator most likely to give the dominant contribution to  $d_n$  (excluding  $G\tilde{G}$ , which is related to  $\theta$  as discussed earlier) is  $G^2\tilde{G}$ . Estimates for the resulting  $d_n$  suggest values  $d_n \sim O(10^{-26}) e\cdot\text{cm}$  [33,34]. (3) Quark color-electric dipole moments,  $d_q^{\text{CED}}$ , (two-loop effects) that lead to large  $d_n$  with values close to the current upper bound [33,35,36]. The corresponding two-loop contribution to  $d_e$  is obtained by replacing gluons in the color-electric dipole operator by electroweak gauge bosons and

attaching them to a lepton. This yields  $d_e \sim \text{few } 10^{-27}$  [33,35-38] which is just at the present experimental bound. Recognizing that this classification is actually quite general and applicable in particular to supersymmetric theories [38a], the EDM of the neutron and the paramagnetic atom  $Tl$  can be expressed in terms of quantities appearing in this classification as [39]

$$d_n = 1.6\left(\frac{4}{3}d_d - \frac{1}{3}d_u\right) + O(10^{-1})d_q^{QCD} + O(1)(\theta/10^{-9})d_n^{1995} \quad (\text{II.5})$$

$$d_{Tl} = -600d_e + O(10^{-4})d_q + O(10^{-3})d_q^{QCD} + O(10^{-3})(\theta/10^{-9})d_{Tl}^{1995} .$$

Corresponding relationships exist for the diamagnetic atoms; a typical result is

$$d_{Xe} = 10^{-3}d_e + O(10^{-4})d_q + O(10^{-3})d_q^{QCD} + O(10^{-1})(\theta/10^{-9})d_{Xe}^{1995} . \quad (\text{II.6})$$

In these expressions, the contribution from strong CP violation involving the  $\theta$ -term, has been expressed in terms of the current upper bounds ( $d_{Tl}^{1995} \leq 6.6 \cdot 10^{-24}$  e-cm,  $d_{Xe}^{1995} \leq 1.4 \cdot 10^{-26}$  e-cm, and  $d_n^{1995} \leq 0.8 \cdot 10^{-25}$  e-cm). A recent analysis [40] within the context of the MSSM has shown that the measurement [41] of the EDM of  $^{199}Hg$  may be providing the most reliable constraint on CP violating phases.

Thus, one cannot rule out the possibility that non-minimal Higgs models will lead to values for  $d_n$  and  $d_e$  that are observable with the improvements in sensitivity planned in next-generation experiments. These models may also make significant contributions to other CP violating observables, such as the transverse polarization in  $K_{\mu 3}$  decay, without necessarily having much effect on kaon decays. They are especially worthy of attention since Higgs dynamics also appears to be capable of providing sufficient CP violation to generate the BAU of today's Universe at the electroweak scale.

There is one very elegant theoretical scheme in which scalars such as Higgs arise quite naturally—namely supersymmetry (SUSY). Here, scalars arise as superpartners of fermions. In the MSSM, only two new observable CP-violating phases emerge: one is analogous to the usual CKM phase, whose effect is felt throughout various sectors of the theory, and the other is a phase reflecting soft SUSY breaking. The latter is severely restricted already by the experimental bound on  $d_n$ , which makes this phase irrelevant to neutral kaon decay [2]. However, within the broad framework of non-minimal SUSY models, including GUTs, there are numerous new sources of CP violation to be found in complex Yukawa couplings and other Higgs parameters that may have observable effects

on  $d_n$  and  $d_e$  [2,39,42,43]. While large effects emerge in beauty decays, there are sizable deviations from the CKM expectations. Within each scenario there can be numerous non-trivial correlations among the CP observables, rare decay rates, and gross features of the particle spectrum; for example, in the SO(10) GUT,  $d_n$  and  $d_e$  scale as  $1/m^2$  with the scale  $m$  of supersymmetry breaking, whereas the  $\mu \rightarrow e\gamma$  rate scales as  $1/m^4$  [42].

## E. Summary and Conclusions

We have seen that there is ample reason to expect a non-zero value for the neutron electric dipole moment, with many theories predicting values lying within the six-orders of magnitude window between the current limit and the value allowed by the Standard Model. We conclude that experiments able to explore the next two orders of magnitude would make a significant contribution to the search for New Physics.

## References

- [1] I. B. Khriplovich and S. K. Lamoreaux, *CP Violation without Strangeness* (Springer-Verlag, Berlin, 1997).
- [2] I. I. Bigi and A. I. Sanda, *CP Violation* (Cambridge University Press, Cambridge, UK, 2000).
- [3] Interesting exceptions include string theory/higher dimensional effects, see G. Barenboim, L. Borissov, J. Lykken, and A. Yu. Smirnov, hep-ph/0108199.
- [3a] D. E. Groom et al. (Particle Data Group), *Eur. Phys. J.* **C15**, 1 (2000).
- [4] V. Baluni, *Phys. Rev. D* **19**, 2227 (1979).
- [4a] R. J. Crewther et al., *Phys. Lett.* **88B**, 123 (1979); Errata, **91B**, 487 (1980).
- [5] R. Peccei and H. Quinn, *Phys. Rev. Lett.* **38**, 1440 (1977); *Phys. Rev. D* **16**, 1791 (1977).
- [5a] S. Barr and A. Zee, *Phys. Rev. Lett* **55**, 2253 (1985).
- [6] J. H. Christenson, J. W. Cronin, V. L. Fitch, and R. Turlay, *Phys. Rev. Lett.* **13**, 138 (1964).
- [7] L. Wolfenstein, *Phys. Rev. Lett.* **13**, 562 (1964).
- [8] G. D. Barr et al., *Phys. Lett.* **317B**, 233 (1993).
- [9] L. K. Gibbons et al., *Phys. Rev. Lett.* **70**, 1203 (1993).
- [10] A. Alavi-Harati et al., *Phys. Rev. Lett.* **83**, 22 (1999).
- [11] A. Angelopoulos et al., *Phys. Lett.* **444B**, 43 (1998).
- [12] G. Buchalla, A. J. Buras, and M. E. Lautenbacher, *Nucl. Phys. B* **370**, 69 (1992); J. Buras, M. Jamin, and M. E. Lautenbacher, *Nucl. Phys. B* **408**, 209 (1993).
- [13] M. Ciuchini, *Nucl. Phys. Proc. Suppl.* **59**, 149 (1997).
- [14] I. B. Khriplovich and A. R. Zhitnitsky, *Phys. Lett.* **109B**, 490 (1982).

- [15] M. B. Gavela et al., *Phys. Lett.* **109B**, 215 (1982); B. McKellar, S. Choudhury, X-G. He, and S. Pakvasa, *Phys. Lett B* **197**, 556 (1987).
- [16] L. Wolfenstein, *Nucl. Phys. B* **77**, 375 (1974).
- [17] M. E. Pospelov and I. B. Khriplovich, *Yad. Fiz.* **53**, 1030 (1991) [*Sov. J. Nucl. Phys.* **53**, 638 (1991)].
- [17a] See B. Aubert, hep-ex/0203007 and K. Abe, hep-ex/0202027 and references therein.
- [18] S. Weinberg, *The First Three Minutes* (Harper-Collins Publishers, NY, 1977), p.95.
- [19] A. D. Sakharov, *JETP Lett.* **5**, 24 (1967).
- [20] V. A. Kuzmin, V. A. Rubakov, and M. E. Shaposhnikov, *Phys. Lett.* **155B**, 36 (1985).
- [21] M. E. Shaposhnikov, *Nucl. Phys. B* **287**, 757 (1987).
- [22] G. 't Hooft, *Phys. Rev. Lett.* **37**, 8 (1976).
- [23] A. G. Cohen, D. B. Kaplan, and A. E. Nelson, *Annu. Rev. Nucl. Part. Sci.* **43**, 27 (1993).
- [24] K. Kajantie et al., *Nucl. Phys. B* **466**, 189 (1996).
- [25] A. Riotto, *Phys. Rev. D* **58**, 095009 (1998).
- [26] A. Riotto and M. Trodden, *Ann. Rev. Nucl. Part. Sci.* **49**, 35 (1999).
- [27] M. Fukugita and T. Yanagita, *Phys. Lett.* **174B**, 45 (1986).
- [28] W. Bernreuther and M. Suzuki, *Rev. Mod. Phys.* **63**, 313 (1991).
- [29] Yale Proposal. De Mille, Search for an Electron Electric Dipole Moment in the  $a(1)$  state of Pb0.
- [30] R. N. Mohapatra, *Unification and Supersymmetry* (Springer-Verlag, 1992).
- [31] P. Herczeg, in *Symmetries and Fundamental Interactions in Nuclei*, ed. W. C. Haxton and E. Henley (World Scientific, 1995).
- [32] G. Beall and N. G. Deshpande, *Phys. Lett.* **132B**, 427 (1983).
- [33] D. Chang, W.-Y. Keung, and T. C. Yuan, *Phys. Lett.* **251**, 608 (1990).
- [34] I. I. Bigi and N. G. Uraltsev, *Nucl. Phys. B* **353**, 321 (1991).
- [35] M. S. Barr and A. Zee, *Phys. Rev. Lett.* **65**, 21 (1990).
- [36] J. Gunion and D. Wyler, *Phys. Lett.* **248B**, 170 (1990).
- [37] R. G. Leigh, S. Paban, and R.-M. Xu, *Nucl. Phys. B* **352**, 45 (1991).
- [38] C. Bowser-Chao, D. Chang, and W. -Y. Keung, *Phys. Rev. Lett.* **79**, 1988 (1997).
- [38a] S. M. Barr, *Int. Journal Mod. Phys. A* **8**, 209 (1993).
- [39] R. Barbieri, A. Romanino, and A. Strumia, *Phys. Lett.* **369B**, 283 (1996).
- [40] T. Falk, K. A. Olive, M. Pospelov, and R. Roiban, *Nucl. Phys. B* **560**, 3 (1999).
- [41] J. P. Jacobs et al., *Phys. Rev. Lett.* **71**, 3782 (1993); M. Romalis et al, *Phys Rev. Lett.* **86**, 2505 (2001)
- [42] S. Dimopoulos and L. J. Hall, *Phys. Lett.* **344B**, 185 (1995).
- [43] I. B. Khriplovich and K. N. Zyablyuk, *Phys. Lett.* **383B**, 429 (1996).

### Chapter III. STATUS OF EXISTING NEUTRON EDM MEASUREMENTS

The history of neutron EDM measurements is closely interwoven with our evolving knowledge of discrete symmetries in physics. In 1950, when parity was considered an inviolable symmetry, Purcell and Ramsey [1] pointed out the need to test this symmetry via detection of a neutron EDM. They then carried out a pioneering experiment [2,3] setting an upper limit at  $5 \times 10^{-20}$  e-cm for neutron EDM. The role of the baryon (proton, neutron, hyperons) EDM in testing parity symmetry was extensively discussed in the seminal paper of Lee and Yang [4], who cited the yet-unpublished neutron EDM result from Smith, Purcell, and Ramsey [2,5].

The discovery of parity violation in 1957 [6–8] prompted Smith et al. to publish their neutron EDM result [3]. By this time, however, it was recognized [9,10] that time-reversal invariance would also prevent the neutron from possessing a non-zero EDM. Since no evidence of T violation was found even in systems that exhibited maximal parity violation, a non-zero neutron EDM was regarded as highly unlikely. However, Ramsey [10a] emphasized the need to check time-reversal invariance experimentally. He also pointed out that Dirac’s magnetic monopole violates both P and T symmetry. The experimental activities on the neutron EDM lay dormant until CP violation, directly linked to T violation via the CPT theorem [11–13], was discovered in 1964 [14].

The interest in the neutron EDM was greatly revived when a large number of theoretical models, designed to account for the CP-violation phenomenon in neutral kaon decays, predicted a neutron EDM large enough to be detected. Many ingenious technical innovations have since been implemented, and the experimental limit of neutron EDM was pushed down to  $10^{-25}$  e-cm, a six order-of-magnitude improvement over the first EDM experiment. Unlike parity violation, the underlying physics for CP and T violation remains a great enigma nearly 40 years after its discovery. As discussed in Chapter II, improved neutron EDM measurements will continue to provide the most stringent tests for various theoretical models and to reveal the true origins of CP violation.

Table III-A lists the results from all existing neutron EDM experiments. In Fig. III-1 the neutron EDM upper limits are plotted versus year of publication. The different symbols in Fig. III-1 signify different experimental techniques. The experimental techniques fall into three categories. Category I, which consists of only two experiments, utilizes neutron scattering to probe the effect of the neutron EDM. The strong electric fields encountered by polarized neutrons in scattering from electrons or nuclei, could affect the

Table III-A. Summary of Neutron EDM experiments.

| Ex. Type<br>(Lab)             | $\langle v \rangle$<br>(m/sec) | $E$<br>(kV/cm) | $B$<br>(Gauss) | Coh. Time<br>(sec) | EDM<br>( $e \cdot \text{cm}$ )   | Ref.<br>(year)   |
|-------------------------------|--------------------------------|----------------|----------------|--------------------|--|------------------|
| Scattering<br>(ANL)           | 2200                           | $\sim 10^{15}$ | —              | $\sim 10^{-20}$    | $< 3 \times 10^{-18}$  | [1,16]<br>(1950) |
| Beam Mag. Res.<br>(ORNL)      | 2050                           | 71.6           | 150            | 0.00077            | $(-0.1 \pm 2.4) \times 10^{-20}$<br>$< 4 \times 10^{-20}$ (90% C.L.)   | [3]<br>(1957)    |
| Beam Mag. Res.<br>(ORNL)      | 60                             | 140            | 9              | 0.014              | $(-2 \pm 3) \times 10^{-22}$<br>$< 7 \times 10^{-22}$ (90% C.L.)       | [22]<br>(1967)   |
| Bragg Reflection<br>(MIT/BNL) | 2200                           | $\sim 10^9$    | —              | $\sim 10^{-7}$     | $(2.4 \pm 3.9) \times 10^{-22}$<br>$< 8 \times 10^{-22}$ (90% C.L.)    | [17]<br>(1967)   |
| Beam Mag. Res.<br>(ORNL)      | 130                            | 140            | 9              | 0.00625            | $(-0.3 \pm 0.8) \times 10^{-22}$<br>$< 3 \times 10^{-22}$              | [23]<br>(1968)   |
| Beam Mag. Res.<br>(BNL)       | 2200                           | 50             | 1.5            | 0.0009             | $< 1 \times 10^{-21}$  | [26]<br>(1969)   |
| Beam Mag. Res.<br>(ORNL)      | 115                            | 120            | 17             | 0.015              | $(1.54 \pm 1.12) \times 10^{-23}$<br>$< 5 \times 10^{-23}$             | [24]<br>(1969)   |
| Beam Mag. Res.<br>(ORNL)      | 154                            | 120            | 14             | 0.012              | $(3.2 \pm 7.5) \times 10^{-24}$<br>$< 1 \times 10^{-23}$ (80% C.L.)    | [25]<br>(1973)   |
| Beam Mag. Res.<br>(ILL)       | 154                            | 100            | 17             | 0.0125             | $(0.4 \pm 1.5) \times 10^{-24}$<br>$< 3 \times 10^{-24}$ (90% C.L.)    | [28]<br>(1977)   |
| UCN Mag. Res.<br>(PNPI)       | • 6.9                          | 25             | 0.028          | 5                  | $(0.4 \pm 0.75) \times 10^{-24}$<br>$< 1.6 \times 10^{-24}$ (90% C.L.) | [31]<br>(1980)   |
| UCN Mag. Res.<br>(PNPI)       | • 6.9                          | 20             | 0.025          | 5                  | $(2.1 \pm 2.4) \times 10^{-25}$<br>$< 6 \times 10^{-25}$ (90% C.L.)    | [32]<br>(1981)   |
| UCN Mag. Res.<br>(ILL)        | • 6.9                          | 10             | 0.01           | 60–80              | $(0.3 \pm 4.8) \times 10^{-25}$<br>$< 8 \times 10^{-25}$ (90% C.L.)    | [36]<br>(1984)   |
| UCN Mag. Res.<br>(PNPI)       | • 6.9                          | 12–15          | 0.025          | 50–55              | $-(1.4 \pm 0.6) \times 10^{-25}$<br>$< 2.6 \times 10^{-25}$ (95% C.L.) | [35]<br>(1986)   |
| UCN Mag. Res.<br>(ILL)        | • 6.9                          | 16             | 0.01           | 70                 | $-(3 \pm 5) \times 10^{-26}$<br>$< 12 \times 10^{-26}$ (95% C.L.)      | [41]<br>(1990)   |
| UCN Mag. Res.<br>(PNPI)       | • 6.9                          | 12–15          | 0.018          | 70–100             | $(2.6 \pm 4.5) \times 10^{-26}$<br>$< 9.7 \times 10^{-26}$ (90% C.L.)  | [38]<br>(1992)   |
| UCN Mag. Res.<br>(ILL)        | • 6.9                          | 4.5            | 0.01           | 120–150            | $(-1 \pm 3.6) \times 10^{-26}$<br>$< 6.3 \times 10^{-26}$ (90% C.L.)   | [47]<br>(1999)   |

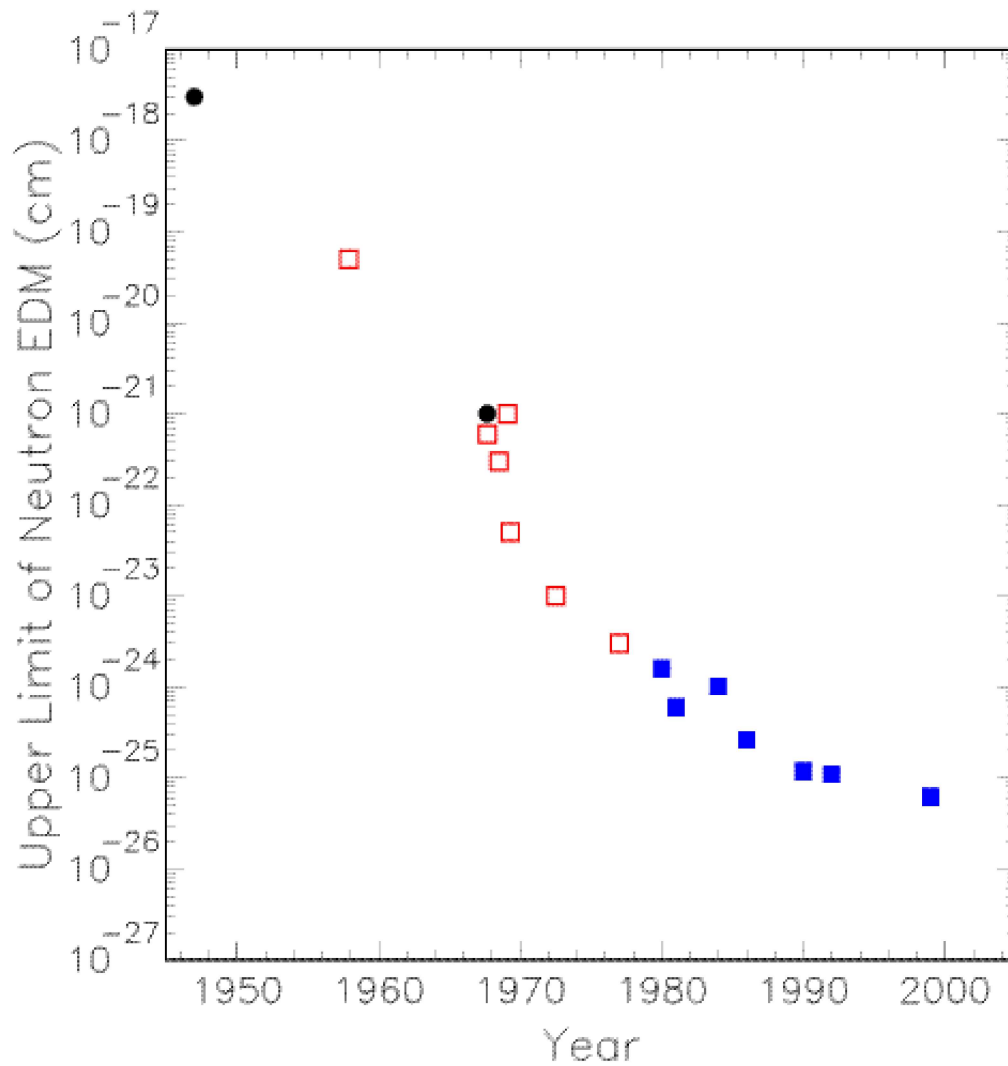


Fig. III-1. Upper limits of neutron EDM plotted as a function of year of publication. The solid circles correspond to neutron scattering experiments. The open squares represent in-flight magnetic resonance measurements, and the solid squares signify UCN magnetic resonance experiments.

scattering amplitudes if the neutron has a non-zero EDM. The second and third categories both involve magnetic resonance techniques. In the presence of a strong external electric field, a finite neutron EDM would cause a shift of the magnetic resonance frequency. From 1950 to mid 1970s, thermal or cold neutron beams have been used in the measurements (category II). Since early 1980s, all neutron EDM experiments have utilized bottled UCNs (category III), which provide the most sensitive measurements to date.

## A) Neutron EDM from Neutron Scattering

The upper limit of the neutron EDM was first determined in 1950 by Purcell and Ramsey [1] from an analysis of earlier experiments of neutron-nucleus scattering [15,16]. In these experiments, the strength of the neutron-electron interaction was deduced from the interference between the neutron-nucleus and neutron-electron scattering. If the observed neutron-electron interaction strength is attributed entirely to the neutron EDM ( $d_n$ ), an upper limit of  $\bar{d}_n \leq 3 \times 10^{-18} e\cdot\text{cm}$  is obtained.

An alternative method to extract the electron-neutron interaction is to scatter electron beam from nuclear targets. Indeed, precise  $e-d$  and  $e\text{-}^3\text{He}$  scattering data have been obtained at various electron accelerators. However, we are not aware of any attempt to extract upper limits of neutron EDM based on these data. Since the electron-neutron interaction is dominated by the electric and magnetic form factors of the neutron, any effect due to neutron EDM is probably too small to be observed.

Another technique to search for the neutron EDM is the Bragg reflection of thermal neutrons from a single crystal. The scattering amplitude of thermal neutrons comes mainly from the nuclear interaction. However, the Coulomb field exerted by the positively charged nucleus on the incident neutron can provide additional contributions. First, it produces an effective magnetic field of  $\bar{v} \times \bar{E}$  in the neutron rest frame. The neutron magnetic moment interacts with this magnetic field (Schwinger scattering) leading to the following contribution to the scattering amplitude:

$$\begin{aligned} f_{\text{Sch}} &= i f'_{\text{Sch}}, \\ f'_{\text{Sch}} &= \frac{1}{2} \mu_n (\hbar/Mc) (Ze^2/\hbar c) (1-f) \cot \theta \bar{P} \cdot \bar{n}, \end{aligned} \quad (\text{III.1})$$

where  $\bar{P}$  is the polarization vector of the neutron,  $\bar{n}$  is the unit vector normal to the neutron scattering plane, and  $\theta$  is the neutron scattering angle.  $\mu_n$  is the neutron magnetic moment and  $f$  is the electron screening factor. The Schwinger scattering amplitude is purely imaginary and is proportional to  $\bar{P} \cdot \bar{n}$ . The effect of Schwinger scattering is maximal when the neutron polarization is perpendicular to the scattering plane. If the neutron polarization lies in the scattering plane, then  $f_{\text{Sch}} = 0$ .

If the neutron has a non-zero EDM, the Coulomb field of the nucleus would lead to an additional potential  $V_d(\mathbf{r}) = -\vec{d}_n \cdot \vec{E}(\mathbf{r})$ , where  $\vec{d}_n$  is the neutron EDM. The scattering amplitude contributed by this interaction is

$$\begin{aligned} f_d &= if'_d, \\ f'_d &= \frac{Ze(1-f)}{\hbar v} d_n \csc \theta \vec{P} \cdot \vec{e}, \end{aligned} \quad (\text{III.2})$$

where  $\vec{e} = (\vec{k}' - \vec{k})/2k \sin \theta$ .  $\vec{k}$  and  $\vec{k}'$  are the wave vectors for the incident and scattered neutron, respectively. Similar to the Schwinger scattering, the neutron EDM interaction also gives rise to an imaginary scattering amplitude. However,  $f_d$  is maximal when the neutron polarization vector  $\vec{P}$  lies on the scattering plane and is aligned with  $\vec{e}$  (note that  $f_{\text{Sch}} = 0$  in this case). This is an important feature that allows the isolation of the  $f_d$  contribution.

In measurements at MIT and BNL, Shull and Nathans [17] attempted to determine the  $f_d$  term by measuring Bragg reflection of polarized neutrons off a CdS crystal. If the neutron polarization is in the plane of scattering, then  $f_{\text{Sch}}$  does not contribute and the Bragg reflection intensity  $I$  is given as

$$I \sim F^2 V \sim \left[ a^2 + (a' - f'_d)^2 \right] V, \quad (\text{III.3})$$

where  $a$  and  $a'$  are the real and imaginary parts of the nuclear scattering length, respectively.  $F$  is the crystal structure factor and  $V$  is the effective volume of the crystal. Upon a reversal of the polarization direction of the neutron beam,  $f'_d$  flips sign and the fractional change in the intensity becomes

$$\Delta I/I = 4a'f'_d / (a^2 + a'^2). \quad (\text{III.4})$$

Equation (III.4) shows that it is important to find a crystal with a large value of  $a'/a$ . In general, however, the value of  $a'/a$  is very small. In a few special cases, when there is a resonance absorption cross section of the order of  $10^4$  barns,  $a'/a \simeq 1$ . In particular, a cadmium crystal has  $a = 0.37 \times 10^{-12}$  cm and  $a' = 0.6 \times 10^{-12}$  cm. Shull and Nathans selected the CdS crystal for their Bragg reflection measurement, because at the [004] orientation of the crystal,  $a = a_{\text{Cd}} - a_{\text{S}}$ , and the real part of the scattering length from S largely cancels that from Cd ( $a_{\text{S}} = 0.28 \times 10^{-12}$  cm and  $a'_{\text{S}}$  is negligible). Following a three-month run with  $4 \times 10^8$  neutrons counted, they obtained [17] an upper limit for the neutron EDM as  $5 \times 10^{-22}$  e-cm.

An important limitation of the crystal reflection method is the difficulty to align the crystal orientation (hence the scattering plane) with the polarization direction of the incident neutrons. Any residual misalignment would allow the Schwinger scattering to contribute to  $\Delta I$  in a fashion similar to neutron EDM. A rotation of the crystal-detector assembly by  $180^\circ$  around an axis in the beam direction in principle can isolate the effect of Schwinger scattering, provided that there is no residual magnetic field which does not rotate with the apparatus (such as earth's magnetic field). The limit on  $d_n$  of the Shull and Nathans experiment is consistent with a misalignment angle of  $1.6 \pm 1.0$  mrad.

It is likely that the Bragg reflection technique can be further refined to achieve better sensitivity. In particular, Alexandrov et al. [18] suggested that a crystal made of tungsten isotopes enriched with  $^{186}\text{W}$  has several advantages over the CdS crystal. First, tungsten has a higher  $Z$  than cadmium, leading to a twofold gain in  $f_d$ . Second, the real part of the scattering length of the tungsten crystal can be made practically zero by fine-tuning the  $^{186}\text{W}$  concentration. As shown in Eq. (III.4), this leads to a larger effect in  $\Delta I$ . Third, the imaginary part of the scattering length of tungsten is roughly a factor of 150 smaller than that of CdS. This implies a much larger effective volume  $V$  for tungsten, since the penetration depth  $L$  of the Bragg reflection is proportional to  $(a^2 + a'^2)^{-1/2}$ . Putting together all these factors, it was estimated that the running time could be reduced by a

factor of 500 to achieve the same statistical accuracy as obtained in the CdS experiment. However, such improvement is not sufficient to make it competitive with respect to the magnetic resonance method, to be described in the next subsection.

Another type of crystal diffraction experiment has been suggested which can increase the effective neutron interaction time by a factor of  $\sim 100$ . It requires neutrons incident at the Bragg angle on a large perfect crystal oriented in the Laue arrangement. Neutrons will experience multiple Bragg reflections resulting in a wave traveling along the Bragg planes. The intensity of the transmitted neutrons will exhibit an oscillatory pattern along a direction perpendicular to the Bragg planes. Such interference fringes, called Pendellösung (Pendulum) by Ewald in his study of X-ray diffraction, were first observed for neutron beams by Shull [19]. Since the location of the fringe is highly sensitive to the neutron scattering amplitude, a non-zero neutron EDM would generate a shift of the fringe pattern, provided that a non-centrosymmetric crystal (such as BGO) is used. If one selects nuclei with low neutron absorption, a large crystal (several centimeters thick) would allow neutrons to be transmitted with little loss. This corresponds to an observation time of  $\sim 10^{-5}$  seconds which is 100 times longer than for the Bragg reflection method. The expected statistical sensitivity has been estimated to be around  $3 \times 10^{-25}$  e-cm per day, very competitive to any other technique. Unfortunately, the crystal needs to be aligned to an accuracy of  $10^{-7}$  radian, a difficult if not insurmountable problem.

## **B) Neutron EDM from In-Flight Neutron Magnetic Resonance**

The method used in this type of measurement is similar to the magnetic resonance technique invented by Alvarez and Bloch [20] for a neutron magnetic moment measurement. Essentially, transversely polarized neutrons traverse a region of fixed uniform magnetic field  $\vec{B}_0$  and a static electric field  $\vec{E}_0$  parallel to  $\vec{B}_0$ . The neutrons precess at the frequency

$$h\nu = -2\mu B_0 - 2d_n E_0 , \quad (\text{III.5})$$

where  $\mu$  is the neutron magnetic dipole moment and  $d_n$  is the neutron EDM. Upon reversal of the electric field direction, the precession frequency will shift by

$$h\Delta\nu = -4d_nE_0 . \quad (\text{III.6})$$

Therefore, by measuring the precession frequency with the electric field parallel and antiparallel to the magnetic field, the neutron EDM can be determined as

$$d_n = \frac{h\Delta\nu}{4E_0} . \quad (\text{III.7})$$

The neutron precession frequency can be accurately measured using the technique of separated oscillatory fields developed by Ramsey [21]. Oscillating magnetic fields of identical frequency are introduced at each end of the homogeneous-field region. Spin-flip transitions are induced in the neutron beam when the frequency of the applied oscillatory magnetic field approaches the neutron precession frequency. The fraction of neutrons emerging from the spectrometer with their spins flipped depends sensitively on the frequency of the oscillating field. The goal of the neutron EDM experiment is to accurately determine the shift of the resonance frequency when the direction of the electric field is reversed.

Following the pioneering work of Purcell et al. at Oak Ridge in 1950, various improvements of the experimental techniques have been introduced and similar experiments were carried out at Oak Ridge [22–25], Brookhaven [26], Bucharest [27], Aldermaston, and Grenoble [28]. Table III-A lists some characteristics of these experiments. The 1977 measurement [28] at the Institut Laue-Langevin (ILL), Grenoble represented a four order-of-magnitude improvement in sensitivity over the original Oak Ridge experiment. This was accomplished by minimizing the statistical and systematic errors. We will now discuss the factors contributing to the statistical and systematic errors for this type of experiment.

Equation (III.7) shows that  $d_n$  is proportional to  $\Delta\nu$ , given as

$$\Delta\nu = \Delta N / (dN / d\nu) , \quad (\text{III.8})$$

where  $N$  is the number of neutron counts per cycle and  $dN / d\nu$  is the slope of the resonance curve. To achieve maximal sensitivity, the oscillator frequency is set near the steepest slope of  $dN / d\nu$ . In this case,  $(dN / d\nu) / N$  is proportional to the neutron time-

of-flight between the two RF coils and to the neutron polarization  $P$ . The flight time is simply  $L/\langle v \rangle$ , where  $L$  is the distance between the RF coils and  $\langle v \rangle$  is the mean neutron velocity.  $\Delta N$  is proportional to  $(\phi_n t)^{1/2}$ , where  $\phi_n$  is the flux of neutrons and  $t$  is the total running time. Taking these factors into account, one obtains the following relation for the statistical uncertainty in  $d_n$ :

$$\Delta d_n \propto \langle v \rangle / [E_0 L P (\phi_n t)^{1/2}] . \quad (\text{III.9})$$

To obtain maximal sensitivity, the experiment needs to maximize the electric field  $E_0$ , the distance  $L$ , the neutron polarization  $P$ , and the neutron flux  $\phi_n$ . In addition, the mean neutron velocity  $\langle v \rangle$  needs to be minimized. Table III-A lists these parameters for various experiments.

Many sources of systematic errors have been identified and the dominant ones are:

- The  $\bar{v} \times \bar{E}$  effect.
- Fluctuation of the magnetic field.

The  $\bar{v} \times \bar{E}$  effect, also called the motional field effect, refers to the additional magnetic field  $\bar{B}_m$  viewed from the neutron rest frame,

$$\bar{B}_m = \frac{1}{c} \bar{v} \times \bar{E}_0 , \quad (\text{III.10})$$

where  $\bar{v}$  is the neutron velocity in the lab frame. If the electric field  $\bar{E}_0$  is not completely aligned with the magnetic field  $\bar{B}_0$ , then  $\bar{B}_m$  would acquire a non-zero component along the direction of  $\bar{B}_0$ . Upon reversal of the electric field direction, this component will also reverse direction and produce the same signature as would a neutron EDM. An apparent EDM resulting from the motional field effect is

$$d_n = [(\mu_n / \mu_N) / 4\pi] \lambda_c (v/c) \sin \theta , \quad (\text{III.11})$$

where  $\mu_N$  is the nuclear magneton,  $\theta$  is the angle between the  $B$  and  $E$  fields, and  $\lambda_c$  is the Compton wavelength of the proton. Equation (III.11) shows that for a cold neutron of 100 m/sec, a misalignment angle of  $1.5 \times 10^{-3}$  radians would lead to an apparent neutron EDM of  $10^{-23}$  e·cm.

Careful attention has been given to alignment of the  $B$  and  $E$  fields. A tight geometric tolerance was imposed to make the magnetic pole faces parallel to the electric plates. In

one experiment [26], the magnetic pole faces also serve as the electric field electrodes. Stray ambient magnetic fields could also contain components perpendicular to the  $E$  field, and the spectrometer needs to be surrounded by several magnetic shields. By rotating the entire spectrometer by  $180^\circ$  around a vertical axis, the  $\vec{v} \times \vec{E}$  effect can be isolated.

The applied magnetic field needs to be spatially homogeneous and temporally stable. Since neutrons follow different paths in the spectrometer, any spatial non-uniformity would degrade the sharpness of the resonance. The temporal stability is even more critical. In particular, any systematic variation of the magnetic field correlated with the reversal of electric field must be minimized. It can be shown that in order to achieve a sensitivity of  $10^{-24} e \cdot \text{cm}$  for  $d_n$ , the allowable magnetic noise correlated with the electric field reversal must be below a few nano Gauss. A shift of the magnetic field can be caused, for example, by the breakdowns in the electric field. The current pulse associated with the spark could permanently magnetize small portions of the pole faces, and the direction of such magnetic field is correlated with the polarity of the electric field. Another type of spurious magnetic field correlated with the electric field is the leakage current. Fortunately, for neutron beam experiments, the bulk of the leakage current occurs outside the spectrometer and does not pose a problem.

As shown in Table III-A, the most sensitive neutron beam (Category II) experiment [28], obtained:

$$d_n = (0.4 \pm 1.5) \times 10^{-24} e \cdot \text{cm} , \quad (\text{III.12})$$

where the total error contains a systematic error of  $1.1 \times 10^{-24} e \cdot \text{cm}$ . The dominant contribution to the systematic error is the  $\vec{v} \times \vec{E}$  effect, even though the misalignment angle is determined to be as small as  $1.1 \times 10^{-4}$  radians. The limitations from  $\vec{v} \times \vec{E}$  effect and from the magnetic field fluctuation can be removed by using bottled UCN, to be discussed next.

### C) Neutron EDM with Ultra-Cold Neutrons

There are two major limitations in the search for neutron EDM using thermal or cold neutron beams. First, the  $\vec{v} \times \vec{E}$  effect imposes stringent requirements on the alignment of the  $\vec{E}$  and  $\vec{B}$  fields, as discussed earlier. Second, the transit time of neutron beams in the magnetic spectrometer is relatively short, being  $10^{-2}$  seconds roughly. This leads to a

rather large width of the resonance curve and implies the necessity to measure very small variations of the neutron counts. Therefore, any systematic effects associated with the reversal of the electric field would have to be reduced to extremely low levels. These and other limitations are responsible for the fact that the best upper limit for neutron EDM achieved with the cold neutron beam at ILL is  $3 \times 10^{-24} e \cdot \text{cm}$  even though the statistical uncertainty is at a lower level of  $\sim 3 \times 10^{-25} e \cdot \text{cm}$ .

In 1968 Shapiro first proposed [29] using UCN in searches for neutron EDM. The much lower velocities of UCNs will clearly suppress the  $\vec{v} \times \vec{E}$  effect. The amount of suppression is further enhanced in an UCN bottle, which allows randomization of the neutron momentum directions. Another important advantage is that the effective interaction time of UCN in a storage bottle will be of the order  $10^2 - 10^3$  seconds, a factor of  $10^4 - 10^5$  improvement over the neutron beam experiments. This significantly improves the sensitivity for EDM signals relative to EDM-mimicking systematic effects. An important price to pay, however, is the much lower flux for UCN relative to that of thermal or cold neutron beams.

A series of neutron EDM experiments using UCN has been carried out at the Petersburg Nuclear Physics Institute (PNPI) and at the ILL. Although there are many similarities in the approaches of these two groups, important differences do exist. In the following, we summarize the pertinent features and results of these experiments.

### **C.1) UCN Measurements at PNPI**

Immediately following Shapiro's original proposal [29], preparation for an UCN neutron EDM experiment started at PNPI in 1968. The first version of the experiment, reported in 1975 [30], used a single-chamber "flow-through" type spectrometer with separated oscillating fields. An uncooled beryllium converter provided low flux of UCN and the width of the magnetic resonance curve corresponds to an effective storage time of  $\sim 1$  second. The large dispersion of the UCN transit time through the Ramsey-type oscillating fields causes significant broadening of the resonance line width. The sensitivity of this experiment turned out to be  $\sim 2 \times 10^{-22} e \cdot \text{cm}$  per day and was not competitive.

Several significant improvements were subsequently introduced leading to the first competitive result from the PNPI group [31]. First, a beryllium converter cooled to  $30^\circ\text{K}$  resulted in a 10 - 12 fold increase of the UCN flux. Second, an adiabatic method using

inhomogeneous magnetic field was implemented to rotate the neutron spin by  $90^\circ$ . This solved the dispersion problem encountered in the Ramsey method and the effective storage time was increased to 5 seconds. Third, a “differential double-chamber” spectrometer replaces the original single-chamber spectrometer. A common magnetic field was applied to the two adjacent identical chambers, while the applied electric fields in the two chambers have opposite signs. Upon reversal of the polarity of the electric field, the resonance frequency shift due to the neutron EDM, would be opposite in sign for the upper and lower chambers. In contrast, fluctuation of the common magnetic field will cause similar frequency shifts in both chambers. This enabled one to reduce the effect of the magnetic field instability. Finally, neutrons of opposite polarization direction were analyzed at the exit of each chamber with two separate detectors simultaneously. This allowed a two-fold increase in the count rates and also provided useful checks on systematic effects.

In the 1980 paper of the PNPI group [31], the UCN flux at the spectrometer input was  $\sim 1.2 \times 10^4$  neutrons per second. A constant magnetic field of 28 mG and an electric field of  $\sim 25$  kV/cm were applied to the double-chamber of  $\sim 20$  liters each. The uniformity of the magnetic field within the chambers is within  $(1-2) \times 10^{-5}$  Gauss. To achieve magnetic field stability, a passive three-layer magnetic shield provided a shielding factor of  $10^3$ . An active system consisting of a flux-gate magnetometer and Helmholtz coils was used to compensate and stabilize the external magnetic field. Another active system for stabilizing the magnetic field inside the shields was realized with the aid of an optical-pumping quantum magnetometer. From six different sets of measurements, the mean square deviation of the results is consistent with the expected statistical error, suggesting that the systematic error is negligible. The result,  $d_n = (0.4 \pm 0.75) \times 10^{-24}$  e·cm, implied  $|d_n| < 1.6 \times 10^{-24}$  e·cm at 90% confidence level.

In 1981, the PNPI group reported a new measurement [32] of neutron EDM. The major improvements included a new source of UCN based on a  $150\text{-cm}^3$  liquid hydrogen moderator [33] and a new coating for the chambers allowing total internal reflection for more energetic UCNs. The UCN intensity at the output of the spectrometer was improved by a factor of 7 to 8. From four different sets of measurements, they obtained [32],  $d_n = (2.3 \pm 2.3) \times 10^{-25}$  e·cm. At 90% confidence level,  $|d_n| < 6 \times 10^{-25}$  e·cm. In 1984, an updated result of  $d_n = -(2 \pm 1) \times 10^{-25}$  e·cm was reported by Lobashev and Serebrov [34]. This implied  $|d_n| < 4 \times 10^{-25}$  e·cm at 95% confidence level.

Major modifications for the PNPI experiment were reported [35] in 1986. In previous PNPI experiments, UCNs flowed continuously through the magnetic resonance

spectrometer with an average transit time of  $\sim 5$  seconds. At this time the ILL stored UCN experiment [36] reported a confinement time of  $\sim 60$  seconds. The PNPI group modified their spectrometer to allow prolonged confinement of the UCNs. They achieved a confinement time of  $\sim 50$  seconds. A new universal source of cold and ultracold neutrons [37] was also used which provided a 3–4 times increase in UCN flux. The longer confinement time put more stringent requirement on the stability of the magnetic field, and two cesium magnetometers were positioned near the chambers for active stabilization of the magnetic field inside the spectrometer. The result of this experiment was  $d_n = -(1.4 \pm 0.6) \times 10^{-25} e\cdot\text{cm}$ , implying  $|d_n| < 2.6 \times 10^{-25} e\cdot\text{cm}$  at 95% confidence level.

The most recent PNPI measurement was reported in 1992 [38], and a detailed account of this experiment was presented in a later paper [39]. The experimental setup was essentially the same as before [35], with minor modifications such as adding the fourth layer of the magnetic shield and adding the third cesium magnetometer near the chambers. The experiment consisted of 15 runs comprising a total of 13,863 measurement cycles. Each measurement cycle included filling the chambers with polarized UCN (30–40 s), confinement (70–100 s), and discharge and counting (40 s). A 2-second-long oscillating field pulse was applied at the beginning and at the end of the confinement time. The intensity of the uniform magnetic field was 18 mG, and the mean electric field was 14.4 kV/cm.

The result based on the analysis of the yields in the four neutron counters was  $d_n = (0.7 \pm 4.0) \times 10^{-26} e\cdot\text{cm}$ . From the analysis of the readings of the upper and lower magnetometers, a non-zero false EDM was found. Note that there should be no false EDM if the magnetometers faithfully measured the effective mean magnetic fields in the chambers. This false EDM was attributed to inhomogeneous magnetic pick-ups of various origins, including possible magnetization of the magnetic shield by sparks and spurious magnetic field generated by neighboring experimental apparatus affected by the reversal of the electric field. No correlation between  $d_n$  and the leakage current was found, showing that the leakage current was not a main source of the systematic effect. The amount of false EDM registered by the magnetometers suggested that a systematic correction of  $-(1.9 \pm 1.6) \times 10^{-26} e\cdot\text{cm}$  needs to be applied to the measured EDM value. Therefore, the final result was

$$d_n = [2.6 \pm 4.0(\text{stat}) \pm 1.6(\text{syst})] \times 10^{-26} e \cdot \text{cm} . \quad (\text{III.13})$$

This result was interpreted as  $|d_n| < 1.1 \times 10^{-25} e\cdot\text{cm}$  at 95% confidence level. Systematic errors appeared to limit the sensitivity of this experiment to few  $10^{-26} e\cdot\text{cm}$ .

## C.2) UCN Measurements at ILL

Following the completion of the neutron EDM measurement [28] using the neutron beam magnetic resonance method, the interest at ILL shifted to the use of UCN [40], which would bypass the limitation imposed by the  $\vec{v} \times \vec{E}$  effect. Unlike the PNPI group, the ILL group started out with the UCN storage bottle technique and did not use the less sensitive flow-through technique. The first ILL result was published in 1984 [36], which demonstrated the feasibility of measuring neutron EDM with stored UCN. A 5-liter cylindrical chamber contained polarized UCN of a density up to 0.05 per  $\text{cm}^3$ , and neutrons precessed for 60 seconds in a uniform magnetic field of 10 mG and an electric field of 10 kV/cm. In contrast to the PNPI experiment, only one UCN storage chamber was implemented. Moreover, only a single detector was used to determine the number of neutrons having opposite polarization directions at the end of each storage cycle. From data collected in 136 one-day runs, a result of  $d_n = (0.3 \pm 4.8) \times 10^{-25} e\cdot\text{cm}$  was obtained. Only statistical error was included, since the readings from three rubidium magnetometers showed negligible systematic effect.

The sensitivity of the ILL measurement was significantly improved in a subsequent experiment reported in 1990 [41]. A new neutron turbine [42] increased the UCN flux by a factor of 200 and a density of 10 UCN per  $\text{cm}^3$  was achieved in the neutron bottle. The electric field was raised to 16 kV/cm and the leakage current was reduced from 50 nA to 5 nA. Following a three-year running period over 15 reactor cycles, the weighted average of these 15 data sets was  $d_n = -(1.9 \pm 2.2) \times 10^{-26} e\cdot\text{cm}$ , with a rather poor  $\chi^2$  per degree of freedom of 3.1. At this level of statistical accuracy, the difficulty of monitoring the magnetic field in the neutron bottle by the rubidium magnetometers, which were no closer than 40 cm to the axis of the bottle, became a dominant source of systematic error. After taking this uncertainty into account, the final result was reported to be  $d_n = -(3 \pm 5) \times 10^{-26} e\cdot\text{cm}$ , implying  $|d_n| < 1.2 \times 10^{-25} e\cdot\text{cm}$  at the 95% confidence level.

To overcome the systematic uncertainty caused by magnetic field fluctuations in the UCN bottle, Ramsey suggested [43] the use of comagnetometers for EDM experiments. The idea was to store polarized atoms simultaneously in the same bottle as the neutrons. Fluctuation of the magnetic field will affect the spin precession of the comagnetometer atoms, which can be monitored. The ILL collaboration selected  $^{199}\text{Hg}$  as the

comagnetometer. Effects from the  $^{199}\text{Hg}$  EDM are negligible, since earlier experiments [44–46] showed that the EDM of  $^{199}\text{Hg}$  was less than  $8.7 \times 10^{-28} e\cdot\text{cm}$ .

The most recent ILL experiment [47] used a 20-liter UCN bottle containing  $3 \times 10^{10}/\text{cm}^3$  polarized  $^{199}\text{Hg}$ . The UCN precession time was 130 seconds, roughly a factor of two improvement over previous experiment. However, the maximum electric field in this UCN bottle is only 4.5 kV/cm, roughly a factor of 3.5 lower than before. The UCN flux also appeared to be a factor of four lower than in the earlier experiment. Data were collected over ten reactor cycles of 50 days' length, and the  $^{199}\text{Hg}$  comagnetometer was shown to reduce effects from magnetic field fluctuations significantly. The result of this experiment was  $d_n = (1.9 \pm 5.4) \times 10^{-26} e\cdot\text{cm}$ . A much improved  $\chi^2$  per degree of freedom of 0.97 was obtained for 322 measurement runs, and this was interpreted as an evidence for negligible systematic effects. An upper limit on the neutron EDM of  $|d_n| < 9.4 \times 10^{-26} e\cdot\text{cm}$  was obtained at the 90% confidence level. When this result was combined with the result from the earlier ILL experiment [41], an improved upper limit of  $6.3 \times 10^{-26} e\cdot\text{cm}$  was obtained. However, the method used to combine these two results was recently criticized by Lamoreaux and Golub [48], who argued that the two measurements should be treated independently.

The ILL experiment demonstrated the advantage of using a comagnetometer for reducing a dominant source of systematic error. It is conceivable that the sensitivity to the neutron EDM can be improved to a level better than  $10^{-27} e\cdot\text{cm}$ , provided that a more intense UCN flux together with a suitable comagnetometer, become available. In this proposal, we present a new approach for accomplishing this goal.

## References

- [1] E. M. Purcell and N. F. Ramsey, *Phys. Rev.* **78**, 807 (1950).
- [2] J. H. Smith, Ph.D. thesis, Harvard University, 1951 (unpublished).
- [3] J. H. Smith, E. M. Purcell, and N. F. Ramsey, *Phys. Rev.* **108**, 120 (1957).
- [4] T. D. Lee and C. N. Yang, *Phys. Rev.* **104**, 254 (1956).
- [5] N. F. Ramsey, *Molecular Beams* (Oxford University Press, Oxford, 1956).
- [6] C. S. Wu, E. Ambler, R. Hayward, D. Hoppes, and R. Hudson, *Phys. Rev.* **105**, 1413 (1957).
- [7] R. Garwin, L. Lederman, and M. Weinrich, *Phys. Rev.* **105**, 1415 (1957).
- [8] J. Friedman and V. Telegdi, *Phys. Rev.* **105**, 1681 (1957).
- [9] L. Landau, *Nucl. Phys.* **3**, 127 (1957).
- [10] Ia. B. Zel'dovich, *J. Exp. Theor. Phys.* **6**, 1488 (1957) [*Sov. Phys. JETP* **6**, 1148 (1957)].
- [10a] N. F. Ramsey, *Phys. Rev.* **109**, 222 (1958).

- [11] J. Schwinger, *Phys. Rev.* **82**, 914 (1951); **91**, 713 (1953).
- [12] G. Lüders, *Kgl. Danske Videnskab Selskab. Mat. Fiz. Medd.* **28**, No 5 (1954); G. Lüders and B. Zumino, *Phys. Rev.* **106**, 385 (1957).
- [13] W. Pauli, in *Niels Bohr and the Development of Physics* (McGraw-Hill, New York, 1955).
- [14] J. H. Christenson, J. W. Cronin, V. L. Fitch, and R. Turlay, *Phys. Rev. Lett.* **13**, 138 (1964).
- [15] W. W. Havens, I. I. Rabi, and L. J. Rainwater, *Phys. Rev.* **72**, 634 (1947).
- [16] E. Fermi and L. Marshall, *Phys. Rev.* **72**, 1139 (1947).
- [17] C. G. Shull and R. Nathans, *Phys. Rev. Lett.* **19**, 384 (1967).
- [18] Yu. A. Alexandrov et al., *Yad. Fiz.*, **10**, 328 (1968).
- [19] C. G. Shull, *Phys. Rev. Lett.* **21**, 1585 (1968).
- [20] L. W. Alvarez and F. Bloch, *Phys. Rev.* **57**, 111 (1940).
- [21] N. F. Ramsey, *Phys. Rev.* **76**, 996 (1949); *Phys. Rev.* **84**, 506 (1951).
- [22] P. D. Miller, W. B. Dress, J. K. Baird, and N. F. Ramsey, *Phys. Rev. Lett.* **19**, 381 (1967).
- [23] W. B. Dress, J. K. Baird, P. D. Miller, and N. F. Ramsey, *Phys. Rev.* **170**, 1200 (1968).
- [24] J. K. Baird, P. D. Miller, W. B. Dress, and N. F. Ramsey, *Phys. Rev.* **179**, 1285 (1969).
- [25] W. B. Dress, P. D. Miller, and N. F. Ramsey, *Phys. Rev.* **D7**, 3147 (1973).
- [26] V. W. Cohen et al., *Phys. Rev.* **177**, 1942 (1969).
- [27] S. Apostolescu et al., *Rev. Roum. Phys.* **15**, 343 (1970).
- [28] W. B. Dress et al., *Phys. Rev.* **D15**, 9 (1977).
- [29] F. L. Shapiro, *Usp. Fiz. Nauk.* **95**, 145 (1968).
- [30] A. I. Egorov et al., *Yad. Fiz.* **21**, 292 (1975).
- [31] I. S. Altarev et al., *Nucl. Phys.* **A341**, 269 (1980).
- [32] I. S. Altarev et al., *Phys. Lett.* **102B**, 13 (1981).
- [33] I. S. Altarev et al., *Phys. Lett.* **A80**, 413 (1980).
- [34] V. M. Lobashev and A. P. Serebrov, *J. Phys. (Paris)* **45**, 3 (1984).
- [35] I. S. Altarev et al., *JETP Lett.* **44**, 460 (1986).
- [36] J. M. Pendlebury et al., *Phys. Lett.* **136B**, 327 (1984).
- [37] I. S. Altarev et al., *JETP Lett.* **44**, 345 (1986).
- [38] I. S. Altarev et al., *Phys. Lett.* **276B**, 242 (1992).
- [39] I. S. Altarev et al., *Phys. Atomic Nucl.* **59**, 1152 (1996).
- [40] R. Golub and J. M. Pendlebury, *Rep. Prog. Phys.* **42**, 439 (1979).
- [41] K. F. Smith et al., *Phys. Lett.* **234B**, 191 (1990).
- [42] A. Steyerl et al., *Phys. Lett.* **A116**, 347 (1987).
- [43] N. F. Ramsey, *Acta Phys. Hung.* **55**, 117 (1984).
- [44] S. K. Lamoreaux et al., *Phys. Rev. Lett.* **59**, 2275 (1987).
- [45] J. P. Jacobs et al., *Phys. Rev. Lett.* **71**, 3782 (1993).
- [46] J. P. Jacobs et al., *Phys. Rev.* **A52**, 3521 (1995).
- [47] P. G. Harris et al., *Phys. Rev. Lett.* **82**, 904 (1999).

[48] S. K. Lamoreaux and R. Golub, *Phys. Rev.* **D61**, 051301 (2000).

## Chapter IV. PROPOSED MEASUREMENT — OVERVIEW

This experiment is based on a technique to measure the neutron EDM, which is qualitatively different from the strategies adopted in previous measurements (see Chapter III). Chapter IV provides an overview of the general strategy, however, many crucial technical details that are essential to the success of the measurement are deferred until Chapter V.

The overall strategy adopted here [1a], is to form a three component fluid of neutrons and  $^3\text{He}$  atoms dissolved in a bath of superfluid  $^4\text{He}$  at  $\sim 300$  mK. When placed in an external magnetic field, both the neutron and  $^3\text{He}$  magnetic dipoles can be made to precess in the plane perpendicular to the B field. The measurement of the neutron electric dipole moment comes from a precision measurement of the difference in the precession frequencies of the neutrons and the  $^3\text{He}$  atoms, as modified when a strong electric field (parallel) to B is turned on (or reversed). In this comparison measurement, the neutral  $^3\text{He}$  atom is assumed to have a negligible electric dipole moment, as expected for atoms of low atomic number [1a].

### A. General Features

#### 1. Frequency Measurement

As discussed in Chapter III, over the forty-year history of experimental searches for the neutron EDM,  $d_n$ , a number of different techniques have been employed. However, in the last two decades the measurements have focused on the use of UCN constrained to neutron traps. The primary method is to study the precession frequency of neutrons with aligned spins in the plane perpendicular to a static magnetic field,  $B_0$ . Application of a static electric field,  $E_0$ , parallel (anti-parallel) to  $B_0$  can change the Larmor precession frequency,  $\nu_n$ , in proportion to the neutron EDM,  $d_n$ . The precession frequency is:

$$\nu_n = -[2\mu_n B_0 \pm 2d_n E_0]/h \equiv \nu_0 \pm (\Delta\nu/2) \quad (\text{IV.1})$$

where the minus sign reflects the fact that  $\mu_n < 0$ .

Thus the frequency shift,  $\Delta\nu$ , as the direction of  $E_0$  is reversed, is:

$$\Delta\nu = -4d_n E_0/h, \quad (\text{IV.2})$$

In the case of  $B_0 = 1$  mG and  $E_0 = 0$ , the Larmor precession frequency is  $\nu_0 = 2.92$ Hz. With  $E_0 = 50$  kV/cm, and using a nominal value of  $d_n = 4 \times 10^{-27}$  e cm, the frequency shift, as the electric field is reversed, is:

$$\Delta\nu = 0.19\mu\text{Hz} = 0.66 \times 10^{-7} \nu_0 . \quad (\text{IV.3})$$

Note that for the current measurement, it is the absolute frequency shift,  $\Delta\nu$ , that is critical, not the fractional frequency shift. For a known electric field,  $E_0$ , the uncertainty in  $d_n$  is:

$$\delta d_n = h \frac{\delta\Delta\nu}{4E_0} \quad (\text{IV.4})$$

## 2. Statistical and Systematic Errors

The immediate challenge of an EDM measurement of  $\Delta\nu$  is to generate as large an electric field as possible in the presence of a weak  $B$  field, and to measure a precession frequency shift with an absolute uncertainty  $\delta\Delta\nu$  at the sub  $\mu\text{Hz}$  level. Other issues include production of a large neutron sample size as well as having a precise knowledge of the spatial and temporal properties of  $B_0$  and  $E_0$ .

Consider a measurement sequence in which  $N_0$  neutrons are collected in a trap over a time  $T_0$ , followed by a precession measurement for a time  $T_m$ . This measurement cycle can be repeated  $m$  times for a total measurement time:  $t = m T_m$ . A single cycle takes a time:  $T_0 + T_m$  and the time to perform  $m$  cycles is:  $m (T_0 + T_m)$ .

From the uncertainty principle we have

$$\delta\Delta\nu \geq \frac{1}{2\pi T_m \sqrt{N}} \quad \text{per cycle}$$

The statistical contribution to the uncertainty in the EDM for the set of  $m$  measurements is:

$$\sigma \geq \frac{\hbar/4}{E_0 T_m \sqrt{Nm}} = \frac{\hbar/4}{E_0 \sqrt{T_m N t}} \text{ ecm} . \quad (\text{IV.5})$$

Here  $N < N_0$  is the effective number of neutrons contributing to or detected in the measurement. Equation IV.5 is useful since it gives a lower bound on the statistical error. In practice it only gives an order of magnitude estimate for the statistical error of a generic experiment due to the ambiguity in the value of  $N$ . For the experiment discussed here, we do the proper analysis of the statistical error in Section V.H.

Consider the parameters typical of this proposed LANSCE measurement as discussed below:  $E_0 = 50$  kV/cm,  $T_0 = 1000$  sec,  $T_m = 500$  sec,  $N = 4.0 \times 10^6$  neutrons / measurement cycle and  $m = 5.7 \times 10^3$  repeated cycles (1500 sec / cycle and 100 days of live time). Three other parameters, also discussed below, characterize the three neutron loss mechanisms:

Beta decay:  $\tau_\beta = 887$ sec, wall losses  $\tau_{\text{wall}} = 1200$ sec,  
and n -  $^3\text{He}$  absorption  $\tau_3 = 500$ sec

Using Eq. (IV.5) with the overestimate,  $N = N_0$ , gives for one standard deviation uncertainty:  $\sigma \geq 10^{-28}$  e cm. See however, the more realistic calculation (including shot noise) given in Section V.H, which gives a  $2\sigma$  limit of  $9 \times 10^{-28}$  e cm.

One can compare this result to the error on the 1990 Smith [1], ILL measurement where they achieved:

$$d_n = -3 \pm 5 \times 10^{-26} \text{ e cm.}$$

where the error is from both statistical and systematic contributions. For the more recent Harris [2], ILL measurement they achieve:

$$d_n = -1 \pm 3.6 \times 10^{-26} \text{ e cm.}$$

For statistical errors, note that the quality factor,  $E_0 \sqrt{(T_m N)}$  in Eq. (IV.5), gives a relative reduction in  $\sigma$  by a factor of 50 to 100 at LANSCE, in comparison to the Smith [1] ILL measurement and to the Harris [2] ILL measurement.

The challenges in designing this trapped UCN experiment were to maximize  $N_0$ ,  $T_m$ , and  $E_0$ . In addition it is crucial to develop uniform, stable, and well measured  $B_0$  and  $E_0$  fields over the sample volume since these are a major source of systematic errors. The method developed to measure the errors related to  $B_0$  are discussed below. More generally, issues related to systematic errors, such as  $v \times E$  effects, pseudo-magnetic fields, gravitational effects, spatial differences in UCN/  $^3\text{He}$  distributions, etc., are discussed in detail in Section V.H.

In the technique adopted here, there are three critical issues that are addressed in this overview:

1. Optimize the UCN trap design for large  $N_0$ , long trap lifetime, and large  $E_0$ .

2. Make a precision measurement of the  $B_0$  field, averaged over the neutron trap volume and valid for the neutron precession period.
3. Make a precision measurement of the neutron precession frequency,  $\nu_n$ .

The overall layout of the experimental apparatus is shown in Fig. IV.1

## B. Neutron Trap Design

We use the strategy for loading the trap with UCN suggested first by Golub [3]. It relies on using UCN locally produced inside a closed neutron trap filled with ultra-pure, superfluid  $^4\text{He}$ , cooled to about 300 mK. When this neutron trap is placed in a beam of cold neutrons ( $E = 1$  meV,  $v = 440$  m/s,  $\lambda = 8.9$  Å, see section V.A) the neutrons interacting with the superfluid may be down-scattered to  $E < 0.13$   $\mu$  eV,  $v < 5$  m/s with a recoil phonon in the superfluid carrying away the missing energy and momentum.

The properly averaged UCN trapping (production) rate [4], as discussed in Section V.B, gives a nominal trapped UCN production rate,  $P$ , of

$$P \sim 1.0 \text{ UCN/cm}^3 \text{ sec}$$

In order to minimize neutron absorption by hydrogen, deuterated polystyrene coatings have been developed for the surfaces of the trap (see discussions in [5]). The goal for the mean life of a neutron in a trap filled with pure  $^4\text{He}$  and operated at 300 mK is about 500 sec as a result of losses by neutron beta decay and neutron wall interactions.

In  $T_0 = 1000$  sec of UCN production, the neutron density will reach  $\rho_n \sim 500$  UCN/cm<sup>3</sup> in the  $^4\text{He}$ . Note that at other facilities with more intense sources of cold neutrons this density could be considerably higher. This UCN production technique and the UCN production rate calculations for a  $^4\text{He}$  filled UCN trap have been tested and validated by Golub [3], and at the neutron lifetime experiment now in progress at NIST [6] (see Section V.B).

The details of the proposed geometry for the target region of the experiment are shown in Figs. IV.1 and IV.2, with two trap volumes, one on each side of the high-voltage central electrode. Thus two orientations of the electric field for a fixed  $B$  field will be measured simultaneously. Superfluid  $^4\text{He}$  is a very good medium for high electric fields (see [7] and section V.E) and experience has shown that the deuterated polystyrene surfaces are very stable under high  $E$  fields [5]. Independent bench tests are planned in order to

evaluate the trap performance under these conditions. The goal is to operate at an  $E$  field strength of 50 kV/cm (about four times greater than other recent EDM measurements).

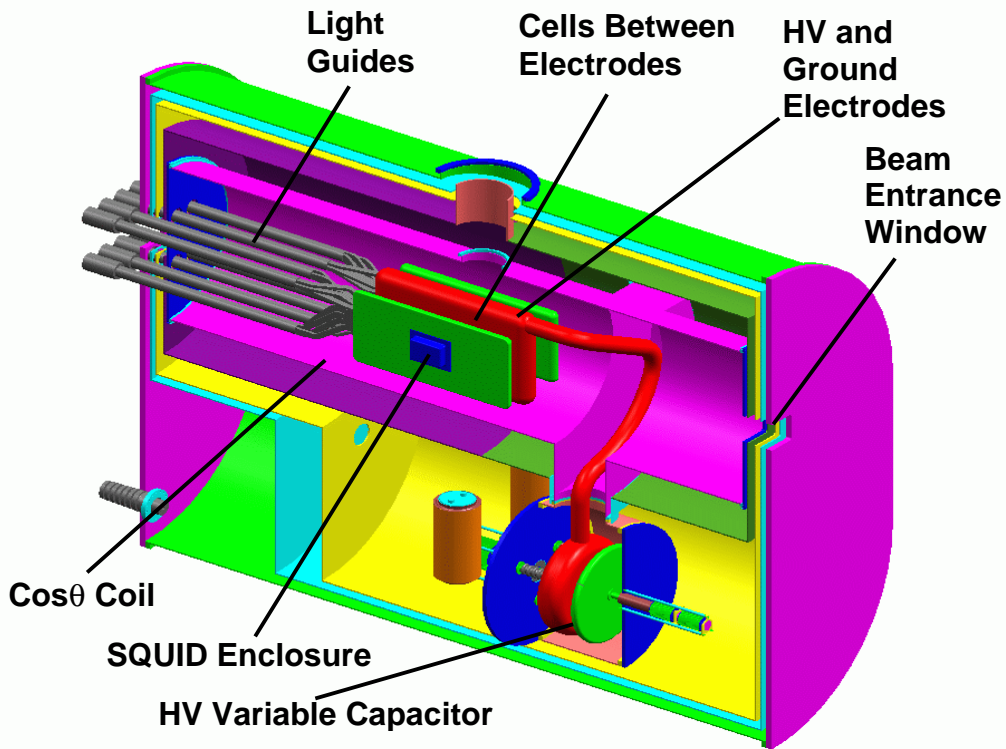


Fig IV-1. Experimental cryostat, length  $\sim 3.1$  m. The neutron beam enters from the right. Two neutron cells are between the three electrodes. Scintillation light from the cells is monitored by the light guides and photomultipliers.

Properties of the magnetic and electric fields are discussed in Section V.E. The region in the cryostat but outside the UCN cells (see Fig. IV-1) will also be filled with  $^4\text{He}$  because of its good electrical insulating properties. Note: The  $^4\text{He}$  fluid in the region outside the two UCN cell volumes will contain  $^3\text{He}$  atoms at normal concentrations (see below). Any UCN produced there will be absorbed in coatings on the vessel wall to prevent wall activation.

### C. Measurement of the $B$ Field with a $^3\text{He}$ Co-Magnetometer

Knowledge of the  $B$  field environment of the trapped neutrons is a crucial issue in the analysis of systematic errors in the measurement. The  $^4\text{He}$ -UCN cells will sit in the uniform  $B$  field of a Cos  $\Theta$  magnet with a nominal strength of 1 mG (up to 10 mG). The  $B$  field must be uniform to 1 part in 1000 (see Section V.E). These features of the  $B$  field must be confirmed by direct measurement in real time.

The magnetic dipole moment of  $^3\text{He}$  atoms is comparable to that of the neutron (see Table I-B) such that the  $^3\text{He}$  magnetic dipole moment is only 11% larger than that of the neutron. In addition, the EDM of the  $^3\text{He}$  atom is negligible due to the shielding from the two bound electrons [1a] i.e. Schiff shielding [8]. These properties make  $^3\text{He}$  an excellent candidate as a monitor of the  $B$  field in the volume where the UCN are trapped, or if  $B$  is stable, as a reference for precession frequency measurements.

To exploit this, the pure  $^4\text{He}$  superfluid is modified by adding a small admixture of polarized  $^3\text{He}$  (with spins initially aligned with the  $B_0$  field). The amount is  $\approx 1 \times 10^{+12}$  atoms /  $\text{cm}^3$  and fractional density of  $X = 0.4 \times 10^{-10}$ . This mixture is prepared in a separate reservoir and then transferred to the neutron cells. The result is a three-component fluid in the cell with densities:  $\rho_n = 5.0 \times 10^{+22} / \text{cc}$ ,  $\rho_3 = 0.8 \times 10^{+12} / \text{cc}$ , and  $\rho_4 = 2.2 \times 10^{+22} / \text{cc}$ .

The UCN cells will be adjacent to SQUID coils mounted in the ground electrodes as discussed in Section V.F and V.H. The spins of the ensembles of  $^3\text{He}$  and neutrons are aligned (see below) and are initially parallel to the  $B_0$  field. An “RF coil”, positioned with its axis perpendicular to  $B_0$  (see Section V.E), is then used to rotate the neutron and  $^3\text{He}$  spins into the plane perpendicular to  $B_0$ . We discuss the resulting n- $^3\text{He}$  interaction below.

As the spins of the  $^3\text{He}$  atoms and the neutrons precess in this plane, the SQUID coils will pick up the signal from the large number of precessing  $^3\text{He}$  magnetic dipoles; the corresponding neutron signal from  $500 \text{ UCN}/\text{cm}^3$  is negligible. Analysis of this

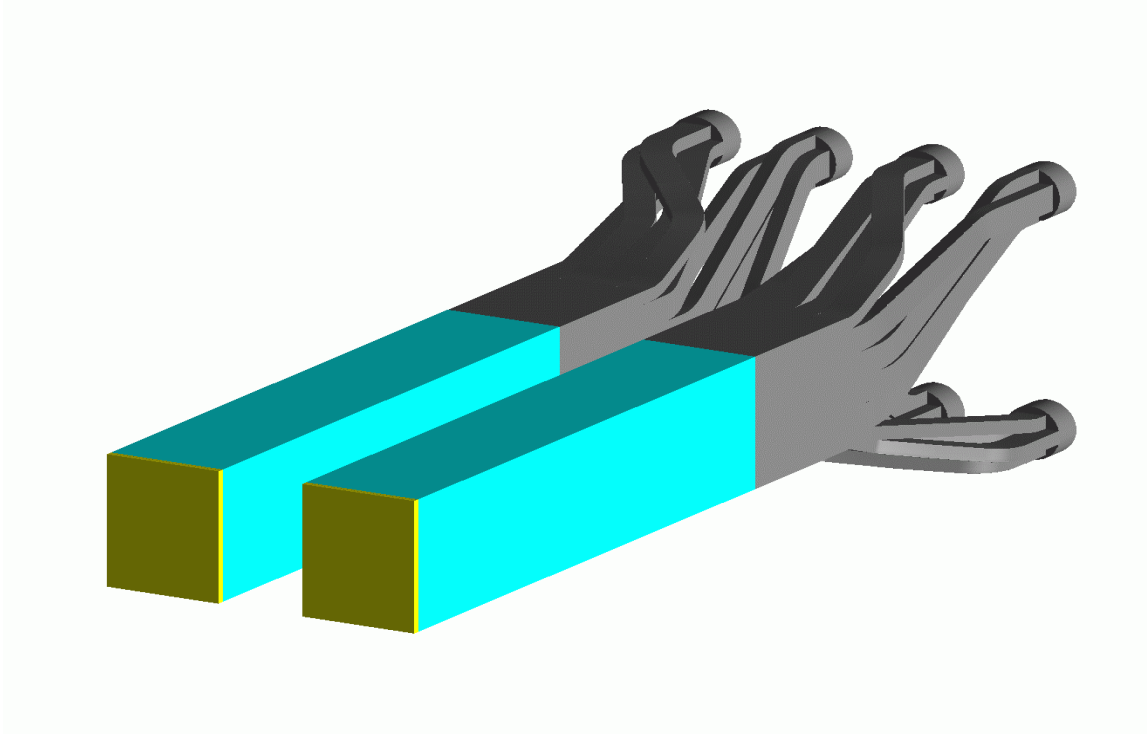


Fig IV-2. Two cell design with light guides which connect to the photomultiplier tubes outside the cryostat. Each cell has a nominal volume of 4 L.

sinusoidal signal will directly measure the  $^3\text{He}$  precession frequency,  $\nu_3$ , and thus the magnetic field,  $B_0$ , averaged over the same volume and time interval as experienced by the trapped UCN's.

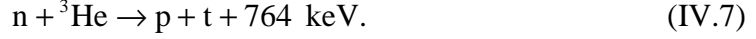
$$B_0 = \frac{\nu_3}{2\mu_3} . \quad (\text{IV.6})$$

In summary, the addition of the  $^3\text{He}$  atoms to the measurement cells and the SQUIDs to the electrodes, provides the opportunity for a direct measurement *in situ* of the  $B$  field averaged over the cell volumes and the time period of the measurement.

#### **D. Measurement of the UCN Precession Frequency**

Knowledge of the neutron EDM depends on a precision measurement of the change in the neutron precession frequency for the two orientations of the electric field. Consider  $N_0$  UCN trapped in a cell. Because the magnitude of the precession frequency shift,  $\Delta\nu_n$ , due to the interaction of the neutron EDM with the electric field, is extremely small,

$<1 \mu\text{Hz}$ , it is imperative to measure it with great precision. The technique adopted here is to make a comparison measurement in which  $\nu_n$  is compared to the  $^3\text{He}$  precession frequency,  $\nu_3$ . The technique relies on the spin dependence of the nuclear absorption cross section for the reaction:



The nuclear absorption reaction products (and the neutron beta decay products) generate scintillation light in the  $^4\text{He}$  fluid, which can be shifted in wavelength and detected with photomultipliers.

The absorption cross section is strongly dependent on the initial spin state of the reaction:

|         | <b>Spin State Cross Section, <math>\sigma_{\text{abs}}</math>, barns [10]</b> |                                    |
|---------|---|------------------------------------|
|         | ( $v = 2200 \text{ m/sec}$ )  | ( $v = 5 \text{ m/sec}$ )          |
| $J = 0$ | $\sim 2 \times 5.5 \times 10^{+3}$  | $\sim 2 \times 2.4 \times 10^{+6}$ |
| $J = 1$ | $\sim 0$  | $\sim 0$                           |

There are two options here. In **option A**, where the cell is irradiated with an unpolarized cold neutron beam, we take  $\sigma_{\text{abs}} = 2.4 \times 10^6 \text{ b}$  as the average  $^3\text{He}$  absorption cross section for UCNs. The mean life of the neutron in the trap due to  $^3\text{He}$  absorption alone,  $\tau_3$ , is given by:

$$1/\tau_3 = \rho_3 [\sigma_{\text{abs}} v]_{\text{UCN}} = \rho_3 [\sigma_{\text{abs}} v]_{\text{thermal}} . \quad (\text{IV.8})$$

The  $^3\text{He}$  density,  $\rho_3$ , is adjusted to give  $\tau_3 = 500 \text{ sec}$ . This corresponds to:

$$\rho_3 = 0.85 \times 10^{+12} \text{ } ^3\text{He} / \text{cm}^3.$$

The net neutron mean life in the trap is 250 sec, due about equally to losses by  $^3\text{He}$  absorption and by neutron beta decay/ wall losses.

In this scheme, the only neutrons which survive are those with spins parallel to the polarization vector of the  $^3\text{He}$  (and aligned with the  $B_0$  field). In the process, half the neutrons in the trap have been lost. We are assuming here 100%  $^3\text{He}$  polarization and that there is no polarization loss in the traps.

An alternative approach, **option B**, is to pre-select the cold neutron beam according to spin direction, with an upstream spin selector, and to direct neutrons of each of the two transverse spin orientations to each of the two cells. Although there may be flux losses in the spin selector apparatus, the subsequent loss of neutrons to  $^3\text{He}$  absorption in a cell will only occur if there is not perfect  $^3\text{He}$  or neutron-beam polarization or if there is loss of polarization in the cell as time passes. Over all this approach makes the measurement less sensitive to the  $^3\text{He}$  polarization in the cells (see Section V.D).

As noted, there are three neutron loss mechanisms in the cells which lead to:  $\tau_{\beta} = 887$  sec,  $\tau_3 = 500$  sec,  $\tau_{\text{cell}} \sim 1200$  sec. During the precession process in the cell, as a result of all three loss mechanisms, the net neutron mean life is:  $1/\Gamma_{\text{avg}} = 250$  sec. On the other hand, during the UCN production phase in which a cold polarized beam of neutrons is aligned with the polarized  $^3\text{He}$  in the cell, there are no absorption losses and the mean neutron life in the cell is 500 sec. Effects due to time dependent polarization changes in the cell are neglected in this discussion (section V.C and V.H). This second strategy, **option B**, is being evaluated and is discussed in Section V.A.

To start the precession process, independent RF coils are used to reorient the neutron and the  $^3\text{He}$  spin directions into the plane perpendicular to  $B_0$  where they both precess about  $B_0$ , initially with their spins parallel. Thus the aligned  $^3\text{He}$  and UCN components are trapped in the cell and continue to precess for up to a time,  $T_m$ , at which point the cell is flushed so a new measurement cycle can begin.

However, because the magnetic dipole moments of the neutron and  $^3\text{He}$  are slightly different :

$$\mu_{^3\text{He}}/\mu_n = 1.11 ,$$

the  $^3\text{He}$  spin vectors will gradually rotate ahead of the neutron spin vectors and destroy the alignment. As the precession continues, the absorption process will alternately appear and disappear.

This absorption process can be observed as scintillation light generated by the recoiling charged particle reaction products in the  $^4\text{He}$  superfluid. The scintillation light is emitted in a broad spectrum centered at 80 nm, and is easily transmitted to the wall of the cell where a deuterated tetraphenyl butadiene-doped polystyrene surface will absorb it and re-emit it at 430 nm. This wave-shifted light can be collected with light pipes and transmitted to photomultiplier tubes outside of the  $B$  field region (see Section V.C).

The net scintillation light signal,  $\Phi(t)$ , due to a constant background,  $\Phi_{\text{bgd}}$ , beta decay, and  $^3\text{He}$  absorption, and with polarizations  $P_3$  and  $P_n$ , can be written as (see V.H):

$$\Phi(t) = \Phi_{\text{bgd}} + N_o \exp(-\Gamma_{\text{avg}} t) \left\{ \frac{1}{\tau\beta} + \frac{1}{\tau 3} (1 - P_3 P_n \cos[(\nu_3 - \nu_n)t + \phi]) \right\}$$

Equation IV.9

where we neglect the loss of both neutron and  $^3\text{He}$  polarization during the measurement period. Here  $\Gamma_{\text{avg}}$  is the overall neutron loss rate for the cell including both wall losses and neutron beta decay as well as absorption. The neutron scintillation rate has a time dependence coming from both the decaying exponential factor and the sinusoidal dependence on:  $\nu_3 - \nu_n = 0.3$  Hz.

The resulting photomultiplier signal gives a direct measure of the neutron precession rate,  $\nu_n$ , when combined with a knowledge of  $\nu_3$ .

In summary, the introduction of  $0.8 \times 10^{+12}$  polarized  $^3\text{He}$  atoms/cm<sup>3</sup> into a cell containing  $5 \times 10^{+2}$  UCN/cc allows one to directly measure the average  $B_0$  field and to confirm the polarization of the UCN. It also permits a direct and precise measurement of the orientation of the UCN spin relative to the  $^3\text{He}$  spin as they precess over a time interval,  $T_m = 500$  sec (two neutron mean cell life times). It is this time-dependent absorption sinusoidal light signal which must be carefully analyzed for changes in its period as the  $E_0$  field is reversed.

For this two component fluid of neutrons and  $^3\text{He}$  dissolved in the  $^4\text{He}$  super-fluid we measure:

$$\nu_3 = -2\mu_3 B_0 , \quad (\text{IV.10})$$

obtained from the SQUID signal, and

$$\nu_n = -[2\mu_n B_0 + 2E_0 d_n] / h , \quad (\text{IV.11})$$

obtained from the combination of the scintillation light and the SQUID signals.

Thus analysis of the shape and the time dependence of the scintillation light signal, throughout the precession period, is critical to the precision of the EDM measurement.

Note that when  $E_0 = 0$ , the two measurements (SQUID and scintillation signals) can be crossed checked since they should both give the common value of  $B_0$ . Alternatively, for a stable  $B_0$  field and when  $E_0 \neq 0$ , the SQUID measurement provides a reference clock against which a shift in the scintillator spectrum can be measured.

## E. Discussion of Errors

The most vexing problem in the design of a neutron EDM measurement is the control of systematic errors. This is amply illustrated by the discussion of previous neutron EDM measurements reviewed in Chapter III. This overview addresses only a few aspects of the problem; the details are deferred to the main discussion in Section V.H.

### 1. *Statistical Errors*

The gross analysis of the statistical errors presented above, equation IV.5, suggests that the proposed technique gives an improvement in the figure of merit  $E_0\sqrt{(T_m N_o)}$  by a factor of 50 – 100 over recent UCN measurements at ILL. Subsidiary measurements planned for LANSCE, involving cell fabrication tests, cold neutron flux measurements, and maximum usable E field tests, will verify whether this gain can be fully realized.

### 2. *Systematic Errors*

The analysis of systematic errors is a challenging and detailed exercise and is at the heart of a successful EDM measurement. The major concerns are related to knowledge of the magnetic and electric fields (since both time-dependent field strengths and nonparallel E and B fields, have the potential to produce a false EDM signal), any differences in the two cells, and any contribution of background sources to the scintillation light spectrum.

The  $^3\text{He}$ -precession measurement allows the magnetic field to be sampled in time and space throughout the precession period and over the volume of the UCN traps. The major limitations come from the quality, stability, and background of the SQUID signals. Bench tests of the performance of the SQUID coils at these low temperatures and in the LANSCE noise environment are in progress as discussed in Section V.F. The goal is a  $B_0$  field uniform to 0.1 % over the cell volume.

The electric field properties are equally critical. The goal for the electric field uniformity is  $< 1\%$  as discussed in Section V.E. In order to achieve the high fields consistent with the dielectric properties of the superfluid  $^4\text{He}$  medium, a program for performing bench tests of the maximum useable electric field is being developed. Issues of leakage currents and sparks are critical and in the end will dictate the upper limit at which the applied voltage can operate.

Other issues, related to the properties of the cold neutron beam, pre-selection of the neutron spin, and the role of gamma-ray and neutron induced backgrounds, are discussed in Sections V.A and V.C. The optimum sequence in the measurement cycles in order to cancel systematic shifts in the data also has to be evaluated.

## F. Measurement Cycle

By way of clarification and review, we describe the measurement sequence over the 1500 sec measurement cycle, as currently envisioned, with some additional details included.

1. **Cold neutron beam preparation.** Cold neutrons ( $v= 440$  m/s, 1 meV) from the LANSCE liquid-hydrogen moderator, are transported by neutron guides through a frame overlap chopper,  $T_O$  chopper, and a Bi filter. This system (see Section V.A) filters out unusable neutrons and gamma rays. In addition the beam is divided into two guides that transport the cold neutrons downstream and through the cryostat wall to the two cells. We are currently evaluating techniques to install a spin filter in the guide (**option B** in the above discussion) to permit pre-selection of the neutron spin state. Spin rotators make both beams have their spins aligned with the  $^3\text{He}$  atoms in the measuring cells. The technology to divide the beam is available, but the cost in loss of flux and beam line floor space is still being evaluated. The splitter is discussed in Section V.A and Appendix A.

For the purposes of this discussion of the measurement cycle, we assume that the beam is split into two components matched to the neutron cell sizes and that the beam spin filter is implemented. We further assume that  $E_O$  and  $B_O$  are on and stable during the entire cycle.

2.  **$^4\text{He}$  and polarized  $^3\text{He}$  transfer to the cells.** – START OF A 5-STEP CYCLE. During a previous measurement phase (step 5 below), polarized  $^3\text{He}$  ( $\sim 99\%$  polarization and density fraction  $X \sim 10^{-10}$ ) from an atomic beam apparatus, is mixed with ultra-pure superfluid  $^4\text{He}$  in a reservoir separate from the target cells. Now, with the beam shutter closed, the mixture is transferred to the measurement cells. A small holding field continues to be used to maintain the polarization during the transfer,  $< 10$  sec. The  $^3\text{He}$  polarization is selected in the polarized source to be either parallel or anti-parallel to the magnetic field,  $B_O$ , generated by the  $\cos \Theta$  magnet. The  $^3\text{He}$  spin vectors are the same in both cells, but, by construction, the electric

fields are opposite of each other, regardless of the sign of the potential on the high-voltage electrode.

3. **Cold neutron beam irradiation and production of the UCN in the cells.** The beam shutter is opened, allowing the cold neutrons to irradiate the cells, some of which produce UCN. The two cells, each filled with superfluid  $^4\text{He}$  ( $2.2 \times 10^{22}/\text{cm}^3$ ) and polarized  $^3\text{He}$  ( $0.8 \times 10^{12}/\text{cm}^3$ ), are irradiated for  $T_0 = 1000$  sec. A trapped sample of UCN is built up with a production rate of  $P = \sim 1 \text{ UCN} / (\text{cm}^3 \text{ sec})$ . The mean life of these neutrons in the cells is  $\sim 500$  sec due to both beta decay and wall losses alone. Assuming that the initial sample of neutrons has been fully polarized, the large n- $^3\text{He}$  cross section in the  $J = 0$  state will reduce only slightly the population of neutrons during the UCN collection process. Neutrons properly aligned with the  $^3\text{He}$  will suffer no absorption losses. The number density produced in  $T_0 = 1000$  sec grows to  $\rho_n \sim 500 \text{ UCN} / \text{cm}^3$  (actually  $430 / \text{cm}^3$  when corrected for beta decay and cell losses) in each of two cells of volume =  $4000 \text{ cm}^3$  per cell. At the end of the UCN fill period, the beam shutter is closed.
4. **Rotation of both magnetic moments into the transverse plane.** The spin vectors are rotated into the plane perpendicular to  $B_0$  and  $E_0$  by pulsing an “RF” coil at  $3.165$  Hz for  $1.58$  sec (see Section V. E). Both the neutrons and the  $^3\text{He}$  start to precess about  $B_0$  in order to conserve angular momentum.
5. **Precession Frequency measurements.** The critical precession frequency measurement occurs over the next  $T_m = 500$  seconds. At the start of the measurement there are  $4 \times 10^{+6}$  neutrons in the two traps. The SQUID detectors measure the  $^3\text{He}$  precession,  $\nu_3$ , at about  $3$  Hz over a set of  $1500$  signal periods. The scintillator detection system measures  $\nu_3 - \nu_n = 0.3$  Hz over a set of  $150$  signal periods. The neutron sample continues to decrease with a mean life of  $250$  sec due to all loss mechanisms and is reduced to  $116 \text{ UCN}/\text{cm}^3$ , i.e. a total of  $0.5 \times 10^{+6}$  neutrons at the end of the measurement cycle. As discussed in detail in Section V.H, this corresponds to a sensitivity of
 
$$\sigma \sim 7 \times 10^{-26} \text{ e cm in one cycle.}$$
 In parallel with the precession measurement, the mixing reservoir is refilled with pure  $^4\text{He}$  and polarized  $^3\text{He}$  in the correct proportions.
6. **Empty the cells.** Valves are opened to drain the cells in about  $10$  sec, and the  $^3\text{He}$ - $^4\text{He}$  mixture is sent to a recovery reservoir for purification. END OF THE CYCLE, return to step #2.

7. **Repeated cycles.** A single cycle takes about  $T_0 + T_m = 1500$  sec plus some transfer times. The cycle can be repeated about  $m = 5.7 \times 10^3$  time in 100 days, which gives a two  $\sigma$  limit of  $< 9 \times 10^{-28}$  e cm in one hundred days.

Over this 100-day period one expects to follow a program of electric field reversals, spin reversals, magnetic field reversals, etc. to study and remove systematic effects.

Altogether this measurement involves the interplay of many technical and practical issues: polarized UCN and  $^3\text{He}$  production, precision measurements of frequencies, UCN trap design, electric and magnetic field measurements, etc. These issues are discussed in detail in the following segment, Chapter V.

## References

- [1a] I B. Khriplovich, S.K. Lamoreaux, “CP Violation Without Strangeness”, Springer-Verlag, (1997).
- [1] K. F. Smith et al., *Phys. Lett.* **234B**, 191 (1990).
- [2] P. G. Harris et al, *Phys. Rev. Lett.* **82**, 904 (1999).
- [3] P. Ageron et al, *Phys Lett.* **A66**, 469 (1978), R. Golub et al, *Z. Phys.***B51**, 187 (1983), R. Golub, *J. Phys.* **44**, L321 (1983); Proc. 18th Int. Conf. on Low Temperature Physics, Pt. 3 Invited Papers (Kyoto, Japan), 2073 (1987), R. Golub and S. Lamoreaux, *Phy. Rep.* **237**, 1 (1994).
- [4] S. K. Lamoreaux and R. Golub, *JETP Lett.* **58**, 793 (1993).
- [5] S. K. Lamoreaux, Institut Laue-Langevin Internal Report 88LAOIT, 1988, unpublished; J.M. Pendlebury, *Nuc. Phys.* **A546**, 359 (1992).
- [6] P. R. Hoffman et al., *Nature* **403**, 62 (2000).
- [7] J. Gerhold, *Cryogenics* **12**, 370 (1972).
- [8] L. I. Schiff, *Phys. Rev.* **132**, 2194 (1963); Quantum Mechanics, third edition (New York: McGraw-Hill, 1968).
- [9] Superfluid He is a well known scintillator for:  
electrons: M. Stockton et al., *Phys. Rev. Lett.* **24**, 654 (1970).  
alpha particles: H. A. Roberts and F. L. Hereford, *Phys. Rev.* **A7**, 284 (1973). D. N. McKinsey et al, *NIM* **B132**, 351 (1997), D. N. McKinsey et al, *Phys. Rev.* **A59**, 200 (1999).

- [10] Als-Nielsen and R. Dietrich, *Phys. Rev.* **133**, B925 (1964), Passel and Schirmer, *Phys. Rev.* **150**, 146 (1966).

## V. EXPERIMENTAL DESIGN ISSUES

### V.A. LANSCE Pulsed Cold Neutron Beam

The UCN production rate in the superthermal LHe source depends upon the neutron beam spectral density  $d^2\Phi/d\lambda d\Omega$  at 8.9 Å, as is discussed in chapter V.B. Neutrons with a different wavelength than 8.9 Å will not downscatter to make UCNs but instead will pass through the apparatus or will be scattered and absorbed by surrounding materials. Some of betas and gamma rays from the decay processes can then interact with the liquid helium in the measurement cells, producing scintillation light that affects the signal-noise ratio of the EDM measurement. To reach its goal, the EDM experiment requires the maximum flux of 8.9-Å neutrons from the source and beamline. The monochromatism,  $\Delta\lambda/\lambda$ , of the 8.9 Å beam should be  $\sim 1\%$ . The beam should be highly polarized with a minimum of fast neutrons or high-energy gamma-rays. Its phase space should match the UCN production cells.

#### V.A.1. Cold Moderator of the LANSCE Spallation Source

At the LANSCE spallation neutron source, 800-MeV proton pulses, at the rate of 20 Hz, interact with the tungsten target producing fast neutrons that are partially moderated by a super-cooled hydrogen gas moderator. The EDM experiment will be mounted behind the  $n+p \rightarrow d+\gamma$  experiment on a new cold neutron beamline, flight path 12, at the Lujan Center. This beamline views the new upper tier cold hydrogen moderator. The calculated performance of this coupled moderator, including the time and energy spectra of a neutron pulse, are described in Ref. [1]. Figure V.A.1. shows the calculated average moderator brightness as a function of the neutron energy (the energy of the 8.9 Å neutron is about 1 meV) for hydrogen with an ortho-para ratio of 1. The brightness is obtained from the MCNPX moderator model calculations [1,2] that have been scaled according to experimental results from the flight path 11A cold moderator [3].

#### V.A.2. Beamline of the EDM experiment

The beamline for the EDM experiment will be built as an extension from the  $n+p \rightarrow d+\gamma$  experiment on the flight path 12. The beamline of the  $n+p \rightarrow d+\gamma$  experiment that is under construction is shown in figure V.A.2. The neutron guide of the  $n+p \rightarrow d+\gamma$  beamline ends 21 m from the moderator. For the EDM experiment, a section of neutron guide will be installed through the  $n+p \rightarrow d+\gamma$  cave. At the end of the cave, a Bi filter will be mounted, and it will be followed by a  $t_0$  chopper located in place of the  $n+p \rightarrow d+\gamma$  beam stop.

Downstream of the chopper, the 8.9-Å neutrons will be split to two beams, polarized in opposite directions, and guided to the measurement cells that are located at 31 m from the moderator. The floor plan of the EDM beamline and the experiment is shown in figure V.A.3.

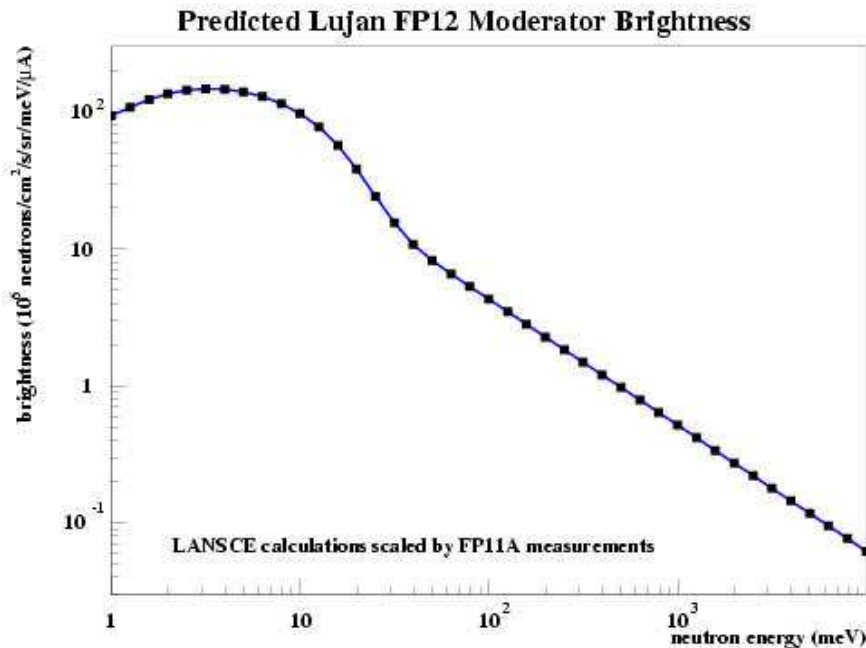


Fig. V.A.1. Calculated average brightness of the coupled-hydrogen moderator, with an ortho-para ratio of 1, viewed by flight path 12.

### V.A.3. Cold Neutron Beam Line

The  $n+p \rightarrow d+\gamma$  beamline has three main components inside LANSCE experimental room 1 (ER1). The first is a 4-m long neutron guide that is placed inside the biological shield and that starts at about 1.3 m from the moderator surface. The second is an external, 2-m long guillotine-type shutter system that contains a neutron guide and is placed next to the biological shield. And the third is a two-blade frame-definition chopper that is located at 9.3 m from the moderator. The heavy integrated radiological shielding that contains all the ER1 beamline components is not shown in figure V.A.2. After the chopper, a guide that ends at 21 m from the moderator transports the neutrons to the  $n+p \rightarrow d+\gamma$  cave. The straight supermirror coated guide has the inner cross section of 9.5 cm  $\times$  9.5 cm and the relative reflectivity of  $m = 3$  ( $m = 1$  is the reflectivity of  $^{58}\text{Ni}$  coated guide). The glass neutron guide is held in a steel vacuum tube. There is considerable uncertainty in the brightness given in Figure V.A.1, and we prefer to use the flux plotted in Figure V.A.4 as

a function of time-of-flight (TOF) on Flight Path 12, 24.3 m from the source. The neutron transport calculations were scaled from measurements on Flight Path 11 assuming an average proton current of  $150 \mu\text{A}$ . The arrow indicates the TOF of 54.5 ms for  $8.9\text{-}\text{\AA}$  neutrons at 24.3 m. The flux of  $8.9\text{-}\text{\AA}$  neutrons is  $1 \times 10^5 \text{ neutrons/ms/pulse/cm}^2 = 5.4 \times 10^7 \text{ neutrons/meV/cm}^2/\text{s} = 1.2 \times 10^7 \text{ neutrons/\AA/cm}^2/\text{s}$ .

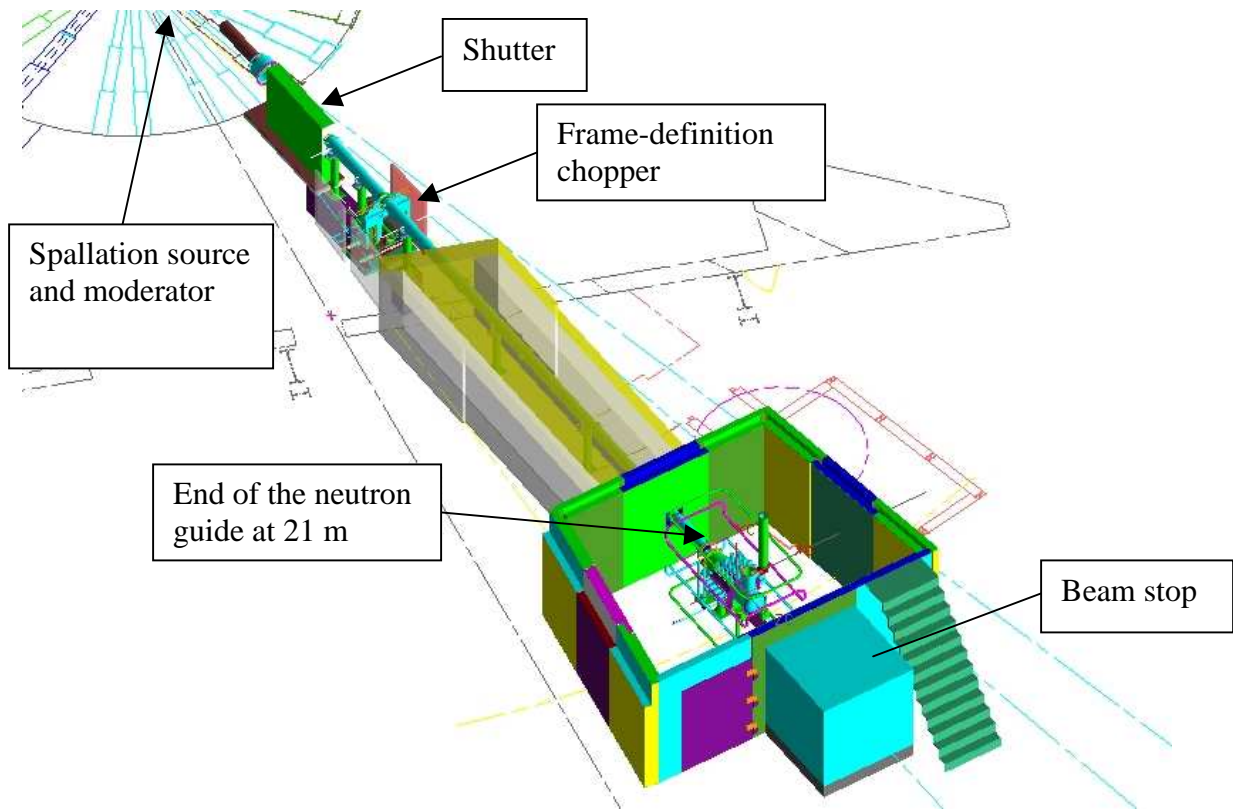


Figure V.A.2 A 3D-model view of the  $n+p \rightarrow d+\gamma$  beamline at the Lujan Center.

#### V.A.4. Frame-Definition Chopper

An advantage of a spallation neutron source is that TOF can be used to select the neutron energy. At low neutron energies a frame-definition chopper is used to select the TOF window of interest. Figure V.A.5. shows an evolution of the flight of the  $8.9 \text{ \AA}$  neutrons from the source to the EDM experiment in three 50-ms wide frame. A two-blade frame definition chopper (FDC) is located at 9.38 m from the moderator. For a 45-cm radius aluminum chopper blade rotating at 20 Hz, it takes 1.88 ms to sweep across the  $9.5 \text{ cm} \times 9.5 \text{ cm}$  guide. If the phase of FDC blade is selected so that the guide is fully open when the  $8.9\text{\AA}$  neutrons have reached the chopper, the 3.76-ms chopper opening corresponds

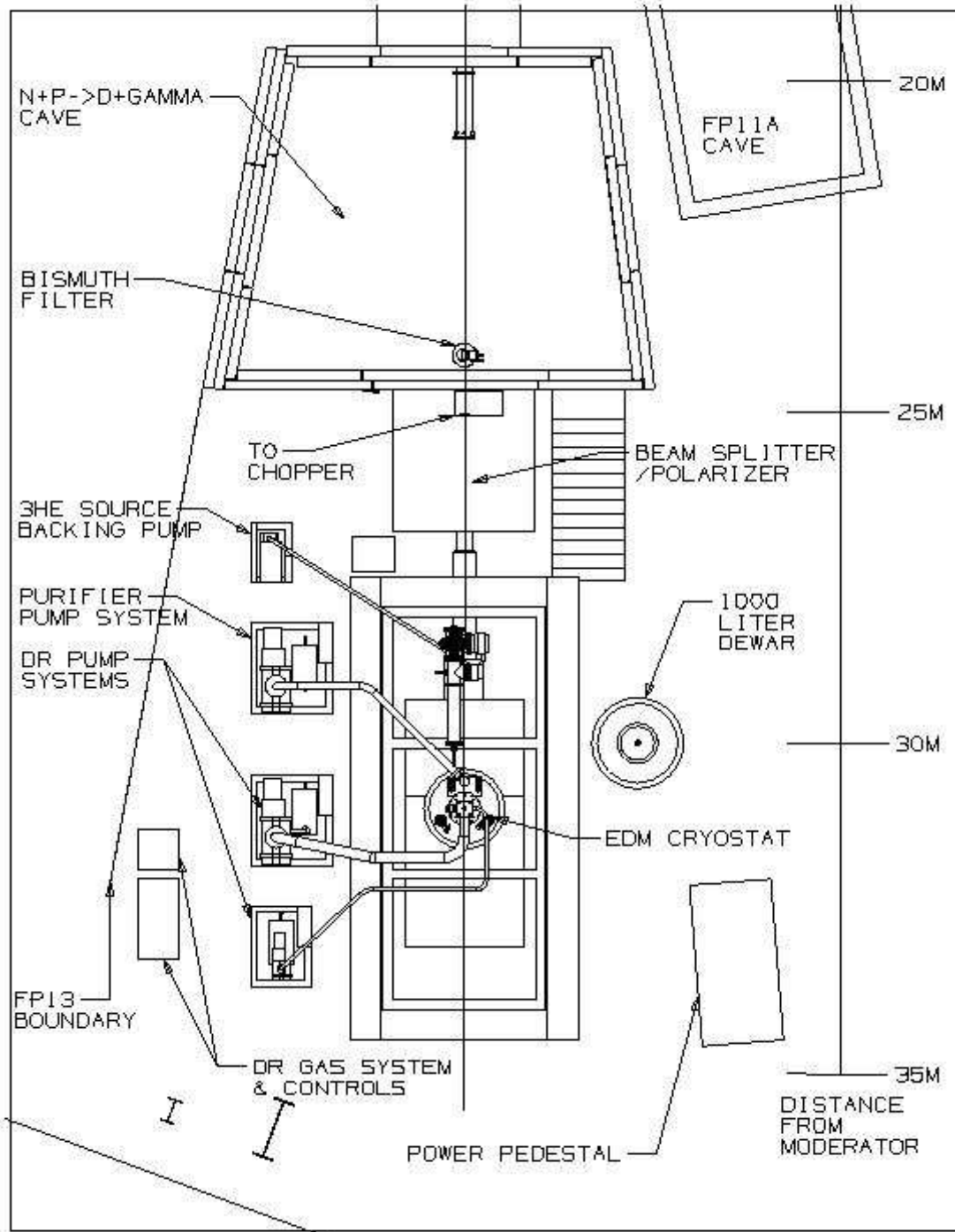


Fig. V.A.3. Floor plan of the EDM experiment on flight path 12 at the Lujan Center.

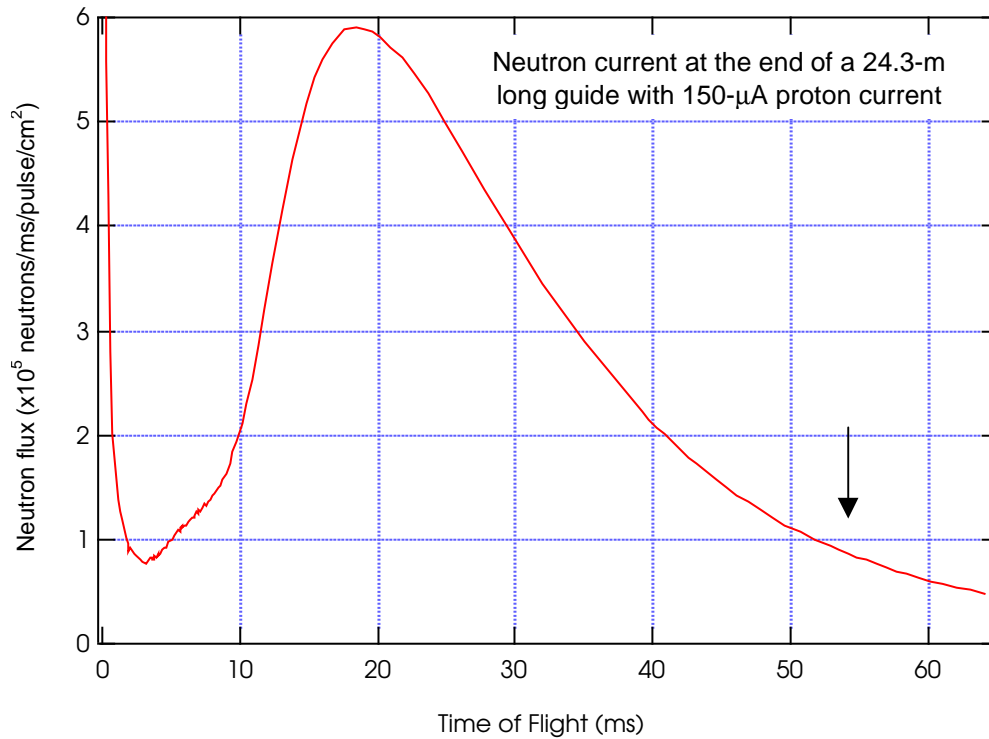


Fig. V.A.4. Neutron flux plotted as a function of TOF at the end of the neutron guide of Flight Path 12, 24.3 m from the moderator. The next proton pulse comes at 50 ms. The arrow indicates a TOF of 54.5 ms corresponding to 8.9-Å neutrons at 24.3m and corresponds to a flux of  $5.4 \times 10^7$  neutrons/meV/cm<sup>2</sup>/s.

to neutron energies from 0.88 to 1.25 meV. When the chopper is closed, the neutrons will be absorbed by a 0.01 inch thick Gd coating on the aluminum plate. This thickness of Gd is sufficient to allow only 0.1% of 100-meV neutrons to be transmitted. At lower neutron energies the neutron-Gd capture cross section increases as  $1/v$ , where  $v$  is the neutron velocity. The brown bands in figure V.A.5. represent the TOF of the fast neutrons down to 100 meV. Most of these neutrons will not be absorbed by the Gd coating and have to be removed from the beam in another way. Figure V.A.5 also indicates the locations of the  $n+p \rightarrow d+\gamma$  cave, the Bi filter, the  $t_0$  chopper in the  $n+p \rightarrow d+\gamma$  beam stop, and the EDM experiment.

### V.A.5 Bismuth Filter for Fast Neutrons

A polycrystalline Bragg scattering filter will remove most of the fast neutrons and gamma rays from a neutron beam. The Bragg filter becomes transparent at wavelengths greater than  $2d$ , where  $d$  is the lattice parameter of the filtering material. The cut-off wavelength of Bi is about 6.8 Å. The cut-off is sharp if the filter is cooled to low

temperatures. A filter length of 20 cm transmits only neutrons with energies less than 1.7 meV (6.8 Å). Figure V.A.6. shows the 20-cm long Bragg-scattering bismuth filter constructed for use in the experiment. The Bi block is cooled with a cryo-cooler to 14 K. This filter system was tested during the 2001-test run in the flight path 11A, and the results obtained relative to transmission data are presented in figure V.A.7. The data are neutron counts measured by a  ${}^6\text{Li}$ -glass scintillator. The long wavelength neutron spectrum was measured through a 0.031-inch diameter hole in a Cd sheet. The fast neutron transmission through the Bi filter was obtained by using a piece of a  ${}^6\text{Li}$ -loaded plastic sheet in the front of the hole to remove the low energy neutrons. The absorber was especially effective on the neutrons from the previous frame, which arrived after the second proton pulse, at the detector positioned at 23 m. From these transmission measurements we can conclude that the transmittance of the short wavelength neutrons through the Bi filter is about 2% and that the filter has no significant effect on the 8.9 Å neutron flux.

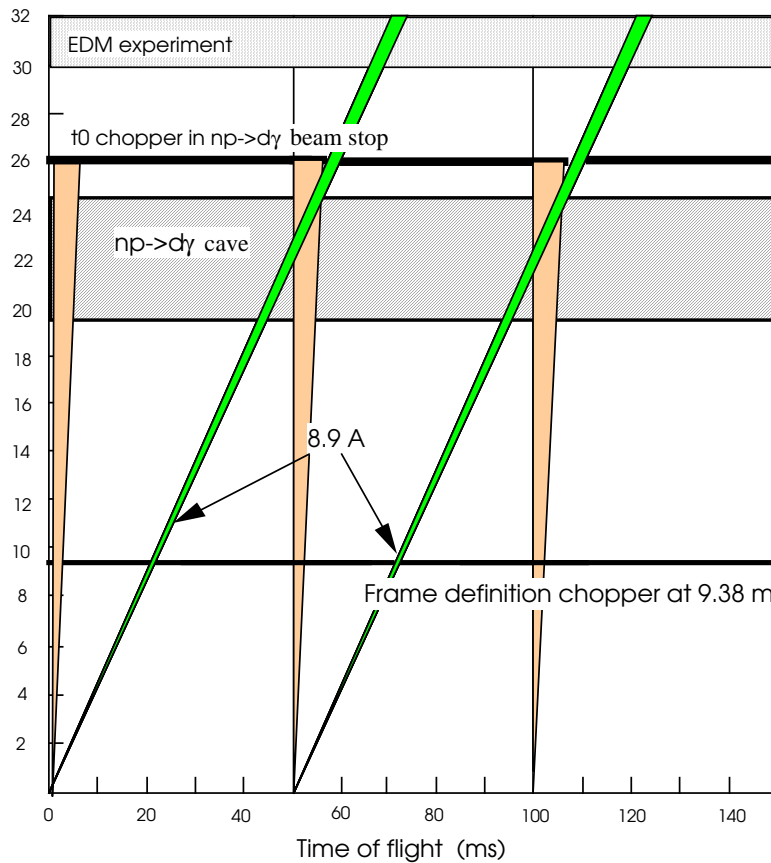


Fig. V.A.5. Timing diagram of the 8.9-Å neutrons from the source to the EDM experiment.

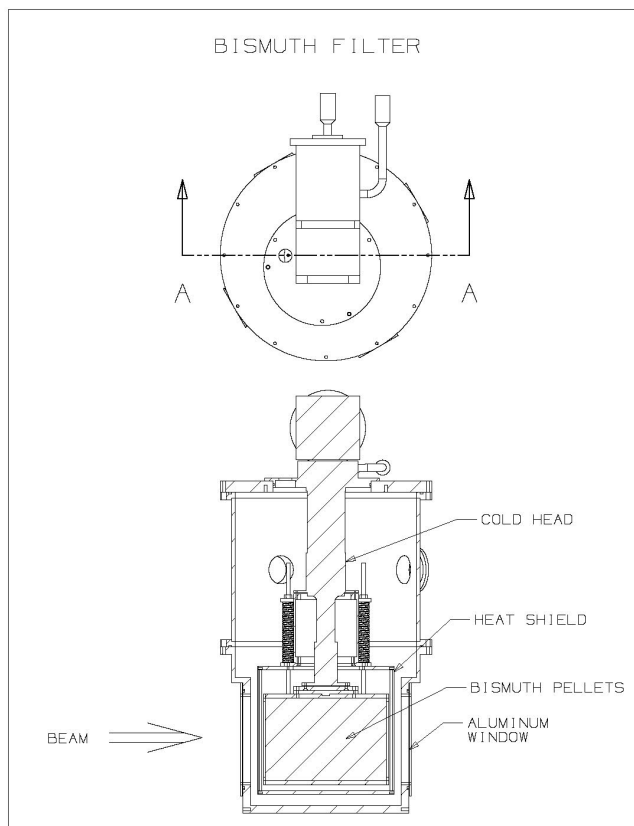


Fig. V.A.6 The cryogenic Bragg scattering Bismuth filter.

### V.A.6. Fast Neutron and Gamma Ray Backgrounds

A proton pulse interacting with the tungsten target in the spallation source creates a high-intensity gamma ray and fast neutron burst that decays in a few milliseconds. In addition to the gamma rays and fast neutrons, activated beam line components create an additional small constant gamma ray background. The fast neutrons and gamma rays in the beam can be removed without affecting the flux of the long wavelength neutrons of interest with a  $t_0$  chopper. The rotor of a typical Lujan  $t_0$ -chopper is made from 30-cm thick heavy material like Inconel or tungsten. To minimize the opening and closing times of the chopper, they normally run at two or three times the repetition rate of the neutron source. With the  $t_0$ -chopper located in the  $n+p \rightarrow d+\gamma$  beam stop, there is about 2 ms separation between the 8.9-Å neutrons and the tail of the fast neutron pulse, and therefore the high rotational rate of the chopper will need to be reserved.

The total neutron cross section on Inconel alloy (Ni-Fe-Cr-Ti) in the eV-keV energy range is about 7 barns, giving an effective transmission through a 30-cm thick Inconel rotor of about  $1 \times 10^{-8}$ . For 2-MeV photons the transmission factor is  $3 \times 10^{-6}$ .

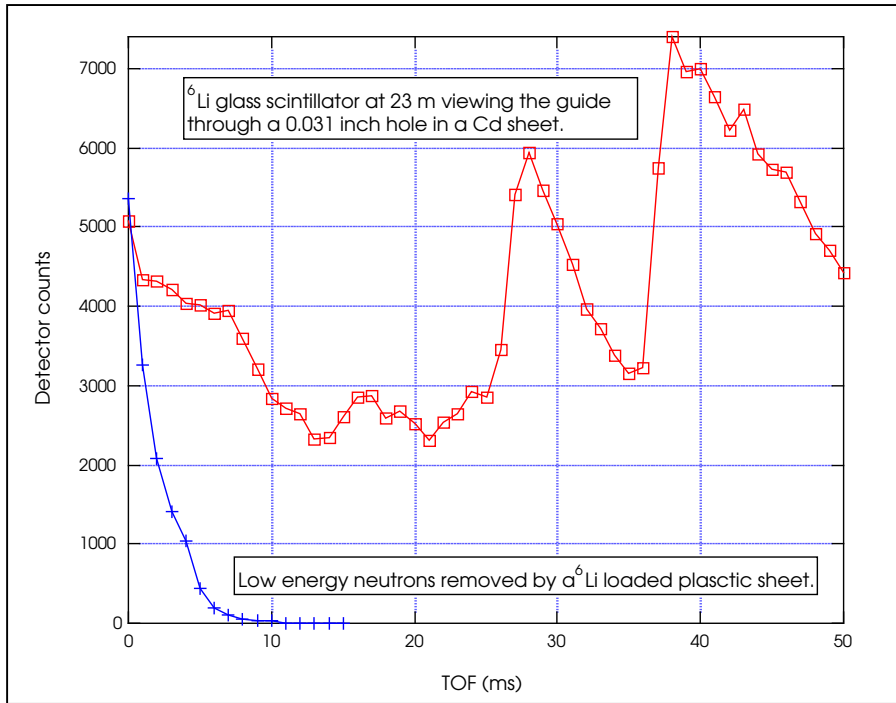


Fig. V.A.7. Relative transmission of the 20-cm long cold Bi filter as a function of TOF. The transmission of the fast neutrons is also shown when a sheet of  $^6\text{Li}$ -loaded plastic was used to remove the long-wavelength neutrons.

In addition to the  $t_0$  chopper attenuation, the Bi filter also significantly attenuates fast neutrons and gamma rays. If the effective thickness of the Bi filter is 15 cm, then the transmission fraction for the photons is about  $6 \times 10^{-4}$ . The thickness of the  $t_0$  chopper will be reevaluated with MCNPX calculations to account for the effect of the Bi filter.

Both the Bi filter and the  $t_0$  chopper are proposed because the Bi filter always attenuates the high-energy particles, regardless of its temperature. This fail-safe behavior permits the use of lower cost shielding downstream of the chopper, especially for the cover of the EDM cryostat.

### V.A.7. Neutron Spin State Selector and Spin Rotator

The reference design of the EDM apparatus has two measurement cells in order to cancel systematic errors. To effectively fill the cells, the neutron beam must be split in two. The optimization of the available floor space behind the  $n+p \rightarrow d+\gamma$  beam stop requires that the  $t_0$  chopper be placed inside the beam stop. Then in roughly four meters between the chopper and the cryostat, the neutron beam must be divided. Additionally, if these two beams are polarized, the sensitivity of the experiment to the polarization of the  ${}^3\text{He}$  is significantly reduced because the  ${}^3\text{He}$  will not be needed to polarize the neutrons. The design concept of the polarizing neutron beam splitter guide is shown in Fig. V.A.8. This concept is an adaptation of the splitter used at the Hahn-Meitner Institute [4].

In the ferromagnetic medium the refractive index has two-values

$$n^\pm \cong 1 - \frac{\lambda^2}{2\pi} N(a_n \mp a_m),$$

where  $\lambda$  is the wave length of the neutrons,  $N$  is the density,  $a_n$  is the nuclear scattering length, and  $a_m$  is the magnetic scattering length given by

$$a_m = \frac{m_n \mu_n}{2\pi \hbar^3} \int B d^3 r.$$

Here  $m_n$  is the neutron mass,  $\mu_n$  the neutron magnetic moment, and  $B$  is the magnetic field in the magnetized ferromagnetic material. The integral is over the volume of lattice occupied by the ferromagnetic atom. The polarizing neutron beam splitter is formed by two total reflecting magnetic supermirror surfaces set at the angle of  $\pm\theta_c/2 = 1.6^\circ$ . The magnetic supermirror elements are fabricated by alternating layers of a FeCo alloy and Si deposited on Si wafers that have a high neutron transmission. The application of a 300-gauss magnetic field will change the critical angle of the reflection depending on the direction of the neutron spin. The critical angle of one spin state will be increased by the magnetic scattering length and the supermirror surface will reflect the neutron up to the critical angle and transmit the other spin state. Hence, a neutron with one spin state is reflected into one of the deflected guides while the opposite spin state is reflected into the second guide. The outgoing guides are set to  $\pm\theta_c = 3.2^\circ$ . The guides will be turned parallel just before entering the cryostat. Before the cryostat, adiabatic spin-rotating RF coils will be mounted to allow a manipulation of the neutron-spin direction.

A rudimentary Monte-Carlo simulation has been used to evaluate the performance of the polarizing neutron beam splitter. The simulation assumes perfect reflection from supermirror walls and perfect performance of the magnetic supermirrors. The result is that there is a total transmission of 45% of the incident beam down each channel, i.e. half

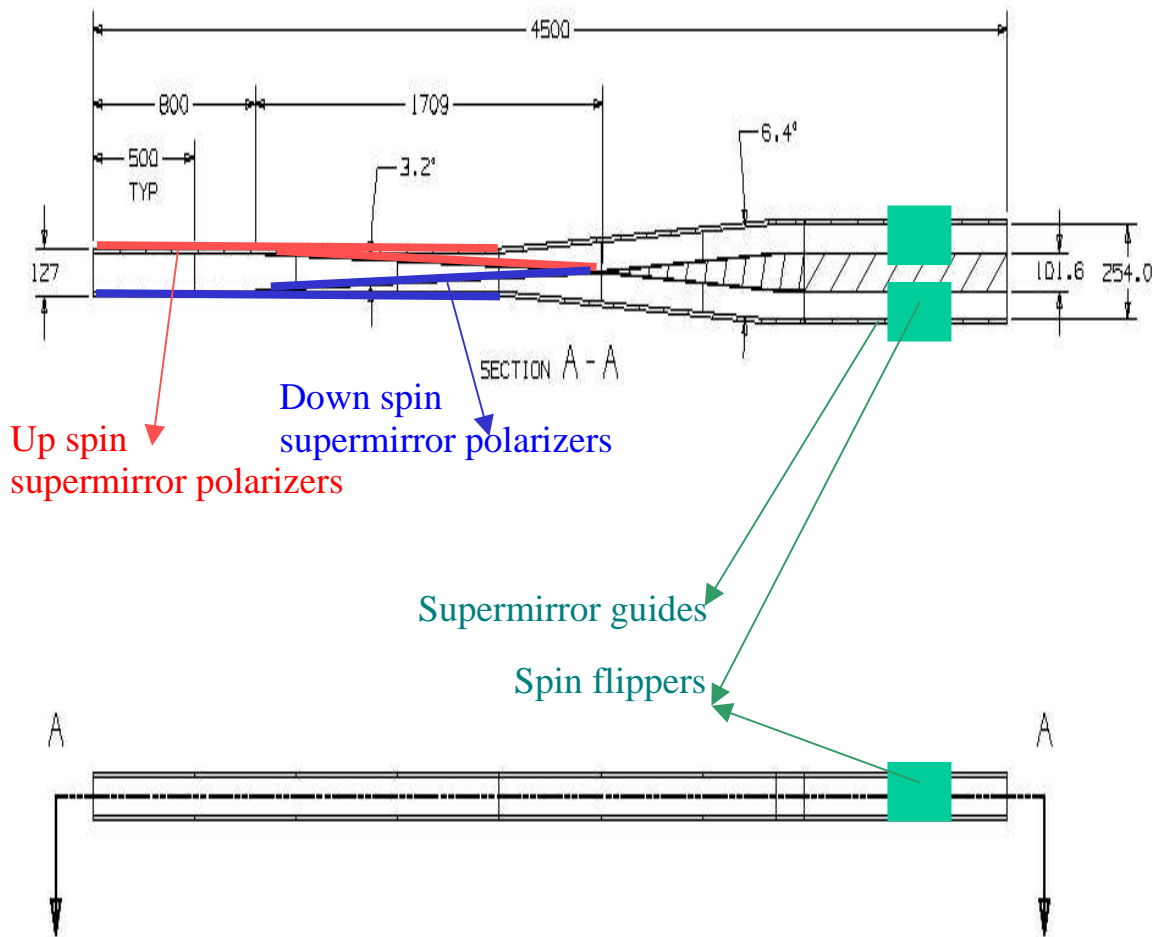


Fig. V.A.8. Polarizing neutron beam splitter, dimensions are in mm. The scales in the two dimensions are not the same.

of the total beam is lost. The losses are because the critical angle needs to be  $\pm\theta_c/4$  for high transmission and polarization. There is insufficient space between the  $t_0$  chopper and the cryostat to accommodate the proper length of the splitter guide that should be  $\sim 14$  m. Many neutrons incident the walls with an angle greater than  $\pm\theta_c$  after reflections. Additionally, polarization of the beams is only 16%. This low polarization is due to a nearly equal superposition of trajectories with an angle greater than  $\pm\theta_c/2$  with trajectories with an angle less than  $\pm\theta_c/2$ . The polarization can be recovered at the cost of neutron flux by placing magnetic supermirrors, backed with a neutron absorbing material,

along the incoming guide with their magnetization as shown in the Fig. V.A.8. With the length adjusted to remove only large-angle events, the simulation predicts that the transmission of the channels will be reduced to 24% of that possible, but the polarization will be 99%. The polarization sensitive lining effectively reduces the phase space. More modeling is required to optimize the beam splitter parameters for the needs of the experiment.

The splitter losses depend strongly on the assumption that the phase space is uniformly filled with neutrons up to  $\pm\theta_c$ . The losses in the guide, taken into account in Fig. V.A.4 are essentially all the large angle neutrons, and the splitter performance can be expected to be much better than calculated. In fact, the polarization absorbers on the walls may not be needed.

During the evaluation of the splitter, an arrangement was investigated where all the angles were set to  $\pm\theta_c/4$ . This splitter has a transmission of 63% down each channel and a polarization of 99%. Unfortunately, the length of the splitter is 14 m and cannot fit to the available footprint in the LUJAN experimental room 2. However, there is an ample room to match the ballistic transport of the proposed SNS beam line. The tiles of magnetic supermirrors from the flight path 12 arrangement at LANSCE can be reused in the SNS setup. The factor of 2.5 in the intensity from the SNS splitter is an additional gain over the relative neutron flux from the SNS spallation sources.

#### **V.A.8. Neutron Beam in the Cryostat**

The neutron beam will enter the cryostat through Be windows. Beryllium was selected because it has no long-lived isotopes made in neutron capture reactions. It also does not become superconducting at low operating temperatures of the cryostat. The distance between the cryostat entry window and the measuring cells is about one meter. Due to the phase space, half of the neutrons would not enter the measuring cells. To keep the neutrons, supermirror guide sections will be installed into the cryostat, one for each measuring cell. Gradual cooling will be necessary in order not to damage these guides, and they must stop far enough in front of the cells so that the dielectric will not distort the electric field.

#### **V.A.9. Radiological Shielding of the EDM apparatus**

Because of the long flight path (a small solid angle), the frame-definition chopper, the  $t_0$  chopper, and the Bi filter, only 8.9 Å neutrons can reach the EDM experiment. The short

wavelength neutrons are scattered by the  $t_0$  chopper and the Bi filter, and finally blocked by the beam splitter. After the  $t_0$  chopper additional gamma rays are created in the splitter where half of the neutron beam will be absorbed. This section of the beamline requires a thicker shielding that must be evaluated along with the rest of the neutron shielding around the experiment.

#### **V.A.10. Flux of the 8.9 Å Neutrons to the UCN Production Cells**

We can estimate the flux of 8.9-Å neutrons in the UCN production cell. At the end of the guide at 24 m the flux is  $5.4 \times 10^7$  neutrons/meV/cm<sup>2</sup>/s. Due to the phase space of the beam, there will be losses in the Bi filter and the  $t_0$  chopper. The total length of the section without guide is about 50 cm long and will transmit 80% of the neutrons. The transmission of the polarizing beam splitter is quite uncertain as noted above. Due to the uncertainties, we use unit transmission in this region for our calculations, and future results can be scaled later.

#### **References**

- [1] Phillip D. Ferguson, Gary J. Russell, and Eric J. Pitcher, "Reference Moderator Calculated Performance For The LANSCE Upgrade Project," *ICANS-XVIII: Proceedings of the Thirteenth Meeting of the International Collaboration on Advanced Neutron Sources*, Paul Scherrer Institut report PSI Proceedings 95–20, ISSN 1019-6447, pp. 510–517 (November 1995).
- [2] G. J. Russell, P. D. Ferguson, and E. J. Pitcher, "The Lujan Center: A Pulsed Spallation Neutron Source At Los Alamos," in *the Proceedings of ICON-8: the Eighth International Conference on Nuclear Engineering*, April 2–6, 2000, Baltimore, Maryland, pp.1–12.
- [3] G. Mitchell *et al.*, The LANSCE flight path 11A moderator brightness. Private communication.
- [4] Th. Krist, C. Pappas, Th. Keller, and F. Mezei, *Physica* **B213&214** 939 (1995).

## Section V.B Production of UCN in superfluid $^4\text{He}$

Recent neutron EDM experiments were limited by the UCN flux produced in cold moderators. The Liouville theorem dictates that the phase space density of UCN can not be increased beyond its value in the source moderator by, for example, gravitational deceleration or reflection from a moving surface. In 1975, Golub and Pendlebury [1] pointed out that UCNs produced via an inelastic down-scattering process in certain moderator materials could achieve much higher UCN densities than in conventional moderators. In particular, they suggested [2] that superfluid  $^4\text{He}$  has many unique features making it an ideal moderator for producing an intense source of UCN. In this so-called “superthermal” UCN source, the incident neutrons do not reach thermal equilibrium with the moderator.

The underlying principle of a superthermal UCN source can be appreciated [3] by considering a moderator with only two energy levels: a ground state and an excited state of excitation energy  $\Delta$ . An incident neutron with energy near  $\Delta$  could excite the inelastic level of the moderator and lose almost all its energy to become an UCN (the “down-scattering process”). However, the UCN could later regain some energy by interacting with the excited states of the moderator and cease to be an UCN (the “up-scattering” process). To maintain a high density of UCN, it is necessary to minimize the up-scattering probability. The principle of detailed balance demands that the up-scattering cross section,  $\sigma_{UP}$ , is related to the down-scattering cross section,  $\sigma_{DOWN}$ , by the expression

$$E_{UCN} \sigma_{UP} = (E_{UCN} + \Delta) e^{-\Delta/kT} \sigma_{DOWN}, \quad (1)$$

where  $k$  is the Boltzmann constant and  $T$  is the temperature of the moderator. Typically,  $\sigma_{DOWN}$  is practically independent of  $T$  and Eq. 1 shows that the up-scattering cross section can be made arbitrarily small by lowering the temperature until  $kT \ll \Delta$ . Therefore, the UCN density could reach a value  $\sim (E_{UCN}/\Delta)e^{\Delta/kT}$  in such a superthermal source. This is to be contrasted with conventional moderators in which the UCN density is proportional to  $1/T^2$ .

In rare situations, the materials suitable for producing UCN via the superthermal process are also ideal for storing the UCN. Superfluid  $^4\text{He}$  is such a material. The tightly bound  $^4\text{He}$  nucleus allows no neutron absorption, and no UCN can be lost due to absorption on  $^4\text{He}$ . As mentioned above, the UCN can still be lost via the up-scattering process, which fortunately can be minimized by decreasing the superfluid  $^4\text{He}$  temperature.

Several experiments have been performed to study the production and storage of UCN in superfluid  $^4\text{He}$  [4, 5, 6, 7, 8, 9]. Evidence for UCN production has been reported in these experiments, although the observed UCN production rate was not always in agreement with the theoretical expectation [7, 10, 11]. A most recent neutron lifetime experiment carried out at NIST [8, 9] made use of this technique for UCN production, and the observed production rate was found to be consistent with the theoretical expectation.

In the following sections, we summarize the characteristics of the interaction of cold neutron beam with superfluid  $^4\text{He}$ . Results of numerical calculations for the UCN production rate using the proposed cold neutron source and the proposed beam line at LANSCE will also be presented.

### V.B.1 UCN production via the single – phonon process

The study of the interaction of cold neutron with condensed matter has a long history. Placzek and Van Hove first pointed out that the energy-versus-momentum relation, i.e. the dispersion curve, of a solid could be measured with cold neutrons inelastically scattered from the solid [12]. Cohen and Feynman [13] suggested that the dispersion curve in liquid helium could also be directly determined via this technique. Consider a neutron of incident momentum  $\hbar\mathbf{k}_i$  inelastically scattered from superfluid  ${}^4\text{He}$  to a momentum of  $\hbar\mathbf{k}_f$  while the superfluid is excited into a state of excitation energy  $E$ . Conservation of energy and momentum requires

$$\mathbf{Q} = \mathbf{k}_i - \mathbf{k}_f, \quad (2)$$

and

$$\hbar^2 k_i^2 / 2m = \hbar^2 k_f^2 / 2m + E(Q), \quad (3)$$

where  $\hbar\mathbf{Q}$  is the momentum transfer and  $E(Q)$  is the energy-versus-momentum dispersion relation for superfluid  ${}^4\text{He}$ . For single-phonon excitation, the Landau-Feynman dispersion curve has been well determined from neutron scattering experiments. In Fig. 1 the data from a measurement of Cowley and Woods [14] are shown. For the low momentum region ( $Q < 1\text{\AA}^{-1}$ ), the dispersion relation is approximately linear and is well parameterized [15] as

$$\omega = aQ(1 + \gamma Q^2 \frac{1 - Q^2/Q_A^2}{1 + Q^2/Q_B^2}), \quad (4)$$

where  $a = 2.383 \times 10^4$  cm/sec,  $\gamma = 1.112\text{\AA}^2$ ,  $Q_A = 0.5418\text{\AA}^{-1}$ , and  $Q_B = 0.3322\text{\AA}^{-1}$ . This parameterization is shown as the dotted curve in Fig. 1.

At certain beam momenta, the incident neutron can transfer practically all its momentum (and energy) to the phonon and emerge as an UCN. This condition is met when the free-neutron dispersion curve intersects the dispersion curve of the superfluid  ${}^4\text{He}$ . Using the above parameterization for the single-phonon excitation, this occurs at  $k_i = 0.7038\text{\AA}^{-1}$  (or  $\lambda \equiv 2\pi/k = 8.928\text{\AA}$ ), as shown in Fig. 1. We call this momentum the ‘‘critical momentum’’  $k_c$ . For a neutron beam with momentum near  $k_c$ , a phonon emitted along the beam direction would carry off essentially all the beam energy and leave an UCN behind.

It is clear that UCN can be produced only for neutrons scattered into certain angles. To illustrate this point, Eqs. 2 and 3 can be solved numerically for  $k_f$  as a function of  $k_i$  and  $\theta$ , the neutron laboratory scattering angle. In Fig. 2 we show results of the calculation for several incident neutron momenta. Several remarks are in order:

1. At  $\theta = 0^\circ$ , there is always a solution,  $k_f = k_i$ , corresponding to an elastic scattering.
2. For  $k_i > k_c$ , all scattering angles are allowed for the neutrons.

3. For  $k_i < k_c$ , only  $\theta < 90^\circ$  is allowed. For each allowed scattering angle, there exist two solutions for  $k_f$ .
4. For  $k_i < 0.3777\text{\AA}^{-1}$ , no inelastic scattering is allowed, and the neutron beam will traverse the superfluid  ${}^4\text{He}$  without attenuation. At  $k = 0.3777\text{\AA}^{-1}$ , the group velocities,  $d\omega/dk$ , for free neutrons and phonons are identical. Below this momentum, phonons travel faster than neutrons.

The horizontal dashed curve in Fig. 2 corresponds to 200 neV, a typical wall potential for UCN bottles. For neutrons emerging with  $k_f$  below the dashed curve, they can be stored as UCNs. Figure 2 shows that only neutrons with  $k_i$  very close to  $k_c$  are capable of generating UCNs. It is worth noting that for  $k_i > k_c$ , UCNs are predominantly produced at  $\theta > 90^\circ$ . In contrast, UCNs are only produced at  $\theta < 90^\circ$  for  $k_i < k_c$ .

To evaluate the UCN production cross sections, we use the following expression from Cohen and Feynman [13] (See Ref. [10] for a detailed derivation):

$$\frac{d\sigma}{d\Omega} = a^2 \frac{k_f}{k_i} \frac{Z(Q)}{\left|1 + \frac{M_p}{\hbar^2} \frac{E'(Q)}{Q} \left(1 - \frac{k_i}{k_f} \cos\theta\right)\right|}, \quad (5)$$

where  $a$  is the scattering length of neutron on a bound  ${}^4\text{He}$  nucleus ( $4\pi a^2 = 1.1 \pm 0.15$  barns [16]),  $M_n$  is the neutron mass,  $E'(Q)$  is the derivative of the  ${}^4\text{He}$  dispersion curve, and  $Z(Q)$  is the single-phonon structure factor for  ${}^4\text{He}$ . From the strength of the single-phonon peak measured in neutron scattering experiments,  $Z(Q)$  is well determined experimentally. Figure 3(a) shows the data for the low momentum region ( $Q < 1\text{\AA}^{-1}$ ), while Fig. 3(b) shows the  $Z(Q)$  data over a broader range covering roton excitations [14]. The solid curve in Fig. 3(a) corresponds to the following parameterization [14]:

$$Z(Q) = \frac{\hbar Q}{2M_s} (1 - 1.5 Q^2 + 0.9 Q^4), \quad (6)$$

where  $s$  is the sound velocity in  ${}^4\text{He}$  ( $s = 238.3$  cm/sec),  $M$  is the mass of  ${}^4\text{He}$ , and  $Q$  is in unit of  $\text{\AA}^{-1}$ . Note that  $Z(Q)$  exhibits a peak near the roton minimum (near  $Q = 2.0\text{\AA}^{-1}$ ). The solid curve in Fig. 3(b) is a parameterization of  $Z(Q)$ :

$$Z(Q) = \frac{\hbar Q}{2M_s} (1 - 1.5 Q^2 + 0.9 Q^4) \quad \text{for } 0 \leq Q \leq 0.918\text{\AA}^{-1}; \quad (7)$$

$$Z(Q) = 0.688 Q^2 - 1.285 Q + 0.715 \quad \text{for } 0.918 \leq Q \leq 1.787\text{\AA}^{-1}; \quad (8)$$

$$Z(Q) = 0.93 - 5.8(Q - 2.02)^2 \quad \text{for } 1.787 \leq Q \leq 2.35\text{\AA}^{-1}. \quad (9)$$

Eqs. 5-9 allow us to calculate numerically the differential cross sections of neutrons as a function of  $k_i$  and  $\theta$ , as shown in Fig. 4. Again, for  $k_i < k_c$ , there are two solutions for each allowed scattering angles. Note that for  $k_i < k_c$ , the differential cross section diverges at  $\theta_{max}$ , where the denominator of Eq. 5 vanishes. The integrated cross section, however, remains finite. The total UCN production cross section can now be calculated as a function of  $k_i$  using

$$\sigma_{UCN}(k_i) = \int d\sigma/d\Omega \theta(E_{UCN} - E_f) d\Omega, \quad (10)$$

where the step function  $\theta$  ensures that the neutrons are produced with an energy  $E_f$  below the wall potential  $E_{UCN}$ . The results are shown in Fig. 5 for  $E_{UCN} = 100, 200, 400$  nev. For a typical UCN wall potential of 200 nev, the useful  $\Delta k_i/k_i$  is  $\sim 1.2\%$  centered around  $k_c$ . The full-width at half-maximum,  $\Delta k_{FWHM}$ , is  $\sim 0.006 \text{ \AA}^{-1}$ .

It is worth noting that the total  $n - ^4\text{He}$  cross section at  $k_c = 0.7038 \text{ \AA}^{-1}$  is  $\sim 0.027$  barns [18]. Figure 5 shows that roughly 0.07% of the scattered neutrons end up being UCNs at this incident momentum. This probability drops rapidly as  $k_i$  deviates from  $k_c$ .

The energy distribution of the produced UCN is also calculated and the result is shown in Fig. 6(a). The energy distribution follows an  $E_f^{1/2}$  dependence, in agreement with the prediction of an analytical approach [3].

The angular distributions of the UCNs have also been calculated. Figure 6(b) shows that they are largely isotropic with a small forward-backward asymmetry. For  $E_{UCN} = 200$  nev, the angular distribution is described by  $d\sigma/d\Omega \sim 1 + 0.029 \cos\theta$ . This result can be compared with an earlier analysis by Lamoreaux and Golub [10].

We are now ready to calculate the expected UCN production rate for the neutron EDM experiment using flight path 12 at LANSCE. The UCN production rate is given by

$$\frac{dN_{UCN}}{dt dV} = \int \frac{d\phi}{dk_i} \sigma_{UCN}(k_i) \rho dk_i, \quad (11)$$

where  $d\phi/dk_i$  is the flux of incident neutrons,  $\sigma_{UCN}(k_i)$  is the UCN production cross section at  $k_i$ ,  $\rho$  is the density of  $^4\text{He}$  ( $2.18 \times 10^{22} \text{ atoms/cm}^3$ ), and  $V$  is the volume of the UCN cell.  $d\phi/dk_i$  is practically independent of  $k_i$  for the narrow window around  $k_c$ . Hence, Eq. 11 becomes

$$\frac{dN_{UCN}}{dt dV} = \frac{d\phi}{dk_i} \rho \int \sigma_{UCN}(k_i) dk_i. \quad (12)$$

For a 200 nev wall potential,  $\int \sigma_{UCN}(k_i) dk_i = 1.13 \times 10^{-7}$  barns  $\text{ \AA}^{-1}$ . Hence, we obtain

$$\frac{dN_{UCN}}{dt dV} = 2.46 \times 10^{-9} \times \frac{d\phi}{dk_i} \text{ \AA}^{-1}/\text{cm}. \quad (13)$$

Based on Fig. V.A.4, the expected flux from flight path 12 for 8.9- $\text{ \AA}$  neutrons is  $d\phi/dE = 5.4 \times 10^7 / \text{sec/cm}^2/\text{meV}$  with 150  $\mu\text{A}$  of protons, which implies  $d\phi/dk_i = 1.5 \times 10^8 / \text{sec/cm}^2/\text{ \AA}^{-1}$ . Hence,

$$\frac{dN_{UCN}}{dt dV} \approx 0.4 / \text{sec/cm}^3. \quad (14)$$

This value can be compared with our measurement made in December 2002 on flight path 11 that gave  $0.56 \pm 0.18 / \text{sec/cm}^3$  when scaled to flight path 12. The result is also in reasonable agreement with earlier measurements of the production rate [5, 8]. Finally, assuming a UCN storage time of 500 seconds, one obtains a UCN density of  $\sim 200$  per  $\text{cm}^3$ , a factor of  $\sim 50$  over the recent ILL experiment. The final UCN density will be significantly affected by the transmission of the final stages of the guide, in particular the

losses in polarizing the neutrons. Whereas this part of the experiment is still under development as noted in Appendix A, we use a production rate of  $1/sec/cm^3$  for calculations later in the proposal.

If one compares Eq. 13 with Eq. (3.38) of Golub, Richardson, and Lamoreaux [3], the present result is lower than Ref. [3] by roughly 20%. This difference is attributed to the larger value of  $\sigma_{coh}$  used in Ref. [3] ( $\sigma_{coh} = 1.3$  barns) than used here ( $\sigma_{coh} = 1.1$  barns). We conclude that these two approaches are consistent with each other.

## V.B.2 UCN production via the multi – phonon process

It is well known that superfluid  ${}^4\text{He}$  can also have multi-phonon excitations. Unlike the single-phonon excitation which has a delta-function dispersion curve, the multi-phonon process gives a broad energy-versus-momentum band. The location of this multi-phonon band, as measured in a neutron scattering experiment, is shown in Fig. 7. As shown in Fig. 7, the neutron dispersion curve intersects the multi-phonon band at  $Q$  around  $1.1\text{\AA}^{-1}$ . Therefore, UCN could also be produced via the multi-phonon process.

The UCN production cross section via the multi-phonon process can be calculated using the following expression (Eq. (A.11) of Ref. [3] and Eq. 7 of Ref. [14]):

$$\frac{d^2\sigma}{d\Omega d\omega} = a_{coh}^2 \frac{k_f}{k_i} S(Q, \omega); \quad S(Q, \omega) = Z(Q)\delta(\omega - \omega(Q)) + S_{II}(Q, \omega). \quad (15)$$

Note that the structure factor contains both the single-phonon part ( $Z(Q)$ ) and the multi-phonon part ( $S_{II}(Q, \omega)$ ). We assume a gaussian distribution for  $S_{II}(Q, \omega)$  as follows:

$$S_{II}(Q, \omega) = S_{II}(Q) \frac{1}{\sqrt{2\pi}\sigma(Q)} e^{-(\omega - \omega(Q))^2 / 2\sigma^2(Q)}. \quad (16)$$

Note that  $\int_0^\infty S_{II}(Q, \omega) d\omega = S_{II}(Q)$ .  $S_{II}(Q)$  is taken from the neutron scattering experiment [14], and the  $Q$ -dependence of the centroid ( $\omega(Q)$ ) and width ( $\sigma(Q)$ ) can be extracted from Fig. 7.

We have calculated the multi-phonon UCN production cross sections as a function of  $k_i$ , as shown in Fig. 8. Unlike the single-phonon case, the multi-phonon UCN production cross section has a very broad  $k_i$  dependence. For a 200 neV wall potential, we obtain  $\int \sigma_{UCN}(k_i) dk_i = 0.375 \times 10^{-7} \text{ barns} \cdot \text{\AA}^{-1}$  for the multi-phonon process. This is approximately a factor of three lower than the single-phonon cross section. If a broad-band neutron beam is used, the total UCN yield can increase by  $\sim 30\%$ . However, the increased background created by such a broad-band neutron beam might be too costly for such a modest gain in the UCN yield. Therefore, we believe that a narrow-band neutron beam centered around  $8.9\text{\AA}$  would be optimal for UCN production, and the contribution from the multi-phonon process can and should be ignored.

## References

- [1] R. Golub and J. M. Pendelbury, Phys. Lett. **53A**, 133 (1975).
- [2] R. Golub and J. M. Pendelbury, Phys. Lett. **62A**, 337 (1977).
- [3] R. Golub, D. J. Richardson, and S. K. Lamoreaux, “Ultra-Cold Neutrons”, Adam Hilger, (1991).
- [4] P. Ageron, W. Mampe, R. Golub and J. M. Pendelbury, Phys. Lett. **66A**, 469 (1978).
- [5] R. Golub et al., Z. Phys. **B51**, 187 (1983).
- [6] E. Gustsmiedl, R. Golub and J. Butterworth, Physica **B169**, 503 (1991).
- [7] H. Yoshiki et al., Phys. Rev. Lett. **68**, 1323 (1992).
- [8] P. R. Huffman et al., Nature **403**, 62 (2000).
- [9] C. R. Brome et al., Phys. Rev. **C63**, 055502 (2001).
- [10] S. K. Lamoreaux and R. Golub, JETP Lett. **58**, 792 (1995).
- [11] R. Golub and S. K. Lamoreaux, Phys. Rev. Lett. **69**, 517 (1992).
- [12] G. Placzek and L. Van Hove, Phys. Rev. **93**, 1207 (1954).
- [13] M. Cohen and R. P. Feynman, Phys. Rev. **107**, 13 (1957).
- [14] R. A. Cowley and A. D. B. Woods, Canadian Journal of Physics, **49**, 177 (1971).
- [15] H. J. Maris, Rev. Mod. Phys. **49**, 341 (1977).
- [16] A. W. McReynolds, Phys. Rev. **84**, 969 (1951).
- [17] R. Golub, Phys. Lett. **72A**, 387 (1979).
- [18] H. S. Sommers, J. G. Dash, and L. Goldstein, Phys. Rev. **97**, 855 (1955).

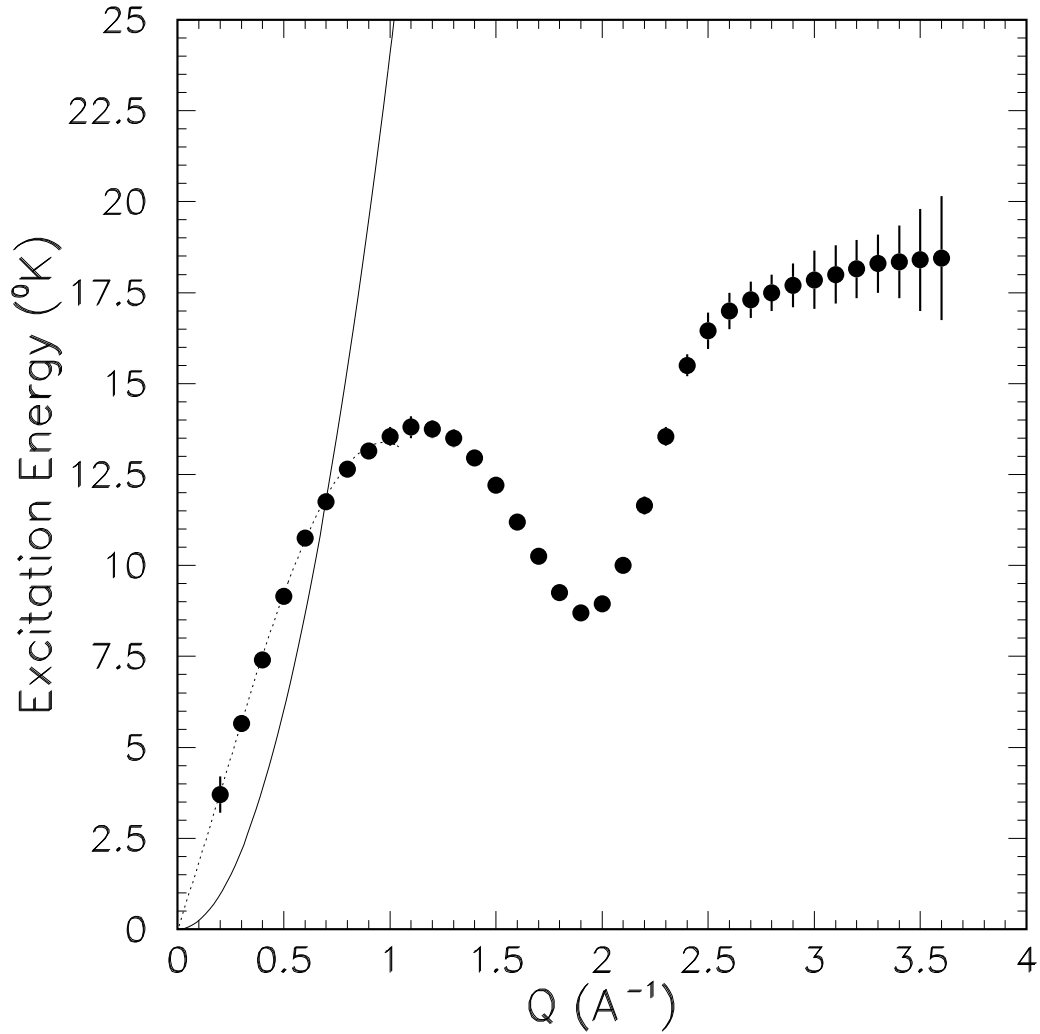


Figure 1: Single-phonon excitation energy (in unit of  $^{\circ}\text{K}$ ) versus momentum transfer ( $\hbar Q$ ) for superfluid  $^4\text{He}$  measured in a cold neutron scattering experiment [14]. The dotted curve is a parameterization by Maris [15]. The solid curve is the energy versus momentum ( $E = \hbar^2 Q^2 / 2M_n$ ) curve for neutrons.

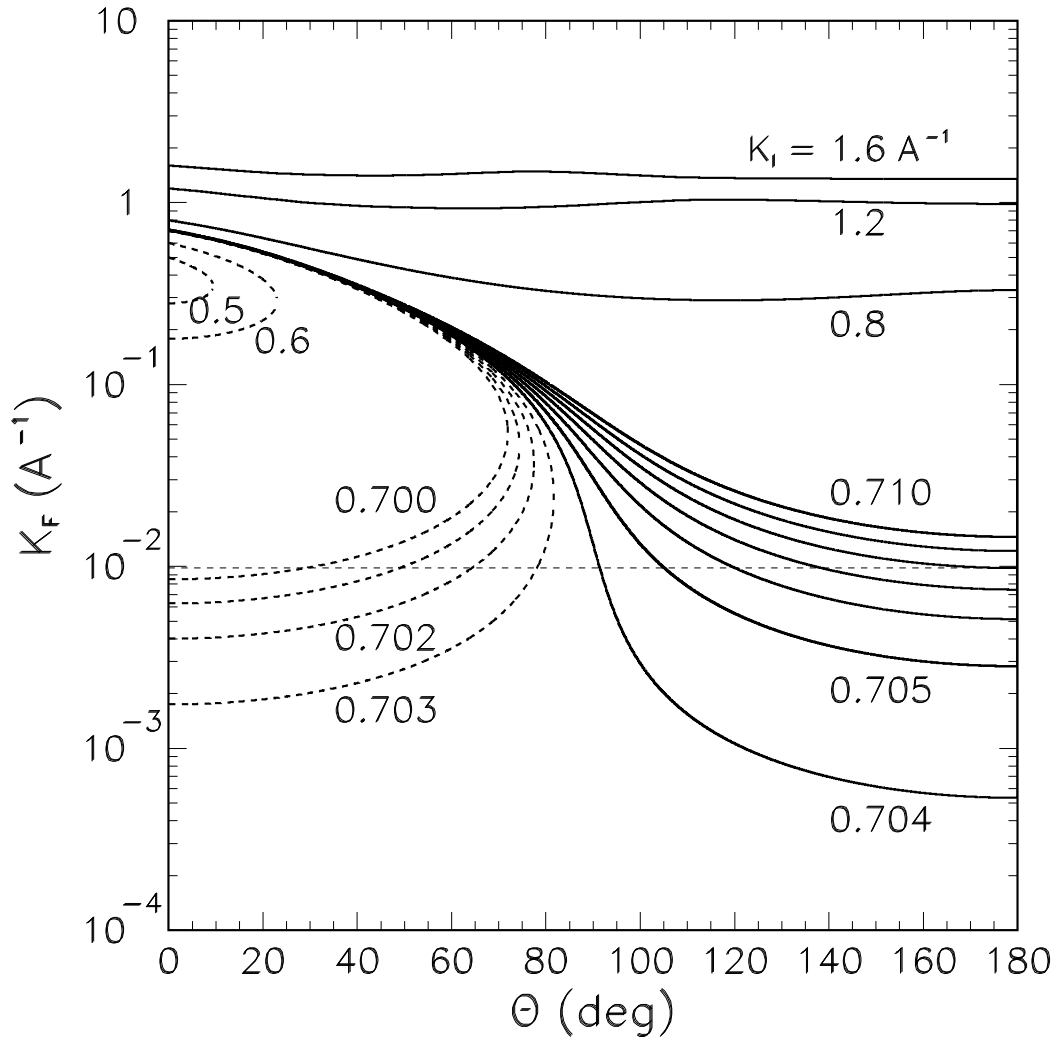


Figure 2: Kinematics of the neutron scattering off a superfluid  ${}^4\text{He}$  target. Momenta of the scattered neutrons ( $k_F$ ) are plotted as a function of the neutron laboratory scattering angle ( $\theta$ ) for several incident neutron momenta ( $k_i$ ). The horizontal dashed curve corresponds to a UCN wall potential of 200 neV.

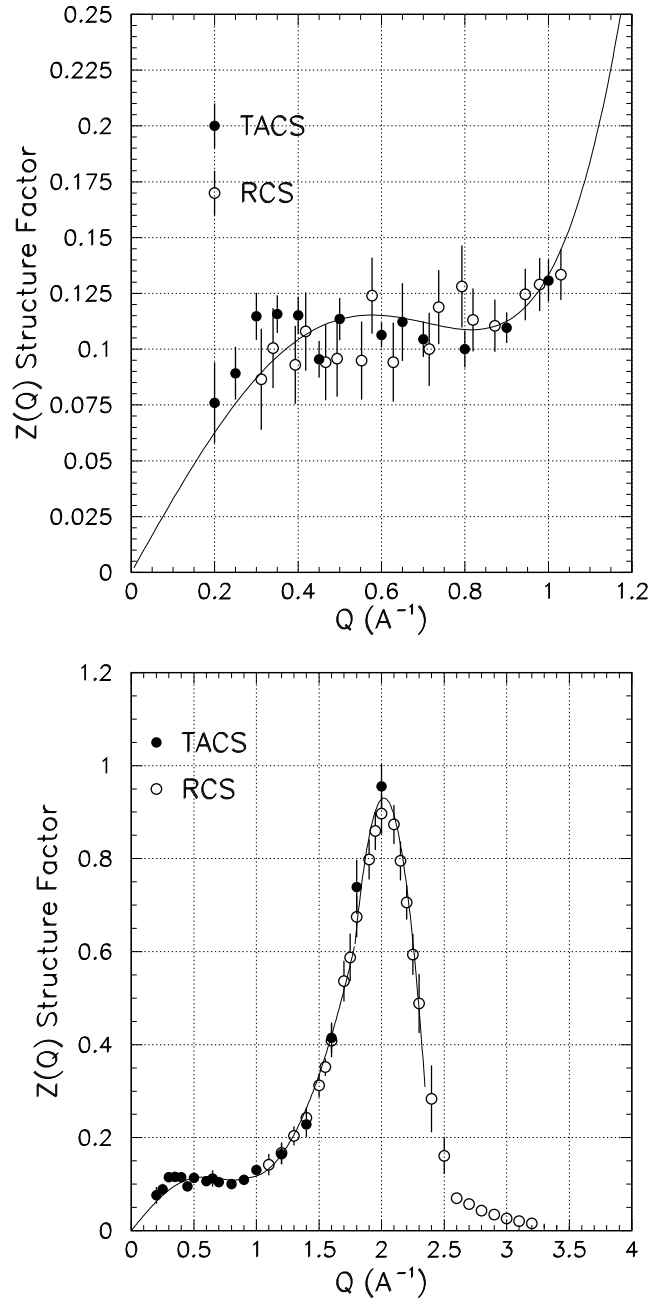


Figure 3: a) Single-phonon structure factor versus momentum transfer for superfluid  ${}^4\text{He}$  measured in a cold neutron scattering experiment [14] using a rotating crystal spectrometer (RCS) and a triple-axis crystal spectrometer (TACS). The solid curve represents a fit [14] to the experimental data. b) Same as a), but for a wider range of momentum transfer. The solid curve represents a fit to the data over the region  $Q < 2.35 \text{ \AA}^{-1}$ .

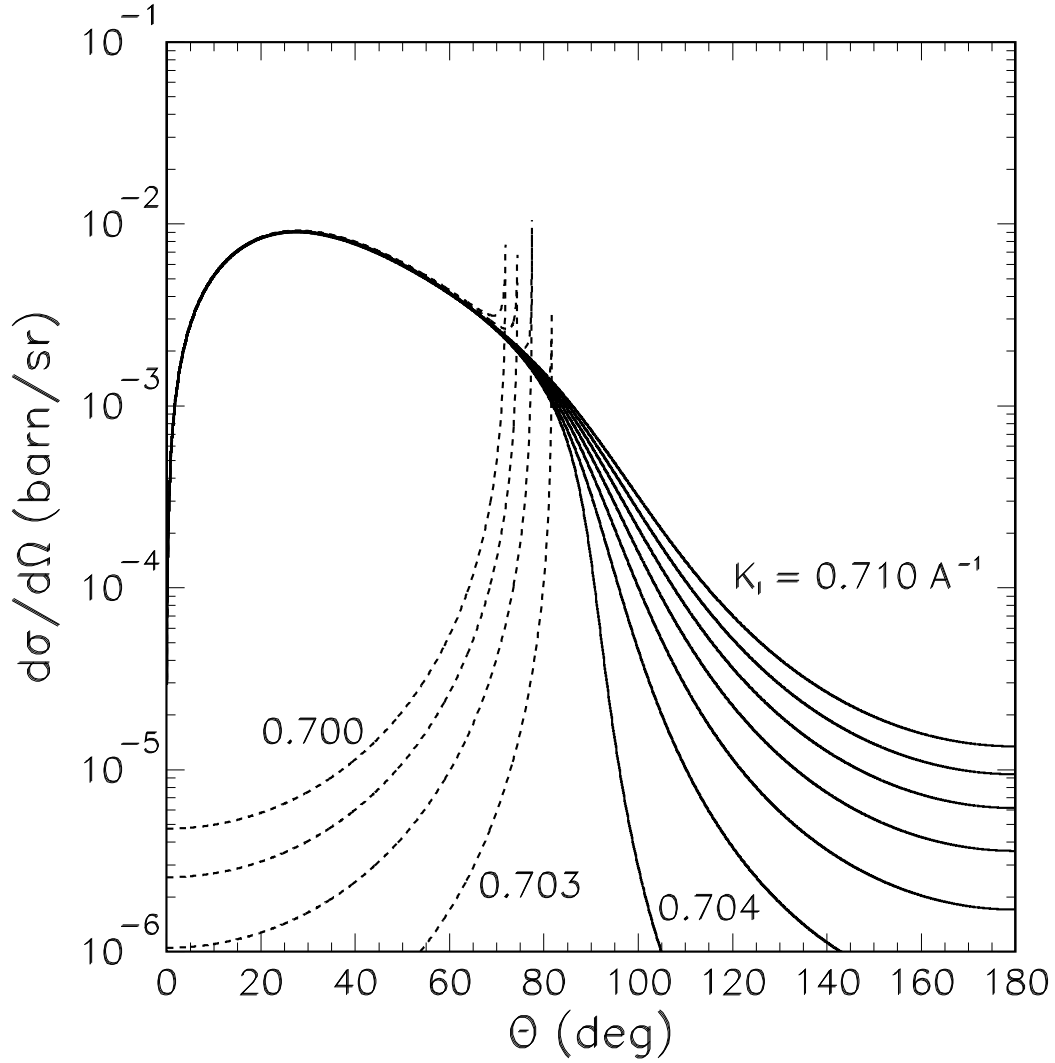


Figure 4: Differential cross sections for neutrons interacting with superfluid  ${}^4\text{He}$  calculated using Eq. 6. For  $k_i < k_c$ , a singularity of the cross section occurs at  $\theta_{max}$ .

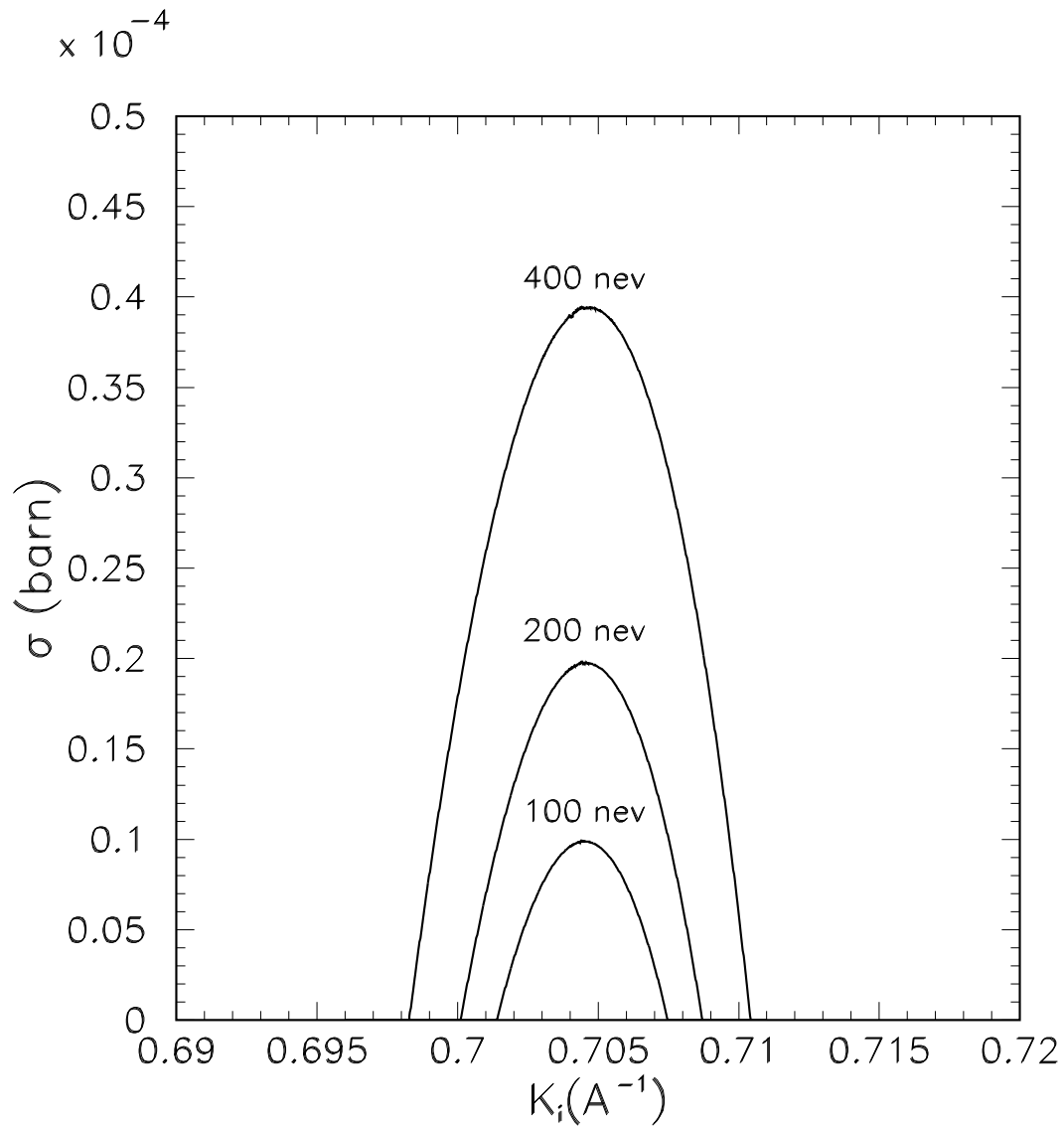


Figure 5: UCN production cross sections in superfluid  ${}^4\text{He}$  via the single-phonon process plotted as a function of the incident neutron wave number,  $k_i$ . The three curves correspond to three different wall potentials for containing the UCNs.

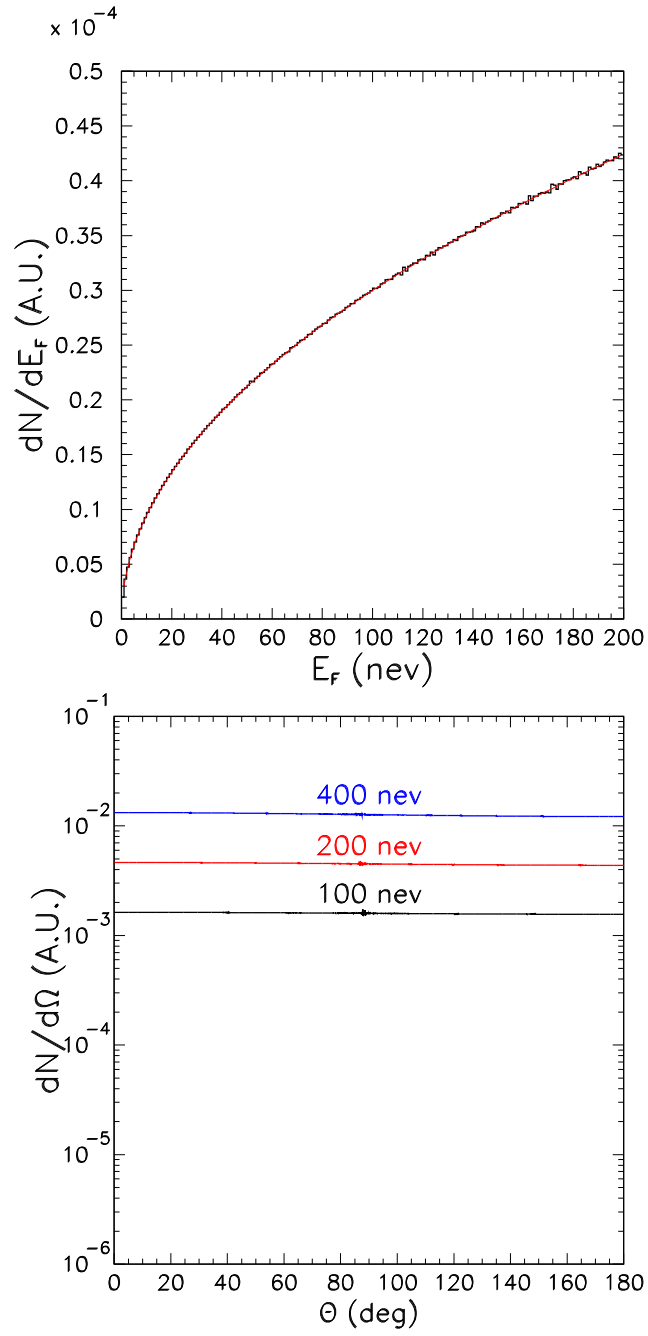


Figure 6: a) Energy distribution of UCN produced in superfluid  ${}^4\text{He}$  calculated using Eq. 6. The solid curve corresponds to a fit,  $dN/dE_F \propto E_F^{1/2}$ , to the histogram. b) Angular distributions for UCNs produced in superfluid  ${}^4\text{He}$ .  $\Theta$  is the laboratory angle of UCN with respect to the incident neutron beam direction. The three curves correspond to three different wall potentials for containing the UCNs.

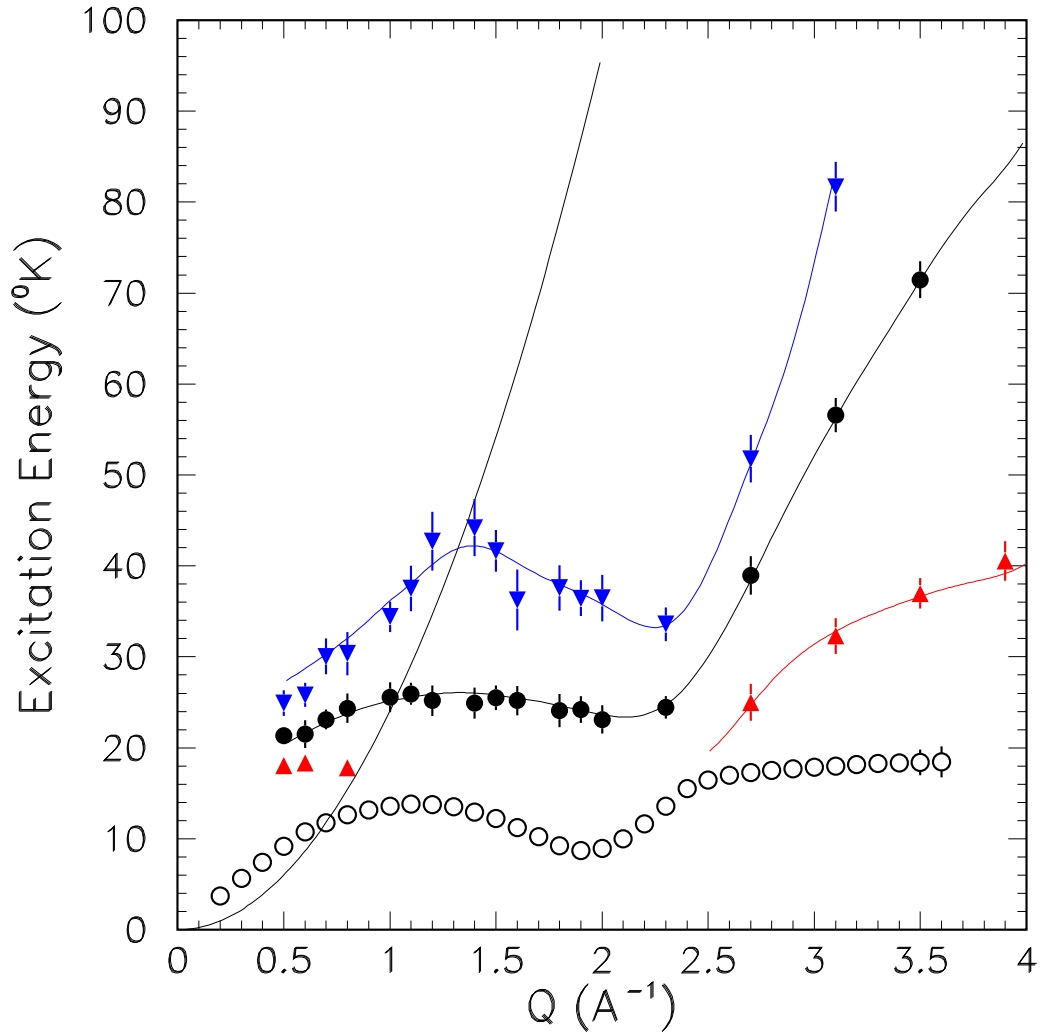


Figure 7: Single-phonon and multi-phonon excitations in superfluid  ${}^4\text{He}$  from Ref. [14]. The open circles indicate the locations of single-phonon excitations. The solid circles correspond to the peak positions for multi-phonon excitations. The triangles mark the locations where the multi-phonon excitation structure factors drop to half of their peak values. The neutron dispersion curve is also shown.

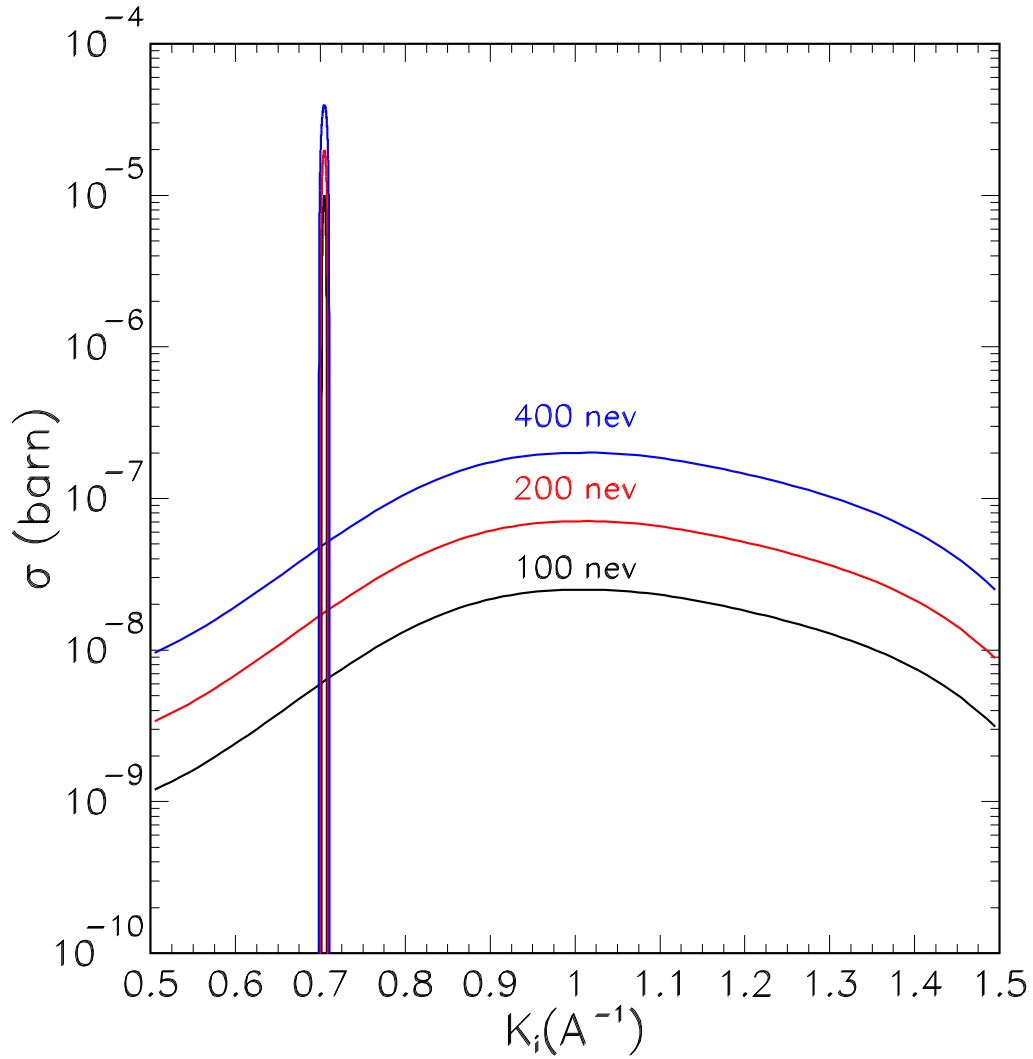


Figure 8: UCN production cross sections in superfluid  ${}^4\text{He}$  via the multi-phonon process plotted as a function of the incident neutron wave number,  $k_i$ . The three curves correspond to three different wall potentials for containing the UCNs. The UCN production cross sections via the single-phonon process are also shown as the curves with narrow peaks.

## Section V.C Trap Design, and Scintillation Light Detection

The ultracold neutron production, confinement, and detection region must satisfy a number of stringent requirements. It must contain the isotopically pure superfluid helium, allow neutrons to pass through such that UCN can be produced, permit long UCN and  $^3\text{He}$  storage times, and it must serve as a detector for the neutron- $^3\text{He}$  capture events.

At first glance, these requirements seem mutually exclusive, but using knowledge obtained from development work with light collection in acrylic cells [1,2] and experiments such as the UCN magnetic trapping experiment, [3] many of these requirements have been well studied and are understood.

### 1) Overview

A schematic of the heart of the experiment in the main cryostat is shown in Fig. V.C.1. The pair of neutron cells that are placed in the gaps between the three electrodes are shown in Fig. V.C.2. The cells consist of two rectangular acrylic tubes, each with dimensions of approximately 7 cm x 10 cm x 50 cm long. The cold neutron beam enters along the long axis of the cell and passes through either deuterated acrylic or deuterated polystyrene windows attached to each end. The beam exits at the rear of the cell and is

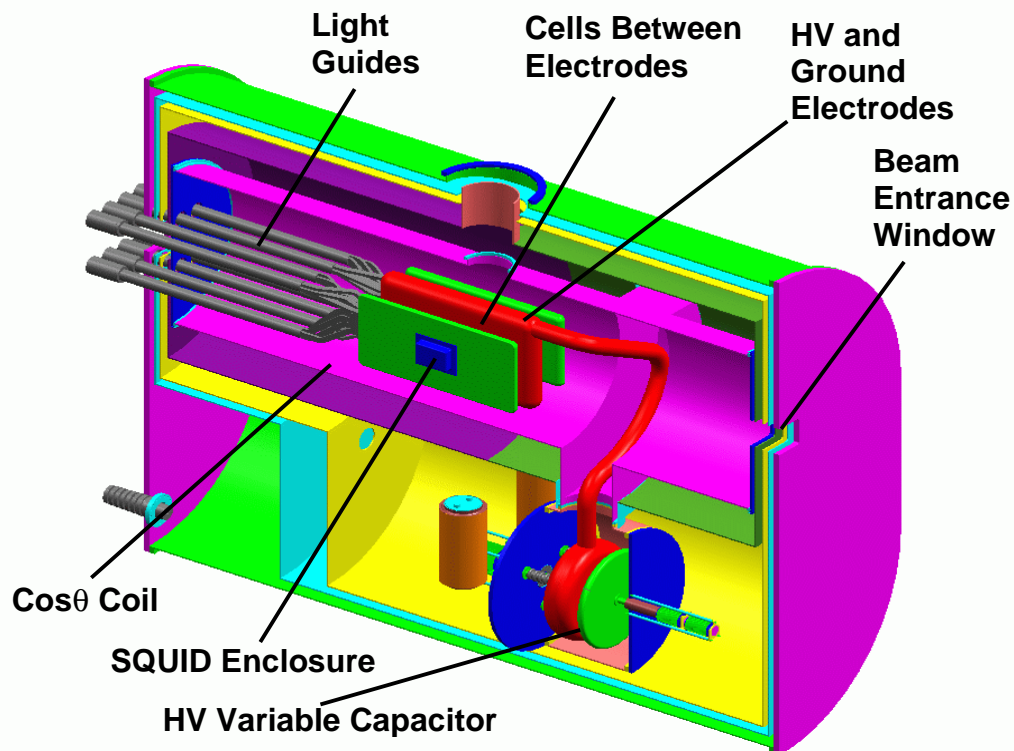


Fig. V.C.1 The UCN production, confinement, and detection region. The neutron beam enters from the right; the internal neutron guides are not shown. The two rectangular cells are placed between the three electrodes. The light guides connect to the PMT's at room temperature.

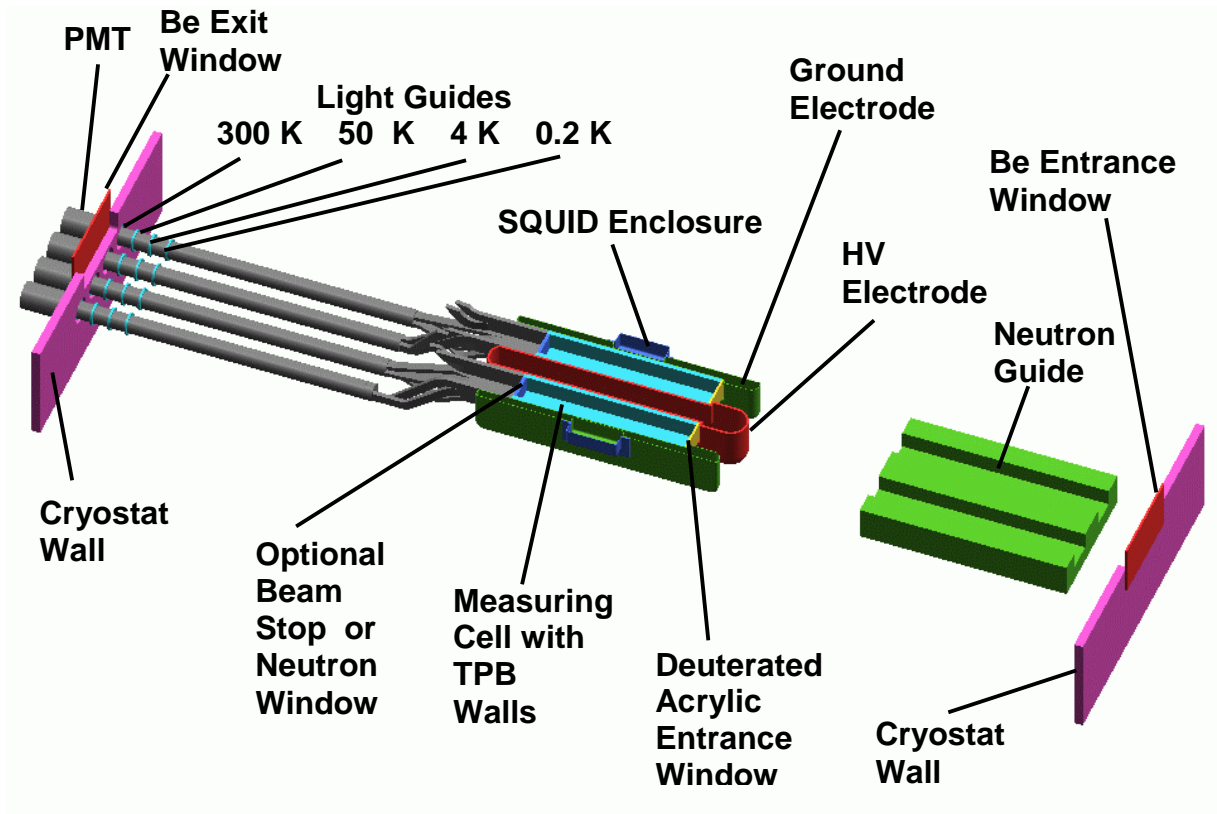


Fig. V.C.2 The path of the neutrons through the cryostat. The beam enters from the right. It is about 3.1 m from Cryostat wall to wall.

absorbed outside the cell in a beam stop made from a neutron absorbing material. The choice of whether to use a transparent or opaque beam stop will be determined based on the detection efficiency of the system.

The collection and measurement sequence has been described in Chapter IV. After the cells are loaded with a mixture of superfluid  $^4\text{He}$  and polarized  $^3\text{He}$ , they are irradiated with polarized cold neutrons to produce polarized UCN that must be confined by the material walls of the cell. After the beam has been switched off, the UCN and  $^3\text{He}$  spin vectors are rotated into the plane perpendicular to the magnetic field and precess until the UCN are either captured by  $^3\text{He}$  or lost due to other processes (beta decay, wall losses, or through small gaps). When the UCN are captured on  $^3\text{He}$ , scintillation light is produced. This light is converted to visible wavelengths and transported out of the detection region and detected using room temperature photomultiplier tubes (PMTs). This process could be repeated until the  $^3\text{He}$  becomes sufficiently depolarized, which could be a single neutron measurement cycle, at which time the cell is emptied and refilled with the  $^4\text{He} / ^3\text{He}$  mixture. This section discusses the UCN confinement,  $^3\text{He}$  depolarization, and transport and detection of scintillation light.

## 2) UCN production and confinement

The UCN are produced inside the acrylic cell through the inelastic scattering (super-thermal) process discussed in Section V.B and [4]. The number of UCN confined is a function of the production rate, the confinement potential of the material surfaces, and the lifetime of UCN in the bottle.

We plan to use walls made from acrylic and coated with deuterated polystyrene doped with a deuterated wavelength shifter (discussed below). The deuterated polystyrene has a UCN potential of 134 neV and should provide a storage lifetime of 500 s due to wall losses and beta decay. The UCN will retain the same polarization sense of the incident neutron and will travel undisturbed in the helium. The UCNs should not depolarize significantly when reflecting from the material walls; typical depolarization rates for plastics are  $\sim 10^{-6}$  per reflection from the wall[5].

A series of test runs were performed at LANSCE in the spring of 2002 to study the production and to measure the storage time of UCN in an acrylic cell coated with deuterated polystyrene. Although the results are preliminary, they indicate that the production rate obtained is consistent with the theoretically predicted rate within a factor of two. The storage time of UCN in the cell was measured to be 180 (+500, -60) s, consistent with the lifetime of 170 s expected from the calculated UCN leakage through the helium fill hole.

## 3) $^3\text{He}$ depolarization

A cell that allows for both long UCN storage times and long  $^3\text{He}$  relaxation times ( $\sim 10^4$  s,  $\sim 80$  h) is a critical need of the experiment. Past work in this area indicates that sufficiently long relaxation times may be possible, but test experiments will be required to determine the achievable relaxation time for the materials and conditions of the EDM experiment. These tests would be most easily carried out using polarized  $^3\text{He}$  produced by metastability-exchange optical pumping, and may be performed at LANSCE or NIST.

To reduce wall relaxation at cryogenic temperatures, one seeks a suitable diamagnetic material with a low value for  $E$ , the energy of adsorption for  $^3\text{He}$ . Although cesium has the lowest value,  $E = 2.3$  K [6], and has been shown to suppress wall relaxation of the  $^3\text{He}$  at the temperatures of interest, cesium is not a suitable coating material because of its large neutron absorption cross section. The next most effective coatings are hydrogen ( $E=12$  K) and deuterium ( $E=20$  K), but only deuterium would be compatible with long UCN storage times. A relaxation time of 128 h was obtained for a 0.07% solution of polarized  $^3\text{He}$  in liquid  $^4\text{He}$ , stored in a hydrogen-coated glass cell at a temperature of 4.2 K and a magnetic field of 3 mG [7]. A relaxation time of about 100 h has also been measured for a gaseous mixture of  $^3\text{He}$  and  $^4\text{He}$  (total density  $10^{17}$  cm $^{-3}$ ) that was stored in a hydrogen-coated, 3-cm diameter glass cell at a temperature of 4 K and magnetic field of 14 G. The relaxation time decreases rapidly at lower temperatures, but recovers to about 1000 s at 0.5 K because of the formation of a

superfluid layer [8, 9]. (Longer relaxation times have been obtained with magnetic fields of 10 kG, but those results are inappropriate for the low magnetic field of the EDM experiment [9].) The hydrogen coating is still required to obtain this relaxation time, but other coatings were not tested. A deuterium coating[10], along with the superfluid layer, might be effective, and would be compatible with the UCN's interaction cross sections. The relaxation time for the large cells discussed here would be enhanced because they would be expected to scale inversely with the surface to volume ratio.

#### 4) Operating Temperature

As discussed in Ref. 11, the operating temperature is determined by the requirement that the motion of the  $^3\text{He}$  is free enough so that there will be adequate motional averaging of the magnetic field fluctuations. The  $^3\text{He}$  relaxation time,  $T_2$  is a function of the magnetic field gradient,  $G$ , the diffusion constant,  $D$ , and the length of the cell,  $L$ ,

$$T_2 = 120 D / \gamma^2 G^2 L^4$$

and is the limiting parameter in selecting the operating temperature. From Fig. V.C.3 one can see that with a gradient of  $G = (1-2) \times 10^{-7}$  G/cm, a working temperature of 0.4 K is reasonable. However achieving a gradient of  $G = (1-2) \times 10^{-7}$  G/cm is very challenging. On the other hand  $G = (1-2) \times 10^{-6}$  G/cm has been demonstrated many times. The constraints on

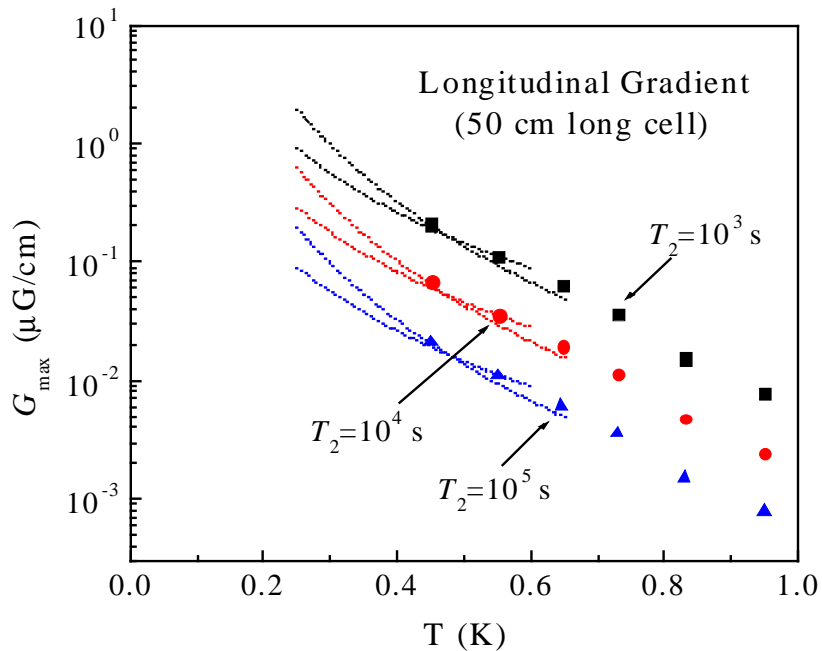


Fig. V.C.3 The maximum permissible gradients in magnetic field as a function of temperature. The gradients are limited by the relaxation rate  $1/T_2$

the allowable gradient become more relaxed when the experiment is operated at lower temperature. On the other hand, operating at higher temperatures makes the experiment technically simpler.

The most effective operating temperature is still an open question. But in the range 0.3 to 0.4 K, the motion of the  $^3\text{He}$  atoms crosses over from diffusive to ballistic. In this regard, the  $^3\text{He}$   $v \times E$  systematic, described in Section V.H.2, has a rapid change in magnitude, and at some temperature in this range, the  $^3\text{He}$  and UCN systematics are equal. Thus, there is some motivation to operate the experiment at several temperatures to address systematic effects. In addition the temperature dependence of the  $^3\text{He}$  polarization lifetime needs to be studied.

## 5) Detection System

The detection system converts the extreme ultraviolet (EUV) scintillation photons produced by helium scintillations to blue photons, pipes them out of the apparatus, and detects them with room temperature photo-multipliers. Each of these functions will be described below.

EUV light (80 nm) is produced by the recoil of the charged proton and triton from the capture of neutrons by  $^3\text{He}$  when they pass through the superfluid helium. The UCN confinement region is surrounded by 1-cm thick acrylic plates on each of the four sides perpendicular to the beam axis, that aid in transporting this scintillation light out of the apparatus. On the inner surface of the acrylic, the walls are coated with deuterated polystyrene doped with the deuterated organic fluor 1,1,4,4-tetraphenyl buta-1,3-diene (dTPB). The dTPB absorbs the EUV photons and emits blue light with a spectrum peaked at 440 nm and a width of approximately 50 nm [12]. This blue light is transported via total internal reflection through the light guides to the PMTs. The fluorescence efficiency (FE) of TPB doped into a polystyrene matrix is 1.0 relative to Sodium Salicylate [2], which has been independently measured to have an absolute FE of 0.37 [13]. We expect deuterated versions to have a similar FE.

Attached to the detector end of the confinement region are four acrylic light guides that transport the light captured in the ultraviolet transmitting (UVT) acrylic walls to photo-multipliers at room temperature. As the light exits the low-temperature region ( $< 500$  mK) of the apparatus, three short breaks in the light guide will be required to minimize the heat loads on the cell from the warmer surroundings. First, an acrylic window mounted to the 4 K shield provides a separation between the low-temperature region and the 4K shield. The scintillation light will pass through this window while blocking blackbody radiation from the 50 K shield. The second break is between this window and the light guide thermally attached to the 50 K shield. This second light guide transports the light to detectors located at room temperature. The nature of the design - four separate light guides attached to each cell - provides a natural means to allow the use of coincidence detection techniques between two or more PMTs. This will be required because of background events that are discussed further below.

From measurements of neutron capture events in helium [1], the size of a scintillation pulse at any one of the four PMTs is expected to be only a few photoelectrons. These measurements were taken in conditions similar to the conditions of this experiment, but without the magnetic and large electric fields. Tests will need to be performed to determine the detection efficiency in the presence of these fields.

Because of backgrounds, the PMTs must have good gain dispersion. This can be accomplished using a bialkali PMT such as the Burle 8850. These tubes have gain dispersions such that one can have separation between single photoelectron events and multi-photoelectron events. In addition, discrimination between photon scattering events and neutron capture events may be possible.

Tests with a hydrogenated cell at higher temperatures have shown that very good discrimination against gamma rays can be achieved by correlating the number of afterpulses with pulse height. (Afterpulses arise from long-lived excited states in the helium, some decaying with time constants as long as several seconds [14].) It is also important to investigate this discrimination technique at temperatures and magnetic fields appropriate for the experiment.

## **6) Backgrounds**

The detector system is developed to have as large as possible light collection efficiency. Since the liquid helium is an efficient scintillator for all forms of ionizing radiation, this also has the down side that a large number of background events are detected from other reactions such as excitations in a variety of locations outside a storage cell itself: inside the helium surrounding the confinement region, inside of the acrylic light guides, or in the PMTs themselves. In general, this light results from a variety of physical processes such as scintillation, luminescence, and Cherenkov radiation.

The primary source of backgrounds is expected to arise from the interaction of neutrons with materials in the apparatus [3]. During the filling phase of the experiment, large ( $10^{10}$  -  $10^{12}$ ) numbers of neutrons must be introduced into the apparatus in order to produce UCN. These neutrons will interact with various materials in addition to the  $^4\text{He}$ . If such an interaction results in the storage of energy in a meta-stable state (such as a radioactive isotope or a color center), then the release of that energy can result in background events once the beam is turned off. These events are generally time dependent, so one must carefully test all materials used in the regions exposed to neutrons. Various types of both active and passive background shielding will also be used.

The background events consist primarily of gammas from various sources (such as the radioactive decay of irradiated materials) that Compton scatter to produce betas. These events must be discriminated from the signal produced by the neutron capture on  $^3\text{He}$ . Conventional pulse shape discrimination techniques use either integration or integration and differentiation of the PMT signals with respect to time (e.g. the zero-time crossover method) to make these cuts. This technique however, breaks down when the intensity of the signal becomes low or shows no shape dependence as in the case of neutron-induced scintillations in liquid helium. However the helium scintillations do produce afterpulses that show up as single photon events after the primary signal and have time constants up to several seconds. One possible method to differentiate the helium events from Compton scattering events is to use the initial main pulse as the signal event and require a certain number of afterpulses to follow. For low afterpulse counting rates in the presence of electronic noise, this method is more sensitive than just integrating the signal over the afterpulse time interval.

In a series of experiments [1]; scintillations in liquid  $^4\text{He}$  were produced by a neutron beam with and without a small admixture of  $^3\text{He}$ . Figure V.C.4 shows the probability distribution for scintillation events where the vertical axis corresponds to the pulse height of the main pulse and the horizontal axis gives the number of afterpulses. The upper plot corresponds to the case when the storage cell is filled with pure  $^4\text{He}$  and the lower plot is that of the  $^3\text{He}$  -  $^4\text{He}$  mixture. Afterpulses were counted for  $4.5\ \mu\text{s}$  after the primary pulse. Gamma rays that have the same pulse height as neutrons can clearly be discriminated against by placing a condition on the number of afterpulses for each event. Gamma discrimination based on afterpulse counting has only been tested in the high temperature region (2 K) with a hydrogenated cell, so it will be important to investigate this discrimination technique at lower temperatures and higher magnetic fields appropriate for the experiment.

Since gamma radiation from neutron activation by cold neutrons is expected to be a main source of background, neutron shielding will be used to minimize irradiation of different materials by the scattered cold beam. Unfortunately, the functions of certain parts of the apparatus, such as windows for introducing neutrons into the apparatus, and the down converting fluor and acrylic portions of the detection system, necessitates that they be unshielded from neutrons. These materials must then be selected with extreme care to minimize neutron activation of impurity elements. The materials in the electrodes are especially critical in this regard due to their proximity to the neutron cells. Copper films evaporated on a suitable substrate are being considered as electrode construction materials (Section V.G).

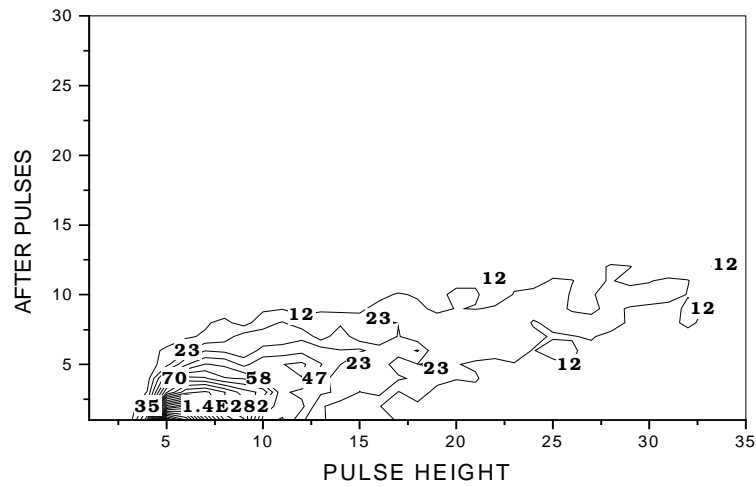
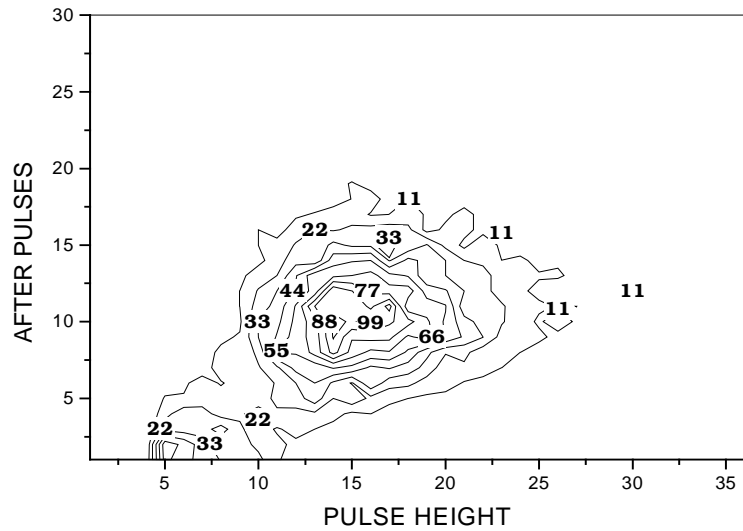


Fig. V.C.4 Tests at 1.8K have shown that very good discrimination against gamma rays can be achieved by correlating the number of afterpulses with the main pulse height. Both plots show data taken with a cold neutron beam. The upper plot shows the probability distribution of scintillation events when the cell was filled only with pure  $^4\text{He}$ ; the lower plot shows data for a mixture of  $^3\text{He} / ^4\text{He}$ .

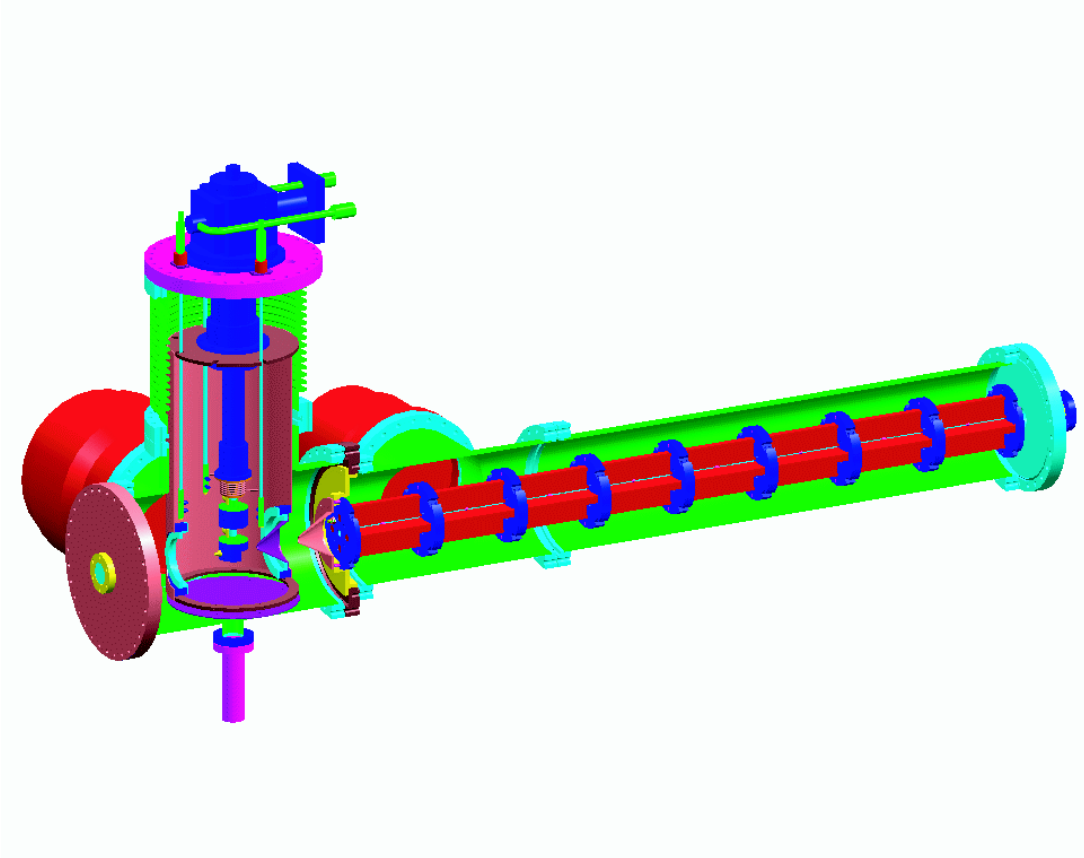
Luminescence of materials can be easily removed through the use of coincidence detection because these events are uncorrelated single photon emissions. Nevertheless, materials used for neutron shielding may need opaque materials placed between them and the photo-multipliers to minimize the detection of luminescence light through spurious coincidence.

External shielding will be used to minimize ambient backgrounds to which the experiment is susceptible, such as external gamma and cosmic radiations. Active vetoing of cosmic ray muons will be performed using scintillation paddles.

## References

- [1] K. Habicht, *Szintillationen in flüsrigen Helium – ein Detektor für ultrakalte Neutronen*, Ph.D. Thesis, Technischen Universität Berlin, 1998.
- [2] D. N. McKinsey *et al.*, *NIM B* **132**, 351 (1997).
- [3] P.R. Huffman *et al.*, *Nature* **403**, 62 (2000).
- [4] R. Golub and J. M. Pendlebury, *Phys. Lett.* **62A**, 337 (1977).
- [5] A. Serebrov *et al.*, *NIM A* **440**, 717 (2000).
- [6] G. Tastevin, *J. Low Temp. Phys.* **89**, 669 (1992).
- [7] M. A. Taber, *J. Physique*, **39**, C6-192 (1978).
- [8] M. Himbert and J. Dupont-Roc, *J. Low Temp. Phys.* **76**, 435 (1989).
- [9] C. Lusher, M. Secca, and M. Richards, *J. Low Temp. Phys.* **72**, 71 (1988).
- [10] V. Lefevre-Sequin *et al.*, *J. Physique* **46**, 1145 (1985).
- [11] R. Golub and S. K. Lamoreaux, *Phys. Rep.* **237**, 1 (1994).
- [12] W. M. Burton and B.A. Powell, *Appl. Opt.* **12**, 87 (1973).
- [13] E. C. Bruner Jr., *J. Opt. Soc. Am.* **59**, 204 (1969).
- [14] D. N. McKinsey *et al.*, *Phys. Rev.* **A59**, 200 (1999).

## Section V.D $^3\text{He}$ Polarization and Transport



Cutaway view of the polarized  $^3\text{He}$  source currently under construction at LANL.

As is illustrated in the discussion on sensitivity for the proposed experiment, the purity of the  $^3\text{He}$  polarization  $P_3$  in the experimental volume is of considerable importance. For a polarized neutron source and  $P_3 \approx 1.0$ ,  $\delta f \propto 1/P_3$  where  $\delta f$  is the final uncertainty in the measurement of the possible neutron EDM. However, if the neutron source is unpolarized, the neutron polarization  $P_n = \eta P_3$ , where  $\eta$  depends on various UCN loss mechanisms, so that  $\delta f \propto 1/P_3^2$ . Moreover, if  $P_3$  and  $P_n$  differ from unity significantly,  $\delta f$  depends more strongly on  $P_3$  than  $1/P_3^2$ .

A number of methods have been used in various laboratories to produce polarized  $^3\text{He}$  [1, 2, 3, 4, 5]. These include melting polarized solid  $^3\text{He}$  at mK temperatures, optically pumping  $^3\text{He}$  in the metastable  $^3S_1$  state, and using spin-exchange collisions with optically-pumped alkali atoms. The first of these techniques has been used to produce a polarization  $P_3 \approx 0.95$ , but requires specialized and expensive apparatus. The latter techniques promise polarizations of nearly 90%, but have not demonstrated a polarization exceeding 70% experimentally. The experiment under consideration in this manuscript

would benefit from  $P_3$  greater than has been achieved with these optical pumping methods.

Another method which has the potential to yield a polarization near unity with a simpler apparatus than that of the cryogenic method is to filter an atomic beam of  $^3\text{He}$  in a magnetic field gradient. While this method is not capable of producing the same quantity of polarized  $^3\text{He}$  as the previously mentioned methods, the intensity of the polarized beam should be adequate for our purposes.

However, unlike most other atoms that have been polarized in this manner, ground-state  $^3\text{He}$  has only a nuclear magnetic moment which is smaller than the electron magnetic moment by three orders of magnitude. Due to the relatively small force which can be applied to the  $^3\text{He}$  through this magnetic moment, the time during which the atom interacts with the field must be increased and the kinetic energy of the atom must be decreased relative to atoms with nonzero electron spin to achieve the same polarization for similar magnetic field gradients. These two requirements can be satisfied by operation of the  $^3\text{He}$  source at a temperature near 1 K and by use of an interaction region about 1 m long.

### V.D.1 Quadrupole Potential

The energy of a magnetic dipole  $\vec{\mu}$  in a magnetic field  $\vec{B}(\vec{r})$  is given by

$$U(\vec{r}) = -\vec{\mu} \cdot \vec{B}(\vec{r}) \quad (1)$$

and the force imposed on the dipole if the field is static is given by

$$\vec{F}(\vec{r}) = \mu(\hat{s} \cdot \nabla)\vec{B}(\vec{r}) \quad (2)$$

where  $\hat{s}$  is the direction of the spin and  $|\hat{s}| = 1$ . For spin-1/2  $^3\text{He}$ ,  $\mu = -\hbar\gamma_3/2$  where  $\gamma_3 = 2.04 \cdot 10^8/\text{Ts}$  is the  $^3\text{He}$  gyromagnetic ratio.

We are considering a magnetic quadrupole configuration such as that shown in Fig. 1. This configuration can have a relatively open geometry which helps to remove  $^3\text{He}$  atoms in the wrong spin state from the interaction region and to reduce the probability that they interact with the atoms confined along the polarizer axis.

However, the magnetic field in the rest frame of an atom will change in magnitude and direction as the atom follows its trajectory through the polarizer. If these changes are too fast, the atom's spin will not maintain its relationship to the magnetic field and the atomic beam will lose polarization. To maintain an atom's polarization throughout its trajectory, its spin must be able to adiabatically follow the direction of the field. Explicitly,

$$\frac{|\dot{B}|}{|B|} \ll |\gamma_3 B|, \quad (3)$$

where  $\dot{B} \equiv dB/dt$  and  $\gamma_3 B$  is the Larmor frequency.

An additional concern is that the magnitude of the field is theoretically zero at the center of the polarizer. Polarized atoms traveling through this region of zero field may become unpolarized and reduce both the net polarization and polarizer throughput. The

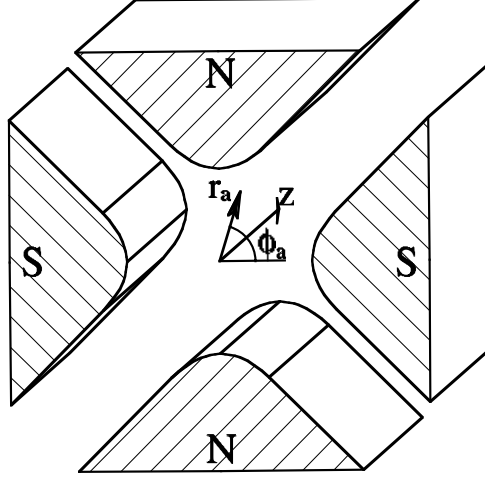


Figure 1: Quadrupole configuration of permanent magnets similar to that being used in the polarizer under construction at LANL.

addition of a weak axial magnetic field  $B_z$  mitigates this potential difficulty. If this weak axial field is included, Eq. 3 can be expressed in terms of the velocity of the atom transverse to the axis of the polarizer  $v_r$  and the radius of the polarizer aperture  $R_a$  as

$$\gamma_3 B_z \gg \frac{|v_r|}{R_a}. \quad (4)$$

As long as this condition is satisfied, an atom's spin will maintain its initial relationship with the magnetic field so that  $\hat{s} = \hat{B}$  always. The force from Eq. 2 can then be expressed as

$$\vec{F}_B(\vec{r}) = \pm \mu \frac{B_0}{R_a} \frac{1}{\sqrt{1 + (B_z/B_0)^2 (R_a/r)^2}} \hat{r} \quad (5)$$

where  $r$  is the distance from the axis of the polarizer to the atom,  $B_0$  is the magnitude of the field near the surface of one of the magnets and  $\pm$  refers to the two spin states anti parallel and parallel to  $\vec{B}$ , respectively. Obviously, atoms whose spin is parallel to  $\vec{B}$  experience a restoring force and the atoms in the other state are repulsed from the axis of the quadrupole. Note that the depth of the potential well is reduced unless  $B_z \ll B_0$ .

## V.D.2 Polarizer Parameters

If the source is a jet of gaseous  $^3\text{He}$  some distance from the entrance aperture of the polarizer, the acceptance angle as a function of atom velocity can be estimated by setting the magnetic potential energy equal to the kinetic energy of the transverse motion. Thus,

$$\sin(\theta_0) \approx \sqrt{\frac{\mu B_0}{mv^2}} \quad (6)$$

for an atom located halfway between the center and edge of the polarizer and a magnetic field of  $B_0 \gg B_z$  at the edge of the polarizer.

The velocity dependence of the intensity,  $I(v)$ , of an atomic beam can be expressed as [6]

$$I(v) = I_0 \frac{2}{\alpha^4} v^3 e^{(-v^2/\alpha^2)} \quad (7)$$

where  $\alpha^2 = 2k_B T/m$ . With  $v_{rms} = \sqrt{2}\alpha$  to replace  $v$  in Eq. 6, the acceptance angle can be expressed as a function of source temperature  $T$  as

$$\sin(\theta_0) \approx \sqrt{\frac{\mu B_0}{4k_B T}}. \quad (8)$$

For  $B_0 = 0.75$  T and  $T = 0.6$  K, this yields  $\theta_0 \approx 0.9^\circ$ .

Eq. 6 can also be used with Eq. 4 (which also requires that  $B_z \ll B_0$ ) to further constrain  $B_z$ . These relationships can be combined to yield

$$\frac{1}{R_a} \sqrt{\frac{\hbar}{2m\gamma_3 B_0}} \ll \frac{B_z}{B_0} \ll 1. \quad (9)$$

For the values of  $B_0$  and  $T$  stated previously,  $B_z \approx 0.03$  T is an appropriate choice.

### V.D.3 Atomic Beam Intensity

The angular dependence of the intensity of an effusing source is given by  $dI_0/d\Omega = n\bar{v}A \cos(\theta)/4\pi$  [6] where  $n$  and  $A$  are the source density and aperture area respectively,  $\theta$  is the azimuthal angle from the source aperture normal and  $\Omega$  is the solid angle. Integrating between  $0 \leq \theta \leq \theta_0$  yields

$$\begin{aligned} I_0 &= \frac{1}{4} n\bar{v}A \sin^2(\theta_0) \\ &\approx \frac{1}{2} \frac{p}{\sqrt{mk_B T}} A \sin^2(\theta_0) \\ &\approx \frac{1}{8} \frac{\mu B_0}{\sqrt{m(k_B T)^3}} pA, \end{aligned} \quad (10)$$

where  $p$  is the source pressure. For  $^3\text{He}$  and the parameters discussed above, Eq. 10 yields  $I_0/pA \approx 1 \cdot 10^{16}/\text{s}\cdot\text{mtorr}\cdot\text{cm}^2$ . The design of the source aperture that we are currently considering will allow for an effective area of about  $1 \text{ cm}^2$ .

The pressure at which the source can be operated depends upon the specific geometry of the source nozzle and there are several concerns that must be addressed to determine an adequate nozzle design. First, the gas pressure in the volume outside the nozzle must be kept much lower than the source pressure. This depends on several items such as the geometry of that volume, the capacity of the pumps acting on that volume and, of course, the flow of  $^3\text{He}$  from the nozzle. Second, we expect that the amount of  $^3\text{He}$  in the system will be relatively small and will need to be used efficiently. Fortunately, the forward flow

and hence the quality of the vacuum outside the source can be enhanced by building the aperture from a collection of small tubes of radius  $\rho_s$  and length  $L_s$ . The forward flow remains the same while the integrated intensity is reduced by  $8\rho_s/3L_s$  [6].

A third concern is that the mean-free-path in the nozzle aperture given by  $\lambda_s \approx 1/\sqrt{2}n\sigma$ , where  $\sigma = 1.0 \cdot 10^{-14} \text{ cm}^2$  is the scattering cross-section of He, should not be much smaller than  $\rho_s$  to insure that the lowest velocity atoms are not scattered out of the beam. The mean-free-path for helium can be expressed as  $\lambda_3/p \approx 4.4 \cdot 10^{-3} \text{ cm/mtorr}$ . With  $\rho_s = 3.5 \cdot 10^{-1} \text{ mm}$ ,  $p$  should be less than a few  $10^{-2} \text{ mtorr}$  and

$$I_0 \approx 1 \cdot 10^{14} / \text{s}, \quad (11)$$

given that only half of the  $^3\text{He}$  enter the polarizer in the spin state where  $\hat{s} = \hat{B}$ .

#### V.D.4 Numerical Simulations

As noted in [7], the actual performance of the polarizer will differ from the simple calculations of the previous section. This is due in part to the fact that several important considerations were ignored in these simple calculations. For example, we must consider a method to inhibit fast atoms in the wrong spin state from traversing the polarizer and we must consider the mechanical angular momentum of the atom about the axis of the polarizer. In defense of the calculation presented in the previous section, these items are difficult to treat analytically.

That the angular momentum of the  $^3\text{He}$  about the polarizer axis is likely to be important, can be illustrated by considering the depth of the potential well relative to an atom's kinetic energy. The radial restoring force including the pseudo-force caused by the atom's centripetal acceleration can be expressed as

$$\begin{aligned} \vec{F}(\vec{r}) &\approx -\frac{1}{2}\hbar\gamma_3\frac{B_0}{R_a}\hat{r} + mr_0^2v_\phi^2\frac{1}{r^3}\hat{r} \\ &= (-\alpha + \beta\frac{1}{r^3})\hat{r} \end{aligned} \quad (12)$$

where  $r_0$  and  $v_\phi$  are the initial radial position and polar velocity of the atom. The potential energy is then given by

$$U(r) = \alpha r + \beta\frac{1}{2r^2} \quad (13)$$

which has a minimum at  $r^3 = \beta/\alpha$ . The potential minimum

$$U_{min} = \frac{3}{2}\alpha^{2/3}r_0^{2/3}(mv_\phi)^{1/3} \quad (14)$$

which depends upon the kinetic energy of the polar motion to the 1/3 power. Clearly, a atom can enter the polarizer with more kinetic energy in the transverse motion than was considered in Eqs. 6 and 8.

#### V.D.5 Equations of Motion

To better analyze the performance of the polarizer and to investigate several different schemes to inhibit fast atoms from traversing the polarizer in the wrong spin state, we chose a numerical analysis. This analysis involves a Runge-Kutta scheme to integrate the differential equations describing the motion of the atom as it traverses the polarizer.

In addition to the restoring force expressed in Eq. 5, the effects of gravity and of bending the horizontally oriented polarizer guide upwards were included. We also included the ability to simulate the effect of cylindrically symmetric baffles placed along the bore of the polarizer to inhibit fast atoms from traversing it unimpeded.

The effects of gravity and of bending of the polarizer bore can be expressed as

$$\begin{aligned}\vec{F}_g &= -m\left(g + \frac{v_z^2}{R_p}\right)\hat{y} \\ &= -m\left(g + \frac{v_z^2}{R_p}\right)(\sin(\phi)\hat{r} + \cos(\phi)\hat{\phi})\end{aligned}\quad (15)$$

where  $g$  is the acceleration due to gravity,  $v_z$  is axial velocity of the atom, and  $R_p$  is the radius of curvature of the “bent” polarizer. The acceleration due to gravity is about 1% of the acceleration due to the interaction of the dipole and magnetic field, but was included for completeness as it introduced no additional complexity to the calculation.

The equations of motion can be immediately expressed in cylindrical coordinates as

$$\begin{aligned}\vec{F}_t &= \vec{F}_B + \vec{F}_g \\ &= m\ddot{\vec{r}} \\ &= m((\ddot{r} - \dot{r}\dot{\phi}^2)\hat{r} + (r\ddot{\phi} + 2\dot{r}\dot{\phi})\hat{\phi} + \ddot{z}\hat{z})\end{aligned}\quad (16)$$

Velocities were chosen randomly from a weighted distribution that accurately reproduces Eq. 7. The directions of atoms leaving the source were also made to accurately reproduce the  $\cos(\theta)$  dependence of an effusing source and no correction was made to simulate a source aperture of finite length. In all cases except otherwise noted, the simulations were made for a polarizer whose dimensions are those of the polarizer currently under construction at LANL. The relevant dimensions are: source aperture radius  $R_s = 6$  mm, separation between source aperture and polarizer entrance aperture  $s = 22$  cm, polarizer aperture (or bore radius)  $R_a = 7.5$  mm, and polarizer length  $L = 1.25$  m. The source temperature has been fixed at  $T = 0.6$  K and the magnetic fields are assumed to be  $B_0 = 0.75$  T and  $B_z = 0.03$  T for these simulations.

#### V.D.6 Straight, Unobstructed Polarizer

Figs. 2 show some results of a simulation for a straight polarizer when  $s = R_a$ . Only a few percent of the incident atoms would successfully traverse the polarizer in this situation due to the large angle relative to the polarizer axis with which most of them enter the polarizer; 1/4 of the atoms leaving the source enter the polarizer. Of particular significance in these data is Fig. 2(d) which shows the distribution of the angle of incidence for atoms which could successfully traverse the polarizer. The standard deviation of these data

from a mean of  $\theta = 0$  is  $\sigma_\theta = 1.1^\circ$ . This is about 20% larger than  $\theta_0 = 0.9^\circ$  from Eq. 8 which better represents a maximum angle than a standard deviation. As mentioned previously, this effect was expected because the simulation treated the transverse motion more accurately than did our previous analysis.

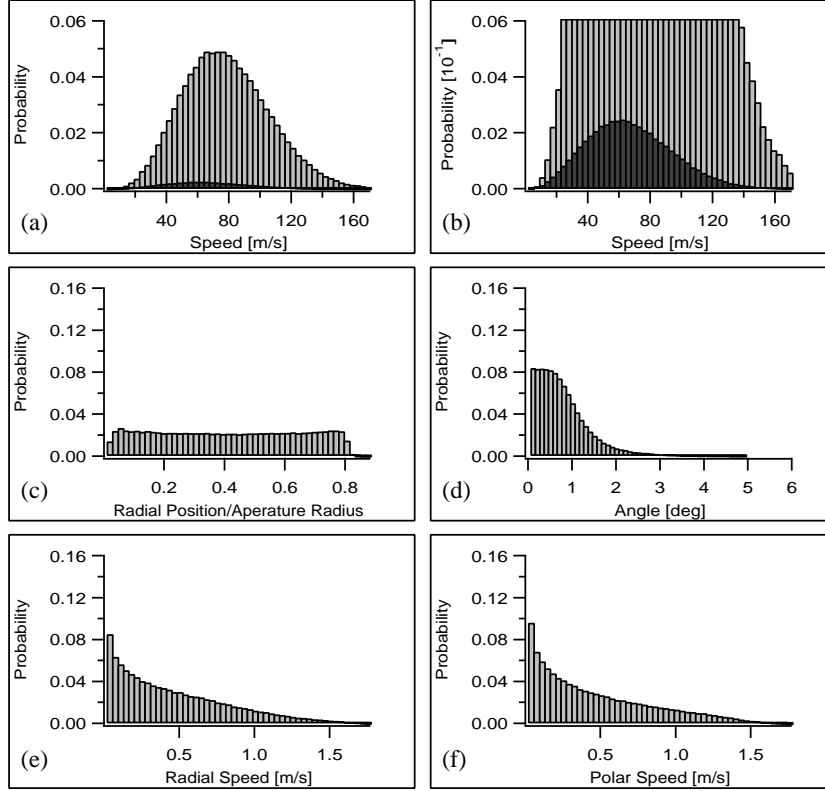


Figure 2: Results of a simulation where  $s = R_a$  for atoms with  $\hat{s} = \hat{B}$ . The polarizer was straight and unobstructed. The light gray bars in (a) represent the velocity distribution of atoms which enter the polarizer and the dark gray represents the subset that successfully traverses the polarizer. Panel (b) shows the same results as (a) with a different vertical scale. Panels (c-f) show the distributions of various initial conditions for atoms which successfully traverse the polarizer. Only 4.8% of the incident atoms travel the full length of the polarizer, but 1/4 of all the atoms leaving the source enter the polarizer. A total of 250,000 successful traverses of the polarizer were used to generate these histograms.

Figs. 3 show some results of a simulation for a straight polarizer as in Figs. 2, but with the source and polarizer separated by the same distance they will be separated in the device being constructed at LANL. Note that the angular dependence in Fig. 3(d) is slightly different from Fig. 2(d). Also note that the probability is very small for an atom to enter the polarizer along the axis and successfully traverse the polarizer. From

conservation of energy and momentum, we can then determine that it is equally unlikely that an atom will pass through the axis during a successful traverse of the polarizer. Because the atoms do not pass through the center of the polarizer where the transverse magnetic field is null, they will not suffer depolarization by entering a region with an undefined quantization axis even if the additional axial field  $B_z = 0$ .

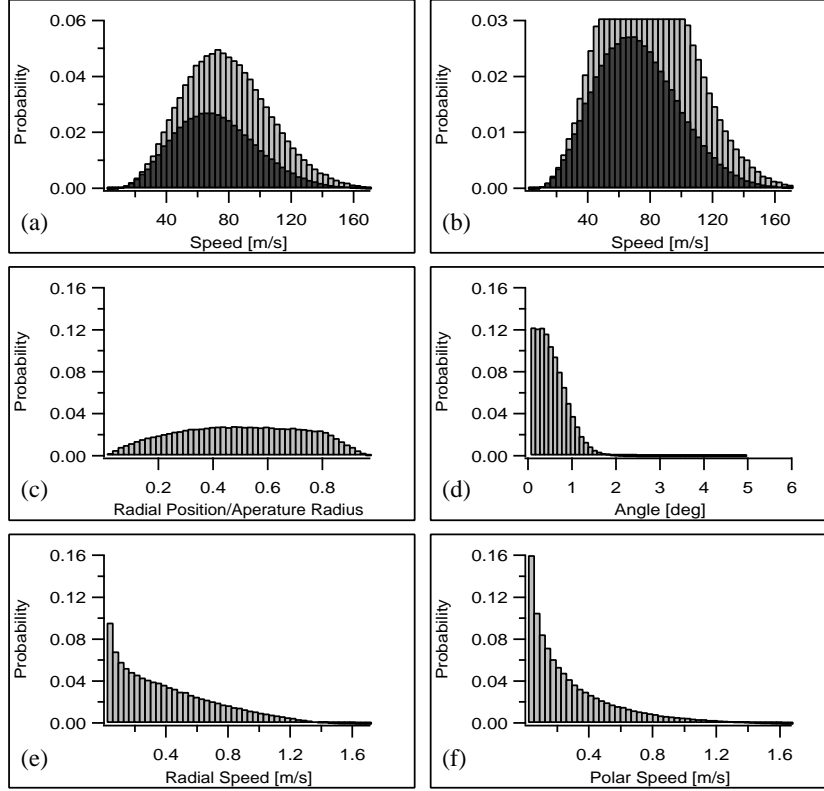


Figure 3: Results of a simulation with a straight polarizer and no obstructions for atoms with  $\hat{s} = \hat{B}$ . The light gray bars in (a) represent the velocity distribution of atoms which enter the aperture of the polarizer and the dark gray represents the subset that successfully traverses the polarizer. Panel (b) shows the same results as (a) with a different vertical scale. Panels (c-f) show the distributions of various initial conditions for atoms which successfully traverse the polarizer. About 53% of the incident atoms successfully traverse the entire length of the polarizer but only 0.1% of the atoms leaving the source enter the polarizer. A total of 250,000 successful traverses of the polarizer were used to generate these histograms.

This calculation suggests that the probability of a  $^3\text{He}$  atom to traverse the polarizer, given that it impinges on the polarizer entrance aperture and  $\hat{s} = \hat{B}$ , is  $P_+ = 0.53$ . To calculate the throughput, Eq. 10 can be used where  $\sin(\theta_0) \approx R_a/s$ . Given that  $B_0 = 0.75 \text{ T}$ ,  $T = 0.6 \text{ K}$ ,  $p = 3 \cdot 10^{-2} \text{ mtorr}$ ,  $A = 1 \text{ cm}^2$  and half of the incident  $^3\text{He}$  have

$$\hat{s} = \hat{B}$$

$$I_0 = 4 \cdot 10^{14}/\text{s}, \quad (17)$$

which is four times larger than Eq. 11

The polarization of the  $^3\text{He}$  can be calculated if the throughput is known for atoms which enter the polarizer in the orthogonal spin state. We have determined that the probability of such an atom to successfully traverse the polarizer is  $P_- = 0.0004$ . The net polarization can be calculated from

$$P = \frac{P_+ - P_-}{P_+ + P_-}. \quad (18)$$

For  $P_+ = 0.53$  and  $P_- = 0.0004$  as determined above,  $P > 0.998$ .

### V.D.7 Two Baffles

Figs. 4 show some results of a simulation for a straight polarizer as in Figs. 3, but with two baffles placed in the bore of the polarizer to eliminate line-of-sight down the bore. The configuration of the baffles chosen was a disk-shaped structure placed in the center of the polarizer midway between the ends and a matching washer placed at the exit baffle. In all cases the edges of the baffles would overlap by 0.5 mm if superposed. In this manner, atoms in the wrong spin state should not be able to traverse the polarizer under any circumstances. Several simulations were compared to arrive at the optimum choice for the size of the baffles. A comparison of these results is displayed in Fig. 5 and shows that the optimum radius of the disk baffle is slightly less than half of the radius of the polarizer bore.

The results displayed in Figs. 4 are those for the baffle size with the largest throughput. In this configuration, only 6.6% of the incident atoms in the proper spin state would pass unimpeded through the polarizer. Note the discreet velocities which would traverse the polarizer as shown in Fig. 4(b). Neglecting the effect of the atoms' mechanical angular momentum, these represent atoms whose trajectories would be parabolas and would make an even number of passes through, or nearly through the axis of the polarizer. Obviously, the throughput is dependent on the velocity profile and therefore on the temperature of the source. A warmer source may be more effective for this arrangement. Also note the profile of the angles of incidence in Fig. 4(d) which has a maximum at about  $0.7^\circ$ . This suggests that a different source nozzle geometry with slightly angled capillaries may be able to increase the number of atoms which can pass the baffles undeflected.

### V.D.8 Bent Polarizer

Figs. 6 show the results of a simulation for a polarizer bent to prevent a simultaneous view of the entrance and exit apertures down the bore of the polarizer. As in the situation with baffles discussed previously, fast atoms in the wrong spin state should not be able to traverse the polarizer and degrade the polarization of the collected  $^3\text{He}$ . The radius of curvature was chosen to be  $R_p = L^2/16R_a \approx 12\text{m}$  where  $L$  is the length of the polarizer. As can be seen in Fig. 6(b), this method would clearly favor the slowest atoms;

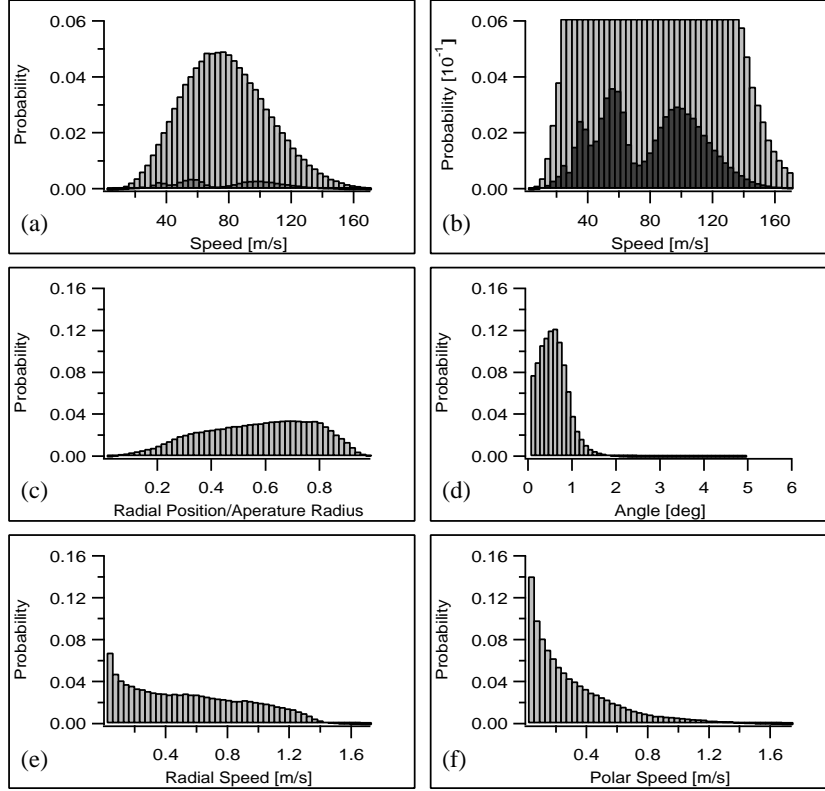


Figure 4: Results of a simulation with a straight polarizer and two baffles along the bore for atoms with  $\hat{s} = \hat{B}$ . The first baffle is a disk of radius 3.3 mm in the center of the bore and midway between the ends. The second baffle is a washer with opening radius 2.8 mm located in the exit aperture. This configuration was found to optimize the throughput for this size polarizer and source temperature. The light gray bars in (a) represent the velocity distribution of atoms which enter the aperture of the polarizer and the dark gray represents the subset that successfully traverses the polarizer. Panel (b) shows the same results as (a) with a different vertical scale. Panels (c-f) show the distributions of various initial conditions for atoms which successfully traverse the polarizer. About 6.6% of the incident atoms travel the length of the polarizer unobstructed. A total of 250,000 successful traverses of the polarizer were used to generate these histograms.

fast atoms would have enough centripetal acceleration to overcome the restoring effect of the magnetic field. This method would be slightly less effective than using the baffles as described previously, as only about 5.7% of the incident atoms could traverse the polarizer without colliding into the walls or passing out of the bore. If the source is colder than 0.6 K this configuration may have better throughput than the baffle configuration. (We may be able to achieve 0.4 K.)

Unfortunately, neither the baffle nor bent polarizer configurations could allow even

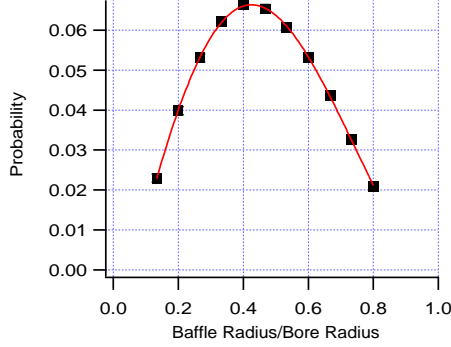


Figure 5: Probability for successfully traversing the polarizer as a function of baffle size for atoms with  $\hat{s} = \hat{B}$ . The two baffles are 1) a disk-shaped structure placed in the center of the polarizer midway between the ends and 2) a matching washer placed at the exit baffle. The edges of the baffles would overlap by 0.5 mm if superposed. The baffle size reported is the radius of the disk less 0.25 mm.

10% throughput, if the results of these simulations accurately reproduce reality. However, another configuration is suggested by the equation  $R_p = L^2/16R_a$ , where the radius of curvature depends on the square of the polarizer length. A numerical simulation was performed with a double-length polarizer of 2.5 m and the results were promising. The calculated throughput increased by more than a factor of 4 to 28% or about half of the throughput of a straight polarizer of half the length (and no baffles). The results for optimally chosen baffles of the same configuration used previously, but adapted for the longer polarizer, showed a small decrease in the throughput.

#### V.D.9 Net Polarization and Throughput for Obstructed and Bent Polarizers

Either the use of baffles or bending the polarizer, to prevent a line-of-sight view of both ends of the polarizer down its bore should prevent any gas which is not  $^3\text{He}$  in the desired spin state from traversing the polarizer, provided the bore is sufficiently open along its length to allow the escape of this other gas into the surrounding vacuum. However, the highest throughput allowed by either of these methods for  $L = 1.25$  m is about 3% of the incident  $^3\text{He}$  so that  $I_0 \approx 5 \cdot 10^{13}$  atoms/s. While this flux is theoretically sufficient for the experiment described in this manuscript, we do not feel that it allows a sufficient margin of error; experiments rarely work as well as is theoretically possible.

The “double-length” polarizer with  $L = 2.5$  m and a bend of  $R_p = L^2/16R_a$  is not an experimentally attractive solution if another solution can be found for  $L = 1.25$  m, due to the additional apparatus required and space constraints. More explicitly, we wish to build two identical polarizer sections and connect them with a short section in which an RF field can be applied to change the direction of polarization and investigate the net polarization of the  $^3\text{He}$ . The length of the entire apparatus would then exceed our

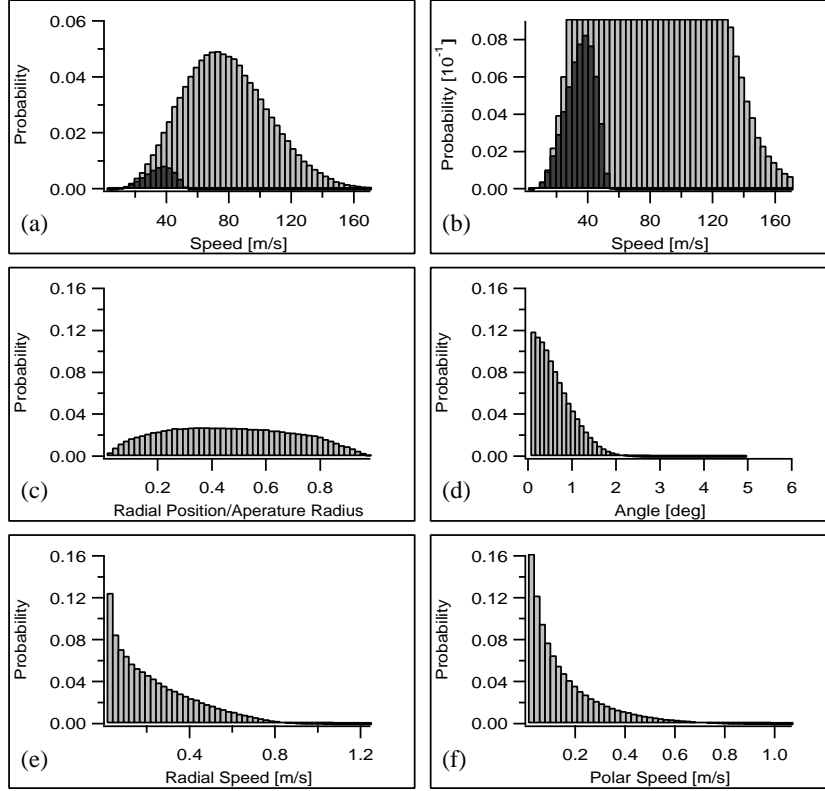


Figure 6: Results of a simulation for a polarizer bent to occlude the view of one aperture from the other looking down the bore and for atoms with  $\hat{s} = \hat{B}$ . The light gray bars in (a) represent the velocity distribution of atoms which enter the aperture of the polarizer and the dark gray represents the subset that successfully traverses the polarizer. Panel (b) shows the same results as (a) with a different vertical scale. Panels (c-f) show the distributions of various initial conditions for atoms which successfully traverse the polarizer. Only about 5.7% of the incident atoms successfully traversed the polarizer. A total of 250,000 successful traverses of the polarizer were used to generate these histograms.

currently available space.

#### V.D.10 Conclusion

In conclusion, it appears that a throughput of about  $I_0 \approx 4 \cdot 10^{14}/s$  is possible for a polarization of  $P > 0.998$  with a polarizer of the type currently being assembled at LANL. It is clear that the straight, unobstructed polarizer configuration is superior to any of the other configurations considered here such as placing a particular series of baffles along the length of the polarizer or a slight bend to occlude a view of one end from the other. Although the polarization is theoretically unity with these other methods, the 0.2% lower polarization with the straight, unobstructed polarizer is insignificant compared with its

tenfold improvement in throughput.

As was suggested previously, the more accurate numerical analysis suggests a four times higher flux than the simple calculation of the first section. A further conclusion, which can be derived from the numerical analysis, is that the axial magnetic field  $B_z$  is not required;  $^3\text{He}$  with  $\hat{s} = \hat{B}$ , that would successfully traverse the polarizer, would not pass through the axis where the transverse field is null.

## References

- [1] G.A. Vermeulen and G. Frossati, *Cryogenics* 27, 139 (1987).
- [2] R.G. Milner *et al.*, *Nucl. Instrum. Methods Phys. Res. A* 274, 56 (1989).
- [3] P.J. Nachor *et al.*, *J. Physique Lett.* 43L, 525 (1982).
- [4] C.G. Aminoff *et al.*, *Rev. Phys. Appl.* 24, 827 (1989).
- [5] K.P. Coulter *et al.*, *Nucl. Inst. Meth. A* 270, 90 (1988).
- [6] N.F. Ramsey, *Molecular Beams* (Oxford Univ. Press, Oxford, 1956).
- [7] R. Golub and S.K. Lamoreaux, *Phys. Reports* 237, 1 (1994).

# Chapter V.E Magnetic and Electric Field Configuration

## 1. Static Fields

### a. Specifications

The neutron EDM measurement requires static magnetic and electric fields surrounding the two target cells that contain the superfluid  $^4\text{He}$  and the ensemble of polarized neutron and  $^3\text{He}$  atoms. The applied static magnetic field,  $B_0$ , is chosen to be about 1 mG resulting in a precession of the magnetic moments of both neutrons and  $^3\text{He}$  nuclei at about 3 Hz. The static electric field,  $E_0$ , should be as strong as possible, consistent with stable operation, to give the largest possible shift of the precession frequency relative to that generated by  $B_0$ . The magnetic field should be uniform to 0.1% averaged over each cell volume with a time stability of one part in  $10^6$  over the period of the precession. The electric field requirement is 1% uniformity over the cell volume and  $< 1\%$  shift over the  $\sim 500$  sec measurement period. The basis for these requirements and a specification for E-B is analyzed in the systematic error discussion in Section V.H and is worked out in Ref. 1.

### b. Geometry

In the current design for the target volume (see Fig. V.E.1, and for construction details, section V.G), a single HV electrode is flanked by two parallel ground plates that provide equal and opposite electric fields over the two cell volumes. The static magnetic field is generated by a  $\text{Cos } \Theta$  coil cylindrical magnet, which gives an iron-free configuration and a sufficiently uniform magnetic field. The design also includes a superconducting shield around the target region to exclude external fields. It is planned that the volume within the superconducting shield will be filled with superfluid  $^4\text{He}$  held at a temperature of  $\sim 300$  mK. Here the  $^3\text{He}$ , with nominal fractional density,  $X \sim 10^{-7}$ , will quickly absorb any UCN created.

The geometry of the electrodes and the magnet coil has to be optimized to achieve the required field uniformity over the two cells. Penetrations through both the superconducting shield and the  $\text{Cos } \Theta$  coil are required to bring in various leads:

- a) current leads to the  $\text{cos } \Theta$  coil,
- b) the HV and ground leads to the electrodes,
- c) SQUID leads,
- d)  $^4\text{He} / ^3\text{He}$  fill tubes, and
- e) light pipes that transport scintillation light from the cell walls to the photomultiplier tubes.

The impact of these penetrations on field uniformity has to be evaluated.

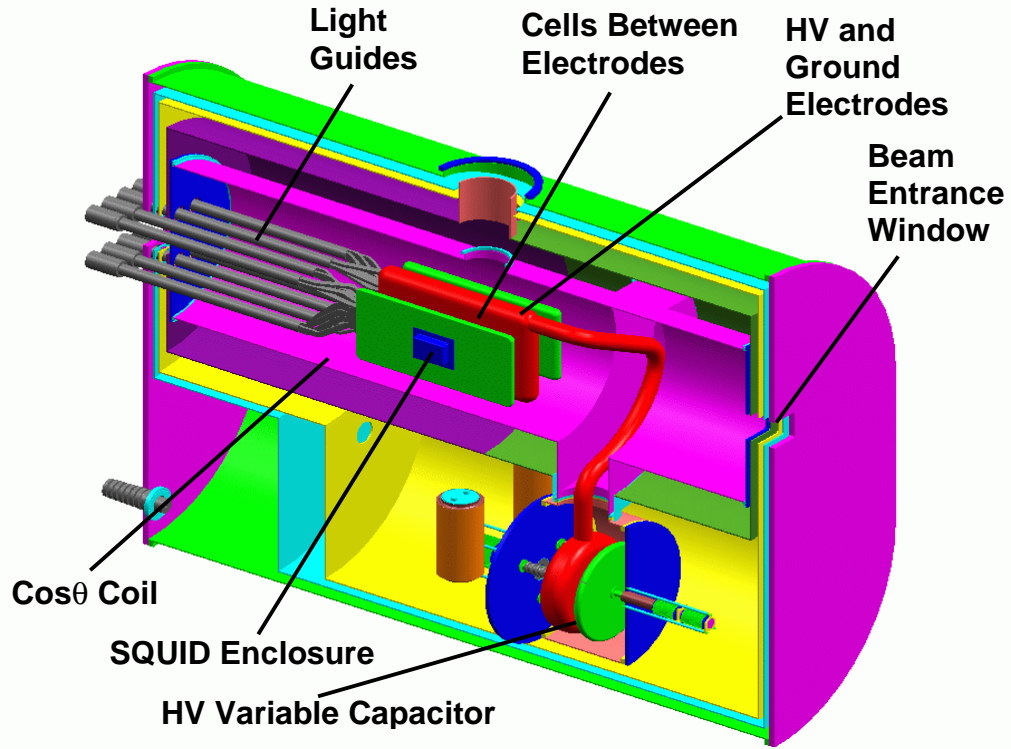


Fig. V.E.1 Design features of the central part of the apparatus including the two neutron /  $^3\text{He}$  cells and the surrounding static electric field electrodes and the magnetic field  $\text{Cos } \Theta$  coil.

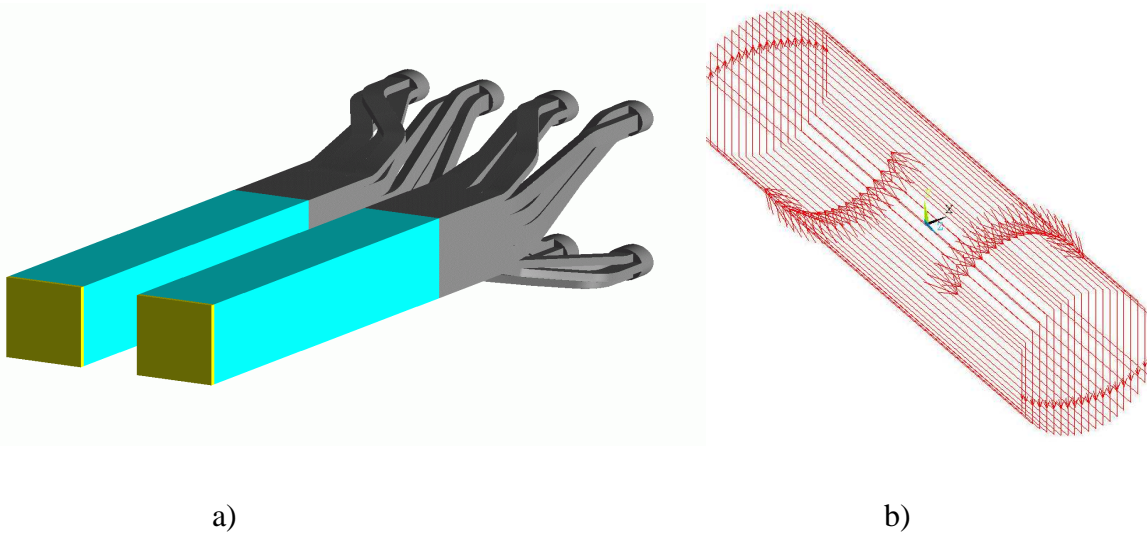


Fig V.E.2 a) design of the two cell system, cell volume  $\sim 4$  l. each. The two matching neutron guides are  $10 \text{ cm} \times 10 \text{ cm}$  (see Section V.A). b) design of the  $\text{Cos } \Theta$  coil cylindrical magnet,  $R_C = 35 \text{ cm}$ ,  $L_C = 200 \text{ cm}$ .

The layout of the two cell geometry and the magnetic field coil are shown in Fig V.E.2. Details of the neutron trap design, shown in Fig V.E.2 a, are discussed in Section V.C of this proposal. The simulation studies described below lead to the specific geometry for the cells, electrodes, magnetic coil, and superconducting shield listed in Table V.E.1.

**Table V.E.1**  
**Nominal Design Parameters**  
(see text for definition of coordinate system)

|                                   |  |                         |   |
|-----------------------------------|--|-------------------------|---|
| <b>Cell(Lucite)</b>               | Interior Size: $l_x = 7.6$ cm                              | $l_y = 10.2$ cm         | $l_z = 50.0$ cm   |
|                                   | Lucite wall thickness 1.3 cm embedded in electrode surface |                         |   |
| <b>Electrodes</b>                 | Size:  | $\text{Gap}_x = 7.6$ cm | $L_y = 24.8$ cm (gnd)<br>$= 29.8$ cm (HV)                                       |
|                                   | Thickness:<br>$\Delta x =$                                 | ground plate<br>5 cm    | $L_z = 76.5$ cm<br>HV plate<br>10 cm<br>ground plate<br>5 cm                    |
| <b>Coil</b> (at ground potential) |  | $R_c = 35$ cm           | Length $L_c = 200$ cm<br>20 loops, 2.5 cm spacing, end loops at 1.25 cm spacing |
| <b>Super-Conducting Shield</b>    |  | $R_s = 45$ cm           | Length $L_s = 210$ cm<br>penetration = 20 cm diam.                              |

### c. Simulation Studies

In order to study the relation of field uniformity to geometry, a series of electric and magnetic field simulation studies [2] were performed using the ANSYS 5.7 Finite Element Modeling Code. A 2-D model was used for the E field and a 3-D model for the B field.

In the following discussion, the z axis is along the horizontal neutron beam direction and the x axis is along the parallel static magnetic and electric fields in the horizontal plane. The y axis is in the vertical direction. The origin was placed at the geometric center of the HV plane, and because of the reflection symmetry, the uniformity of  $B_0$  was tested only in one octant ( $x>0, y>0, z>0$ ) of the overall volume. The  $B_0$  field was evaluated over the eight corners of a rectangular test volume in the above octant. Deviations of the  $E_0$  field were evaluated over a nine point grid within the cell in the x-y plane (at  $z = 0$ ). Many field configurations were studied; one good solution for the  $E_0$  and  $B_0$  fields is shown in Fig V.E.3 and Fig V.E.4 and for the test plane/volume in Fig V.E.5, as discussed below. These results correspond to the design parameters shown in Table V.E.1.

### c.1 Electric Field

The electrostatic analysis used 2D static models, with fixed voltage boundary conditions based on the three electrodes, and the volume containing the LHe (assumed to be at ground potential). A rectangular Lucite double cell, Fig V.E.2.a, was adopted with the Lucite walls recessed into the HV and ground electrodes. The dielectric constant of Lucite [3] is taken to be  $\epsilon = 3.0 \epsilon_0$  (correct for a temperature of -12 C, however it is not known for 300 mK.) The dielectric constant of liquid  $^4\text{He}$  is  $\epsilon = 1.05 \epsilon_0$  [3]. The distribution of electric field strength is shown in Fig.V.E.3 for a nominal HV of 100 kV applied to the center electrode (13.16 kV/cm in the cell and less in the Lucite). The maximum E field is at the edge of the HV plate, not in the target cell, and reaches 18.5 kV/cm in this example. The uniformity of the electric field for this choice of conditions, Table V.E.1, is shown over the test volume in Fig V.E.5.a.

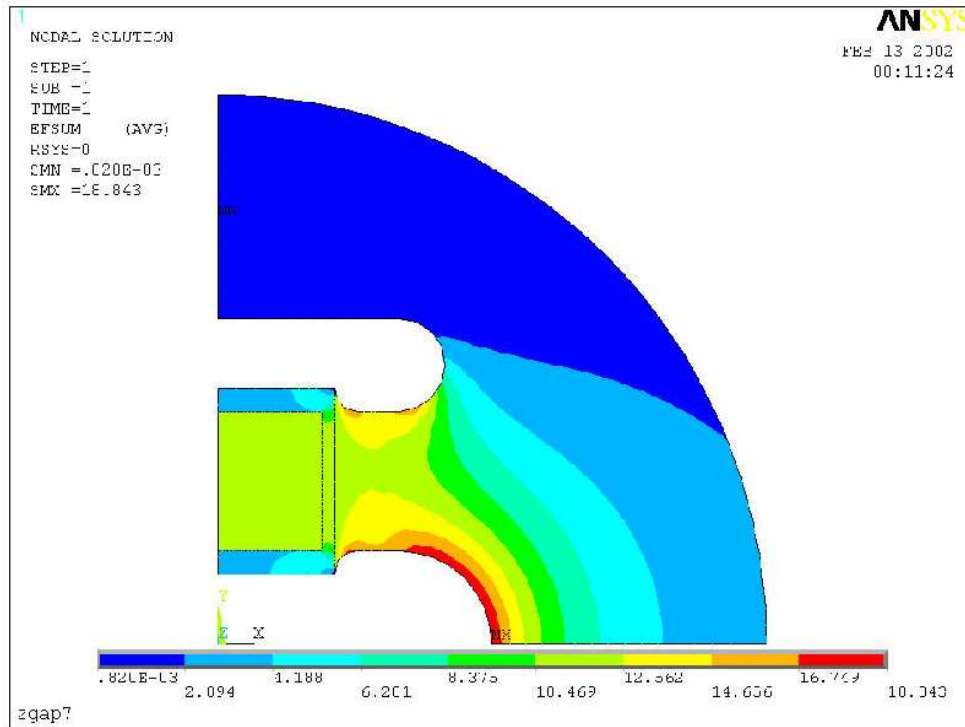


Fig V.E.3 Distribution of electric field strength for the reference design of Table V.E.1.

### c.2 Magnetic Field

The magnetic field calculation was based on an array of 20 coils (with uniform current and a 2.5-cm spacing) in a cylindrical geometry as shown in Fig. V.E.2.b. In the current design, Table V.E.1, the two smallest area coils were shifted to a 1.25-cm spacing. A calculated profile of the  $B_x$  field component, in the octant  $x>0, y>0, z>0$ , is shown in Fig. V.E.4. This

profile is strongly influenced by the radius and length of the superconducting shield. The uniformity of the static magnetic field over the test volume is shown in Fig V.E.5.b.

### c.3 Penetrations

To minimize the impact of the HV connection from the variable capacitor to the HV electrode, only nonmagnetic materials should be used. The connection can penetrate the magnetic field coil by entering parallel to the x axis through the opening in the smallest coil. However, this connection must also penetrate the superconducting shield. Since the magnetic field is very sensitive to the placement of this shield, it was critical to simulate the impact of this penetration. A penetration in the shield (20 cm diam.) has been included in the simulation results discussed below, Figs V.E.5 a and b, and can be seen in Fig V.E.4. (In Fig. V.E.4 the penetration is shown on top, but it is actually on the bottom as seen in Fig. V.E.1.) As shown in Fig. V.E.1, the acrylic light pipes from the cells emerge between the layers of the magnet coil and penetrate through the superconducting shield wall. The latter penetrations have not been included in this simulation. The light pipe design must accommodate the sharp temperature changes and minimize the heat load on the cells as discussed in section V. C.

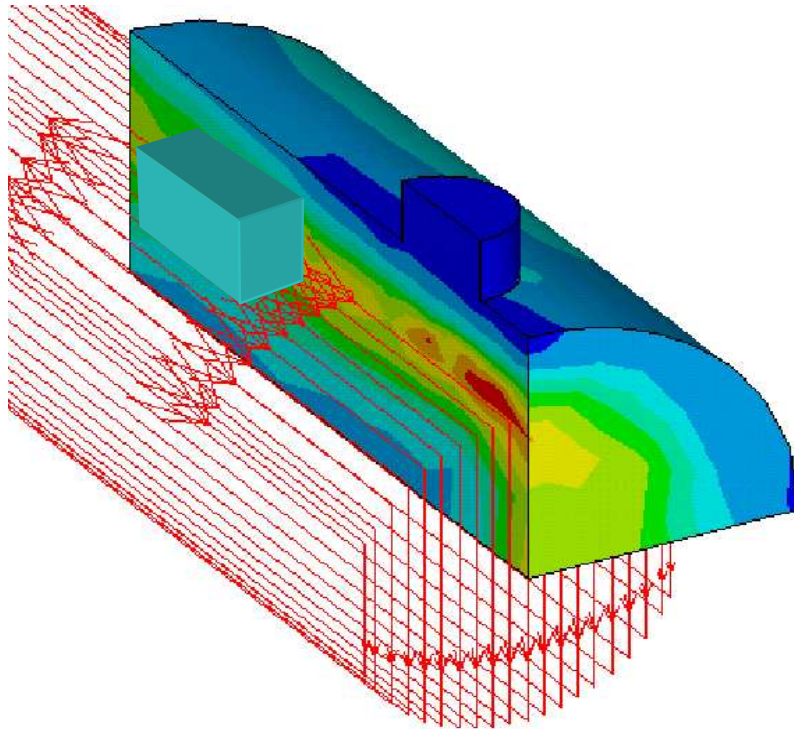
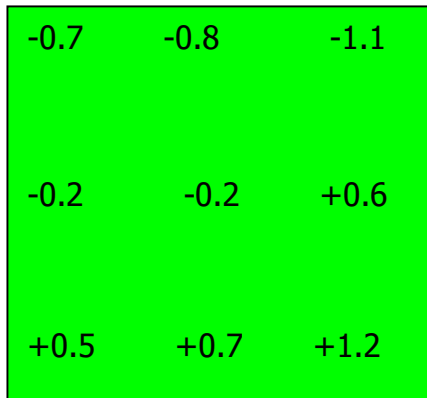
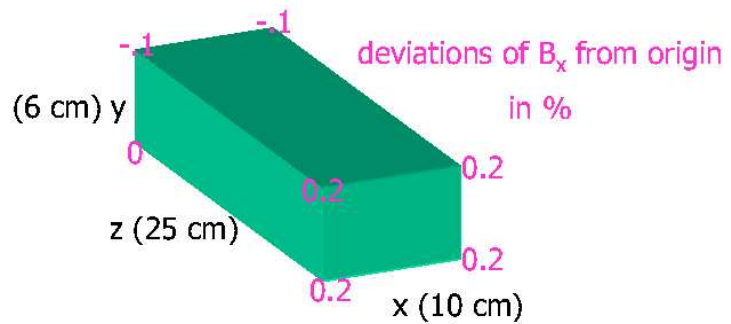


Fig V.E.4 Distribution of magnetic field strength for the reference design of Table V.E.1. The outer cylinder is the superconducting shield with the penetration as shown. The aqua colored rectangle represents the fiducial volume.



a) Electric field test plane (at  $z = 0$ )



b) Magnetic field test volume

Fig V.E.5 Simulation results for tests of uniformity for the static a) electric and b) magnetic fields. The deviations are in units of %.

#### d. Results

Many variations in the geometric parameters were studied. Table V.E.1 summarizes the current optimum choice including the effects of the penetration through the superconducting shield.

The corresponding electric field distribution and test plane results, shown in Figs. V.E.3 and V.E.5.a, indicate that the  $E_0$  field is uniform over the  $z = 0$  plane of the cell to a rms average value of 0.7%. The maximum electric field that must be sustained, is 1.4 times larger than that in the cell and occurs at the edge of the HV electrode.

The uniformity of the B field distribution is shown in Fig V.E.4 and for the test volume is shown in Fig. V.E.5.b. This corresponds to volume averaged rms deviation of 0.15%. These results include the effects of a penetration of the superconducting shield as discussed above.

In conclusion, the design of Table V.E.1 meets the uniformity goals for the static  $E_0$  and  $B_0$  fields adopted for this neutron EDM experiment. Although this design is expected to be further optimized, this study provides an existence proof that the design goals can be met.

Time stability in the E and B fields is crucial to the success of the measurement. The requirement for the E field is  $<1.0\%$  shift over the  $\sim 500$  sec of the measurement. This is discussed in sections V.G and V.H and corresponds to a 1-nA leakage current. This has been achieved in other EDM experiments at higher temperatures. Here operation at 300 mK should improve on this performance measure. Regarding the time stability of the magnetic field, the 1 mG B field generates a precession frequency of 3.0 Hz. The precession frequency shift from the neutron EDM is of the order of  $\sim 3 \mu$  Hz. Thus the B field must be stable to one part in  $10^{-6}$  over one period of the precession ( $\sim 0.3$  sec) or about  $10^{-9}$  G. Typically the coil

requires about 1 mG per mA so a current stability of 1 nA is required. This can be achieved with modern high performance operational amplifiers.

The maximum electric field achievable in this liquid  $^4\text{He}$  environment is expected to be over 10 kV/mm when liquid  $^4\text{He}$  is used as the insulating medium. After a search of the literature, we conclude that knowledge of the maximum field value will have to come from a direct measurement. (Information obtained from the literature for the breakdown voltage for liquid  $^4\text{He}$  is discussed in the V.E Appendix at the end of this section.) A test setup is being built to directly determine the practical limitations of this electric field strength and to investigate long term and short term stability issues. For the  $B_0$  field, the critical issue is the overall uniformity requirement. The B field calculations suggest that the goal of 0.1% can be achieved over cell volumes of 3-5 liters each.

## 2. Kerr Effect-based Measurement of the Electric field

In order to monitor and control the electric field applied to the target cells, a method based on measuring the Kerr effect with optical polarimetry is being developed.

The Kerr effect is the appearance of uniaxial anisotropy in an initially isotropic medium induced by an applied external electric field  $\vec{E}_0$ . The optical axis of the induced anisotropy is oriented along the direction of  $\vec{E}_0$ , and the magnitude of the effect is proportional to  $E_0^2$ . The induced anisotropy of the medium results in the electric field dependence of the refractive index (linear birefringence):

$$\Delta n = n_{||} - n_{\perp} = K\lambda E_0^2 \quad (\text{V.E.1})$$

where  $n_{||}$  denotes refractive index for light with linear polarization direction parallel to  $\vec{E}_0$  and  $n_{\perp}$  - perpendicular to it,  $\lambda$  is the wavelength of the light in vacuum, and  $K$  is the Kerr constant of the medium.

Due to the difference between  $n_{||}$  and  $n_{\perp}$ , an initial linear polarization (with polarization axis directed neither along, nor perpendicular to the applied electric field) of the light passing through the medium, transforms to an elliptical polarization. For input light linearly polarized at  $45^\circ$  to the anisotropy axis, the corresponding ellipticity is

$$\varepsilon = \frac{\pi}{\lambda} l \Delta n = \pi K l E_0^2 \quad (\text{V.E.2})$$

where  $l$  is the path length in the medium. The Kerr effect has very low inertia. The corresponding relaxation time is  $\sim 10^{-11} - 10^{-12}$  sec providing a possibility for very fast measurement of electric field variations.

A possible experimental arrangement for measuring ellipticity of the light, is the so-called “circular analyzer” [4], which consists of a quarter-wave ( $\lambda/4$ ) plate and a polarizing beam splitter (analyzer) with its axis oriented at  $45^\circ$  to the fast axis of the  $\lambda/4$ -plate. A circular analyzer in this arrangement, is sensitive to the outgoing light ellipticity and insensitive to the angle of rotation of the polarization. Reviews of precision polarimetry techniques and discussions of limiting factors can be found in Refs. 5 and 6.

A circular analyzer based experimental arrangement is shown in Fig. V.E.6. The Kerr medium is placed between the polarizer and the analyzer. The electric field is oriented at  $45^\circ$  with respect to the axis of the polarizer. The normalized difference in the light intensities,  $I_1$  and  $I_2$  (in photons per second), in the two arms of the analyzer, is a measure of the electric-field-induced ellipticity of the outgoing light:

$$\varepsilon = \frac{I_1 - I_2}{2(I_1 + I_2)} \quad (\text{V.E.3})$$

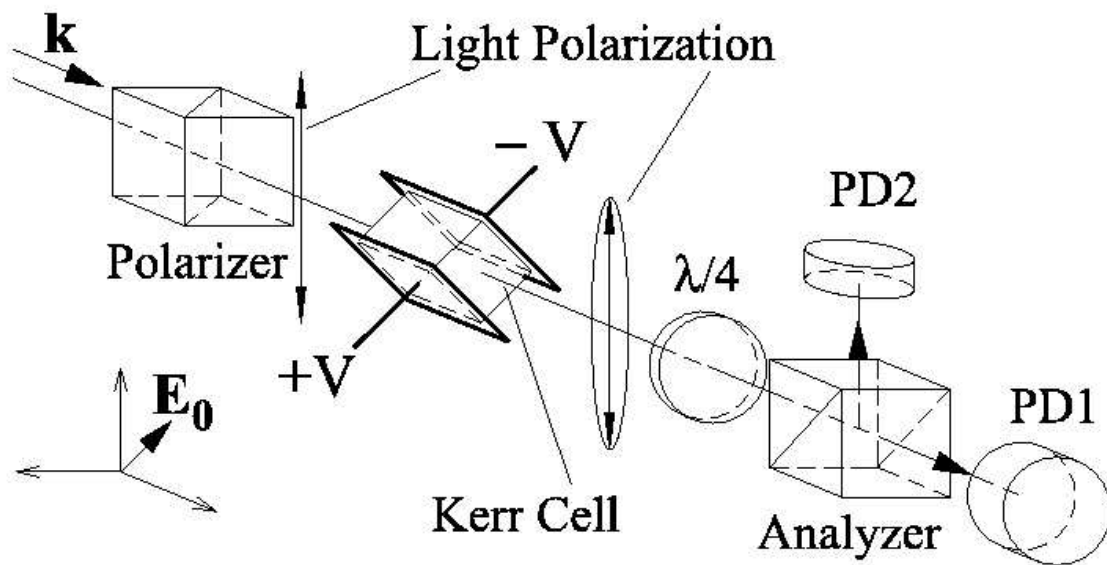


Figure V.E.6. Schematic diagram of an experimental arrangement to measure the Kerr effect.

The shot-noise-limited sensitivity of the polarimeter shown in Fig. V.E.6 is (see, e.g. Ref. 6):

$$\delta\varepsilon \approx \frac{1}{2\sqrt{(I_1 + I_2)T}} \quad (\text{V.E.4})$$

where  $T$  is the data accumulation time. For input light power of a few milliwatts,  $\delta\varepsilon \sim 10^{-8} \text{ rad/s}^{1/2}$ . According to Eq. V.E.2,  $\varepsilon$  is also a measure of the applied electric field. An attractive property of such measurements is the absence of any kind of electric field “probe” or access devices (electrical, mechanical, etc.), except for input/output light access, which can be achieved using simple fiber coupling.

In the framework of the present proposal, there are two choices of the Kerr medium to be used, to measure the high electric field applied to the target cells. First, a few samples made of a Kerr-material can be placed inside the high voltage electrode system but outside the neutron storage cells. An appropriate Kerr material is acrylic which has a large Kerr constant:  $K_A = 3.52 \cdot 10^{-12} \text{ cm/V}^2$  measured at room temperature [7].

The second, and much more attractive possibility is to use the superfluid  $^4\text{He}$  inside the neutron storage cell as the Kerr-active medium. However there is neither experimental nor theoretical published work with data on the Kerr effect in liquid He. Nevertheless a simple estimate of this effect can be performed by using the experimental data available for He gas at room temperature, and by *ab initio* analysis.

In an external electric field  $E_0$ , the induced dipole moment of a He atom is

$$P = \alpha E_0 + \gamma E_0^3 / 6 + \dots,$$

where  $\alpha$  is the scalar polarizability, and  $\gamma$  is the hyperpolarizability of the atom. It is  $\gamma$  that gives rise to the Kerr effect [8]. Room-temperature measurements give  $\gamma = 44.1 \pm 0.6 \text{ au.}$ [9]. For our estimate we assume that this intrinsic atomic parameter,  $\gamma$ , is independent of temperature, and use this value of  $\gamma$ , the density, and the refractive index of LHe to predict:  $K_{\text{LHe}} \approx 1.7 \times 10^{-16} \text{ cm/V}^2$ .

For an electric field of  $E_0 = 50 \text{ kV/cm}$  applied to a 10 cm long sample of LHe, the induced ellipticity is  $\varepsilon = \pi I K E^2 \approx 10^{-5} \text{ rad}$ . With the polarimeter sensitivity of  $\delta\varepsilon \sim 10^{-8} \text{ rad/s}^{1/2}$ , a one second measurement of the electric field,  $E_0$ , gives an accuracy of  $\delta E_0 / E_0 \approx 5 \times 10^{-4}$ . An additional improvement of the sensitivity to the electric field can be achieved using a multipass amplification of the induced ellipticity.

A cryogenic experiment that includes a precise measurement of the Kerr constant of the acrylic (which is considered as a possible material for the neutron storage cells), as well as the Kerr constant of superfluid helium, is in progress at Berkeley.

### 3. RF coil for spin rotation

The function of the “ $\pi/2$ ” RF coil is to rotate the spin orientation of the polarized  $^3\text{He}$  and polarized UCNs from the horizontal ( $x$ ) direction to the vertical direction along the  $y$ - $z$  plane. A static uniform magnetic field,  $B_0$ , along the  $x$ -axis will then precess the  $^3\text{He}$  and the UCNs. In order to accomplish this  $\pi/2$  rotation, an RF coil is turned on to generate an oscillating magnetic field,  $B_{RF}$ , along the horizontal  $z$ -axis;

$$B_{RF}(t) = 2B_1 \cos(\omega_{RF}t) \hat{z}. \quad (\text{V.E.5})$$

Typically, the RF frequency of the coil,  $\omega_{RF}$ , is tuned to the Larmor frequency of the particle to be rotated, namely,  $\omega_{RF} = \gamma B_0$ , where  $\gamma$  is the gyromagnetic ratio of the particle. In order to rotate the spin by  $90^\circ$ , the RF field is turned on for a duration,  $\tau$ , such that  $\gamma B_1 \tau = \pi/2$ .

For this proposed experiment, the RF coil needs to rotate simultaneously the  $^3\text{He}$  and the neutron spins, by  $90^\circ$ . Since the gyromagnetic ratio for  $^3\text{He}$ ,  $\gamma_3$ , is  $\sim 11\%$  higher than the gyromagnetic ratio of the neutron,  $\gamma_n$ , it is not obvious that a suitable RF frequency and pulse duration can be found to accomplish this. In the following we present a numerical solution to this problem.

The linear RF field of Eq. V.E.5 can be expressed in terms of two rotating components:

$$B_{RF}(t) = B_1(-\sin \omega_{RF}t \hat{y} + \cos \omega_{RF}t \hat{z}) + B_1(\sin \omega_{RF}t \hat{y} + \cos \omega_{RF}t \hat{z}) \quad (\text{V.E.6})$$

In a frame rotating counterclockwise at  $\omega_{RF}$  along  $\hat{x}$ , the first field of Eq. V.E.6 would look static while the other would rotate at  $2\omega_{RF}$  for  $B_1 \ll B_0$ . The effect of the counter-rotating field at  $2\omega_{RF}$  on the spin precession can be safely ignored in the so-called “rotating wave approximation.” In this rotating frame, the strength of the static  $B_0$  field appears to be reduced,  $B_0 \rightarrow B_0 - \omega_{RF} / \gamma$ , according to Larmor's theorem. Therefore, the magnetic field in this rotating frame has two components: the first being the  $B_1$  field along the  $\hat{z}'$  axis, and the second being the residual field  $B_0 - \omega_{RF} / \gamma$  along the  $\hat{x}'$ -axis. Note that we use  $\hat{x}'$ ,  $\hat{y}'$ ,  $\hat{z}'$

for the rotating frame. The neutron spin will then precess along the direction  $B_0 - \omega_{RF} / \gamma_n \hat{x}' + B_1 \hat{z}'$ , while the  $^3\text{He}$  spin will precess along the direction  $B_0 - \omega_{RF} / \gamma_3 \hat{x}' + B_1 \hat{z}'$ .

Assuming that the neutron's spin is initially along the  $\hat{x}$  axis, one can readily obtain the following relation for  $t$ , the duration for the RF pulse required to rotate the neutron into the horizontal plane:

$$\cos \omega_n t = -\tan^2 \theta_n . \quad (\text{V.E.7})$$

where  $\omega_n$  is the Larmor frequency of the neutron and  $\theta_n$  is the angle between direction of the total B field and  $\hat{z}'$  for the neutron in the rotating frame:

$$\omega_n = \gamma_n [B_1^2 + (B_0 - \omega_{RF} / \gamma_n)^2]^{1/2} \quad (\text{V.E.8})$$

$$\tan \theta_n = (B_0 - \omega_{RF} / \gamma_n) / B_1$$

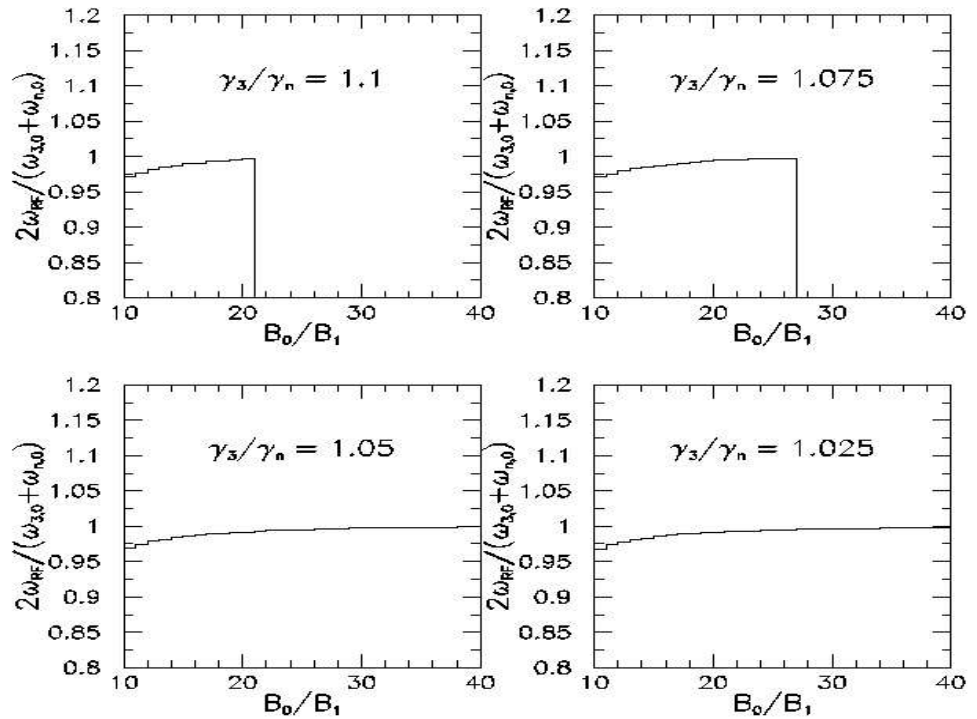


**Figure V.E.7.** Results of the calculations for  $\omega_{RF}$  as a function of  $B_0 / B_1$  for various ratios of  $\gamma_3 / \gamma_n$ .

Expressions analogous to Eqs. V.E.7 and V.E.8 are readily obtained for  $^3\text{He}$ . The appropriate RF frequency for rotating neutron and  $^3\text{He}$  spins simultaneously by  $90^\circ$ , can be obtained by solving the following equation:

$$\cos^{-1}(-\tan^2 \theta_3) = \frac{\omega_3}{\omega_n} \cos^{-1}(-\tan^2 \theta_n). \quad (\text{V.E.9})$$

Figure V.E.7 shows the numerical solutions for Eq. V.E.9.  $\omega_{3,0} = \gamma_3 B_0$  and  $\omega_{n,0} = \gamma_n B_0$  are the Larmor frequencies of the  $^3\text{He}$  and the neutron in the static  $B_0$  field. For  $\gamma_3 / \gamma_n = 1.1$ , a solution exists if  $B_0 / B_1$  is less than  $\sim 21$ . Note that  $\omega_{\text{RF}} \rightarrow \omega_{3,0} + \omega_{n,0} / 2$  as  $B_0 / B_1$  increases.

For this proposed experiment, we can select  $B_0 / B_1 = 20$  and  $\omega_{\text{RF}} = \omega_{3,0} + \omega_{n,0} / 2$ . Assuming  $B_0 = 1$  mG, this implies that the RF coil will have a magnetic field of  $2B_1 = 0.1$  mG with an oscillation frequency of  $\sim 3.165$  Hz and a duration of  $\sim 1.58$  seconds.

## References

- [1] Steve Lamoreaux, *Phy. Rev.* **A53**, 3705 (1996).
- [2] Richard Mischke, Report on ANSYS Model Results, February, March, 2002 ([http://p25ext.lanl.gov/~mischke/edm/edm\\_ppt.html](http://p25ext.lanl.gov/~mischke/edm/edm_ppt.html)).
- [3] Handbook of Chemistry and Physics, The Chemical Rubber Co., Section E.
- [4] S. Huard, *Polarization of light* (Wiley, New York, 1997).
- [5] V. S. Zapasskii and P. P. Feofilov, *Sov. Phys. Uspekhi* **18**(5), 323 (1975).
- [6] G. N. Birich, Y. V. Bogdanov, S. I. Kanorskii, I. I. Sobel'man, V. N. Sorokin, I. I. Struk, and E. A. Yukov, *J. of Russian Laser Research* **15**(6), 455 (1994).
- [7] T. K. Ishii, A. Griffis, *Microwave and Optical Technology Letters* **4**(10), 387 (1991).
- [8] L. W. Bruch, P. J. Fortune, D. H. Berman, *J. Chem. Phys.* **61**(7), 2626 (1974).
- [9] S. C. Read, A. D. May, G. D. Sheldon, *Can. J. Phys.* **75**(4), 211 (1997).

## Chapter V.E Appendix

### High Voltage Considerations

It is important to utilize the maximum electric field achievable in the EDM experiment. Previous experiments have used a field of typically 1 KV/mm. The design goal for this experiment is 5 KV/mm. The feasibility of this goal has been investigated by searching the literature for information on the dielectric strength of liquid Helium. Several measurements have been reported, but typically these are for very small gaps between electrodes. There are no data that match the requirements for this experiment. A reasonable summary of existing data is shown in Fig. V.E.6, which is taken from a paper by J. Gerhold [1].

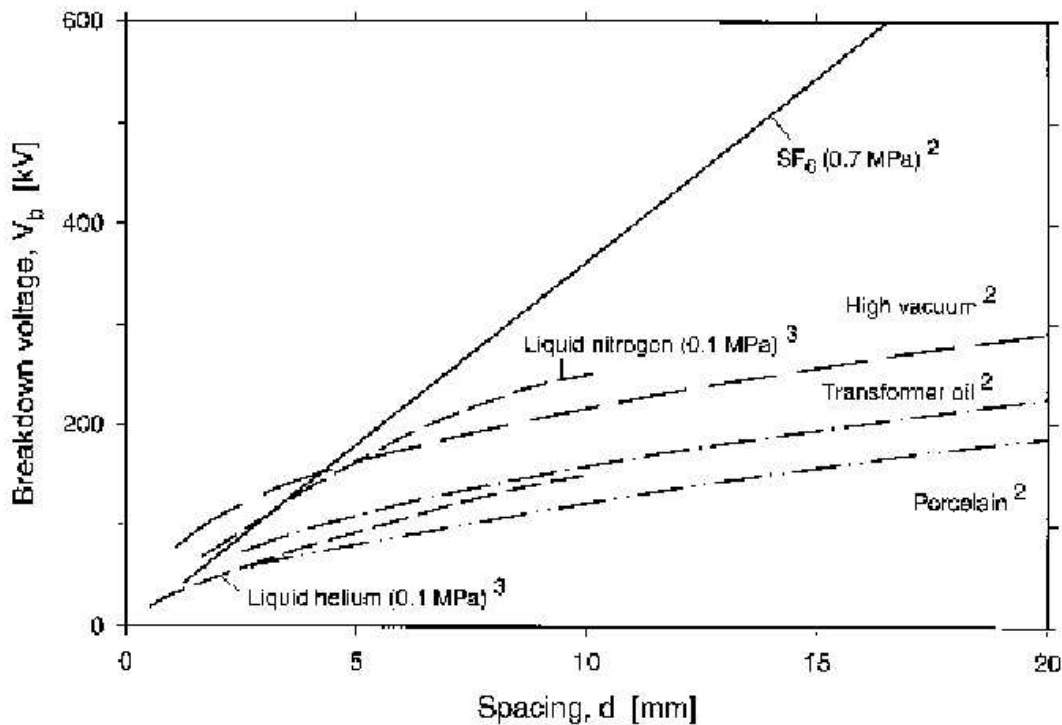


**Figure V.E.6** Breakdown strength of typical solid, cryogenic liquids, and vacuum insulation under D.C. voltage stress in a uniform field.

For very small gaps (under 1 mm), the quoted breakdown strength of LHe is impressive: ~70 KV/mm[2]. However, as seen in Fig. V.E.6, the breakdown strength is only 15 KV/mm for a 1 cm gap. The suggested guidance for extrapolation to larger gaps ( $d$ ) is that the breakdown voltage is proportional to  $\sqrt{d}$ . This implies a value of ~5 KV/mm for a gap of 10 cm, which gives a very small margin of safety for this experiment. Unfortunately, there are additional factors that degrade the breakdown limit. Two of these are time and volume. The measured dependencies from Ref. 1 are shown in Figs. V.E.7 and V.E.8. Again, for this experiment, huge extrapolations are required. The volume in Fig. V.E.7 extends to  $10^5 \text{ mm}^3$  while the volume needed is  $2 \times 10^7 \text{ mm}^3$ .

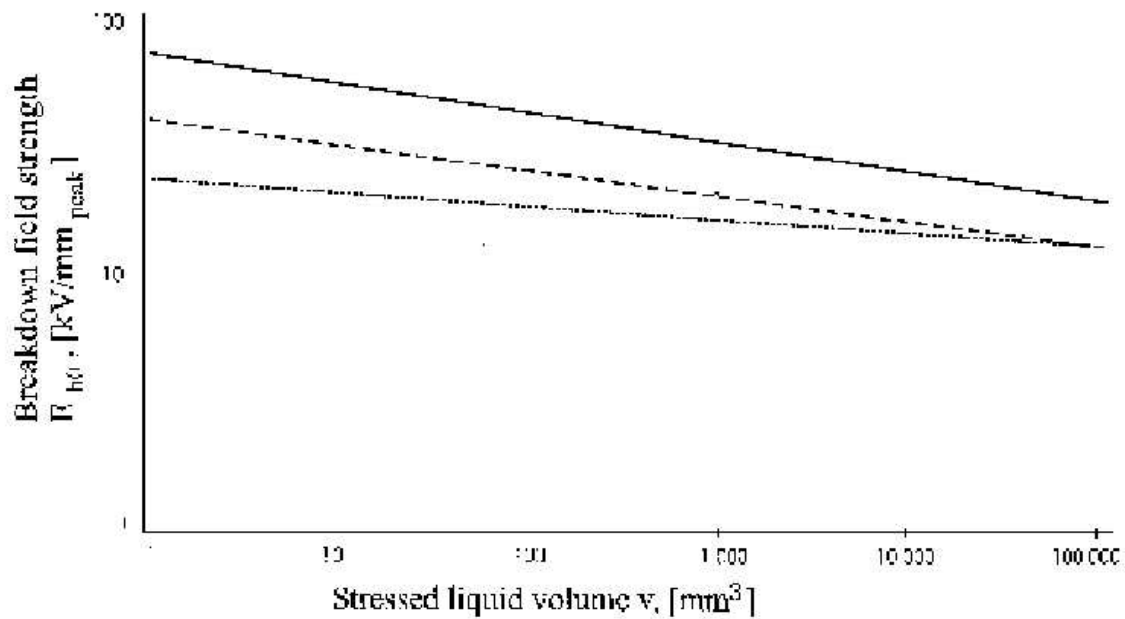


**Figure V.E.7.** Volume effect in liquid helium breakdown. The lowest line is “near zero breakdown probability.”

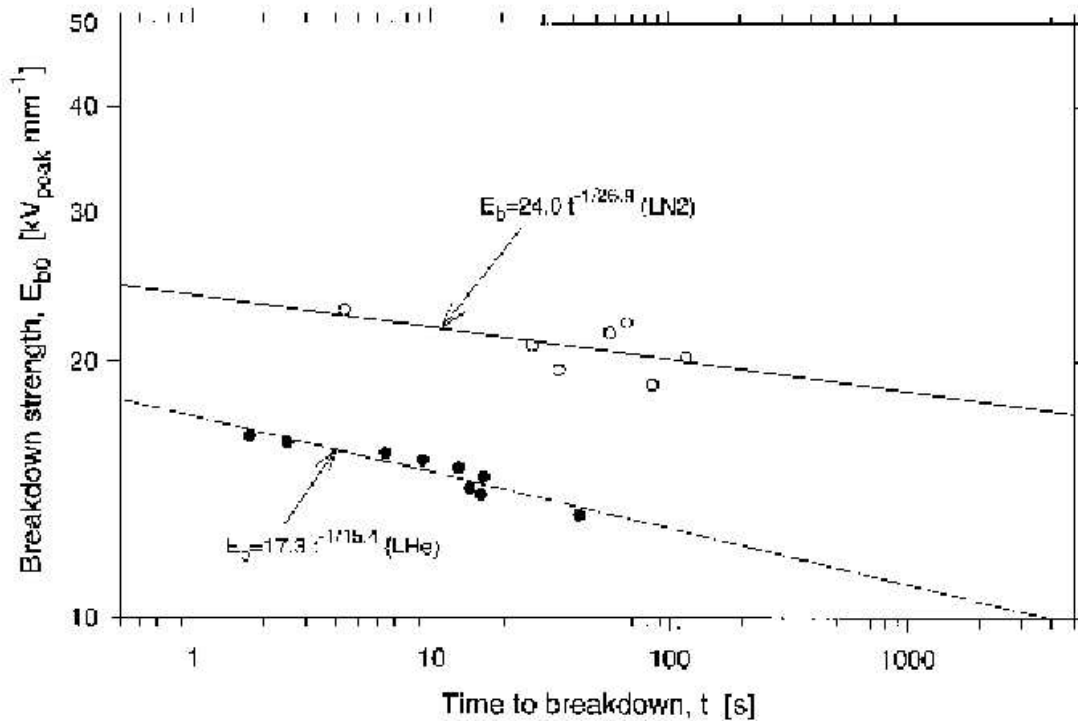


**Figure V.E.8.** Breakdown strength-time characteristics at power frequency in a coaxial cylindrical electrode system; spacing 4.5 mm, cylinder diameter 42.5 mm and length 100 mm.

The data for time to breakdown in Fig. V.E.8 extends to  $\sim 100$  s while the requirement here is for no breakdowns for the duration of the experiment, or  $\sim 10^8$  s because of possible damage to the SQUIDS from a spark.

Naïve extrapolation would lead to predictions for a breakdown strength below that desired for the experiment. However, there is reason for optimism, as Gerhold says that "distinct experimental data are scarce at present, but LHe breakdown much below  $\sim 10$  KV/mm has never been reported." [3] Because of the importance of this topic for the expectations of the experiment and the risks of extrapolation, it is essential that the breakdown strength in LHe be measured directly for the conditions of this experiment.

Another potential issue is the difference in breakdown strength between normal and superfluid He. The measurements displayed in Figs. 1-3 are for normal LHe. In Fig. V.E.9, the breakdown strength for superfluid He is shown [1]. For a gap of 1 mm, the breakdown strength is a factor of 2 below that of normal LHe, but again the behavior for large gaps has not been measured.

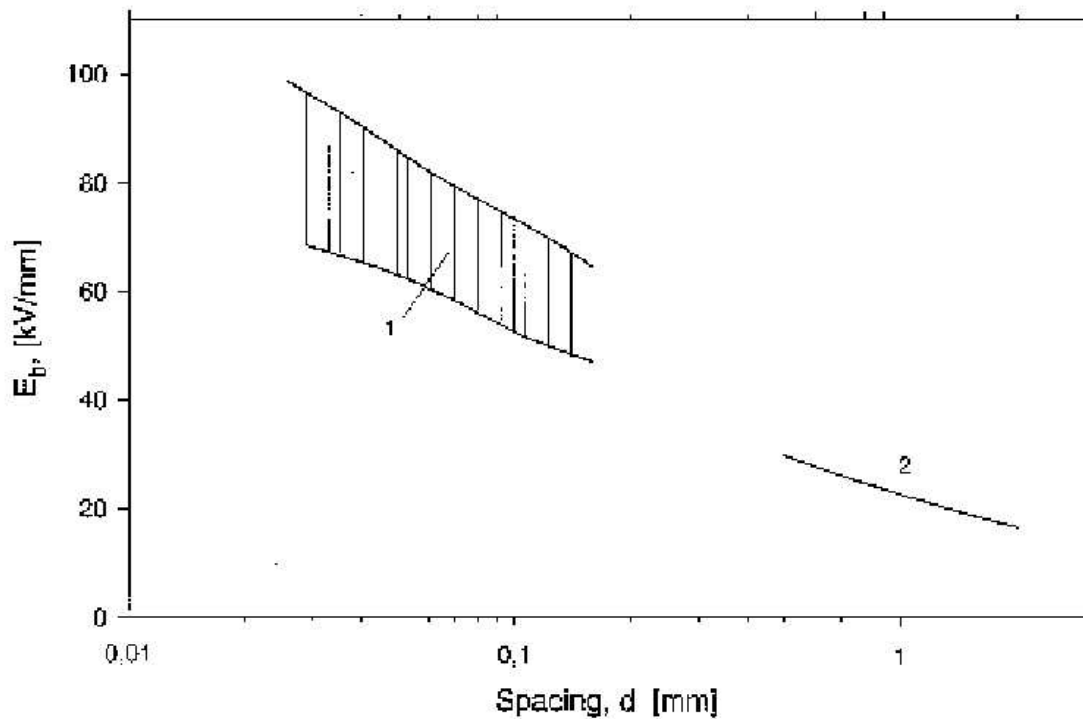


**Figure V.E.9.** Uniform field DC breakdown strength of saturated LHe II near 2.0 K vs spacing.

#### References:

- [1] J. Gerhold, *Cryogenics* **38**, 1063 (1998).
- [2] B.S. Blaisse et al., *Bull. Inst. Int. Froid, Suppl.*, 333 (1958).
- [3] J. Gerhold, *IEEE Trans. on Dielectrics and Electrical Insulation* **5**, 321 (1998).

## Chapter V.F. SQUID Detector Design and Performance

### Introduction

As outlined in Chapter IV, we propose a novel technique of using SQUIDs to directly measure the precession frequency of the  $^3\text{He}$ ,  $\nu_3 = \gamma_{^3\text{He}}B_0$ , which provides a direct measure of the magnetic field,  $B_0$ , averaged over the volume of the cell and the period of the measurement. In addition, appropriately configured SQUIDs could also measure the polarization of the  $^3\text{He}$  introduced into the cell during the filling period, could monitor the orientation of the  $^3\text{He}$  magnetization, and could provide a measure of the stability of the magnetic field  $B_0$  in time. The feasibility of using SQUIDs depends on whether the SQUIDs are sensitive enough under the proposed experimental conditions and whether the signal to noise will be adequate.

### Experimental Requirements and Considerations

The initial concept for the experiment is that there will be a few SQUIDs, coupled to large-area ( $\sim 100\text{cm}^2$ ) pick-up coils, to sample the cell volume. This concept is shown schematically in Fig. V.F.1 and described in Chapter V.G. The upper panel of figure V.F.1 shows a finite element method (FEM) model of the experimental set-up as it is currently proposed. The superconducting vessel contains two test cells (upper and lower cylinders) filled with precessing  $^3\text{He}$ . The pair of coils above and below the test would be connected to SQUIDs. The coils are located away from the test cells to keep them out of the area of high electric field.

The vertically oriented coils will detect the signal from  $^3\text{He}$  as it is precessing. The horizontally oriented coils will be used to measure the initial  $^3\text{He}$  magnetization. The SQUIDs will record the change in magnetic field as the polarized  $^3\text{He}$  are loaded into the cell. This information will enable us to compare the initial magnetization of the  $^3\text{He}$  before data taking and to reduce any systematic error that might be associated with differing  $^3\text{He}$  magnetization between runs. These coils will also provide direct information about the presence of any drifts in the magnetic field. The predicted signals for the vertical coils are shown in the lower panel, along with the expected signals without the external superconducting vessel. The peak-to-peak amplitude is  $\sim 20 \times 10^{-18} \text{ Tm}^2$  or  $.01 \Phi_0$ . The model assumes a configuration with parameters as listed in Table V.F.I. The flux coupled to the SQUID is related to the flux in the pick-up coil by the ratio of the SQUID mutual inductance,  $M$ , to the sum of the input and pick-up coil inductances (see also chapter V.H).

$$\Phi_s = \frac{M\Phi_p}{(L_p + L_i)}$$

Using typical values of  $M = 10 \text{ nH}$  and  $(L_p + L_i) \approx 1 \text{ }\mu\text{H}$  for a large area pick-up coil, the value of flux we expect at the SQUID is  $\sim 10^{-4} \Phi_0$ . The “typical” noise value from a commercial LTS SQUID [1] at 4 K is  $N_{\text{SQUID}} \sim 5 \text{ }\mu\Phi_0/\text{Hz}^{1/2}$ . We expect an additional

decrease in SQUID noise as it scales as  $T^{1/2}$ . The following sections report on experimental work with a large coil to measure the noise level and on measurements of the temperature dependence of the noise. Although the signal increases with coil size, there are also problems associated with large pick-up coils in terms of vibration and other noise mechanisms, which could be avoided by using smaller area pick-up coils. The analysis of Chapter V.H concludes that for a smaller coil the expected signal is  $\Phi = 7.2 A_p \mu\Phi_0$ , where  $A_p$  is the area of the coil in  $\text{cm}^2$ . This implies that adequate signal can be obtained with much smaller coils than in the initial concept.

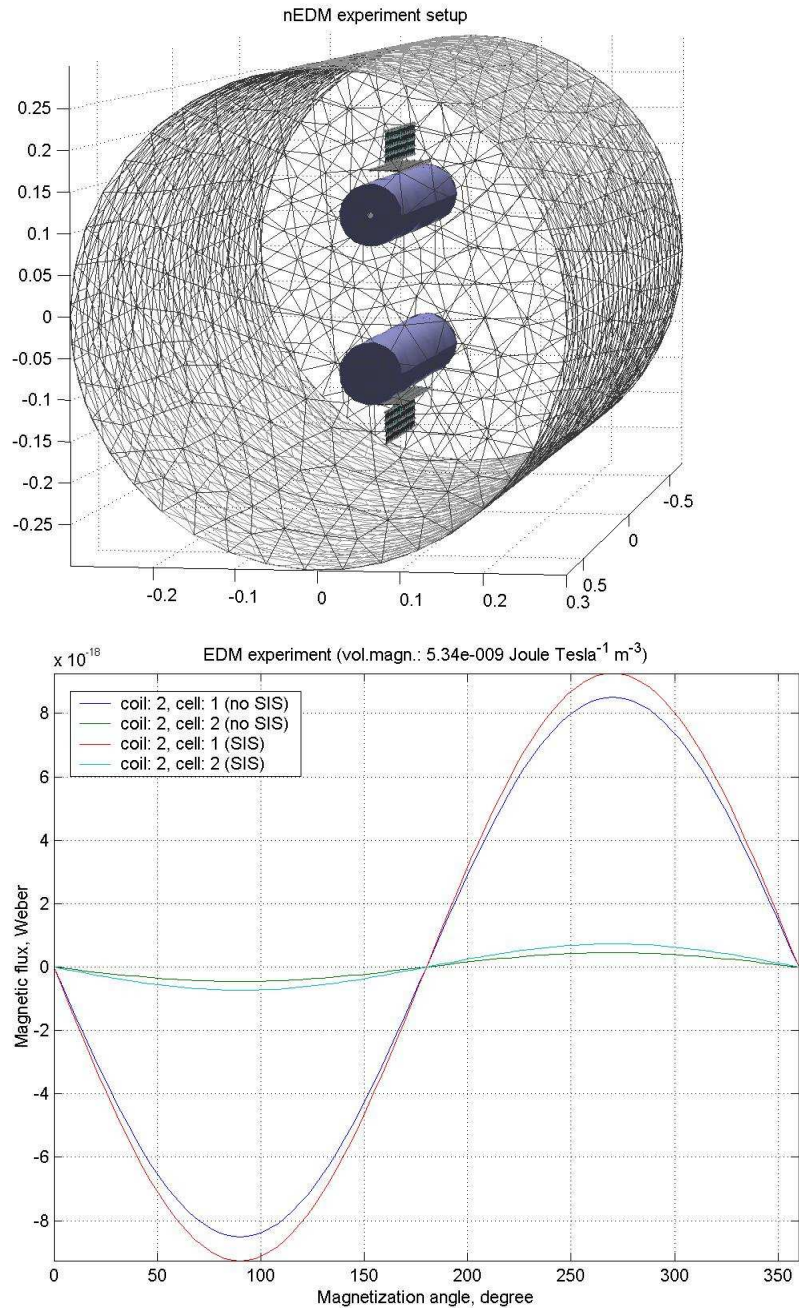


**Figure V.F.1. Upper panel: FEM model of the superconducting vessel, EDM test cells, and SQUID pick-up coils. Lower panel: Predicted values of flux in the vertically oriented pick-up coils expected, both with and without the superconducting vessel.**

**Table V.F.I Parameters for FEM**

| Parameter                        | Value   |
|----------------------------------|---|
| <b><i>SIS Cylinder</i></b>       |   |
| Length                           | 1.34 m  |
| Radius                           | 0.3 m   |
| <b><i>Target cells</i></b>       |   |
| Length                           | 0.5 m   |
| Inner Radius                     | 0.04 m  |
| Center from SIS axis             | +/- 0.1 m   |
| Magnetization                    | $5e^{-9}$ J/(Tm <sup>3</sup> ) assuming $1.25e^{15}$ <sup>3</sup> He/cell |
| <b><i>SQUID pickup coils</i></b> |   |
| Length                           | 0.25 m  |
| Width                            | 0.04 m  |
| Center from SIS axis             |   |
| Coils #1,3 (Horizontal)          | +/- 0.145 m   |
| Coils #2,4 (Vertical)            | +/- 0.175 m   |

**Superconducting test cell**

To investigate whether or not we could achieve the desired SQUID noise level,  $N_{SQUID} \sim 5 \mu\Phi_0/\text{Hz}^{1/2}$ , with the large pick-up coils attached, we built a lead test cell 8 in. in diameter and 4 in. high that resembled the proposed EDM apparatus. We then carried out a series of experiments [2] that achieved a noise level of  $\sim 15 \mu\Phi_0/\text{Hz}^{1/2}$  at 10 Hz, the expected amplitude of the <sup>3</sup>He precession signal. We noted that, despite the large superconducting shield, at frequencies below 100 Hz we still observed noise from vibrations and external sources in the laboratory, implying that great care will be required to shield the system and prevent the large pick-up coils from vibrating. The modulation technique of the electronics may also have prevented us from reaching the intrinsic SQUID noise level. This method averages over many working points of the SQUID, not all of them optimal.

**Two-Squid readout technique**

To improve the noise performance of our system, we developed a two SQUID read-out technique in parallel with the above experiments; the results are also presented in [2]. With the two-squid (picovoltmeter) system we measured a noise power spectrum with a white noise level of  $3 \mu\Phi_0/\text{Hz}^{1/2}$  down to frequencies  $\sim 1$  Hz, which is a factor of 5 improvement

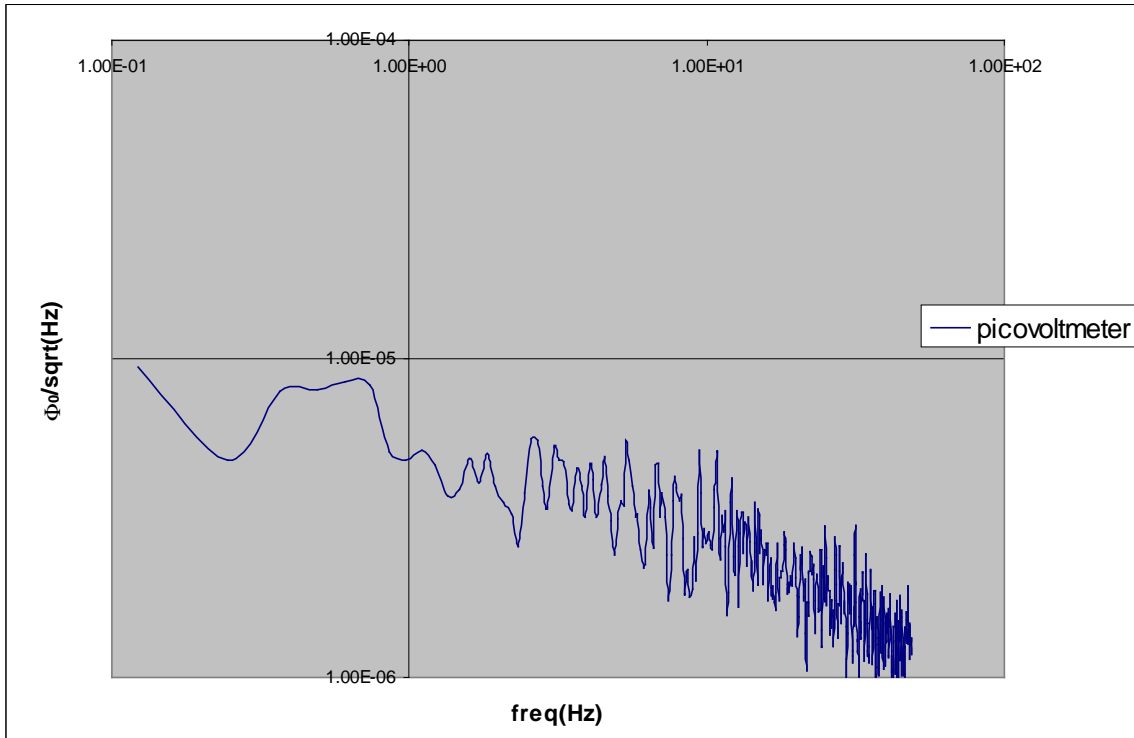


**Fig. V.F.2. SQUID noise as a function of frequency.** The data were taken with the picovoltmeter inside a superconducting shield and a small-area pick-up coil with the same inductive load as the large-area coil (see text). At the frequency of interest, 10 Hz, the noise was  $3 \mu\Phi_0/\text{Hz}^{1/2}$

over that achieved with the conventional magnetometer in the lead test can. This white noise level was achieved at lower frequencies due to the better shielding of the probe and because we used a smaller area pick-up loop. The loop provided the same inductive load as the large-area coil,  $\sim 1.4 \mu\text{H}$ , but was much less sensitive to ambient noise. Figure V.F.2 shows the results of the picovoltmeter noise measurements. The issue of the coupling of ambient noise to the SQUIDs when they are connected to the large-area pick-up coils still needs to be fully addressed, and will be re-visited in our discussion of noise sources.

### Studies of Temperature Effects

Because of the importance of achieving the predicted noise behavior, we undertook a series of tests of the effects of temperature on SQUID noise. Previous studies of SQUID noise as a function of temperature report that white noise scales as  $T^{1/2}$  [3,4], but with  $1/f$  noise the behavior with temperature can be very unpredictable [5]. Figure V.F.3 shows a schematic drawing of the picovoltmeter. The experiments were performed at the National High Magnetic Field Laboratory at Los Alamos in a pumped  $^3\text{He}$  refrigerator able to attain temperatures down to 0.3 K. The picovoltmeter SQUID was located in section of the probe that was maintained at 4 K. The SQUIDs under test were located in the tip, which could range from 4 K to 0.3 K. A superconducting lead shield surrounded both the picovoltmeter and test SQUIDs.

*Noise vs. Temperature Measurements for a Quantum Design SQUID*

V- $\Phi$  curves at various bias currents were measured for a Quantum Design SQUID (model 50) at temperatures from 0.3K to 4K. These curves were measured both with the input coil open (no load attached to the SQUID) and with a 1  $\mu$ H pickup coil. We recorded the power spectral density of the SQUID voltage noise at points along the V- $\Phi$  curve where the slope of the V- $\Phi$  curve,  $\Delta V/\Delta\Phi$ , was steepest. The SQUID's flux noise was calculated by the formula  $N_{\text{SQUID}} = V_n(\Delta\Phi/\Delta V)$ , where  $V_n$  is the measured voltage noise. The noise values recorded were for the white component of the voltage noise. Some of the data summarized below are also presented in more detail in [6].

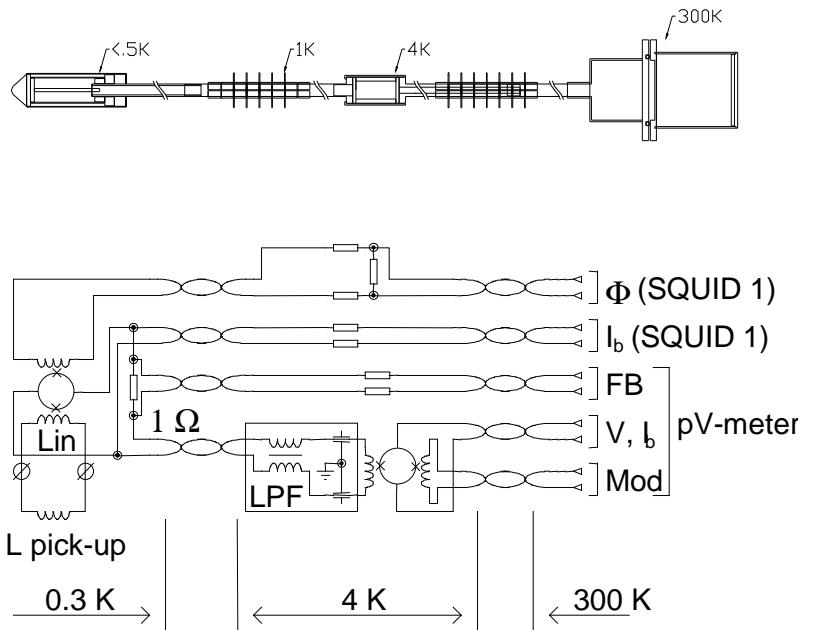


**Fig. V.F.3. Schematic drawing of picovoltmeter probe.**

We were primarily interested in how the SQUID noise changes as a function of temperature. We expect that the flux noise squared,  $N_{\text{SQUID}}^2$ , should scale linearly with temperature. In Fig. V.F.4 we show a plot of  $N_{\text{SQUID}}^2$  vs. temperature for the SQUID with the pickup coil (upper) and with the input left open (lower). The data are lowest values of  $N_{\text{SQUID}}$  for each particular temperature. The solid lines are a linear fit to the data,  $N_{\text{SQUID}}^2 = a \cdot T + b$ . The flux-noise energy exhibits the characteristic linear dependence on T, however the slope is slightly different for the two curves. The slope is  $a = 0.81$  for the SQUID with a pickup coil and  $a = 1.00$  for the open SQUID. For the open SQUID the intercept term (excess noise energy at  $T = 0$ ) is  $b = 0.08$ , while for the SQUID with a pickup coil, it is  $b = 0.61$ . This excess noise energy behavior has been seen before [6] and was found to be due to either the SQUID chip materials, or the material the SQUID was mounted on. In our case the excess noise is very small for the SQUID with no load. However, when the pick-up coil is attached we see an overall increase in noise. We believe that the greatest contributor to the increased noise is due to Johnson noise from the materials on which the SQUID is mounted, is now being coupled into the pickup coil. At certain frequencies we also saw noise from mechanical vibration. The issue of vibration will have to be a serious consideration in the actual experimental design.

For a comparison of the flux noise from the picovoltmeter technique vs. the conventional modulation readout electronics, we measured the noise at 4 K for both cases, with a pickup coil attached. The noise for the conventional electronics was  $3.5 \mu\Phi_0/\sqrt{\text{Hz}}$  while for the

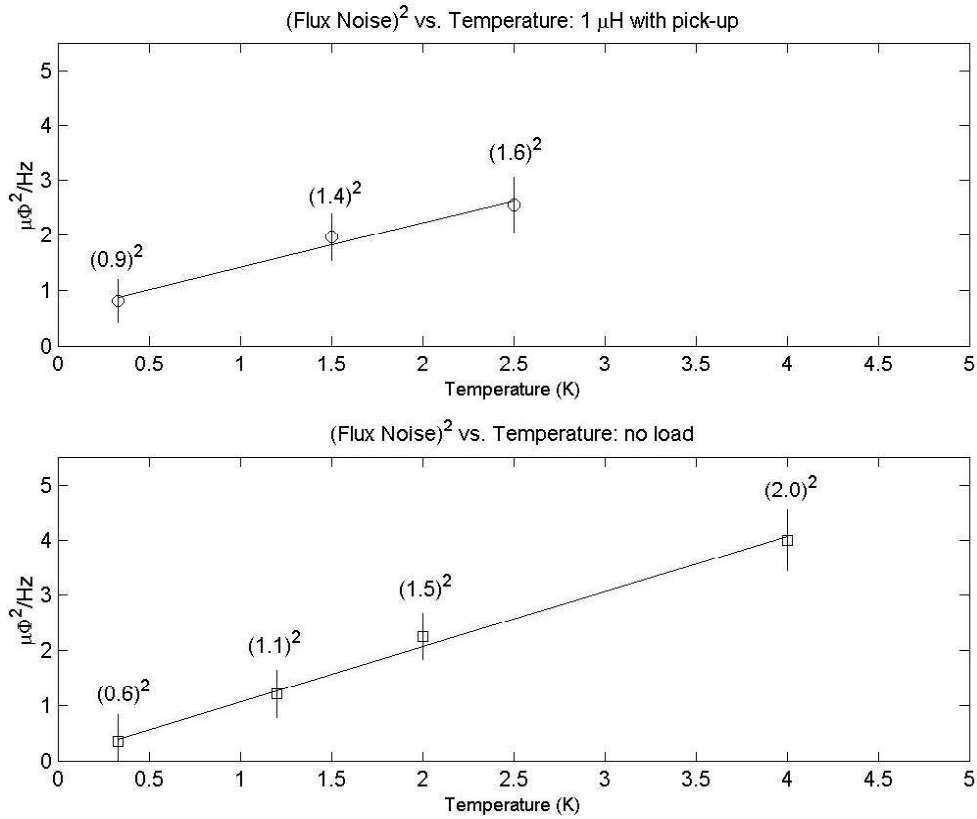


**Fig. V.F.4. Plots of flux noise squared vs. temperature. The data are the best values at each temperature. The solid lines are a fit to the expression  $\Phi_n^2 = a \cdot T + b$ . Upper: SQUID with a 1  $\mu\text{H}$  pickup coil. Lower: SQUID with no load.**

picovoltmeter it was  $1.8 \mu\Phi_0/\sqrt{\text{Hz}}$ . It should be noted that this measurement was made on a slightly different probe than the other noise measurements presented.

#### *Noise vs. Temperature Measurements for a Conductus Mag8 Magnetometer*

Noise vs. temperature measurements were also made for a Conductus Mag8 magnetometer [1]. The difference between the magnetometer and the Quantum Design SQUID is the area of the pick-up loop. The Quantum Design SQUID is made to attach an external pick-up loop of the user's design such as the  $100 \text{ cm}^2$  loop. However, one should note that the effective area of the  $100 \text{ cm}^2$  loop is only  $100 \text{ mm}^2$  because the coupling is not ideal. The magnetometer has an integrated pick-up loop with an effective area of  $\sim 2.5 \text{ mm}^2$ . The loss in signal would be a factor of 40. However an advantage of using a magnetometer is that with the smaller pick-up loop, the SQUID measurements are less likely to be contaminated by noise due to vibrations. Since the pick-up area is much smaller, one would have to use an array of such devices to achieve the required signal-to-noise for the experiment. Present SQUID systems for brain imaging use arrays of many hundreds of SQUIDs.

The behavior of SQUID noise as a function of temperature for the Mag8 is shown in Fig. V.F.5. The data are still preliminary, but the expected behavior with temperature is again

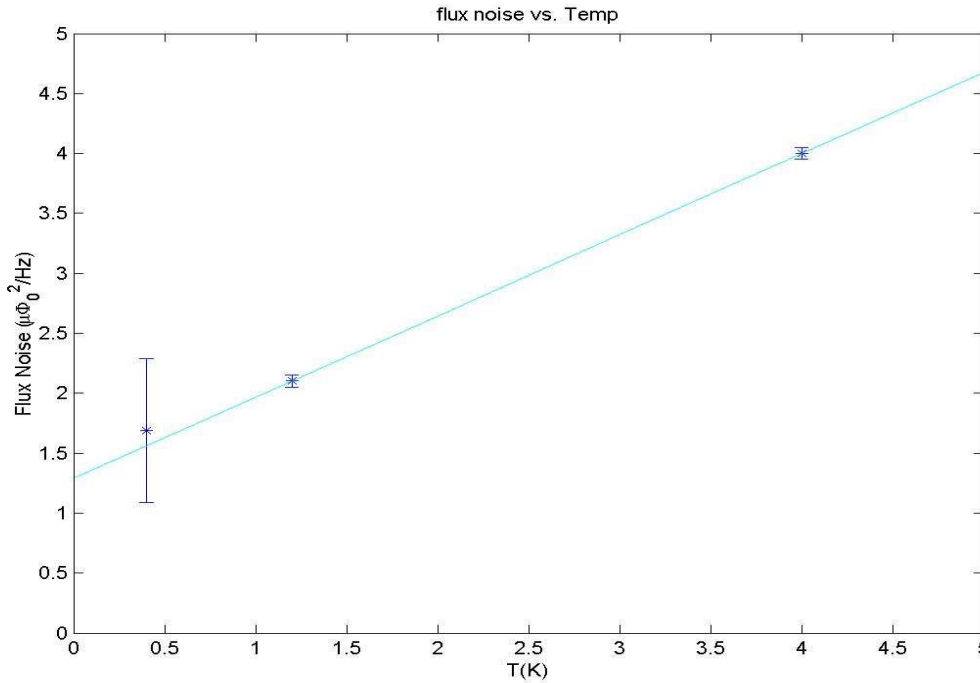


**Figure V.F.5.** Plots of flux noise squared vs. temperature for a magnetometer. The data are the best values at each temperature. The solid lines are a fit to the expression  $\Phi_n^2 = a \cdot T + b$ .

seen. The solid line is a best fit to the expression  $N_{SQUID}^2 = a \cdot T + b$ , with  $a = 0.68$  and  $b = 1.29$ .

### External Noise Sources

It is anticipated that the most critical issue for using SQUIDs to measure the  $^3\text{He}$  precession signal successfully will be keeping noise sources at the frequency of interest to an acceptable level. Experimental noise sources of concern are vibrations of the SQUID pick-up loop in the  $B_0$  field, the magnetic fields due to leakage current from the high voltage plates, Johnson noise from non-superconducting elements, magnetic noise from power lines and electrical equipment leaking into the superconducting shield through penetrations, and non-uniformity in the  $B_0$  field.

To address the issues of noise sources in the experiment, many studies will take place throughout the entire design and development of the EDM experiment. A simple set of experiments to measure environmental noise in the experimental hall were conducted during the run cycle in December 2001. Three HTS SQUIDs were placed in a temporary dewar and background noise levels were measured. This represents a “worst-case” measurement, since the SQUIDs had no shielding and were HTS devices, with inherently

worse noise performance than helium cooled devices. The data are currently being analyzed.

As the design of the cryostat and superconducting shield for the experiment are developed, tests can be conducted to study the effects of penetrations and how to defeat them (i.e. 90° bends or other ways to “choke” field before it enters the superconducting vessel). These tests do not require the ultra-low temperature or the presence of the polarized  $^3\text{He}$ . Tests such as these can be made at every stage of the design of the shield. The effectiveness of different designs of the superconducting shield with penetrations might possibly be modeled using commercially available software such as Elektra [7] or with the finite element model.

Some of the effects of vibration can be tested with the existing lead can developed for SQUID noise measurements. When the coils used to produce the magnetic holding field,  $B_0$ , have been built, we can test again. Also, the SQUIDs can be used to test the stability of the field produced by the  $B_0$  coils. We anticipate that if we can use the small area magnetometers, the problem of vibration in an external field will be greatly reduced.

All materials proposed to make the cell can be tested with a simple SQUID set-up to see if they are suitable. The materials can be placed inside the existing lead can and their noise measured by SQUIDs. It is possible to try and calculate the B-fields expected from leakage currents, but they can be measured without beam etc. as soon as the high voltage plates are in place.

## Conclusions

Initial work has shown that obtaining SQUIDs with sufficient sensitivity will not be an issue. We have also recently demonstrated that the SQUID noise will scale with temperature as  $T^{1/2}$  for a variety of SQUIDs available to us. Thus we expect an improvement in SQUID performance from our laboratory tests at 4 K to the real experiment at 0.3 K. All of our initial work has confirmed our suspicion that ambient noise will be our greatest problem. In particular, vibration appears to be a large problem. One way to mitigate the effects of vibration is to use an array of SQUIDs with small-area pick-up coils instead of a few SQUIDs coupled to large-area coils. The suitability of this technique is currently under study. Another method to reduce ambient noise effects would involve using SQUID gradiometers, this method is also presently being investigated.

Many of the sources of experimental noise that are detrimental to the SQUIDs would need to be addressed anyway in the context of other experimental techniques. In addition, SQUIDs provide many other useful pieces of information to the experiment and its design. SQUIDs can be used to record the initial magnetization (during the fill of the  $^3\text{He}$  atoms), reducing the systematic error. SQUIDs can be used to keep track of the stability of the magnetic holding field  $B_0$ . At many points during the experimental design the SQUIDs can

be used as diagnostics and to provide feedback about suitability of the experimental design.

### References

- [1] Conductus, Inc., 969 West Maude Avenue Sunnyvale, CA 94085 USA
- [2] M. A. Espy, A. Matlashov, R. H. Kraus, Jr., P. Ruminer, M. Cooper, S. Lamoreaux, IEEE Trans. Appl. Supercond., Vol 9, No. 2, June 1999, pp. 3696-3699.
- [3] F. C. Wellstood, C. Urbina, and J. Clarke. Appl. Phys. Lett. 54 (25), June 1987.
- [4] C. D. Tesche and J. Clarke, J. Low Temp. Phys. 29, 301 (1977).
- [5] F. C. Wellstood, C. Urbina, and J. Clarke. Appl. Phys. Lett. 50 (12), March 1987.
- [6] M. G. Castellano *et al.*, Il Nuovo Cimento 15C, 2, March-April 1992.
- [7] Vector Fields, Inc. 1700 North Farnsworth Avenue, Aurora, IL 60505, USA

## V.G EDM Experimental Apparatus

### Overview

The neutron EDM measurement described in this proposal involves a series of carefully orchestrated interactions and measurements that must be engineered into a complicated apparatus. We briefly describe here the main features of the measurement process that drive the design and then give a detailed description of the experimental apparatus that can achieve the goals of the experiment.

There are many requirements needed for the experiment, and some of these requirements are given in what follows to illustrate the engineering challenge. The sensitivity of EDM experiments depends linearly on the electric field. The separation between the two cells and the horizontal size of the cells is set to achieve the maximum field. The uniformity requirement for the electric and magnetic fields across the measurement cells determine the overall dimensions of the target-region cryostat. The combination of these dimensions and the space occupied by the  $n+p \rightarrow d+\gamma$  experiment place significant constraints on the beam line. A number of systematic effects are suppressed at temperatures below the reach of a  $^3\text{He}$  refrigerator; hence the selection of a dilution refrigerator (DR). The inevitable depolarization of the  $^3\text{He}$  requires that a cycling system for removing the  $^3\text{He}$  and introducing freshly polarized  $^3\text{He}$  be incorporated into the cryogenics system. The reduction of backgrounds from neutron-capture places constraints on the materials used in construction of the components. The SQUIDs for measuring the  $^3\text{He}$  precession must be placed close to the measuring cells. The SQUIDs need isolation by a superconducting shield from external magnetic noise. All these requirements lead to a grand compromise in the engineering of the apparatus. While still in development, the description that follows is an example of how the compromise will be reached.

Figure V.G.1 shows the reference 3D-layout of the EDM experiment with the beam entering from the right. The major components are as follows:

- the beam line, including the Bi filter and the beam splitter-polarizer
- the target cells
- the cryostat, including the target cryostat, upper cryostat and DR
- the helium purifier
- the high-voltage (HV) generator
- the polarized  $^3\text{He}$  source
- and some other elements.

## Beam Line

The EDM experiment will be installed on LANSCE flight-path 12 immediately downstream of the  $n+p \rightarrow d+\gamma$  experiment (see Section V.A). Gamma rays in the transmitted neutron beam will be removed with a Bi filter that will be installed in the downstream end of the  $n+p \rightarrow d+\gamma$  cave. In addition, the beam stop will be modified to accept the  $t_0$  chopper and one end of the beam splitter-polarizer. The shielding will be configured such that the radiation level outside of this region will be less than 1 mR/hr. The Bi filter, Fig V.A.6, consists of water-quenched Bi shot in a 150-mm x 150-mm x 200-mm (beam direction) block cooled to ~15 K by a 10-watt (at 20 K) cold-head refrigerator. Thin beryllium foils will serve as windows and cryogenic heat shields for both the bismuth filter and the cryogenic apparatus if backgrounds from the filter pose a problem.

The  $t_0$  chopper will be very closely related to existing devices already in use at LANSCE. Its function was described in section V.A, and it will be placed in the  $n+p \rightarrow d+\gamma$  beam stop.

Upstream of the EDM experimental apparatus, the neutrons are split into two polarized neutron beams (see Section V.A.) The polarizers are arranged to form two walls 100-mm high x 1700-mm long and are installed in the neutron guide at  $1.6^\circ$  relative to the beam direction. Polarizers also line the walls as discussed in Section V.A. The resulting polarized split neutron beams emerge at  $3.2^\circ$  relative to the beam direction and are allowed to separate until they match the separation of the two downstream target cells. In this way the irradiation of the HV electrode is minimized. Supermirror guides, 75 mm x 100 mm in cross section, transport the neutrons to the cells.

## Target Cells

Our design has two cells to minimize the systematic error caused by the pseudo-magnetic field (see section V.H.) The organization of the target region is shown in Fig. V.G.2. The two beams of neutrons irradiate a pair of target cells sandwiched between three hollow electrodes (see Sections V.C and V.E). The two target cells have inside dimensions of 76.2-mm wide x 101.6-mm high x 500-mm along the beam direction and a volume of ~3.8 liters each. The target cell walls are 12-mm acrylic and act as light guides. The entrance and exit windows are made of 6-mm deuterated acrylic. All inner surfaces of the target cells are coated with a deuterated wave shifter. The target-cell light

guides are connected to special light guide assemblies that connect to room temperature photo-multiplier tubes.

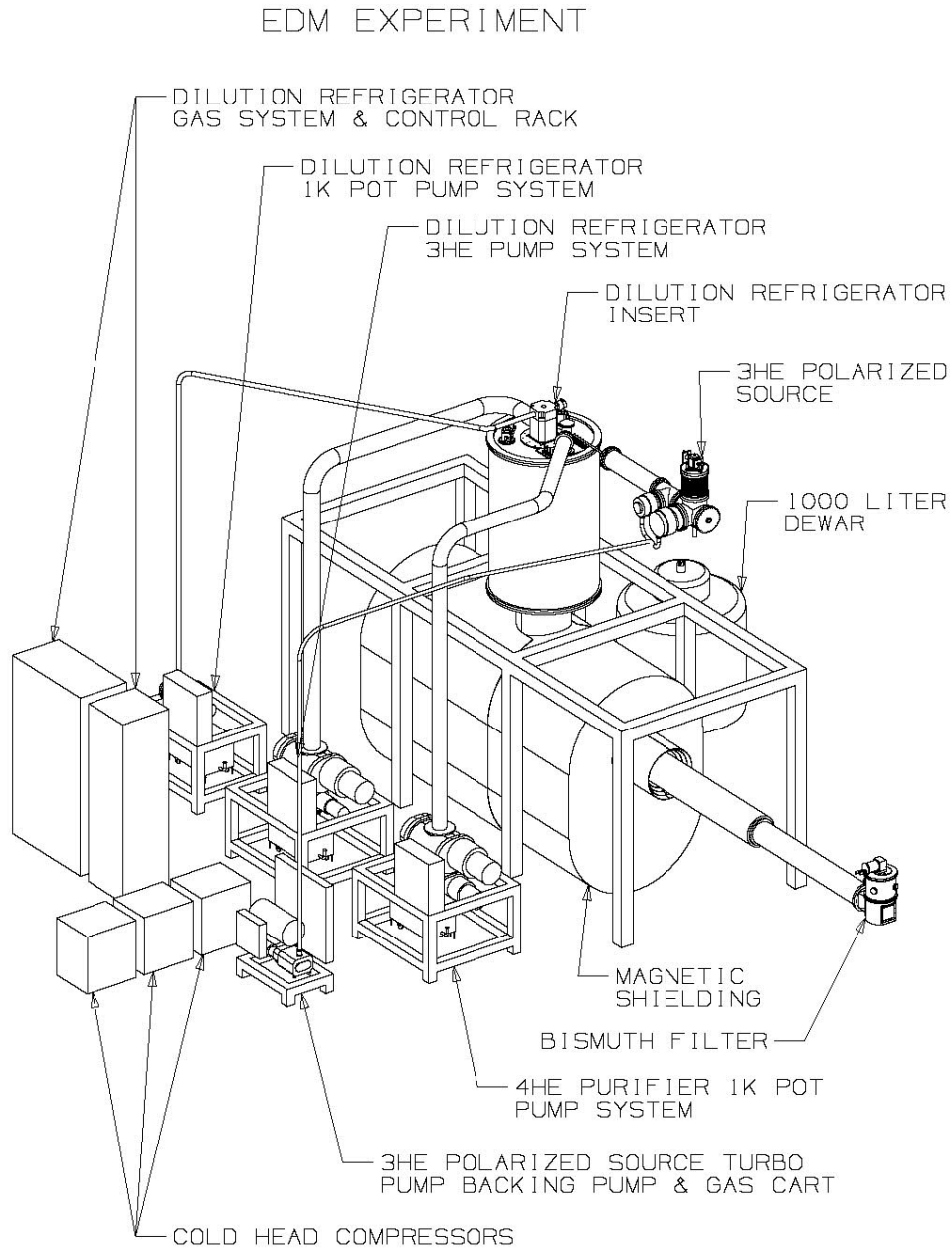


Figure V.G.1. Overall layout of the EDM experiment. The main structure is 2.5 m wide, 5 m high, and ~ 6 m long. The neutron beam guide is 1.4 m above the floor.

Inside the cryostat, the beams are collimated with a structure that is thermally anchored to the heat shields. The choice of materials for the beam collimators is important to minimize activation of the target region.

Each target cell sits between and is embedded in a ground electrode and the high voltage electrode as shown in Fig. V.G.3. The dimensions of the electrodes were set by the field uniformity requirements as set forth in Section V.E. The ground electrode is an acrylic shell 250-mm wide, 38-mm thick, and 715-mm along the beam direction. The side facing the HV electrode has a 25-mm radius on the outer edges and a pocket at the center to accept the target cell. A second pocket is located on the opposite side of the ground electrodes in order to accept the SQUID sensor array (see Section V.F). The pockets bring the SQUID sensor coils as close as possible to the n-<sup>3</sup>He cell. The outer surfaces of the acrylic ground electrode are polished and coated with a thin layer of copper to serve as the ground plane. This copper coating also serves as a shield for the SQUID sensor array.

The HV electrode is an acrylic shell with pockets on opposite sides for the two target cells. This electrode is 300-mm wide, 101.6-mm thick and 765-mm along the beam direction. The outer edges have a 50-mm radius. The outer surfaces of this electrode are polished and coated with a thin layer of copper. The ground electrodes have a mechanical connection to the target enclosure can. An insulating structure provides support for the HV electrode.

## **Cryostat**

The cryostat (Fig. V.G.4) is divided into two parts. The lower target-region cryostat is pictured in Fig. V.G.2, while the upper cryostat is shown in Fig. V.G.5.

### **Target-Region Cryostat**

The upper part of the target cryostat contains the cylindrical magnetic enclosure that houses the two target cells, the light guides, the electrodes, the  $\cos\theta$ -magnet coils, and the RF- $\pi/2$  rotation coils. This volume is filled with approximately 1300 liters of superfluid liquid helium. The lower part of the target enclosure is the can holding the variable capacitor for the HV system and another 200 liters of liquid helium. Also below the target enclosure are the two target-sample transfer bellows. The overall target enclosure is a large T shaped copper can with stainless steel wire seal flanges brazed onto the ends.

The gasket for these flanges is copper wire. The target enclosure also provides space to route the HV connection between the target-cell HV electrode and the HV generator.

### EDM TARGET ENCLOSURE CRYOSTAT

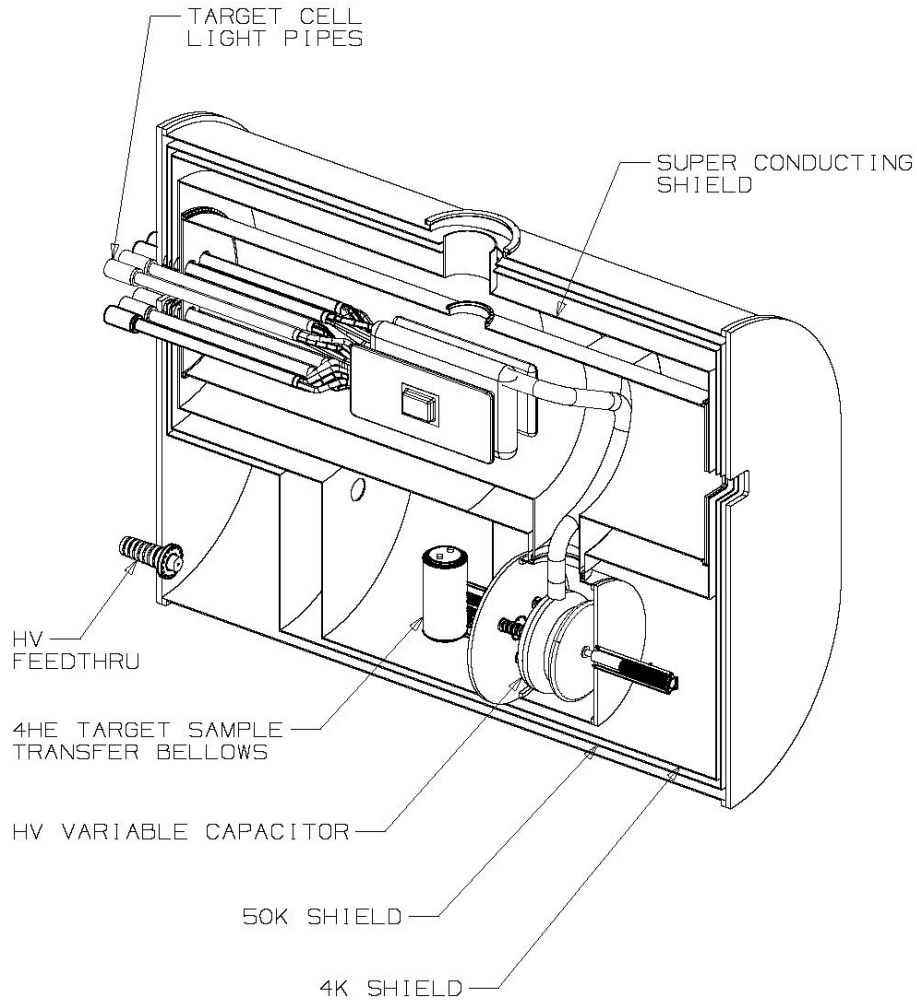


Figure V.G.2. The target-region cryostat is seen in as a cut away. The neutron beam comes in from the right. The target cell light pipes connect to photo-multiplier tubes at room temperature at the left. This volume is 1.5-m wide by 2.3-m high and has a length of 3 m.

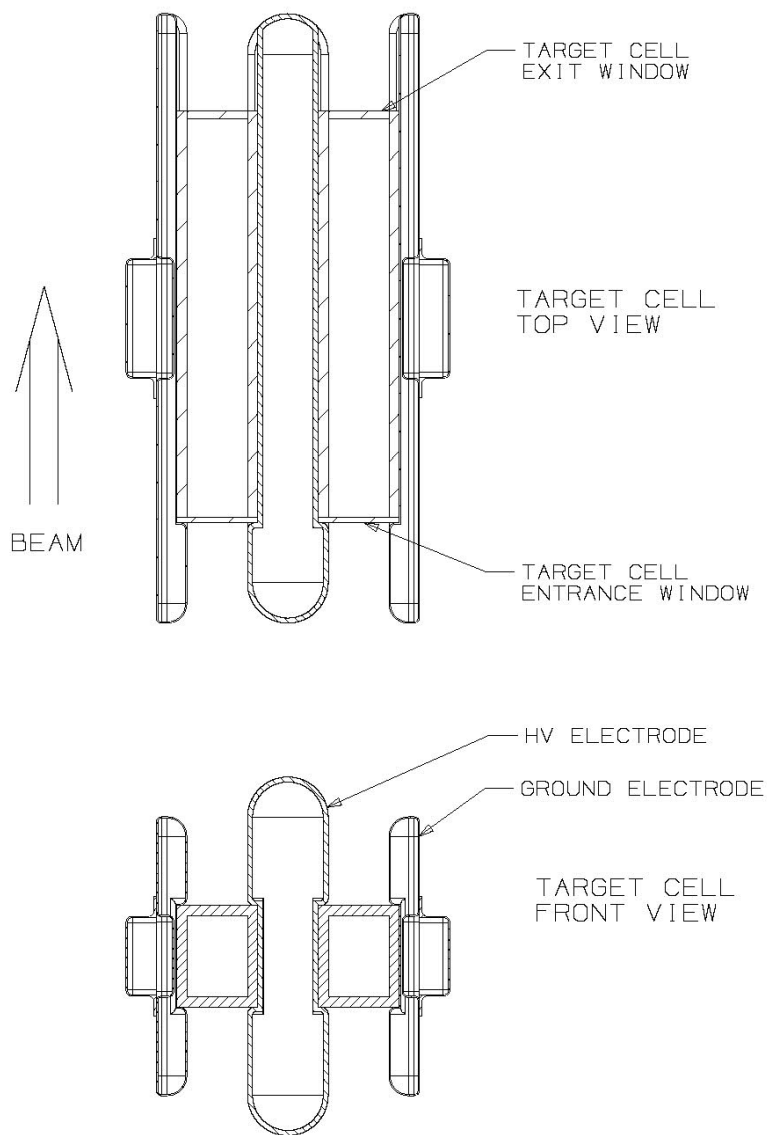


Figure V.G.3. Neutron target cells sandwiched between three hollow electrodes. The two cells are ~50 cm long. The SQUID detectors are embedded in the two ground (outside) electrodes.

### Upper Cryostat

The design of the upper cryostat is shown in Fig. V.G.5. It has two major, interconnected components, the DR and the He purifier, that are discussed below. A schematic of the organization of the cryogenics is given in Fig. V.G.6.

## **Dilution Refrigerator**

The central feature of the EDM upper cryostat (Fig. V.G.5) is the DRS 3000 DR insert from Leiden Cryogenics. The DR is rated at 3000  $\mu$ W at 120 mK. The functions of the DR are to cool the target enclosure to  $\sim$ 0.3 K and to cool the new target sample output from the  $^4\text{He}$  purifier. The DR  $^3\text{He}$  pump system consists of a 4000- $\text{m}^3/\text{hr}$  Roots blower backed by a 500- $\text{m}^3/\text{hr}$  Roots blower backed by an 80- $\text{m}^3/\text{hr}$  sealed dry pump. The DR's 1-K pot ( $^4\text{He}$  reservoir) pump system consists of a 500- $\text{m}^3/\text{hr}$  Roots blower backed by an 80- $\text{m}^3/\text{hr}$  sealed dry pump. The DR is vertically inserted into an internal, 100-l liquid helium Dewar with a 330-mm diameter neck.

The bottom tube of the Dewar serves as the main support for the target enclosure and consists of three sections so that connections to the DR still and the DR mixer can be made using OFHC copper braid. The connections to the DR still and mixer are made when the DR insert is in place.

During data taking operation, heaters on the DR still and mixer are modulated to keep the DR operation in thermal equilibrium. The upper-cryostat top flange is independently supported from the upper-cryostat bottom flange, which is in turn supported by an external framework. The outer vacuum enclosure of the upper cryostat can be removed to facilitate upper cryostat assembly and maintenance.

The internal liquid-helium Dewar is serviced by two or three Sumitomo RDK-415D (1.5 W at 4K/45 W at 50 K) two-stage cold heads and a transfer line to an external 1000-l Dewar. The cold head second stages are used to condense return  $^4\text{He}$  from the 1-K pot pump-systems (DR and Purifier). The first stages of the cold head cool the 50-K heat shields, the internal Dewar neck, and the return- $^4\text{He}$  gas. The refrigeration power of the cold head is matched to the liquid-helium needs of the EDM experiment during normal operation. The external Dewar is necessary during the initial cool down and filling of the cryostat.

## **The Helium Purification Cycle**

The polarization lifetime of the  $^3\text{He}$  may be only 100h, so that the polarization will drop below 97% during a measuring cycle. Thus, we want to be able to remove all the  $^3\text{He}$  from the 8 liters of the target cells every measurement cycle, as short as 20 min. The  $^4\text{He}$  is purified by utilizing the heat flush technique developed by McClintock.[1] The heat flush technique works above 1 K, where the phonon coupling is substantial. This

coupling varies as  $T^7$ , and at the operational temperature of the target cell, the  $^3\text{He}$  is unaffected. Therefore, the He must be warmed from  $\sim 0.2\text{ K}$  to  $1.2\text{ K}$  for spent  $^3\text{He}$  removal and cooled again after purification for the next cycle. The He recycling system consists of target cell drains, compression bellows to move the He to the top of the purifier, the purifier, and a staging volume for the addition of highly polarized  $^3\text{He}$  into ultra pure  $^4\text{He}$ .

#### EDM CRYOSTAT

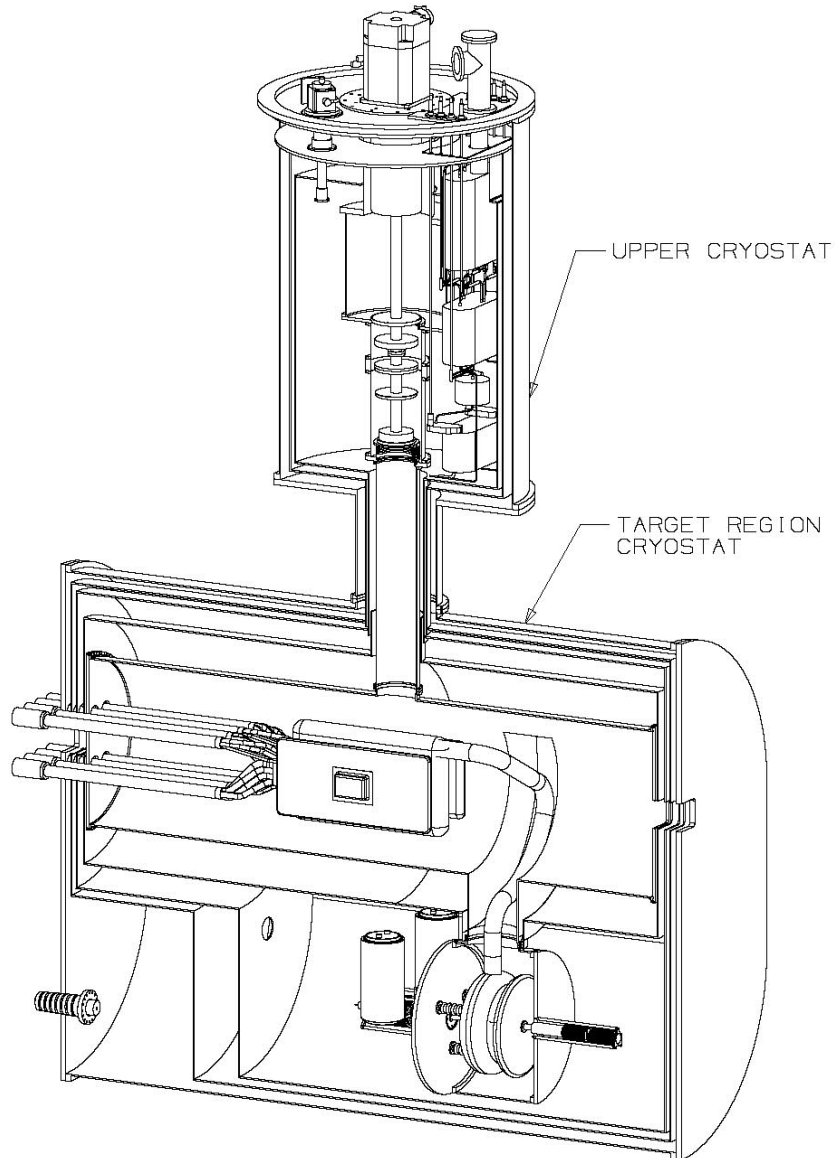


Figure V.G.4. Target region and upper cryostats. The neutron beam enters from the right.

## EDM UPPER CRYOSTAT

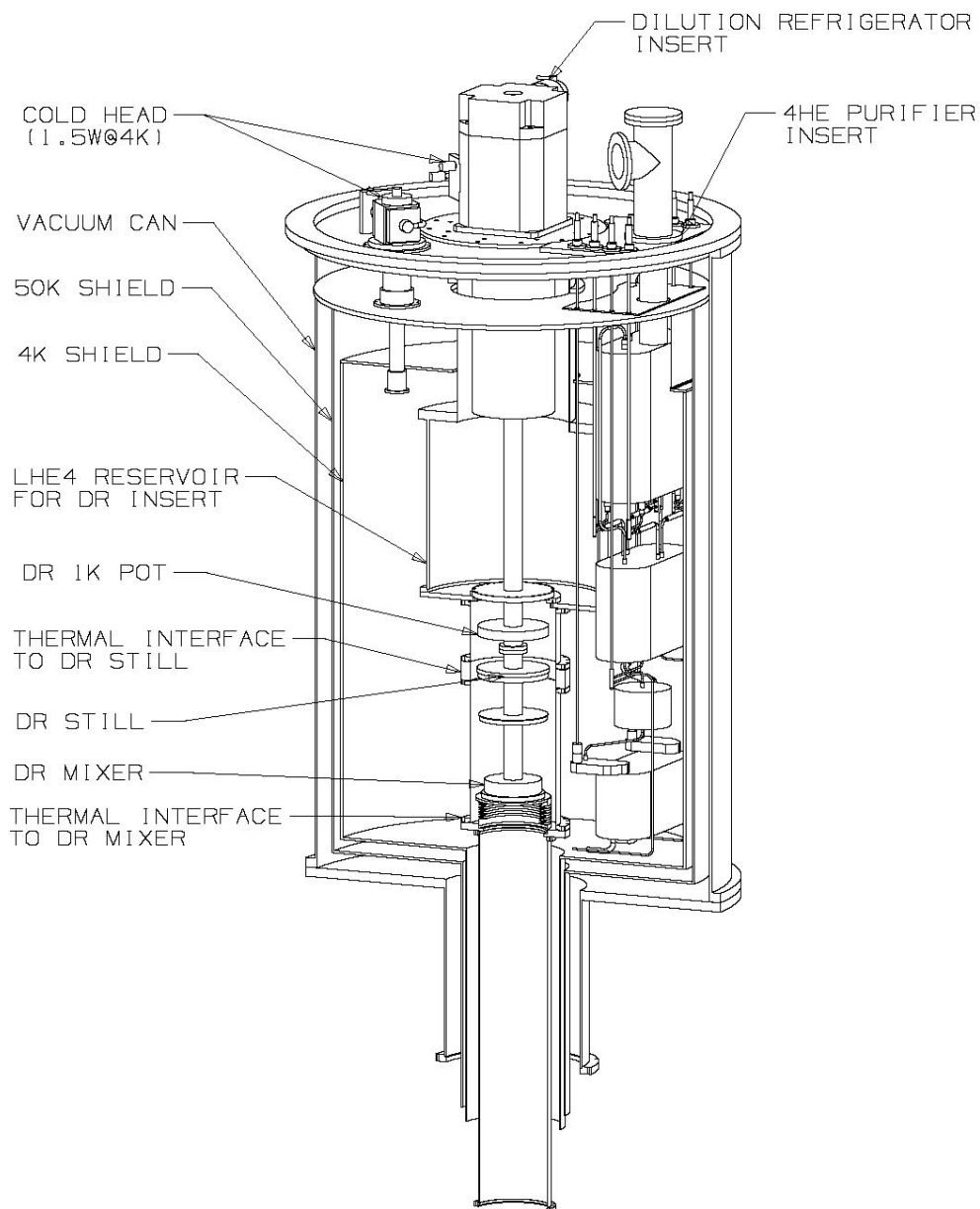


Figure V.G.5. Upper cryostat that encloses the DR, the  $^4\text{He}$  purifier apparatus, and the target-preparation reservoir, V3. This cylinder has a height of 2 m and a diameter of 1.2 m.

The upper cryostat houses a large-capacity, continuous-cycle helium purifier. (Fig. V.G.7). The purifier insert consists of three volumes that are separated vertically and thermally isolated from each other. Gravity is used to move the helium through the purifier and to the target cells. Volume 1 (V1) is a copper can that receives the spent

liquid helium target samples when the transfer bellows are compressed. V1 resides inside a can that is a high-capacity, continuous-cycle  $^4\text{He}$  refrigerator.

The phonon wind, initiated by heaters, pushes the  $^3\text{He}$  impurities back toward V1. Helium from V1 flows through a set of four helium purifiers heat flush tubes, see Fig V.G.7. Each purifier consists of a metering valve and a horizontal 100-mm length of 10-mm diameter tube with a  $\frac{1}{4}$ -watt heater at the downstream end. The heater raises the local temperature of the liquid helium to  $\sim 1.2$  K. The 1-K pot removes the 1 watt of heat generated by the purifier heaters. The 1-K pot is serviced by a large sealed Roots-blower system consisting of a 4000- $\text{m}^3/\text{hr}$  Roots pump backed by a 1200- $\text{m}^3/\text{hr}$  Roots blower backed by a sealed 80- $\text{m}^3/\text{hr}$  dry pump.

The purified  $^4\text{He}$  flows into a second  $^4\text{He}$  volume, V2, which is thermally isolated from the purifiers by long capillary tubes. Thermal links made of OFHC copper braid connect V2 to the DR still that is at  $\sim 0.6$  K. A heat exchanger in V2 helps to cool this volume when the spent target samples are moved from the transfer bellows to V1. The purifier is initially filled with ultra-pure helium that has been generated using the same heat flush technique in a separate apparatus. This apparatus is currently being modified from an existing device built at the Hahn-Meitner Institut. It serves as a development prototype for the upper-cryostat purifier. The purifier insert can then supply the experimental needs for pure liquid  $^4\text{He}$  for approximately 6 months, until the build up of  $^3\text{He}$  in V1 becomes a problem.

After V2, the purified liquid helium flows through a metering valve and into a heat exchanger with thermal contact to the DR mixer (see Figs. V.G.6 and V.G.7). The liquid helium then continues into the target preparation volume (V3). The size of V3 is carefully matched to the volume of the two target cells. In V3, polarized  $^3\text{He}$  atoms are introduced until a fractional density of  $\sim 10^{-10}$  is achieved. The inner walls of V3 must be coated to preserve the  $^3\text{He}$  spin. A magnetic holding field, carefully matched to the main field, is used to keep the target samples polarized. The liquid helium in V3 is kept at the nominal target operating temperature. At the end of the EDM-measurement cycle, valves below the target cells are opened to drain the spent target samples. At the end of this operation the valves are closed. A prototype valve to fill and empty the target cells has been developed for other applications.[2] The valve needs some modifications to prevent it from absorbing neutrons, and it must be tested for reliability over thousands of cycles. The newly prepared target material in V3 now flows through a valve into the target cells.

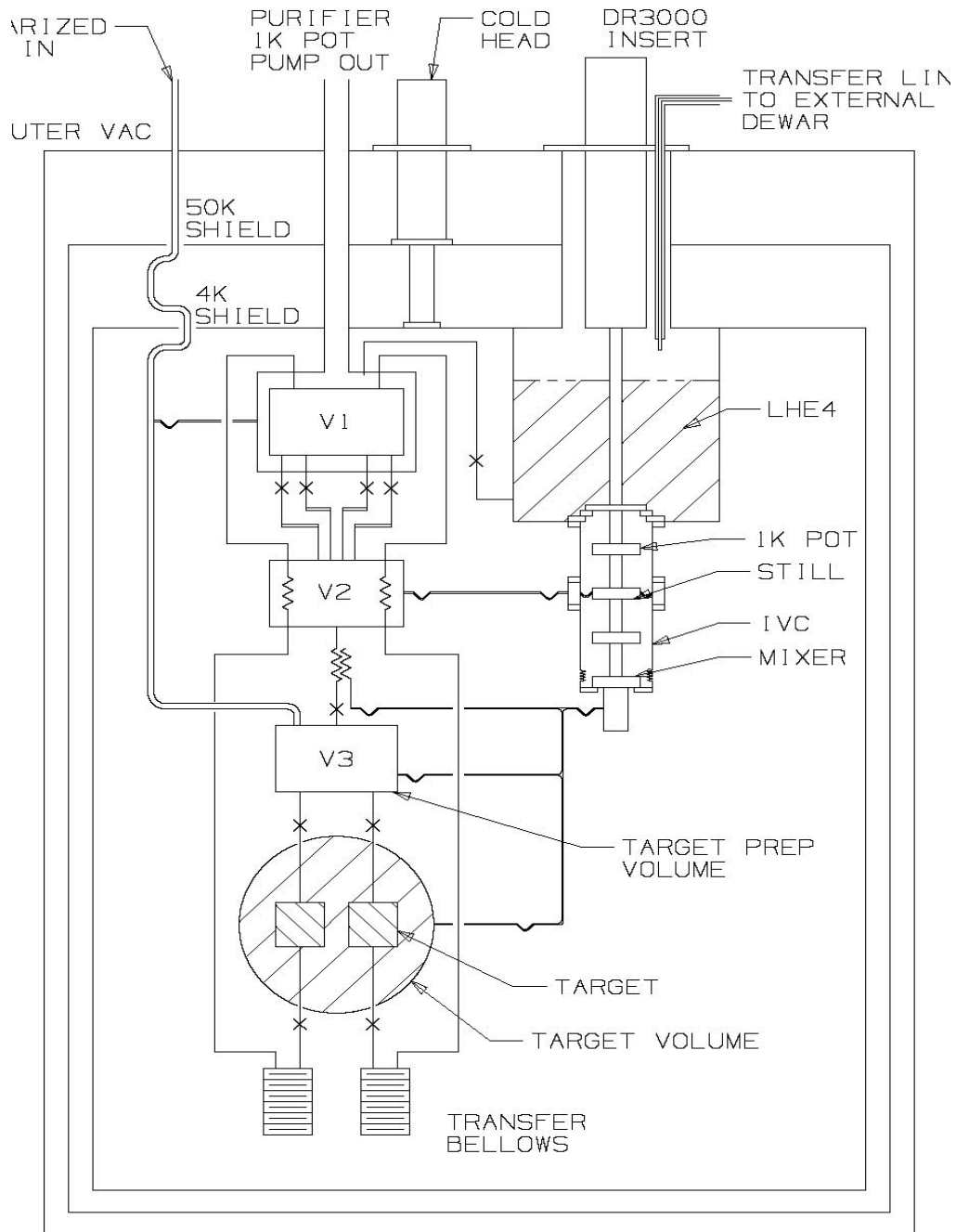


Figure V.G.6. Schematic of the Upper cryostat with the  $^4\text{He}$  purifier and the dilution refrigerator.

### HV Generator

A design requirement of the EDM experiment is a high electric field across the target cells. The field strength assumed for the pre-proposal is 50 kV/cm (section V.H.). The

spacing between the ground electrode and the HV electrode is currently 76 mm. The voltage requirement is then 360 kV. It does not appear to be practical to bring the full voltage into the apparatus from an external source. Commercially available ceramic vacuum feed-throughs suitable for our apparatus have a maximum voltage rating of 100 kV. Also, an existing 125-kV power supply is available for use in the experiment.

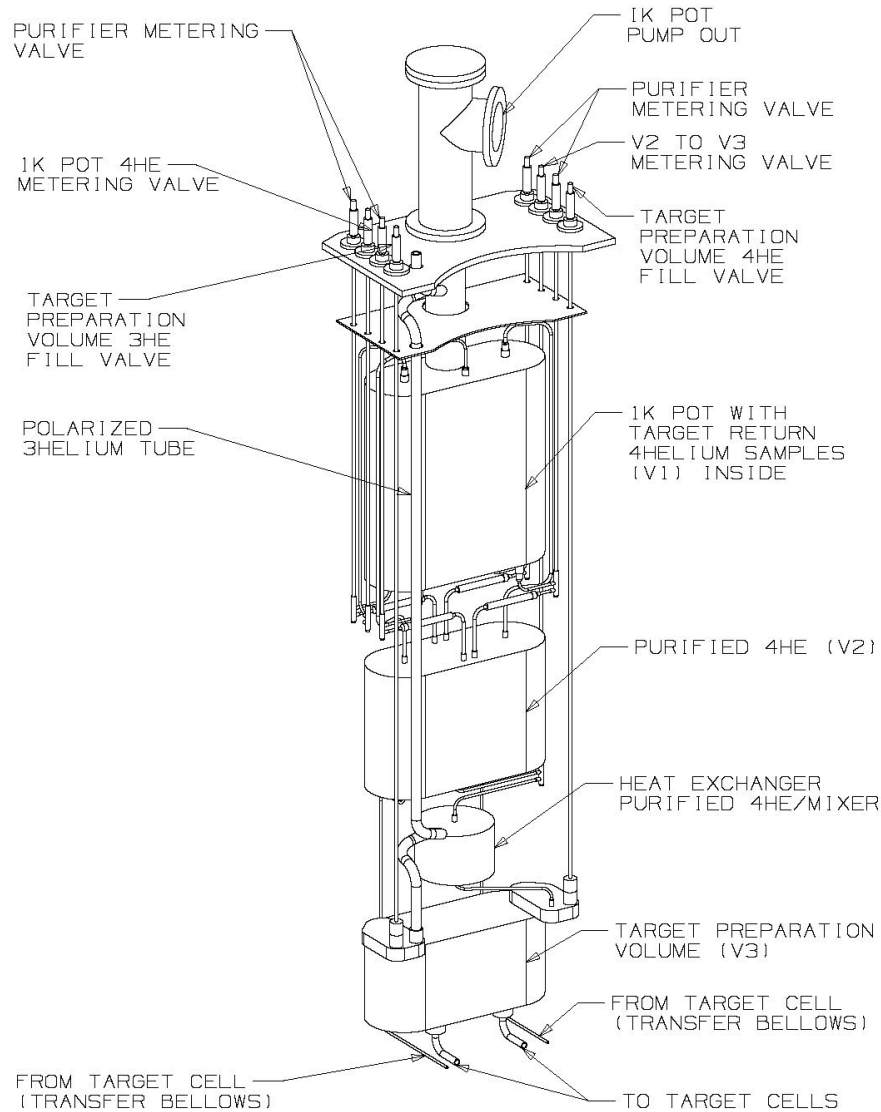


Figure V.G.7 The  $^4\text{He}$  purification apparatus and the polarized  $^3\text{He}$  and  $^4\text{He}$  target preparation reservoir (V3).

The alternative approach being adopted here is shown in Figs. V.G.2 and V.G.8. A variable capacitor is connected in parallel with the two target capacitors formed by the three target-region electrodes. The variable capacitor (and the target capacitors) is

initially charged from an external HV source, isolated, and then adjusted to step up the voltage inside the liquid helium volume. The procedure will be to engage the HV plate of the variable capacitor with a rod that carries the applied external voltage; the ground plate is held close to the HV plate to maximize the capacitance. After the charge build up, the HV rod contact is broken, and the ground plate is moved away from the HV plate of the variable capacitor. The movement decreases the capacitance of the variable capacitor; increasing the voltage across both the variable capacitor and the two target capacitors. The net result is that charge is moved from the variable capacitor to the target capacitors, increasing their electric fields.

To be more quantitative, all together there are four capacitors to be charged. The HV variable capacitor (1 pF to 1000 pF) is in parallel with the 2 x 53-pF capacitance of the two target cell electrodes. In addition, the capacitance due to the HV connection between the variable capacitor and the target cell HV electrode is ~54 pF. During the charging operation, when the ground electrode has been moved to close proximity with the HV electrode (~1 mm), the combined capacitance is ~1150 pF. The moveable HV contact is translated so as to be in contact with the HV electrode. A charging voltage of 50 kV is applied to this configuration. After the charging operation is complete, the moveable HV contact is withdrawn ~100 mm and the high voltage power supply is turned off so that the internal capacitor system is isolated. The ground electrode is then moved out so that the spacing between the ground electrode and the HV electrode is ~100 mm. The net capacitance of this configuration is 165 pF and the voltage gain factor is ~7. Thus the voltage can be increased to the required ~360 kV across the cell.

It is important that the net leakage current in super-fluid helium be small in order to meet the time-stability requirement of the measurement. In order to limit the change of the voltage across the target cell to 1-2%, during a 1000-s measuring period, the net leakage current must be < 1 nA. This specification is also sufficient to eliminate the systematic effect associated with spiral currents.

The variable capacitor and its actuators will be enclosed in a can, Fig. V.G.8, which is tee shaped and made of copper with the flanges brazed on at the ends. The flanges are wire seal flanges made from stainless steel with copper wire gaskets. The ground electrode and its actuator are mounted off of one large diameter flange. The ground electrode includes an actuating rod, which is supported by linear ball bushings that are immersed in a super-fluid helium bath common with the rest of the variable capacitor. A pair of stainless steel bellows allows the ground electrode to move, with external control,

through a range of 100 mm without changing the super-fluid helium volume. During actuation, one bellows expands while the other contracts to keep the volume constant.

The HV electrode is mounted from a second flange using custom ceramic HV standoffs. The HV moveable contact has a similar bellows arrangement with the additional requirement that the moveable contact and its linear ball bushings be isolated from ground. The HV feed-through is fixed in position and a spring makes the electrical connection to the HV contact. The requirement of a ceramic HV-insulator feed-through between a super-fluid helium volume and vacuum is a challenging requirement. Discussions with an engineer, who designs ceramic feed-throughs, led us to choose a commercially available feed-through that could be welded to a stainless-steel flange.

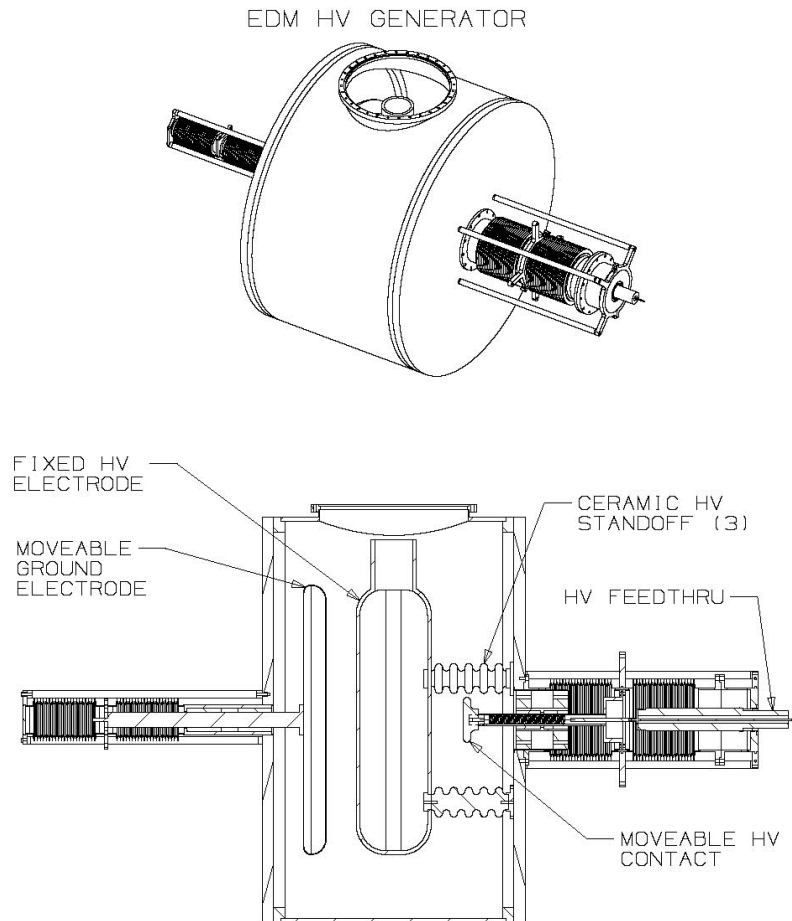


Figure V.G.8. Voltage amplification technique using a variable capacitor and an external HV disconnect. The main volume is filled with superfluid  $^4\text{He}$ .

The connection between the variable-capacitor HV electrode and the target-cell HV electrode passes through the top flange in Fig. V.G.8. This flange has a 250-mm ID and keeps the spacing between the 100-mm diameter HV connection and ground at 75 mm.

## Polarized $^3\text{He}$ Source

The design goals for the performance of the polarized  $^3\text{He}$  source are the following:

- pressure in the cold head region  $< 10^{-5}$  mbar
- pressure in the magnet region  $< 10^{-6}$  mbar
- polarized  $^3\text{He}$  source output rate  $> 10^{14}/\text{sec}$
- $^3\text{He}$  polarization  $> 97\%$

The polarized  $^3\text{He}$  source assembly, discussed in Section V.D, is shown in Fig. V.G.9, with the details of the injection region pictured in Fig. V.G.10. A recirculating flow of  $^3\text{He}$  gas is cooled to  $\sim 0.5$  K and ejected from a nozzle pointed at the axis of an array of quadrupole magnets. The nozzle consists of multiple 1-mm diameter x 20-mm long tubes, 0.7-mm inner diameter (ID), filling the ID of a 9-mm ID stainless steel tube. The gas stream is defined by a beam skimmer and a beam collimator; they match the nozzle aperture to the acceptance of the quadrupole-magnet array. The gas atoms that fail to enter the magnet acceptance are pumped away by the Varian V2000 turbo pump (2000 liters/second). The gas atoms that fail to traverse the quadrupole array are pumped away by the Varian V1000 turbo pump (1000 liters/second). The turbo pumps are backed by a Pfeiffer Unidry 050 sealed dry pump. This pump is part of the  $^3\text{He}$  gas system that services the source.

Each quadrupole magnet sector is constructed from four neodymium bar magnets that have dimensions of 159 mm x 12.7 mm x 38 mm. The nominal magnetic field is  $\sim 0.7$  T. Each magnet sector has a central tube that provides support for the magnet bars and has multiple holes for good pumping of the beam volume. The magnet array resides inside of a 200-mm diameter tube with conflate flanges on the ends.

The gas flow and cooling is organized as follows. A Sumitomo RDK-415D cold head is used to cool the  $^3\text{He}$  gas stream to a design goal of  $< 0.5$  K. The first stage of this cold head is rated for 45 W at 50 K and is used to cool a heat shield and to cool gas streams of both  $^3\text{He}$  and  $^4\text{He}$ . The second stage of the cold head is rated for 1.5 W at 4 K and 0.3 W at  $\sim 3.2$  K. The  $^4\text{He}$ -gas stream is liquefied by the second stage of the cold head, and the liquid helium continues through a metering valve into a volume that serves as a 1-K pot.

An Edwards XDS10 sealed scroll pump is used to recirculate the  $^4\text{He}$  gas. The  $^3\text{He}$ -gas stream is cooled to approximately 4 K by the cold head second stage. Some of the  $^3\text{He}$  gas continues to a heat exchanger, with its 1-K pot, where it is liquefied. The  $^3\text{He}$  liquid flows through a metering valve into a pumped liquid bath. A Varian 551 turbo pump backed by the Pfeiffer Unidry 050 sealed dry pump (same pump that backs the big turbo pumps) lowers the temperature of the  $^3\text{He}$  bath to  $\sim 0.3$  K. The remaining  $^3\text{He}$  gas is cooled below 0.5 K in a heat exchanger in contact with the pumped  $^3\text{He}$  bath. This gas stream continues through a third metering valve to the nozzle that points the gas stream at the quadrupole-magnet array.

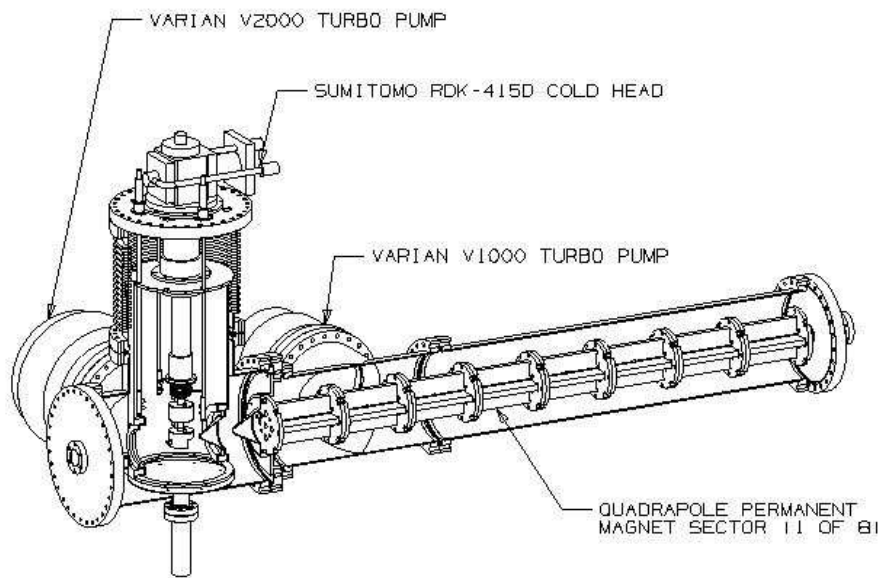


Figure V.G.9. The polarized- $^3\text{He}$  source with its quadrupole magnet spin filter array.

### Other Components

The  $\cos\theta$  magnet,  $\pi/2$  RF Helmholtz coils, and the outer ferromagnetic-shield have less detailed designs. These constructs are in use in other experiments like the current

neutron EDM experiment at the ILL. We will rely heavily on their design. As noted in Appendix A, there is a question of whether the  $\cos\theta$  coil, when in a cryogenic environment, can be wrapped on a ferromagnetic material. The uncertainty should be resolvable with some measurements on a prototype.

The superconducting shield is necessary for noise isolation of the SQUIDs. As a new feature of this measurement, it requires development. The main uncertainty is the nature of trapped fields inside the shield as it is cooled through the superconducting transition. We hope to measure the size of such effects by measuring the fields inside a prototype shield using nuclear magnetic resonance. A  $\cos\theta$  coil wrapped on a ferromagnetic material would mitigate the problem.

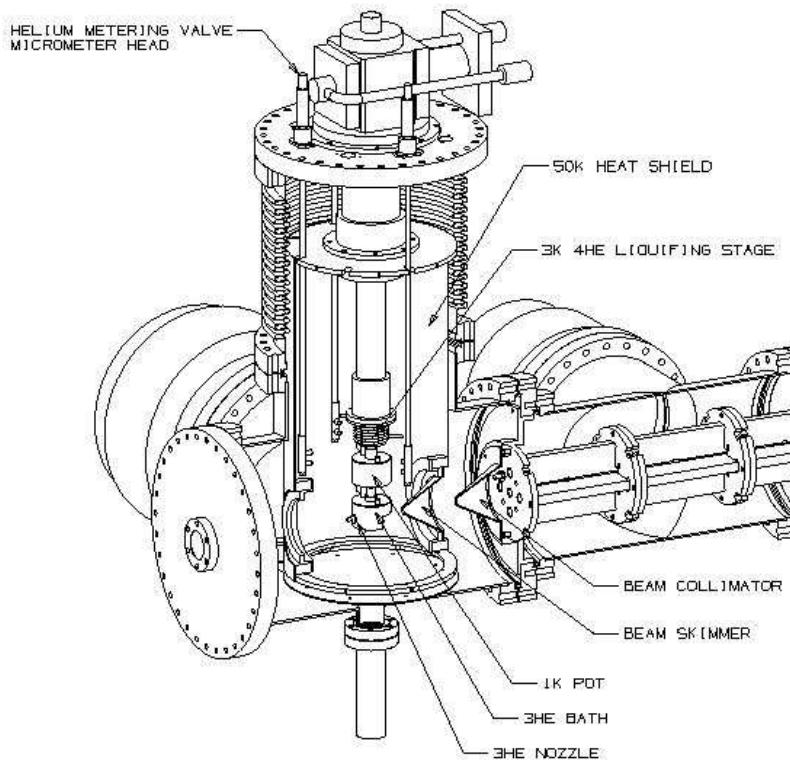


Figure V.G.10. Details of the injection region of the  $^3\text{He}$  source.

## References

1. P. V. E. McClintock., *Cryogenics* **18**, 201 (1978); P. C. Hendry and P. V. E. McClintock, *Cryogenics* **27**, 131 (1987).
2. R. Duncan, (private communication).

## Section V.H

### Expected Sensitivity and Systematic Effects

#### 1.A Scintillation Signal Sensitivity

##### Scintillation Rate

The system frequency measurement sensitivity can be estimated using the mathematical techniques outline in [1]. At the start of the measurement, we assume  $N$  UCN are trapped in each storage vessel, and scintillation light is produced as previously described through  $^3\text{He}$ -UCN spin-dependent reactions. We also include here scintillation light produced by UCN beta decay, and possible background scintillation due to gamma Compton scattering and apparatus beta-activation. This treatment is slightly different from that presented in [2] because there we assumed it would be possible to discriminate between the  $^3\text{He}$ -UCN reactions from UCN and neutron activation beta decay, and from Compton backgrounds; as we now expect 5-10 photoelectrons per  $^3\text{He}$ -UCN capture event, the possibility of such discrimination remains an open question. Furthermore, the analysis presented here is for free-precession of the  $^3\text{He}$  and UCN (dressing as described in [2] is not used; SQUID magnetometers will pick up the  $^3\text{He}$  magnetization signal and therefore provide a direct measurement of the average magnetic field seen by the  $^3\text{He}$  which, to high accuracy, is the same for the UCN as described later in this Section).

The net scintillation rate from each cell can be written

$$\Phi = \Phi_B + Ne^{-\Gamma_{ave}t} \left[ \frac{1}{\tau_\beta} + \frac{1}{\tau_3} [1 - P_3 P_n e^{-\Gamma_p t} \cos(\omega_r t + \phi)] \right] \quad (\text{V.H.1})$$

where  $\Phi_B$  is the background rate (assumed constant),  $\Gamma_{ave}$  is the total of the UCN  $\beta$  decay rate, cell loss rate (accounting for wall losses and upscattering from superfluid  $^4\text{He}$ ), and average  $^3\text{He}$  absorption rate

$$\Gamma_{ave} \equiv \frac{1}{\tau_\beta} + \frac{1}{\tau_{cell}} + \frac{1}{\tau_3}$$

and  $\tau_\beta \approx 885$  s,  $1/\tau_3 = 2.4 \times 10^7 X$  where  $X$  is the  $^3\text{He}$  concentration,  $P_3$  and  $P_n$  are the  $^3\text{He}$  and UCN polarizations,  $\Gamma_p$  is the sum of the  $^3\text{He}$  and UCN polarization loss rates,  $\omega_r$  is the difference in precession frequencies, and  $\phi$  is an arbitrary phase. The variance in the determination of  $\omega_r$  together with the high voltage magnitude determines the experimental sensitivity. At this point, it is useful to define

$$\Gamma \equiv \frac{1}{\tau_\beta} + \frac{1}{\tau_{cell}}.$$

We can estimate the experimental sensitivity simply by making some reasonable assumptions. A real experiment will be slightly more sensitive by careful choice of cell filling time, total measurement time, and  $^3\text{He}$  concentration. But for our purposes here, we assume that UCN are accumulated for two UCN storage lifetimes ( $2/\Gamma$ ). We adjust  $X$

so that  $\tau_3 = 1/\Gamma$ . The measurement time is taken as  $T_m = 1/\Gamma$ . We also assume that  $\Gamma \gg \Gamma_p$  so spin relaxation can be ignored in the following discussion.

### Sample Size and Polarization

Another change from the sensitivity calculation in [2] is required because we now plan to produce polarized UCN from polarized 8.9Å neutrons. The initial UCN polarization and density, assuming UCN are accumulated with polarized  $^3\text{He}$  in the superfluid bath, can be determined by considering the time dependence of the number of UCN with spin parallel ( $N_+$ ) and antiparallel ( $N_-$ ) to the  $^3\text{He}$  initial polarization:

$$\begin{aligned}\dot{N}_+ &= \frac{(1 + P_{cn})PV}{2} - \left[ \Gamma + \frac{1 - P_3}{\tau_3} \right] N_+ = P_+V - \Gamma_+N_+ \\ \dot{N}_- &= \frac{(1 - P_{cn})PV}{2} - \left[ \Gamma + \frac{1 + P_3}{\tau_3} \right] N_- = P_-V - \Gamma_-N_-\end{aligned}$$

where  $P_{cn}$  is the cold neutron beam polarization,  $P$  is the total UCN production rate (UCN/cc sec), and  $V$  is the storage chamber volume. These equations are easily solved, yielding

$$\begin{aligned}N_+(t) &= \frac{P_+V}{\Gamma_+}(1 - e^{-\Gamma_+t}) \\ N_-(t) &= \frac{P_-V}{\Gamma_-}(1 - e^{-\Gamma_-t}).\end{aligned}$$

In the limit  $P_{cn}, P_3 \approx 1$ ,

$$N(t) = N_+(t) + N_-(t) \approx N_+(t) = \frac{PV}{\Gamma}(1 - e^{-\Gamma t}).$$

In this approximation,

$$\begin{aligned}P_n(t) &= \frac{1 - N_-(t)/N_+(t)}{1 + N_-(t)/N_+(t)} \approx 1 - 2\frac{N_-(t)}{N_+(t)} \\ &= 1 - 2 \left[ \frac{1 - P_{cn}}{1 + P_{cn}} \right] \left[ \frac{\Gamma + (1 - P_3)/\tau_3}{\Gamma + (1 + P_3)/\tau_3} \right] \left[ \frac{1 - e^{-\Gamma_-t}}{1 - e^{-\Gamma_+t}} \right]\end{aligned}$$

which, when  $\tau_3 = 1/\Gamma$  and  $t = 2/\Gamma$ , implies for the initial number of UCN and polarization

$$N = 0.86PV/\Gamma; \quad P_n = 1 - (0.4)(1 - P_{cn})$$

which, if  $P_{cn} = .90$ ,  $P_n = 0.96$ .

The oscillating signal described by Eq. (V.H.1) commences when  $\pi/2$  pulses are applied, flipping the spins perpendicular to the applied static field.

## Frequency Variance

By use of the formalism presented in [1], the frequency variance per measurement cycle of length  $T_m$  can be estimated. This requires the average oscillating signal amplitude  $A(t)$ , and the constant (or slowly) decaying background signal  $\overline{I(t)}$ , which we will assume is principally due to beta decay, imperfect polarization, and the constant (non-oscillating) component in Eq. (V.H.1).

From Eq. (1), the signal amplitude due to  $^3\text{He}$  absorption (one-half peak-to-valley scintillation difference between spins parallel and antiparallel) is (assuming  $\Gamma - p = 0$ )

$$A(t) = \frac{NP_3P_n}{\tau_3} e^{-\Gamma_{ave}t}$$

while the average per cycle scintillation rate, due to beta decay and  $^3\text{He}$  absorption, is

$$\overline{I(t)} = \Phi_B + Ne^{-\Gamma_{ave}t}(1/\tau_\beta + 1/\tau_3)$$

Over the measurement time  $T_m$ , the average amplitude and average current is, recalling that we assume  $\Gamma = 1/\tau_3$

$$\bar{A} = (0.43) \frac{NP_3P_n}{\tau_3}$$

and

$$\bar{I} = \Phi_B + 0.43N \left[ \tau_\beta^{-1} + \tau_3^{-1} \right].$$

From Eq. (9) of [1], the average uncertainty in the frequency after observing the oscillating scintillation for  $T_m$  seconds is, recalling that  $\tau_3 = 1/\Gamma = T_m$ ,

$$\begin{aligned} (\Delta f)^2 &= \frac{6}{\pi^2} \left( \frac{\bar{I}}{A^2} \right) \frac{1}{T_m^3} \\ &= \frac{1.41}{P_3^2 P_n^2 N T_m} \left( \left[ \frac{\Phi_B}{0.43N(T_m^{-1} + \tau_\beta^{-1})} + 1 \right] (1/\tau_\beta + 1/T_m) \right) \text{Hz}^2 \end{aligned} \quad (\text{V.H.2}).$$

Taking  $T_m = \tau_3 = 1/\Gamma = 500$  sec,  $P = 1/\text{cc}/\text{sec}$ ,  $V = 4,000$  cc and assuming  $\Phi_B/N \ll 1/\tau_\beta$ , then

$$\Delta f = 2.6 \mu\text{Hz}$$

which, assuming 50 kV/cm, corresponds to  $2\sigma$  EDM sensitivity of  $10^{-25}$  ecm, for each cell. Now, we are comparing two cells with oppositely directed electric fields, so the sensitivity per measurement cycle is

$$7 \times 10^{-26} \text{ e cm.}$$

Each measurement cycle requires 1,500 sec, so the experimental sensitivity of the measurement is

$$9 \times 10^{-27} \text{ e cm} \cdot \sqrt{\frac{\text{day}}{T}} \quad (\text{V.H.3})$$

or, in  $T = 100$  days of running, the  $(2\sigma)$  limit will be  $9 \times 10^{-28} e$  cm, a factor of at least 50 improvement over the present experimental limit. The calculation presented here is not optimized for accumulation vs. measurement time, and not optimized for  $^3\text{He}$  density; on the other hand, certain idealizations (e.g., polarization does not decay, activation background is small) were assumed. However, this simplified calculation clearly shows the expected experimental sensitivity. It is a worst-case estimate in the sense that we assumed the beta-decay background can not be discriminated from the  $^3\text{He}$ -UCN reactions.

Operating the experiment at a more intense neutron source will improve the sensitivity; the purpose of this calculation was to show the possibilities at LANSCE. The cold neutron flux available at the Institut Laue-Langevin is approximately 50 times greater, corresponding to a factor of 7 increase in sensitivity. In addition use of the dress-spin technique described in [2] offers a significant increase in sensitivity.

## 1.B Required SQUID Magnetometer Sensitivity

It is necessary to use the  $^3\text{He}$  precession signal to determine the average magnetic field affecting the UCN precession. Ideally, the field would be constant, however, there are changes due to finite shielding of ambient magnetic field changes, and systematic fields due to leakage currents associated with the application of high voltage.

Because the  $^3\text{He}$  and neutron magnetic moments are equal to within 10%, and the electric field does not affect the  $^3\text{He}$  precession, we need only know the difference in magnetic Larmor precession frequencies to high accuracy. The sensitivity per measurement cycle is  $2.6 \mu\text{Hz}$ , so the minimum required accuracy on  $\delta B$  is

$$\delta B = \frac{2.6 \mu\text{Hz}}{|\gamma_3 - \gamma_n|} = 8 \text{nG}$$

per measurement cycle; practically, we would like the accuracy on  $\delta B$  to be a factor of three smaller so that it does not contribute noise to the measurements.

Our plan is to use SQUID magnetometers to pick up the  $^3\text{He}$  precession. The uncertainty  $\delta B$  is related to the uncertainty on the determination of the  $^3\text{He}$  precession frequency,

$$\delta f_3 = \gamma_3 \delta B = 2.6 \times 10^{-5} \text{Hz}$$

which, as expected, about a factor of ten larger than the neutron frequency uncertainty.

The amplitude of the  $^3\text{He}$  magnetization signal can be estimated as follows. The magnetization of the sample is

$$M = \frac{h\gamma_3\rho_3}{2} = \frac{h\gamma_3}{2} \frac{9.2 \times 10^{14} (\text{s/cc})}{\tau_3} = 2.3 \times 10^{-11} \text{ cgs units.}$$

It is reasonable to expect that the magnetic induction at a region close to the cell, coupled to the SQUID pickup coil, is something like 1/2 the value at the surface of the cell, so

$$B_P = 4\pi M/4 = 7.2 \times 10^{-11} \text{G.}$$

If the pickup loop has inductance  $L_p$  and the SQUID input inductance is  $L_i$ , the flux coupled to the SQUID is

$$\Phi_S = \frac{MB_P A_p}{L_p + L_i}$$

where  $M$  is the SQUID mutual inductance. Typically,  $M = 10$  nH,  $L_i + L_p \approx 500$  nH. This implies, in terms of  $10^{-6}$  of a flux quantum  $\mu\Phi_0 = 2.07 \times 10^{-11}$  G cm<sup>2</sup>, a pickup loop area (assuming  $L_p < L_i$  so we can ignore the change in  $L_p + L_i$ )

$$\Phi_S = 7.2 A_p \mu\Phi_0,$$

with  $A_p$  in cm<sup>2</sup>, which is the signal to be expected at the SQUID. We can use Eq. (11) of [1] to determine the maximum noise per root Hz bandwidth required to measure the <sup>3</sup>He precession frequency to 26  $\mu$ Hz accuracy in a measurement time  $T_m = 500$  s,

$$(\delta f_3)^2 = (26 \mu\text{Hz})^2 \left(\frac{n_1}{A}\right)^2 \frac{3}{\pi^2} \frac{1}{T_m^3} = \left(\frac{n_1}{(7.2\mu\Phi_0 A_p)}\right)^2 \frac{3}{\pi^2} \frac{1}{(500 \text{ s})^3} \quad (\text{V.H.4})$$

$$\rightarrow n_1/A_p = 4\mu\Phi_0/\sqrt{\text{Hz}}/\text{cm}^2$$

and taking 1/3 this value to ensure no extra noise is introduced implies

$$n_1/A_p = 1.3\mu\Phi_0/\sqrt{\text{Hz}}/\text{cm}^2. \quad (\text{V.H.5})$$

A Conductus 1020 has  $n_1 = 3\mu\Phi_0/\sqrt{\text{Hz}}$  implying a 2 cm<sup>2</sup> pickup loop is required to attain the requisite signal-to-noise, for which  $L_p = 30$  nH.

This calculation assumes that the <sup>3</sup>He polarization does not decay significantly over the measurement period.

## 2. Systematic Effects

In this section, we will address possible systematics that are ‘‘fundamental’’ as opposed to the usual concerns of external magnetic fields associated with reversing high voltage apparatus, etc. Of course, such effects can be important, but for the proposed experiment, will be largely suppressed by the internal <sup>3</sup>He comagnetometer. Here will address issues that lead to real differences in the effective magnetic field seen by the <sup>3</sup>He and UCN.

### 2.A. Pseudomagnetic Field

The effective UCN potential is given in terms of the coherent scattering length as

$$U_f = \frac{2\pi\hbar^2}{m} \rho \langle a \rangle$$

where  $m$  is the neutron mass,  $\rho$  is the density and  $\langle a \rangle$  is the average coherent scattering length. Each spin state of every constituent contributes to this potential; in the case where

a constituent is polarized, there will be a different potential for each spin state; this energy difference creates a pseudomagnetic field. For polarized  $^3\text{He}$ ,

$$a_+ = 3.0 \pm 0.1 \text{ fm}$$

$$a_- = 8.2 \pm 0.3 \text{ fm}$$

which leads to a pseudomagnetic spin precession frequency of

$$6.6 \times 10^6 X \text{ Hz}$$

where  $X \approx 10^{-10}$  is the  $^3\text{He}$  concentration. Thus there is a shift in frequency of  $660 \mu\text{Hz}$  when the  $^3\text{He}$  polarization lies along the static magnetic field. Note that this frequency shift is not dependent on the electric field, but can introduce noise into the system if it varies between the two cells between fillings.

This rather large value is suppressed by a number of factors. First, the  $^3\text{He}$  spins are flipped into the plane for the free precession measurement, so the average field seen by the UCN has near-zero average; the only contribution to the precession frequency is that due to the imprecision of the  $\pi/2$  pulse. Achieving 5% accuracy for this pulse reduces the pseudomagnetic precession to  $33 \mu\text{Hz}$ . Furthermore, the cells will be filled with nearly exactly the same  $^3\text{He}$  density because both are filled from the same source, so the difference frequency is even smaller; we can assume the initial  $^3\text{He}$  density is the same within 5%. Furthermore, the relative difference in the  $\pi/2$  pulse between cells can be accurate to within 1%. These various factors bring the pseudomagnetic precession frequency difference to less than  $1 \mu\text{Hz}$ , which is sufficiently below the expected accuracy of about  $2 \mu\text{Hz}$  per measurement cycle so that no extra noise will be introduced. However, the importance of comparing two cells filled from the same source is evident.

It should be noted that EDM experiments in the presence of a large pseudomagnetic field are not without precedence. The  $^{129}\text{Xe}$  EDM experiment [3] suffered a spin shift of about  $5 \text{ mHz}$  while the final experimental sensitivity was around  $2 \times 10^{-26} \text{ ecm}$  with a field of  $2 \text{ kV/cm}$ . This implies that the spin shift did not contribute noise at the level of  $0.04 \mu\text{Hz}$ .

The direct  $^3\text{He}$  magnetic field and its effect on the UCN is too small to be of concern compared to the pseudomagnetic field.

## 2.B. Gravitational Offset and other Spatial UCN/ $^3\text{He}$ Differences

Because the UCN kinetic energy is so low, the density “sags” under the influence of the Earth’s gravitational field. The  $^3\text{He}$  energy (effective temperature) will be around  $0.3 \text{ K}$  compared to  $3 \text{ mK}$  for the UCN, so the effect of gravity on the  $^3\text{He}$  distribution is extremely small. The shift in center of mass of UCN in a storage chamber of height  $h$  was estimated in [4], p. 93:

$$\Delta h = \frac{mgh^2}{3kT}$$

so for  $h = 10 \text{ cm}$ ,  $3 \text{ mK}$ , implies  $\Delta h = 0.13 \text{ cm}$ . The principal concern is that, if there is a spurious field from leakage currents, the  $^3\text{He}$  and UCN will not average it in the same way.

The problem cannot be solved exactly because we don't know what the leakage current distribution will be, but we can estimate the effect.

The usual rule of thumb is that the current is assumed to flow in a 1/4 turn loop around the cell; assuming a current of 1 nA which is likely achievable at low temperature

$$B_{\text{sys}} = \frac{1}{4} \frac{2\pi I (3 \times 10^9 \text{ statamp/amp})}{cR} \approx 31 \text{ pG}$$

This corresponds to an EDM of about  $10^{-27}$  e cm at 50 kV/cm. Now we must factor in the spatial difference to get the net systematic shift between the  $^3\text{He}$  magnetometer and the UCN. The shift could be first order in the displacement, or (0.13 cm/10 cm), up to factors of order unity, leaving a maximum residual systematic error of  $10^{-29}$  e cm, which is comfortably below the anticipated statistical limit.

Our efforts to detect a non-uniformity in the  $^3\text{He}$  distribution in a test cell (by use of neutron tomography) showed no substantial effects. In fact, it is anticipated that the  $^3\text{He}$  will be repelled by the superfluid-cell interface. Unlike the case of most atoms that experience a Van der Waals attraction, or even near chemical binding, to walls of storage cells, the case of  $^3\text{He}$  in superfluid helium is special.

Another concern is the effects of unavoidable small heat currents on the  $^3\text{He}$  distribution. At our anticipated operating temperature of less than 0.3 K, these effects are extremely small, with the effect of heat decreasing as the temperature  $T^{-7}$ .

## 2.C. $v \times E$ effects

The final systematic we will consider involves the motional or  $v \times E$  magnetic field. The problem is that the UCN and  $^3\text{He}$  atoms have very different average velocities. However, the motional field is randomly fluctuating because the velocity changes on subsequent collisions with the cell walls. The problem is discussed in [3], Sec. 3.5.3, and in [5], where it is shown that the effect is "quadratic" in that it is proportional to the square of the electric field. The direct motional field adds in quadrature with the static field and is reduced by a factor  $x^2 = (\omega\tau_c)^2$  where  $\omega$  is the Larmor frequency and  $\tau_c$  is the time between subsequent wall collisions; this relation holds when  $x < 1$ . In [3] and [5] it is shown, extrapolated to a 50 kV/cm field, that the electric field must reverse with an accuracy of 10% to maintain a systematic shift below  $5 \times 10^{-28}$  ecm. This is a modest requirement on the electric field reversal accuracy.

Another point worth mentioning is that the relative shift will be temperature dependent when the temperature is high enough so that the  $^3\text{He}$  atoms move diffusively in the superfluid bath. In this limit, the time between collisions that substantially change the  $^3\text{He}$  velocity, hence  $\tau_c$ , varies rapidly with temperature. In fact it might be possible to "tune" the temperature to a value where the relative shift is the same for the  $^3\text{He}$  atoms and the UCN.

## References

- [1]. Y. Chibane, S.K. Lamoreaux, J.M. Pendlebury, and K.F. Smith, "Minimum variance of frequency estimates for a sinusoidal signal with low noise," Meas. Sci. Technol. **6**, 1671-1678 (1995).

- [2] R. Golub and S.K. Lamoreaux, Physics Reports **237**, 1 (1994).
- [3] T.G. Vold et al., Phys. Rev. Lett. 52, 2229 (1984).
- [4] “CP Violation without Strangeness,” I.B. Khriplovich and S.K. Lamoreaux (Springer-Verlag, Heidelberg, 1997).
- [5] S.K. Lamoreaux, Phys. Rev. A **53**, 3705 (1996).

## VI. Collaborators and Responsibilities

The EDM collaboration has been assembled from a combination of universities and national laboratories both in the United States and from around the world. The collaborators have great breadth of experience in the many areas of expertise needed for a successful outcome. These areas include neutron science, nuclear instrumentation, nuclear magnetic resonance, polarized  $^3\text{He}$  and neutrons, SQUID technology, strong electric and weak magnetic fields of high uniformity, and cryogenics. The collaboration currently consists of 14 institutions and 32 members. The collaboration contains many world experts.

### A. Collaboration

Members of the EDM collaboration, “A New Search for the Neutron Electric Dipole Moment.”

| Institution                                    | Collaborators  |
|--|--|
| University of California at Berkeley           | D. Budker, A. Sushkov, V. Yashchuk   |
| California Institute of Technology             | B. Filippone, T. Ito, R. McKeown   |
| Hahn-Meitner Intitut                           | R. Golub, K. Korobkina   |
| Harvard University                             | J. Doyle   |
| University of Illinois                         | D. Beck, D. Hertzog, P. Kammel, J.-C. Peng, S. Williamson  |
| Institut Laue-Langevin                         | J. Butterworth   |
| University of Leiden                           | G. Frossati  |
| Los Alamos National Laboratory                 | P. D. Barnes, J. Boissevain, M. Cooper, M. Espy, S. Lamoreaux, A. Matlachov, R. Mischke, S. Penttila, J. Torgerson |
| University of Maryland                         | E. Beise, H Breuer, P. Roos  |
| Massachusetts Institute of Technology          | D. Dutta, H. Gao   |
| National Institute of Standards and Technology | T. Gentile, P. Huffman   |
| University of New Mexico                       | A. Babkin, R. Duncan   |
| Oak Ridge National Laboratory                  | V. Cianciolo   |
| Simon-Fraser University                        | M. Hayden  |

The spokespersons for the collaboration are Martin Cooper and Steve Lamoreaux.

The list of collaborators is expected to grow beyond those listed above as each institution adds colleagues, postdoctoral researchers, and graduate students. We expect a significant

number of Ph.D. and M.S. theses to come from this project, both from the development of the technique and the results of the search.

Future memberships in the collaboration by additional institutions shall be approved by the existing collaboration at a collaboration meeting. The executive committee (see chapter VII) may grant a temporary membership.

The Los Alamos National Laboratory's Physics Division will enter into formal agreements, memoranda-of-understanding (MOUs), with the universities and laboratories in the EDM collaboration. These MOUs outline the activities that members of each group are carrying out in collaboration with LANL Physics Division, and their responsibilities, funding and scheduling plans. Relevant managers at the collaborating institutions sign the MOUs, stating formally that their institute will support the efforts of their group's duties as outlined in the MOU. Although not legally binding in the strictest sense, these MOUs are the formal method to guide the relationship between LANL Physics Division and collaborators from other institutions.

An MOU between Physics Division and LANSCE Division will be negotiated that outlines the use of the beam. This MOU will cover the LANSCE commitment to the project, the allocation of beam time, funding of facility modifications, the safety envelope, and other issues.

## **B. Institutional Interests**

The areas of interest of the institutions are listed in the table below. The list covers the topics in the work breakdown structure (WBS) in Appendix B. At this time, we are forming teams from several institutions to address the tasks and to tackle the challenges. The details of assignments will be worked out by the time of the conceptual design review (CDR).

## Institutional Interests

| Institution                                    | Responsibility  |
|--|---|
| University of California at Berkeley           | cos $\theta$ magnet and enclosure, HV Measurement, SQUID pickup loops   |
| California Institute of Technology             | cos $\theta$ magnet and enclosure, $^3\text{He}$ transfer and polarization lifetime   |
| Hahn-Meitner Intitut                           | UCN production rates and lifetimes, Meaurement cell designs, Particle identification via afterpulses  |
| Harvard University                             | Measurement cell design   |
| University of Illinois                         | UCN production rates and lifetimes, Simulation, $^3\text{He}$ transport, Signal Detection   |
| Institut Laue-Langevin                         | Cryostat and radiation shields, Measurement cell designs, Light guides, Cryogenic feedthroughs  |
| University of Leiden                           | Dilution refrigerator, Cryostat and radiation shields, Polarized $^3\text{He}$ transfer   |
| Los Alamos National Laboratory                 | Neutron beam line and shielding, Dilution refrigerator, $^4\text{He}$ purifier prototype, HV capacitor prototype, SQUIDS, Physical plant, Integration and commissioning |
| University of Maryland                         | Simulation, $^3\text{He}$ polarization lifetime, Light detection  |
| Massachusetts Institute of Technology          | $^3\text{He}$ atomic beam source, Polarized $^3\text{He}$ transfer, Light guides  |
| National Institute of Standards and Technology | Meaurement cell designs, Light guides, $^3\text{He}$ transfer and polarization lifetime   |
| University of New Mexico                       | Superfluid valves   |
| Oak Ridge National Laboratory                  | Light guides  |
| Simon-Fraser University                        | $^3\text{He}$ source, spin-flip, transfer and polarization lifetime, Measurement cell design, SQUID response to $^3\text{He}$   |

## **VII. Management, Cost and Schedule**

The EDM collaboration will develop a management plan for the experiment as part of its preparations for a full technical review. This plan will be modeled after the one used by the  $np \rightarrow d\gamma$  experiment at LANSCE but with appropriate modifications to suit the needs of the EDM project. In this chapter, we will summarize the elements of the plan and will include a description of the proposed management team. Additionally, we will present the costs and schedule as part of the work breakdown structure down to level 2. A breakdown to level 3 and a discussion of the methodology will be found in Appendix B. Finally, we will enumerate the tools we will use to control cost and schedule overruns.

### **A. Management Team**

The management organization specifies responsibilities for getting the EDM experimental hardware designed, built, installed, and commissioned. Special attention will be given to the quality and integration of components of the experiment. The management team consists of the spokespersons, the project manager, the executive committee, and the work package leaders.

The spokespersons have overall responsibility for the design, construction, installation, and commissioning of the experiment and the beam line. They must control costs, keep the schedule and deliver performance. In their roles, the spokespersons report directly to the P-23 and P-25 Group Leaders and the LANL Nuclear Physics Program (NPP) manager. The spokespersons also have the responsibility of coordinating the work of the collaboration and responding to technical and scientific initiatives from the collaboration.

A project manager from LANL assists the spokespersons. The project manager is responsible for the project management of the construction project. He is responsible to provide information on the schedule and budget so that the spokespersons can deliver all necessary equipment on schedule and within the budget guidelines defined in this document. He shall establish the budgets and schedules for the construction of the experiment based on the information provided by the work package leaders. The project manager is responsible for tracking the progress of the project - cost and schedule - and reporting progress to the spokespersons, LANL management, and the DOE. He shall formulate the guidelines for making changes in the budget, the schedule or the performance, following the clear rules for the handling of contingency funds. He will give progress reports at meetings of the executive committee and at collaboration

meetings. Also, written EDM monthly status reports will be sent to the appropriate people.

The executive committee assists the spokespersons in the management of the project. The executive committee is composed of the spokespersons, the project manager, and four representatives of the collaboration representing the broad interests of the collaboration. Unresolved issues in the executive committee are reviewed by the collaboration. The collaboration meeting is the highest authority for decision making. The membership of the Executive Committee will be selected by the collaboration and may be changed in subsequent collaboration meetings. The elected members of the executive committee, with the exception of the spokespersons and project manager, will serve for a maximum two-year term. The executive committee has specific responsibilities regarding the approval of major change requests. The other functions of the committee will be to serve as the stewards of the experiment, consult regularly with each other and with the collaboration to facilitate communications, and to monitor the overall status of the project. The executive committee represents the collaboration in an advocacy role to funding agencies, LANSCE, Physics Divisions, and in other situations.

The work of constructing the EDM experiment is divided into work packages that are managed by work package leaders. A work package leader is responsible to lead and oversee the specifications, design, maintenance and operation of his/her work package. The allocation to carry out the work will be distributed by the spokespersons. The definition of all specifications and design parameters for the work packages will be given in the work package dictionary of the management plan. The work package leaders serve as information resources for the project manager by providing advice and additional information as needed. The work package leaders are responsible to report monthly on the status and progress of their work packages to the project manager.

## **B. Costs Summary**

The full capital-cost of the EDM construction will be \$11.1M based on the rollup of Microsoft Project file from level 3. In addition, \$1.5M will have already been spent on equipment from LANL LDRD funds during the development period, FY'01-'03, and it is expected that \$0.3M will be spent in FY'04. The collaboration will seek additional funds from LANL LDRD and from other institutions, e.g. from agencies that normally fund the operating costs of the collaboration. Whereas these future funds are not guaranteed, they are not counted below.

The cost estimate includes 23.5% taxes (LANL capital equipment rate) at the participating institutions and 40% average contingency. By the time of a future conceptual design review (CDR), it should be possible to reduce the contingency. Approximately \$1M of contingency has been pushed into FY'07 because it is most likely to be needed at the end of the project. The profile has been prepared in FY'02 dollars. In accordance with DOE escalation-rate assumptions, the cost have been converted to “then-year” dollars to produce the table below.

| Source        | US FY'01-03<br>\$k | US FY'04<br>\$k | US FY'05<br>\$k | US FY'06<br>\$k | US FY'07<br>\$k |
|---------------|--------------------|-----------------|-----------------|-----------------|-----------------|
| LDRD          | 1500               | Possible        | Possible        | Possible        | Possible        |
| Collaborators |                    |                 | Possible        | Possible        | Possible        |
| DOE NP        |                    |                 | 5400            | 3878            | 1805            |
| Total         | 1500               | 310             | 5400            | 3878            | 1805            |

The following summary has been taken from the WBS displayed to level 2. These costs are only for the construction project and do not include the LANL funds for FY'01-'04. WBS item1 (development) and those with zero cost have been deleted. For more details, refer to Appendix B.

| WBS      | Task                           | Cost    | Rolled-Up Cost   |
|----------|--------------------------------|---------|------------------|
| <b>2</b> | <b>Neutron Beam Line</b>       |         | <b>510,000</b>   |
| 2.1      | 6-m Guide                      | 130,000 |                  |
| 2.2      | t0 Chopper                     | 50,000  |                  |
| 2.4      | Bi Filter                      | 20,000  |                  |
| 2.5      | Beam Splitter                  | 300,000 |                  |
| 2.6      | Spin Flippers                  | 10,000  |                  |
| <b>3</b> | <b>Shielding</b>               |         | <b>110,000</b>   |
| 3.1      | Beam Line (BL)                 | 10,000  |                  |
| 3.2      | Experiment                     | 90,000  |                  |
| 3.3      | Beam Stop                      | 10,000  |                  |
| <b>4</b> | <b>Cryogenics</b>              |         | <b>1,280,000</b> |
| 4.1      | Gas Handling                   | 50,000  |                  |
| 4.2      | 4He Purifier                   | 200,000 |                  |
| 4.3      | Cryostat and Radiation Shields | 400,000 |                  |
| 4.5      | Gases                          | 80,000  |                  |
| 4.5      | Auxilliary Volumes             | 100,000 |                  |
| 4.6      | Support Equipment              | 150,000 |                  |
| 4.8      | 4He Recirculation System       | 300,000 |                  |
| <b>5</b> | <b>3He Atomic Beam Source</b>  |         | <b>80,000</b>    |
| 5.1      | Transport Tubes                | 50,000  |                  |
| 5.2      | Polarization Holding Coils     | 10,000  |                  |
| 5.3      | Procure 3He                    | 20,000  |                  |
| <b>6</b> | <b>Magnetic Shielding</b>      |         | <b>415,000</b>   |

|           |                                      |                   |                   |
|-----------|--------------------------------------|-------------------|-------------------|
| 6.1       | 5 Layer Conventional Shield          | 250,000           |                   |
| 6.2       | Superconducting Shield               | 100,000           |                   |
| 6.3       | Other Shielding                      | 15,000            |                   |
| 6.4       | Magnetic Penetrations                | 50,000            |                   |
| <b>7</b>  | <b>Magnets</b>                       |                   | <b>270,000</b>    |
| 7.1       | Constant Field Coil                  | 200,000           |                   |
| 7.2       | Power Supply                         | 30,000            |                   |
| 7.3       | Field Monitors                       | 20,000            |                   |
| 7.4       | 3He Spin Flip Coils                  | 20,000            |                   |
| <b>8</b>  | <b>High Voltage</b>                  |                   | <b>370,000</b>    |
| 8.1       | Gain Capacitor                       | 100,000           |                   |
| 8.2       | Electrodes and Corona Domes          | 150,000           |                   |
| 8.3       | Penetrations                         | 50,000            |                   |
| 8.4       | Cables                               | 50,000            |                   |
| 8.5       | Kerr Rotation HV Monitor             | 20,000            |                   |
| <b>9</b>  | <b>Measuring Cells</b>               |                   | <b>100,000</b>    |
| 9.1       | Cells                                | 50,000            |                   |
| 9.2       | Valves                               | 50,000            |                   |
| <b>10</b> | <b>SQUIDs</b>                        |                   | <b>150,000</b>    |
| 10.1      | SQUIDs                               | 80,000            |                   |
| 10.2      | Pick-up Loops                        | 10,000            |                   |
| 10.3      | Enclosures                           | 10,000            |                   |
| 10.4      | DR Insert                            | 50,000            |                   |
| <b>11</b> | <b>Light System</b>                  |                   | <b>110,000</b>    |
| 11.1      | Fiber Optics or Guides               | 10,000            |                   |
| 11.2      | Cryogenic Feedthroughs               | 50,000            |                   |
| 11.3      | Photomultiplier Tubes                | 50,000            |                   |
| <b>12</b> | <b>Electronics / Computers</b>       |                   | <b>110,000</b>    |
| 12.1      | Electronics                          | 75,000            |                   |
| 12.2      | Cables                               | 10,000            |                   |
| 12.3      | Computers                            | 25,000            |                   |
| <b>13</b> | <b>Conventional Construction</b>     |                   | <b>940,000</b>    |
| 13.1      | Platforms                            | 100,000           |                   |
| 13.2      | Electrical Plant                     | 200,000           |                   |
| 13.3      | Plumbing                             | 300,000           |                   |
| 13.4      | Mechanical Supports                  | 300,000           |                   |
| 13.5      | Jib Crane                            | 25,000            |                   |
| 13.6      | Isolation Platform                   | 15,000            |                   |
| <b>14</b> | <b>Management and Engineering</b>    |                   | <b>1,290,000</b>  |
| 14.1      | Project Manager                      | 190,000           |                   |
| 14.4      | Engineering During Construction      | 500,000           |                   |
| 14.5      | Technicians During Construction      | 600,000           |                   |
| <b>15</b> | <b>Integration and Commissioning</b> |                   | <b>100,000</b>    |
| 15.1      | Integration                          | 50,000            |                   |
| 15.2      | Commissioning                        | 50,000            |                   |
| <b>16</b> | <b>Institutional Costs</b>           |                   | <b>5,248,000</b>  |
| 16.2      | 40% Contingency During Construction  | 2,334,000         |                   |
| 16.3      | 23.5% Burden During Construction     | 1,920,000         |                   |
| 16.4      | Escalation                           | 994,000           |                   |
|           | <b>Totals</b>                        | <b>11,083,000</b> | <b>11,083,000</b> |

### C. Schedule Summary

In order to begin construction in FY'05, we anticipate having the project successfully pass a CDR and a technical, cost and schedule review. These reviews should be scheduled consistent with the needs of the funding agencies. Our expectation is that a year or so will pass between submission of the proposal and the reviews, and that many refinements will have been made to the apparatus as well as many new measurements will have been made that further support the feasibility of the experiment.

The EDM project has established 13 top-level milestones to mark progress toward an apparatus capable of making the EDM measurement. These milestones will be monitored to keep the project on schedule. The top-level milestones are

| WBS  | Milestone                                | Finish Date |
|------|--|-------------|
| 1    | EDM Development Complete                 | 9/30/04     |
| 5.4  | <sup>3</sup> He Atomic Beam Source Ready | 2/27/06     |
| 3.4  | Shielding Ready                          | 3/27/06     |
| 7.6  | Magnets Ready                            | 5/24/06     |
| 9.4  | Measuring Cells Ready                    | 5/24/06     |
| 11.4 | Light Systems Ready                      | 5/24/06     |
| 6.3  | Magnetic Shield Ready                    | 7/23/06     |
| 8.6  | High Voltage Ready                       | 9/21/06     |
| 10.4 | SQUIDs Ready                             | 9/21/06     |
| 13.5 | Conventional Construction Ready          | 9/21/06     |
| 2.7  | Beam Line Ready                          | 9/27/06     |
| 4.8  | Cryogenics Ready                         | 3/20/07     |
| 15.3 | First Data                               | 1/14/08     |

Most of these milestones occur in 2006 because this time is when the subsystems are completed and ready for integration into the full detector. The time coincidence is due to the significant amount of work that can be done in parallel. More details can be seen in the project charts in Appendix B. This schedule is heavily dependent on the funding profile actually achieved.

The goal of the milestones is to produce a working experiment at the beginning of 2008. The anticipation is that the experiment will be shaken down for a year by accumulating data that are ever closer to the required level of systematic errors. Roughly 6 months of data taking will follow, leading to an initial physics publication bettering the current limit by a factor of roughly 10. At this time, an evaluation will be made to select the best facility to complete the measurements to the  $10^{-28}$  e•cm level.

## **D. Management Tools**

In all respects, the construction, installation, testing, and commissioning of the EDM experiment must follow the LANL quality assurance guidelines. Additionally, all work has to be conducted in accordance with LANL Integrated Safety Management (ISM) and LANL Safe Work Practices. All the work has to satisfy fully LANL ES&H requirements.

The schedule for the construction of the EDM experiment was developed using Microsoft Project software and is based on planning information and milestones submitted by the collaborators. By the time of the technical review, the work package leaders will have reviewed these items. The main constraints on the overall schedule are the running periods of the facility and the final funding profile. The project manager will use Microsoft Project to monitor the progress of the construction project. The input will come from the management team and work package leaders. Variances will be reported to the experiment leadership and the oversight officials.

The progress of the EDM project will be reported to the DOE on a quarterly basis in the form of an EDM Project Quarterly Progress Report. This report will follow the format as set by the Nuclear Physics Division of the Department of Energy. The reports will be compiled and distributed by the project manager.

These reports will contain:

1. A narrative report of accomplishments and problems;
2. A milestone schedule and status reports, and;
3. A cost performance report.

In addition, the project manager will provide monthly progress reports to the LANL management, the executive committee, and the collaboration.

The management team, aided by the collaboration, has the responsibility for the technical decisions regarding R&D, engineering, design, fabrication, assembly, testing and installation of all the components. Technical changes require approval if they impact cost, schedule, or performance at levels exceeding those indicated in the following table:

Change request classification for the EDM project. Guidelines for changes in cost, schedule and/or performance with their respective approval levels.

| Class | Change in                                       |  |   | Approval  |
|-------|---|--|---|---|
|       | Cost  | Schedule                                     | Performance   |   |
| 1     | Minor, within WBS line item (<\$5k or 1%)       | “float”                                      | No impact   | Project Manager   |
| 2     | Within Work Package contingency, (>\$10k or 1%) | < 1 quarter delay of milestone               | Change in a part of work package that does not affect work package performance or scope | Above, plus Spokespersons                               |
| 3     | Within overall EDM contingency (>50k or 10%)    | > 1 quarter delay of milestone               | Change affects work package performance but does not effect EDM performance             | Above, plus Executive Committee and NPP Program Manager |
| 4     |   | > 1 quarter delay of major project milestone | Technical scope change, affects project capability                                      | Above, plus DOE   |

The EDM project manager will monitor the technical progress of the project, evaluating progress against the plan. Whenever technical changes are anticipated or proposed, the project manager will evaluate all ramifications. The project manager will monitor and evaluate schedule, cost, and interrelated construction and technical work variances to assess programmatic impacts. Should a baseline change be required, the project manager will initiate a change action to propose a baseline revision depending on whether the change is technical or cost/schedule related.

The basis for cost control is the baseline cost estimates of the EDM construction project established at WBS level 4 and shown in this document to level 3. Any changes to the cost of a WBS line item at Level 4 or above must follow the approval requirements indicated in the change request table. Cost control at lower WBS levels is the responsibility of the work package leaders, who will report to the project manager on a monthly basis. Using the Microsoft Project software, the project manager will track the costs.

The basis for schedule control is the milestone schedule contained in this document, which represents the best information available to the management team at the time of the technical review. The work package leaders will track and report their work package to WBS level 5 to the project manager, who, using the Microsoft Project software, will track and report down to WBS level 5. The project manager, together with the work package leaders, will update and revise the milestone schedule as needed.

The variance thresholds that would initiate corrective actions are described as follows:

Variance thresholds that will trigger corrective action

|            | Cost Variance | Schedule Variance |
|------------|---------------|-------------------|
| Period     | 25% & \$20k   | 25%               |
| FY         | 15% & \$50k   | 15%               |
| Cumulative | 10% & \$100k  | 10%               |

The EDM monthly status report will provide an explanation of the corrective action to be taken to address the problem that is causing the variances. This variance reporting and corrective action approach will provide an early warning of potential problems. Prompt recognition and corrective action at this level will help prevent implementation of the change management actions earlier.

Contingency funds are included in the EDM project estimate to cover uncertainties and risks. The current uncertainties in the scope of the project have led to the assignment of an overall contingency of 40%. The contingencies will be estimated prior to the CDR at the lowest WBS level as follows:

Guidelines used in estimating the contingencies for items in the EDM project budget.

| Contingency Formulae for EDM Budget Estimate |  |        |
|--|--|--------|
| Category                                     | Description  | Amount |
| Catalog                                      | <ul style="list-style-type: none"> <li>Equipment to be purchased through catalog</li> <li>Fixed price contract (with no rework expected)</li> </ul>                        | 5%     |
| Engineered                                   | <ul style="list-style-type: none"> <li>Design complete, fully estimated, before bid award</li> <li>Fixed price contracts (with some rework expected)</li> </ul>            | 15%    |
| Designed                                     | <ul style="list-style-type: none"> <li>Design complete, not fully estimated, before bid award</li> <li>Fixed price contracts (with significant rework possible)</li> </ul> | 25%    |
| Conceptual                                   | <ul style="list-style-type: none"> <li>Design incomplete, concept clear</li> </ul>   | 50%    |
|  | <ul style="list-style-type: none"> <li>Design incomplete, concept "notional"</li> </ul>  | >50%   |

The contingency funds are held in a separate account by the LANL NPP manager. All the EDM work packages that are funded with DOE capital funds shall follow the rules for contingency spending as outlined in the change request classification table. The use of contingency funds will be monitored closely, and the status of these funds will be reported to key project participants so that the project will not be jeopardized by a cost overrun.

## Appendix A Technical Issues

The design and information presented in this Pre-Proposal are not fixed or complete. A number of technical issues that are currently under study, both at Los Alamos through LDRD funding, and by the collaboration, are described in this Appendix. None of these issues will prevent the project from achieving its goals, but, rather, they are matters of technical optimization.

An important question is whether it will be possible to incorporate ferromagnetic shielding at temperatures below 4 K. If possible, the size of the low-temperature magnetic shield and  $^4\text{He}$  volume could be substantially reduced. The use of ferromagnetic shielding is preferable to superconducting shielding when a homogeneous field within the shield is required. The boundary condition for a superconductor cancels the field from a current carrying wire placed against it so there has to be a substantial spacing of the field generation wires from the shield surface. On the other hand, the boundary condition for an ideal high permeability ferromagnetic material is such that the field from a constant pitch winding on the inner surface is perfectly homogeneous [1]. A study of amorphous ferromagnetic materials is currently in progress.

The  $T_1$  and  $T_2$  lifetimes of polarized  $^3\text{He}$  for wall coatings compatible with UCN storage must be studied. Previous work has largely focussed on cesium coated cells; this coating is incompatible with UCN. On the other hand, long  $^3\text{He}$  polarization lifetimes have been obtained with solid hydrogen coated cells. This would suggest the possibility that frozen deuterium would be a mutually compatible wall coating. This issue remains to be studied, as well as the technology associated with transport of polarized  $^3\text{He}$  to cell; in this case, cesium coating can be used. The UCN polarization lifetime of these materials remains to be investigated; while there is essentially no useful experimental or theoretical information in the literature regarding this question, a simple estimate suggests that the depolarization per wall collision should be much less than  $10^{-5}$ . This is supported by recent experimental and theoretical work by the UCN A Coefficient Collaboration.

There are a number of issues associated with the scintillation light that require study. One question is whether the afterpulses from the  $\text{He}_2$  dimers can be used for event identification. This technique, in principle, could improve the signal-to-noise by discriminating beta decay and gamma backgrounds from the  $^3\text{He}$ -UCN reaction signal. Also there is only scant information regarding high voltage effects on scintillations. In particular, the effects of high voltage on our proposed storage cell geometry must be experimentally studied. One possible effect is that continuous microdischarges might generate intense background light that swamps the desired scintillation signal.

Other questions regarding the high voltage effects on the cell include the field homogeneity, charge buildup on the inner surfaces, and the magnitude of field that can be stably achieved. These are questions that we will study over the next year. A method of measuring the *in situ* field by use of the Kerr effect in liquid helium is under development at U.C. Berkeley.

The design of the cold neutron beam splitter and polarizer are also presently being studied. In principle, it should be possible to split into two oppositely polarized beams, and each of these directed to either of the cells (with a spin flipper in one beam), thereby utilizing the entire cold neutron flux. In practice, based on our initial calculations, the

length required for the spin separation and beam redirection is quite large, precluding its use at LANSCE. Such a system, if successful, would increase the number of stored UCN by up to a factor of two. It might be possible to use a Soller [2] configuration of multiple curved supermirror polarizer plates to reduce the length. On the other hand, traditional neutron beam polarization techniques that absorb the “wrong” spin state can be used within the available space at LANSCE.

Appropriate valves, possibly superfluid tight, that do not relax the  $^3\text{He}$  polarization must be developed.

Although we have experimentally investigated the diffusion and distribution of  $^3\text{He}$  in a superfluid filled cell, this work was done at comparably high concentration. Issues of spin diffusion, temperature gradient effects, and spatial distribution at very low concentrations remain to be studied. We are considering measurements using tomography with polarized  $^3\text{He}$  and a polarized cold neutron beam to study spin diffusion.

The “dressed spin” technique as discussed in the Physics Report [3] offers up to a factor of three increase in sensitivity. We did not discuss this technique in this Pre-Proposal because of the added complication. However, this technique could be studied using polarized  $^3\text{He}$  stored in a cell and a polarized cold neutron beam. We plan to design an experiment that will be compatible with this technique and incorporate it after we have a convincing demonstration of the SQUID based system.

[1.] I.B. Khriplovich and S.K. Lamoreaux, *CP Violation Without Strangeness* (Springer-Verlag, Heidelberg, 1997). See pp. 40-41.

[2.] J.M. Hayter, J. Penfold, and W.G. Williams, *Jour. Phys. E* **11**, 454 (1978).

[3.] R. Golub and S.K. Lamoreaux, *Phys. Rep.* **237**, 1 (1994).

## **Appendix B. Work Breakdown Structure**

This section describes the methodology used in creating the work breakdown structure (WBS) for the EDM project. The cost and schedule are planned with the project management program Microsoft Project. Following this description, the balance of this appendix is the output from that program. For the most part, the majority of the construction project is a single detection system consisting of many closely related components. The division into a WBS is a bit arbitrary, but it is an attempt to break the project into definable subsystems that can be built by separate groups of workers. This report will need to be supplemented with a much more detailed and carefully researched plan for the cost and schedule review.

The process to obtain the most significant pieces of equipment is broken into three parts, “design”, “procure”, and “install”. The division allows times, which can vary dramatically from item to item, to be individually assigned to the three stages. Design includes all engineering and prototype work. Procure is the time to obtain the parts from a vendor. Install means the effort to complete the task once the parts are owned by the collaboration. “Float” time has not been explicitly identified, but approximately 1/3 extra time has been added to each task.

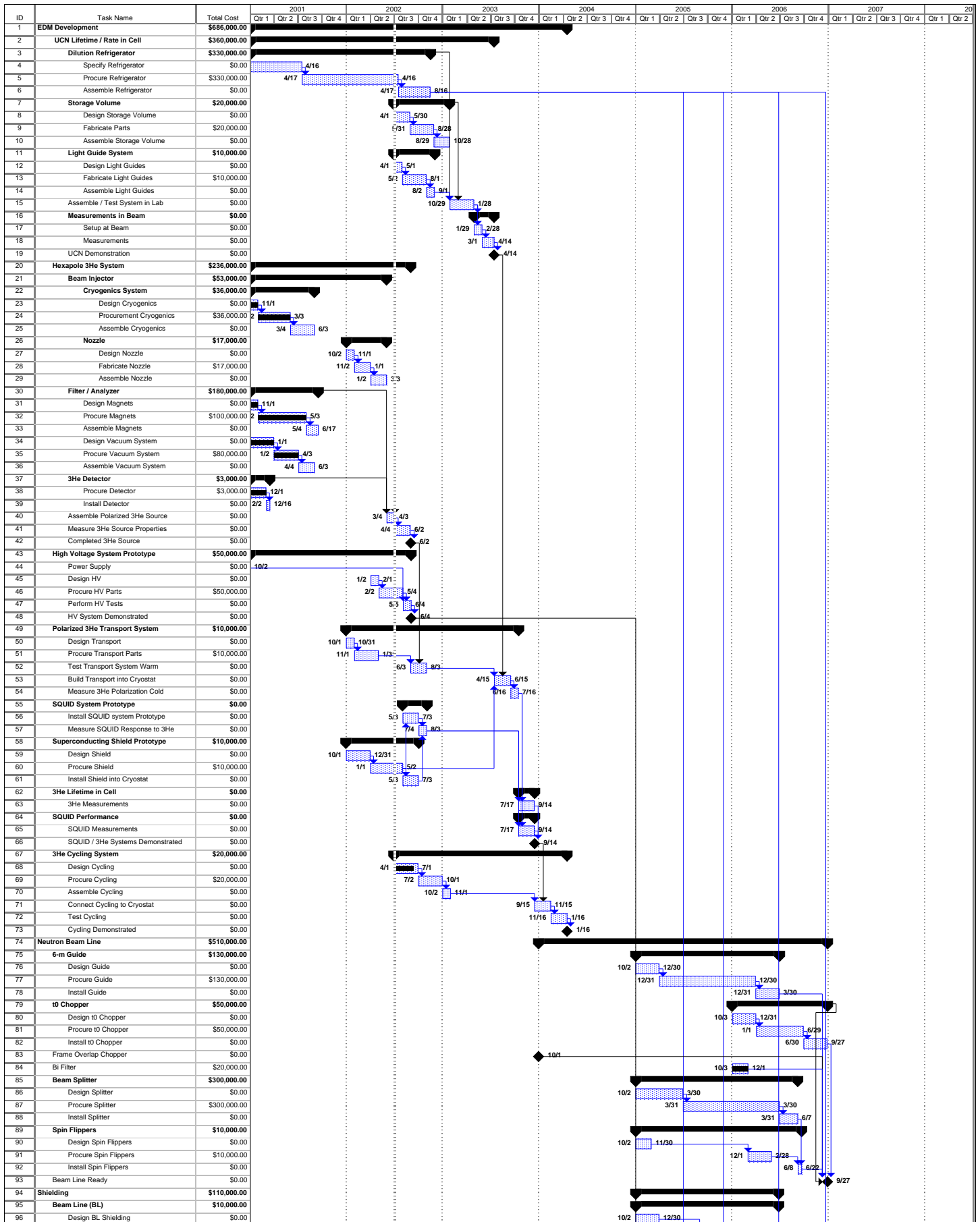
All costs are in “base” dollars. Base dollars are the money paid to vendors. The overhead or taxes at the procuring institution are handled as a lump sum (23.5% for capital equipment at LANL) at the end of the project under WBS element 16.3. Hopefully, some savings can be obtained in the future by purchasing through collaborating institutions. All costs are ascribed to the procure step. This assignment is made because the other steps are made with the labor of scientists that is not part of the construction project or of engineers and technicians that is included as a lump sum under WBS element 14. The level of engineering and technical support needed is based on experience, and no attempt to load level the staff resources has been made at this time.

For its current level of development, the contingency funds for the project are set to 40% of base cost, consistent with DOE guidelines as presented in Chapter VII. The contingency funds for the construction project are also calculated as a lump sum in WBS element 16.2.

The funding profile reported in Chapter VII is created using the summary report function within the Project program. About \$1M of the contingency funds have been moved manually into FY’07 because they will most likely be needed at the end of construction.

Institutional taxes have been applied to the contingency also. Finally, all costs were calculated in FY'02 dollars. WBS element 16.4 adds a lump sum for escalation base on the DOE escalation-rate assumptions calculated on a year-by-year basis.

WBS element 1 covers the research and development phase of the project and is shown for completeness. The burden rates are calculated somewhat differently because the majority of the money was not capital equipment. Engineering and technician costs are included in analogy with the construction project. The loaded result is reported in Chapter VII.



Project: EDM  
Date: Sun 3/31/02

Task: [Blue shaded bar] Summary: [Black arrow] Rolled Up Progress: [Thick black bar] Project Summary: [Thin black bar]

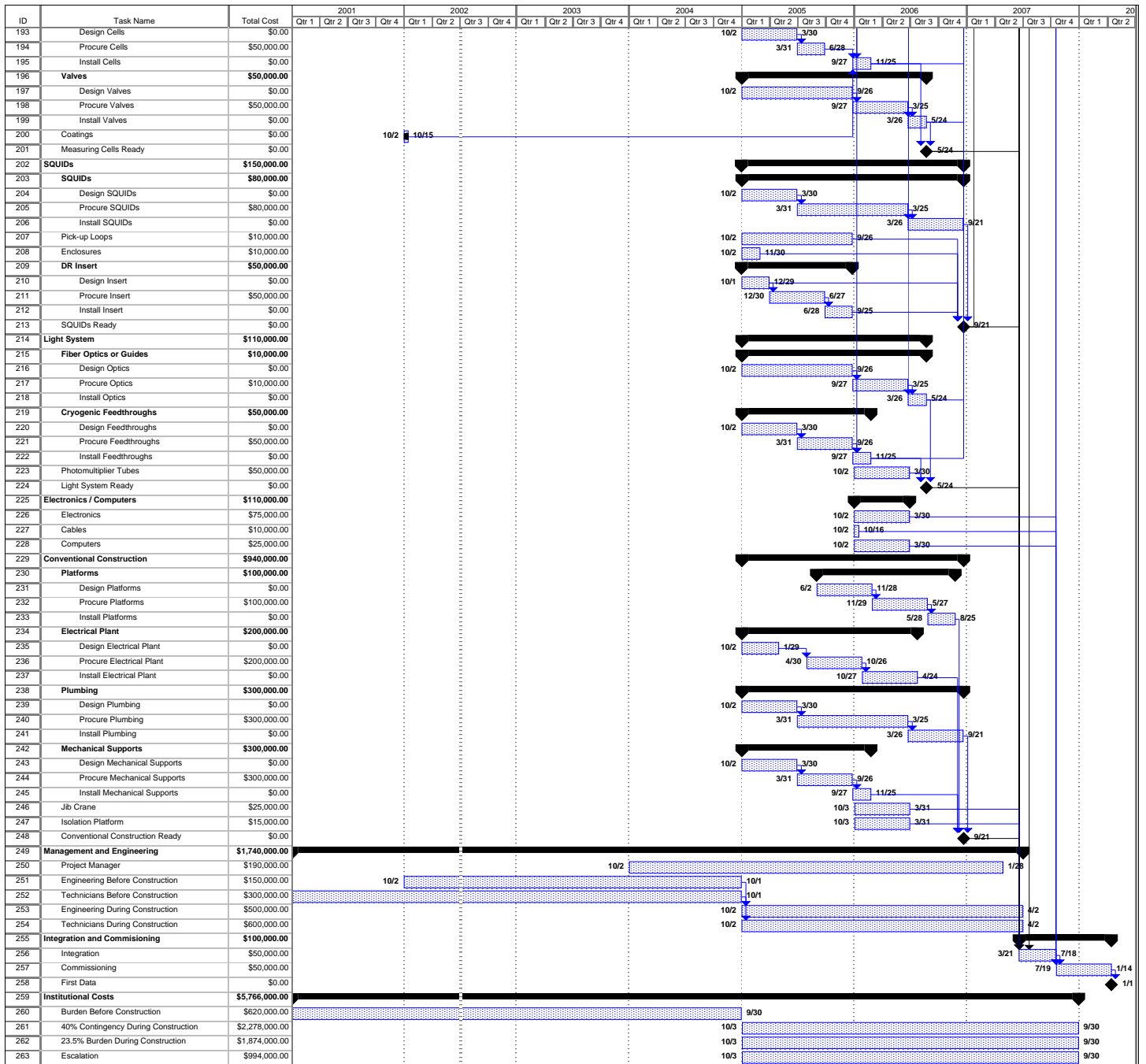
Progress: [Thin black bar] Rolled Up Task: [Blue shaded bar] Split: [Dotted line] Group By Summary: [Thick black bar]

Milestone: [Diamond] Rolled Up Milestone: [Diamond]

External Tasks: [Grey bar]

Page 1





## Appendix C: Biographies for the Collaboration

### Berkeley (University of California)

**Dmitry Budker**, Associate Professor in the Physics Department

Education: Ph.D. (Physics) UC at Berkeley (1993); MS Novosibirsk State U, USSR (1985)

Employment: UC at Berkeley and Faculty Scientist with LBNL (2001-), Assistant Professor (1995-2001), Postdoctoral Researcher (1993-95)

Publications: ~ 50 journal articles and 25 invited talks

Research: Dimitry Budker has worked on atomic physics tests of fundamental symmetries, laser spectroscopy, and high-sensitivity magnetometry.

**Alexander Sushkov**, Graduate Student in the Physics Department

Education: Graduate Student (Physics) UC at Berkeley, B.S. U of New South Wales, Sydney, Australia (1999)

Employment: LANL-Staff Research Assistant (2001-), UC at Berkeley (Physics) Graduate Student Research Assistant and Graduate Student Instructor (1999-2001)

Publications: 1 journal article

Experience: Alexander Sushkov has conducted research in theoretical and experimental condensed matter physics. His graduate research is in atomic low-temperature precision magnetometry.

**Valeriy Yashchuk**, Assistant Researcher in the Physics Department

Educational: Ph.D. (Physics) St. Petersburg Nuclear Physics Institute (PNPI), Russia (1994), MS (Nuclear Physics) St. Petersburg State U, Russia (1979).

Employment: UC at Berkeley Physics-Assistant Researcher (2000-), Postdoctoral Researcher (1997-2000), PNPI-Molecular Beam Laboratory, Junior Researcher, Researcher, (1981-97), Nucleus Fission Laboratory, Research Assistant (1979-81).

Publications: 28 journal articles, 6 Russian patents, and ~15 invited talks.

Research: Val Yashchuk has used atomic and molecular spectroscopy and beams for tests of fundamental symmetries. He has also employed nonlinear magneto- and electro-optics effects as well as high-sensitivity magnetometry.

## California Institute of Technology

**Brad Filippone**, Professor of Physics

Education: Ph.D. (Nuclear Physics) U of Chicago (1983), M.S. U of Chicago (1979), B.S. Pennsylvania State U (1977)

Employment: Caltech-Professor of Physics (1995-), Associate Professor (1990-95), Assistant Professor (1984-90), Argonne National Lab-Postdoctoral Physicist (1982-83)

Publications: Many journal articles and invited papers

Research: Brad Filippone is a member of the UCN A experiment and works in other areas of nuclear physics.

**Takeyasu Ito**, Senior Postdoctoral Scholar in Physics

Education: D.Sc (Physics) U of Tokyo (1997), M.S. (Physics) U of Tokyo (1994), B.S. (Physics) U of Tokyo (1992).

Employment: Caltech-Senior Postdoctoral Scholar (2001-), Postdoctoral Scholar (1998-2001), Laboratori Nazionali di Frascati, INFN, Italy-Postdoctoral Fellow (1998)

2. Institution and Department

W.K.Kellogg Radiation Laboratory

California Institute of Technology

Publications: 12 journal articles and 4 invited talks

Research: Takeyasu Ito has studied the low-energy kaon-nucleon interaction, exotic atoms, parity violating electron scattering, neutron beta decay, and ultracold neutrons.

**Robert McKeown**, Professor of Physics

Education: Ph.D. (Physics) Princeton U. (1979), B.A. (Physics) State U. of New York at Stony Brook (1974).

Employment: Caltech-Professor (1992-), Associate Professor (1986-92), Assistant Professor (1981-86), Argonne National Lab-Assistant Physicist (1979-80), Research Associate (1978-79).

Publications: 99 journal publications, 1 book edited, many invited talks.

Research: Bob McKeown has experience in nuclear physics, weak interactions, polarized  $^3\text{He}$  target development, parity violating electron scattering, neutrino oscillations, ultra-high energy cosmic rays.

## **Hahn-Meitner Institut**

### **Robert Golub, Research Fellow**

Education: Ph.D. (Physics) Mass. Inst. of Technology (1968), M.Sc (EE) Mass. Inst. of Technology (1960), B.Sc. (EE) City College, NY (1959).

Employment: Hahn-Meitner Institut (1991-), Technical U Berlin (1986-91), Max Plank Institut for Physics, Freimann, Germany (1985-86), Technical U Berlin (1980-85), U of Sussex, England (1968-80), Brandeis U (1967-68).

Publications: 97 journal articles, 1 book, and 7 review papers and ~100 invited talks.

Research: Robert Golub's research interests are concentrated in three areas at present: ultracold neutrons (UCN), spin echo spectroscopy and general considerations in the design of neutron scattering instruments. UCN studies include the interaction of neutrons with superfluid He and applications of UCN-induced scintillations in He to neutron EDM and lifetime experiments. His spin echo work concerns development of the technique of zero field neutron spin-echo high-resolution spectroscopy. There are currently 6 instruments in existence or under construction. He is also applying space-time correlation functions to the design of neutron scattering instruments.

### **Ekaterina Korobkina, Research Scientist**

Education: Ph.D. (Nuclear Physics) Moscow Engineering Physics Institute (1990), Diploma (Engineering Physics) Moscow Engineering Physics Institute (1981), Degree (Physics) Far Eastern U (1978).

Employment: Hahn-Meitner-Institut-Research Scientist (2000-), Johannes Gutenberg U-Visiting Scientist (1999-2000), RRC Kurchatov Institute-Staff Physicist (1992-), Institute of Space Research, Moscow-Staff Engineer (1986-91).

Publications: 9 journal articles

Research: Ekaterina Korobkina is interested in ultra cold neutron interaction with condensed matter, radiative capture and its application to surface and coating studies, downscattering in LHe for UCN production, upscattering at low temperature and quasielastic scattering on liquid surface. UCN storage and production; application of non and polarised He-3 to neutron polarization and detection, search for parity and time non-invariant correlation in reactions with slow neutrons.

## Harvard University

**John Doyle**, Professor of Physics

Education: Ph.D. (Condensed Matter and Atomic Physics) Massachusetts Institute of Technology (1991) Thesis: Energy Distribution Measurements of Magnetically Trapped Spi- Polarized Hydrogen: Evaporative Cooling and Surface Sticking.

Employment: Harvard-Professor of Physics (2000-), John L. Loeb Associate Professor of the Natural Sciences and Associate Professor of Physics (1997-99)

Harvard University, 1993-1997, Assistant Professor of Physics (1993-97), MIT-Postdoctoral Associate (1991-93).

Selected Publications: Buffer-gas Loading and Magnetic Trapping of Atomic Europium, J.Kim, B. Friedrich, D.Katz, D. Patterson, J. Weinstein, R. DeCarvalho and J.M Doyle, Physical Review Letters 78, 3665-8 (1997).

Magnetic Trapping of Calcium Monohydride Molecules at Millikelvin Temperatures, J.D.Weinstein, R. deCarvalho, T. Guillet, B. Friedrich, and J.M.Doyle, Nature 395, 148-50 (1998).

Magnetic Trapping of Neutrons, P.R. Huffman, C.R. Brome, J.S. Butterworth, K.J. Coakley, M.S. Dewey, S.N. Dzhosyuk, R. Golub, G.L.Greene, K.Habicht, S.K.

Lamoreaux, C.E.H. Matooni, D.N. McKinsey, F.E.Wietfeldt, J.M. Doyle, Nature 403, 62 (2000).

No-sticking effect and quantum reflection in ultracold collisions, Areez Mody, Eric Heller, and J.M.\ Doyle, Physical Review B 64 085418-1/15 (2001).

Evaporative Cooling of Atomic Chromium, J.D. Weinstein, R. deCarvalho, C.Hancox, J.M.Doyle, Physical Review A 65 0216

Research: John Doyle's interests include trapping of ultracold neutrons and trapping of atoms and molecules. Past work has included (from oldest to newest) the cryogenic hydrogen maser, trapping of atomic hydrogen, evaporative cooling of atomic hydrogen, theory of evaporative cooling in magnetic traps, study of particle motions in magnetic traps, the demonstration of quantum reflection of atomic hydrogen from liquid helium, 1S-2S two-photon spectroscopy of trapped atomic hydrogen and theory of collisions, proposal and demonstration of buffer-gas loading of magnetic traps, magnetic trapping of atomic chromium and europium, magnetic trapping of CaH molecules, spectroscopy of VO and CaH, spectroscopy of PbO for EDM searches, study of scintillations in helium, magnetic trapping of ultracold neutrons, proposal for cryogenic detection of p-p neutrinos, development of methods for creation of large Bose condensates, trapping and cooling of fermionic chromium, measurement of the neutron beta-decay lifetime, direct beam loading into buffer-gas, trapping of NH, scintillation properties of neon.

## **University of Illinois at Urbana-Champaign**

**Douglas Beck**, Professor in the Physics Department

Education: Ph.D. (Physics) Mass. Inst. of Tech. (1986).

Employment: U. of Illinois-Professor of Physics (1989-), Caltech-Senior Research Fellow (1986-89).

Publications: ~ 40 journal articles and 40 invited talks.

Experience: Doug Beck has research experience in few-body nuclear and precision electroweak parity-violation physics.

**David Hertzog**, Professor in the Physics Department

Education: Ph.D. (Particle Physics) College of William & Mary (1983), M.S. (Particle Physics) College of William & Mary (1979), B.S. (Physics) Wittenberg U. (1977)

Employment: U. of Illinois-Professor of Physics (1997-), Associate Professor (1992-97), Assistant Professor (1986-92), Carnegie-Mellon U.-Research Associate, (1983-1986).

Publications: ~135 journal and conference papers and >70 invited talks.

Research: David Hertzog has worked on medium-energy experiments at the AGS, CERN, TRIUMF and PSI. His research activities include experiments in low-energy antiproton physics (at LEAR), exotic atoms, and precision measurements of muon properties such as the anomalous magnetic moment and the muon lifetime. He is co-spokesman of the muLan experiment at PSI.

**Peter Kammel**, Research Associate Professor in the Physics Department

Education: Ph.D. (Physics) U. of Vienna, Austria (1982).

Employment: U. of Illinois-Research Associate Professor (2000-), UC at Berkeley-Co-Principal Investigator, Medium Energy Physics Group (2000), Research Scientist (1985-86, 1994-2000), Austrian Academy of Sciences-Research Scientist (1982-94).

Publications: >100 refereed articles and 12 invited talks.

Research: Peter Kammel has worked on medium-energy physics experiments at PSI, TRIUMF, BEVELAC, AGS and CERN. The projects include, in particular, high precision electro-weak experiments with muons. He is co-spokesman of the MuCap experiment at PSI.

**Jen-Chieh Peng**, Professor in the Physics Department

Education: Ph.D (Nuclear Physics) U of Pittsburgh (1975), B.S. (Physics) Tunghai U, Taiwan (Republic of China) (1970)

Employment: Professor of Physics, U of Illinois (2002-), Technical Staff Member of Subatomic Physics Group / Lab Fellow, LANL (1978-2002), Senior Research Associate, U of Pittsburgh (1977-78), Research Associate in Nuclear Physics, Centre d'Etudes Nucleaires de Saclay, France

Publications: ~150 journal articles and 50 invited talks.

Research: Jen-Chieh Peng had worked on accelerator based medium-energy experiments at LAMPF, AGS, Fermilab and CERN. He has been spokesman or co-spokesman of 8 experiments at these facilities. His research activities include parton structure in nucleon and nuclei, hypernuclei, proton-nucleus interactions, meson production, heavy-quark production, and fundamental physics with neutrons.

**Steven Williamson,**

**Institut Laue-Langevin**

**James Butterworth**, Co-responsible for the PF2 Ultracold Neutron Source

Education: Ph.D. (Physics) U of Grenoble, France (1996), MSc. (Superconductivity and Cryogenics) U of Southampton, UK (1992), BSc. (Electronic Engineering and Physics) U of Loughborough, UK (1990).

Employment: ILL, Grenoble, France-Co-responsible for the PF2 Ultracold Neutron Source (1999-), Harvard U-Postdoctoral Research Associate (1996-98), Brush Traction Ltd., Loughborough, UK-Design Engineer (1991)

Publications: 18 journal articles

Research: James Butterworth has done a spectroscopic study of the upscattering of UCN from superfluid helium, ultra-high resolution thermometry in the region of the superfluid Transition, and magnetic trapping of ultracold neutrons in superfluid helium.

**University of Leiden**

**Giorgio Frossati**, Professor of Experimental Physics

Education: Ph.D. Centre des Recherches sur les Très Basses Températures of the CNRS (1980), M.S. U of S. Paulo (1967), B.S. U of S. Paulo (1969)

Employment: Leiden-Professor of Experimental Physics (1980-), Chairman of the Kamerlingh Onnes Laboratory (1991-93).

Publications: ~170 papers and 100 talks

Research: Giorgio Frossati has specialized in quantum fluids and solids, particularly solid and liquid  $^3\text{He}$ ,  $^4\text{He}$ , mixtures of  $^3\text{He}$  in  $^4\text{He}$  and the quantum effects due to nuclear polarization of  $^3\text{He}$ , magnetic resonance imaging for medical application and nuclear fusion. Cryogenic techniques associated with the production and measurement of ultralow temperatures. Visual observation of quantum crystals using a cold CCD camera at ultra low temperatures in high magnetic field. Low temperature gravitational wave detectors

## **Los Alamos National Laboratory**

**Peter D. Barnes**, Technical Staff Member of the Subatomic Physics Group

Education: Ph.D. (Physics) Yale University, 1965, B.S. (physics) University of Notre Dame, 1959

Employment: LANL-Technical Staff Member, SubAtomic Physics Group (1999-), Director of the Physics Division (1993-99), Director of LAMPF and MP Division (1991-93), Carnegie-Mellon U.-Professor of Physics (1968-91), LANL-Postdoctoral Fellow (1966-68), Niels Bohr Institute, Copenhagen, Denmark-Postdoctoral Fellow (1964-66).

Publications: ~150 journal articles and ~40 invited talks at Conferences

Research: Peter Barnes has worked on accelerator based nuclear and particle physics experiments at LANSCE, RHIC, AGS, CERN, LAMPF, the ZGS, and various Van de Graaff accelerator facilities, and as leader of the nuclear and particle physics group at CMU. His research has addressed: formation and x-ray decay of kaonic, antiprotonic, and sigma atoms, pion and kaon -nuclear interactions, spectroscopy of hypernuclear systems, studies of hyperon-antihyperon interactions, time reversal invariance tests, measurement of the sigma magnetic dipole moment, investigation of the hyperon-nucleon weak interaction, collisions of relativistic heavy ions at ultra high energies and energy densities, and fundamental physics with neutrons.

**Jan Boissevain**, Technical Staff Member of the Subatomic Physics Group

Education: B.A. (Physics) UC at Santa Barbara (1969).

Employment: LANL- Technical Staff Member (1986-), Technician (1973-85).

Publications: ~50 journal articles

Experience: Jan Boissevain has extensive experience designing and constructing a wide range of physics experimental apparatus: cryogenic refrigerators, wire chambers, silicon detectors, scintillators, and electronics system integration.

**Martin Cooper**, Deputy Group Leader of the Subatomic Physics Group

Education: Ph.D. (Physics) U of Maryland (1971), B.S. (Physics) Cal. Inst. of Technology (1967)

Employment: LANL-Deputy Group Leader of Subatomic Physics Group (1999-), Technical Staff (1975-99); Director's Postdoctoral Fellow, LANL (1974-75), Research Associate, U of Washington (1971-74).

Publications: ~90 journal articles and 35 invited talks.

Research: Martin Cooper has worked in fundamental symmetry measurements, pion-nuclear physics, rare-muon decays, and neutron physics. He was spokesman for the MEGA experiment

**Michelle Espy**, Technical Staff Member of the Biophysics Group

Education: Ph.D. (Physics) U of Minnesota (1996), B.S. (Physics) UC at Riverside (1991).

Employment: LANL-Technical Staff Member of Biophysics Group (1999-), Director's Postdoctoral Fellow (1996-99) of Biophysics Group

Publications: 17 journal articles

Research: Michelle Espy has development of novel SQUID-based systems for detection of minute ( $<10^{-12}$  T) magnetic fields of biological and non-biological origin. She has a background in experimental nuclear physics including polarized  $^3\text{He}$  targets.

**Steve Lamoreaux**, Laboratory Fellow of the Neutron Science Group

Education: Ph.D. (Physics) U of Washington (1986), M.S. (Physics) University of Oregon (1982), B.S. (Physics) University of Washington (1981).

Employment: LANL-Laboratory Fellow (1998-), Technical Staff Member (1996-98), U Washington, Physics Dept.-Research Associate Professor (1995-96), Postdoctoral Fellow (1986-94).

Publications: 70 journal articles, two books, ~50 invited talks

Research: Steve Lamoreaux has worked on cold and ultracold neutron (both experimental techniques and theory). He also works in atomic and laser spectroscopy with applications to fundamental measurements, ultra-sensitive magnetometry; radio frequency spectroscopy; quantum cryptography and quantum computing (both theory and experiment).

**Andrei Matlachov**, Technical Staff Member of the Biophysics Group

Educational: Ph. D. (Physics) Russian Academy of Sciences (1988)

Employment: LANL-Technical Staff Member (1998-), Conductus, Inc., Sunnyvale, CA

Publications: ~70 journal articles and 8 invited talks

Research: Andrei Matlachov works with LTS and HTS SQUID design and applications, biomagnetism and SQUID instrumentation for biomagnetic applications, SQUID-based instrumentation for non-destructive evaluation (NDE), material science, solid state physics, fundamental physics; high-resolution SQUID susceptometry.

**Richard Mischke**, Technical Staff Member of the Subatomic Physics Group

Education: Ph.D. (Physics) U. of Illinois (1966), M.S., U. of Illinois (1962), B.S. U. of Tennessee (1961)

Employment: LANL-Technical Staff Member (1971-), Princeton University (1966-71)

Publications: 72 journal articles and many invited talks.

Research: Richard Mischke works in experimental nuclear and particle physics with an emphasis on weak interactions and symmetry tests including parity violation in nucleon-nucleon scattering and rare decays of the pion and muon.

**Seppo Penttila**, Technical Staff Member of the Neutron Science Group

Education: Ph.D. (Physics) U. of Turku, Finland (1975), Licenciante of Philosophy, U. of Turku, Finland, M.Sc. (Physics) U. of Turku, Finland

Employment: LANL-Technical Staff Member (1985-), CERN-Scientific Associate (1982-84), U. of Turku, Finland-Assistant Professor of Physics (1976-84).

Publications: 96 journal articles and 30 invited talks.

Research: Seppo Penttila has searched for parity violation and time reversal invariance violation in neutron reactions, the neutron electric dipole moment, and extensions to electroweak SM through neutron beta decay. He has studied other fundamental physics with low energy neutrons, searched for the proton's weak charge in electron scattering, and studied the spin structure of nucleon with electron and photon scattering. He has extensive experience in cryogenics and neutron technology.

**Justin Torgerson**, Fredrick Reines Postdoctoral Fellow in the Neutron Science Group

Education: Ph.D (Physics) University of Rochester

Employment: LANL- Frederick Reines Postdoctoral Fellow, U. of Washington-Postdoctoral Researcher.

Publications: 15 journal articles and 4 invited talks.

Research: Justin Torgerson has studied a variety of optical coherence phenomena including quantum phase, two-photon coherences and fundamental tests of quantum mechanics and local realism. He has also studied single trapped ions as possible ultra-precise optical frequency references. In particular, he was involved in two experiments

that were based on In II and Ba II ions for which he designed, constructed and employed a wide variety of experimental apparatus.

## **University of Maryland**

**Elizabeth Beise**, Professor of Physics

Education: Ph.D. (Physics) Massachusetts Institute of Technology (1988), B.A. Carleton College (1981).

Employment: U. of Maryland-Professor (2002-), Associate Professor (1997-2002), Assistant Professor (1993-97), Caltech-Senior Research Fellow (1990-93), Research Fellow (1988-90).

Publications: 42 journal articles, 1 book, 21 invited talks

Research: Elizabeth Beise has performed experimental studies of the structure of the nucleon and of light nuclei using electromagnetic and weak electron scattering. She was co-spokesperson of two recent experiments: parity-violating electron-deuteron scattering at 200 MeV at MIT-Bates (SAMPLE-II) and measurement of deuteron tensor polarization at high momentum transfer at JLAB ("JLab-t20"). She is presently computation manager for the Jlab G0 experiment and has experience with data acquisition and analysis and cryogenic target systems.

**Herbert Breuer**, Associate Research Scientist

Education: Ph.D. (Physics) University of Heidelberg (1976), Diploma (Physics) University of Heidelberg (1974)

1968-74, Physics at the Universities of Mainz, Hamburg, and Heidelberg, West Germany

Employment: U. of Maryland-Associate Research Scientist (1985-), Assistant Professor (1979-85), Research Associate (1977-79), Max-Planck-Institut fuer Kernphysik, Heidelberg-Research Associate (1976-77).

Publications: 109 journal articles and 9 invited talks

Research: Herbert Breuer planned, mounted, performed, and analyzed experiments in nuclear spectroscopy, heavy ion reactions, pion absorption, electron induced reactions. He is currently mostly involved in the preparation of experiments at Jlab (primarily G0) and detector development.

**Philip Roos**, Professor of Physics

Education: Ph.D. (Physics) Massachusetts Institute of Technology (1964) B.A. Ohio Wesleyan U. (1960)

Employment: U. of Maryland-Professor of Physics (1975-), Associate Professor of Physics (1971-75), Assistant Professor of Physics (1967-71), ORNL-Atomic Energy Commission Postdoctoral Fellow (1965-67), U. of Maryland-Visiting Assistant Professor of Physics (1964-65).

Publications: 111 journal articles and 23 invited talks

Research: Philip Roos has more than 38 years of experience in experimental nuclear physics research, most of it accelerator based research. I have had extensive experience in the measurement of nuclear reactions, particularly reactions induced by hadrons (p, alpha, pi-mesons) and more recently by electrons. I have utilized almost all types of particle detectors and electronics currently in use in the field of nuclear and particle physics. Currently I am Deputy Spokesperson for a major parity violation measurement in elastic electron-nucleon scattering at Jefferson Lab (G0 experiment).

### **Massachusetts Institute of Technology**

**Dipankar Dutta**, Postdoctoral Research Associate, Laboratory for Nuclear Science

Education: Ph.D. Northwestern University (1999)

Employment: MIT-Postdoctoral research associate (1999-)

Publications: 18 refereed articles and 7 invited talks.

Research: Dipankar Dutta has studied inclusive and exclusive electron scattering in nuclear interactions, nucleon propagation through nuclear matter and its significance to nucleon-nucleon interactions. He has also studied the spin structure of the nucleon and the quark-gluon description of the strong force. The tools have been electron scattering with polarized beams and targets. He has participated in experiments searching for signatures of QCD in nuclei and precision measurements of fundamental properties of the nucleon that involved the development of a laser driven polarized hydrogen target. He also has experience with a polarized helium-3 target that was part of a measurement of neutron magnetic moment.

**Haiyan Gao**, Associate Professor of Physics

Education: Ph.D. (Nuclear Physics) Cal. Inst. of Technology (1994), B.S. Tsinghua U, Beijing, China (1988).

Employment: MIT-Associate Professor (2002-), Assistant Professor (1997-2002), Assistant Physicist, Argonne NL (1996-97), Postdoctoral Research Associate, U of Illinois, Urbana-Champaign (1994-96).

Publications: ~36 journal articles and 29 invited talks.

Research: Haiyan Gao's research focuses on understanding the structure of nucleon and exclusive nucleon and nuclear processes at high energies in terms of the quark and gluon degrees of freedom of quantum chromodynamics using high energy electron and photon beams as probes. Most of her work utilizes the novel experimental technique of scattering longitudinally polarized electrons from polarized nuclear targets. She has conducted research at MIT-Bates, SLAC, DESY, IUCF and Jefferson Lab and has had more than 10 years of experience in polarized He3 external gas targets, laser-driven polarized H/D internal gas targets and the NMR techniques.

### **National Institute of Standards and Technology**

**Thomas Gentile**, Physicist in the Ionizing Radiation Division

Education: Ph.D. (Physics) Massachusetts Institute of Technology (1989), B.S. (Physics) State U. of New York at Stony Brook (1979).

Employment: NIST-Physicist (1993-), Caltech-Postdoctoral Fellow (1990-93).

Publications: 21 journal and 12 invited talks

Research: Tom Gentile has worked on the development and application of neutron spin filters based on polarized 3He; metastability-exchange and spin-exchange optical pumping of 3He, optical radiometry, Rydberg atom studies.

**Paul Huffman**, Physicist

Education: Ph.D. (Nuclear Physics) Duke U. (1995), M.A. (Physics) Duke (1992), B.S. (Physics) North Carolina State U. (1990).

Employment: NIST-Physicist (2000-), National Research Council Postdoctoral Associate (1998-2000), Harvard-Associate (1998-), Postdoctoral Fellow (1995-98).

Selected Publications:

C. R. Brome *et al.* *Magnetic Trapping of Ultracold Neutrons*. Phys. Rev. C, **63**, 055502 (2001).

P. R. Huffman *et al.* *Magnetically Stabilized Luminescent Excitations in Hexagonal Boron Nitride*. J. Lumin., **92**, 291 (2001).

P. R. Huffman *et al.* *Magnetic Trapping of Neutrons*. Nature, **403**, 62 (2000).

D. N. McKinsey *et al.* *Radiative Decay of the Metastable  $He^2(a^3\Sigma_u^+)$  Molecule in Liquid Helium*. Phys. Rev. A, **59**, 200 (1999).

P. R. Huffman, C. R. Gould and D. G. Haase. *The Deformation Effect and Time-Reversal Violation in Neutron Resonances*. J. Phys. G, **24**, 763 (1998).

P. R. Huffman *et al.* *Test of Parity-Conserving Time-Reversal Invariance Using Polarized Neutrons and Nuclear Spin Aligned Holmium*. Phys. Rev. Lett., **76**, 4681 (1996).

C. D. Keith *et al.* *Measurements of the Total Cross Section for the Scattering of Polarized Neutrons from Polarized  $^3\text{He}$* . Phys. Rev. C, **54**, 477 (1996).

W. S. Wilburn *et al.* *Measurements of Polarized Neutron – Polarized Proton Scattering: Implications for the Triton Binding Energy*. Phys. Rev. Lett., **71**, 1982 (1993).

Research: Paul Huffman's research has centered around the production and trapping of ultracold neutrons for use in experiments to determine the weak force coupling constants and also to search for the permanent electric dipole moment of the neutron.

## **University of New Mexico**

**Alexei Babkin**, Research Associate Professor of Physics

Education: Dr. Sci Kapitza Institute for Physical Problems (1999), Ph.D. Kapitza Institute for Physical Problems (1986), M.A. Moscow Institute for Physics and Technology (1980)

Employment: U. of New Mexico-Research Associate Professor of Physics (2001-), Research Assistant Professor of Physics (1999-2001), Helsinki U. of Technology, Finland-Research Fellow (1991-96), Lebedev Physical Institute, Moscow-Head of Cryogenic Department (1987-91).

Publications: ~60 journal articles and 1 book.

**Robert Duncan**, Professor of Physics

Education: Ph.D. (Physics) U. of California at Santa Barbara (1988), S.B. (Physics) Massachusetts Institute of Technology (1982).

Employment: U. of New Mexico-Professor of Physics (2001-), Associate Professor of Physics (1996-2001), Sandia National Lab-Distinguished Member of the Technical Staff (1995-96), Technical Staff (1988-95).

Publications: Many journal articles, 1 patent, and many invited talks.

Research: Rob Duncan is an experimental physicist specializing in critical phenomena near the  $^4\text{He}$  superfluid transition, superconductivity, and in the development of ultra low-noise measurement techniques and their associated miniature cryogenic refrigeration systems for space and terrestrial deployment.

## **Oak Ridge National Laboratory**

**Vincent Cianciolo**, Staff Member

Education: Ph.D. (Physics) Massachusetts Institute of Technology (1994), B.S. (Physics) U. of Michigan, Ann Arbor (1988).

Employment: ORNL-Staff Member (1997-), Lawrence Livermore-Postdoctoral Research Associate (1995-96), MIT-Postdoctoral Research Associate (1994).

Publications: 24 journal articles.

Research: Vince Cianciolo has significant experience in a variety of experimental nuclear physics areas, including: design and implementation of an advanced second-level trigger for BNL experiment E859; design, prototyping and construction of the PHENIX Muon Identifier (MUID) panels (\$3.5M worth of Iarocci-tube based detectors covering 1300 m<sup>2</sup>); design and management responsibilities for the MUID readout electronics (\$1.4M, >6000 channels); development of experimental Monte Carlo simulation and calibration packages; world's first HBT analysis of identical kaons in heavy-ion collisions; development of the "default" PHENIX run plan emphasizing systematic exploration of species variation (light ions and asymmetric collisions).

## **Simon-Fraser University**

**Michael Hayden**, Assistant Professor of Physics

Education: Ph.D. (Physics) U. British Columbia, Vancouver BC Canada (1992), M.A.Sc. (Engineering Physics) 1986 U. British Columbia, Vancouver BC Canada (1986), B.Eng. Univ. Sask. Saskatoon SK (1984).

Employment: Simon-Fraser-Assistant Professor (1998-), U. of Brit. Col.-Research Associate and Lecturer (1997-98), LANL-Postdoctoral Fellow (1994-97), Ecole Normale Supérieure-NSERC Postdoctoral Fellow (1992-94), U. of Brit. Col.-Research Engineer (1986-87).

Publications: 28 journal articles and 20 invited talks

Research: Mike Hayden has experience with precision AMO techniques, magnetic resonance, superfluid 4He and cryogenic transport of highly spin-polarized 3He, metastability-exchange optical pumping of 3He, neutron radiography, and thermoacoustics.